Doctoral Dissertation
博士論文

Search for the scalar top quark in the final state with jets and missing transverse momentum with the ATLAS detector at the LHC

(LHC-ATLAS 実験におけるジェットと消失横運動量を持つ終状態を用いたスカラートップクォークの探索)

A Dissertation Submitted for the Degree of
Doctor of Philosophy
November 2020
令和2年11月博士（理学）申請

Department of Physics, Graduate School of Science,
The University of Tokyo
東京大学大学院理学系研究科物理学専攻

Yi-Lin Yang
楊易霖

Abstract

Supersymmetry theory (SUSY) can explain unsolved problems in the Standard Model of particle physics, such as, dark matter observed in the universe, the unification of coupling constants of the electromagnetic, weak, and strong interactions and hierarchy problem of the mass of the Higgs boson. The 125 GeV mass of the Higgs boson, which was observed at the LHC, is too light for the naturalness in the Standard Model unless new mechanism to stabilize the Higgs mass is introduced. The superpartners of the top quarks, which are called scalar top quarks, can provide a key solution for the observed Higgs mass according to the prediction of natural SUSY, but they have not been observed so far. The search for the scalar top quarks has been performed at the ATLAS. The scalar top quark decays into a top quark and a neutralino if it is kinematically allowed. In the hadronic final states of top quarks, the method of the top reconstruction is one of the principal features in the analysis for the production of boosted tops due to the large mass difference of a scalar top quark and a neutralino. The top reconstruction is performed in two steps: to reconstruct jets of top-quark decay products and to identify top-quarks, called top-quark tagging, using the reconstructed jets. In this thesis, a new method, DNN top tagger, is introduced for both the jet reconstruction and top-quark tagging, optimized for the high-mass scalar top quarks. The new method shows high top-tagging efficiencies and good background rejections, which help significantly improve 27% of the significance for signal models where the final states top-quarks are highly boosted. The search uses at 139 fb^{-1} of $\sqrt{s}$ = 13 TeV data of proton-proton collisions at Large Hadron Collider recorded by the ATLAS. No significant excess over the Standard Model predictions is observed. The exclusion of the mass of the scalar top quark is extended up to 1.4 TeV for the mass of the neutralino below 200 GeV at 95% confidence level.

Contents

1 Introduction

The achievements of the particle physics theories and experiments establish the description of the four forces in our world, which are electromagnetic force, weak force, strong force, and gravitational force. The Standard Model describes the interaction of three forces except for the gravitational force. Although it is the outstanding achievement in the Standard Model, the hierarchy problem, the unification of coupling constants, and the dark matter still cannot be explained in the Standard Model. The Higgs mass has been measured to be 125.10$\pm$0.14 GeV as the average of the results from the ATLAS and CMS [1]. The mass is too light in the Standard Model if we believe in the so-called naturalness. The Higgs mass is partly contributed from the self-coupling λ, which results in quadratic divergence. If the Standard Model holds up to the Planck scale, which is the scale of unification of gravity, the Higgs bare mass will also run up to the Planck scale. The bare mass largely depends on the cut-off scale. Since the Higgs mass is 125 GeV, there must be a fine-tuning between bare mass and radiation corrections, which has no theoretical motivation in the Standard Model. This is known as the problem of the fine-tuning.

Supersymmetry (SUSY) is one of the Beyond the Standard Model (BSM) theory. There are many new particles which are predicted in the supersymmetry theory. In the minimal supersymmetric Standard Model (MSSM) with two Higgs doublets, the observed Higgs boson at the LHC can be considered as the lower mass Higgs boson, h_0. The h_0 mass no longer depends on the self-coupling λ and only the radiative corrections contribute to the h_0 mass in the MSSM. The radiative corrections of h_0 largely depend on the stop (scalar top) mass and top mass due to the large Yukawa coupling to the top quark. The stop is the superpartner of the top with spin 0 predicted in the supersymmetry theory. The contributions from the other quarks are usually not considered since their Yukawa coupling constants are smaller than the Yukawa coupling of top quarks. Therefore, the stop mass can be the smallest one among all the superpartners of the quarks.

In the recent searches for the stop with full hadronic final states, Figure 1 summarizes the search results at 36 fb^{-1}of the LHC Run2 data (2015-2016). Figure 1 (a) shows the exclusion limit of the stop mass $m_{\tilde{t}}$ at the low neutralino mass $m_{\tilde{\chi}_1^0}$ is extended around 1020 GeV by the CMS [2]. The $m_{\tilde{\chi}_1^0}$ has been excluded up to 420 GeV, which depends on the $m_{\tilde{t}}$. Figure 1 (b) shows the results from the ATLAS [3]. The limit of the $m_{\tilde{t}}$ at the low $m_{\tilde{\chi}_1^0}$ is around 1000 GeV, and the limit of the $m_{\tilde{\chi}_1^0}$ is up to

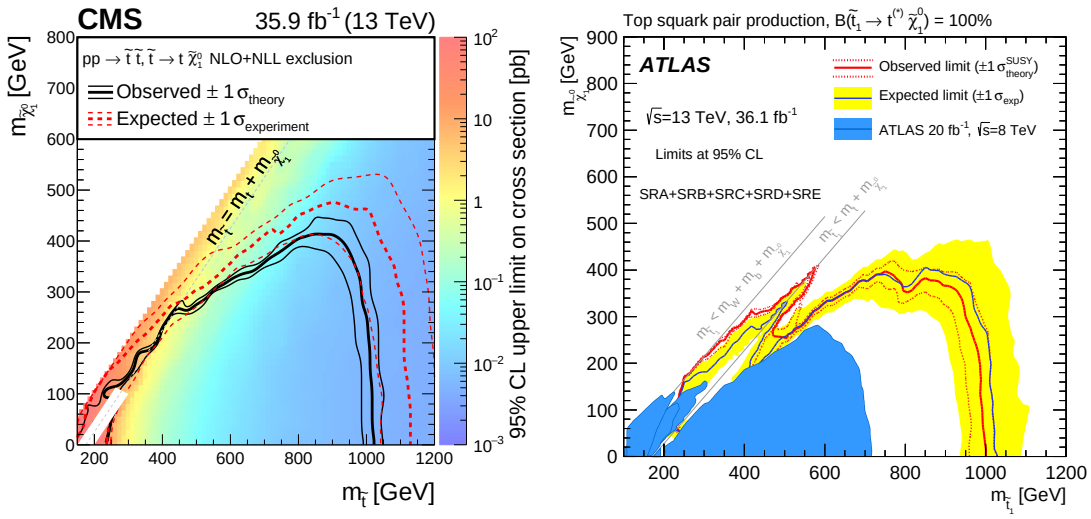

(a) (b)

Figure 1: Exclusion limits of the $m_{\tilde{t}}$ and $m_{\tilde{\chi}_1^0}$ with 36 fb^{-1}of 2015 and 2016 dataset published by (a) CMS collaboration [2] and (b) ATLAS collaboration [3].

400 GeV, which depends on the $m_{\tilde{t}}$.

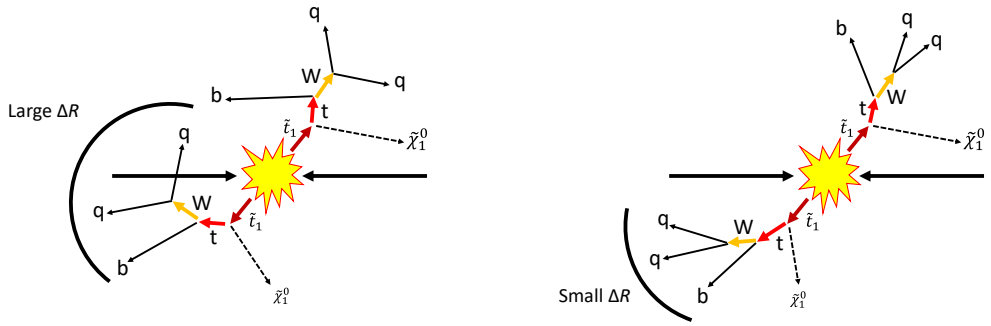

(a) (b)

Figure 2: Schematics of pair production of stops in the fully hadronic final states with (a) $\Delta m(\tilde{t}_1,\tilde{\chi}_1^0)$ close to top mass and (b) $\Delta m(\tilde{t}_1,\tilde{\chi}_1^0)$ much larger than top mass. ΔR is the separation of decay products of a top quark (see Eq. (29) for the definition).

The stop mass can be as low as several hundred GeV if the mixing of right-handed stop $\tilde{t}_\mathrm{R}$ and left-handed stop $\tilde{t}_\mathrm{L}$ is large, which is needed to be 125 GeV Higgs mass. Since the lower mass limit of the stop quark has reached up to about 1 TeV, it is naturally important to explore even higher mass region. In this thesis, we focus on the search in the $\tilde{t} \to t\tilde{\chi}^0$ channel with the hadronic decay of the top quarks in the boosted region, where the $\Delta m(\tilde{t}_1,\tilde{\chi}_1^0)$ is much larger than the top mass. The top can be fully reconstructed from the decay products in the absence of $E_\mathrm{T}^\mathrm{miss}$, and the boosted topology allows us to exploit small angular separation of the decay products for the top reconstruction (see Figure 2). The decay products of top quarks with small

angular separation can be reconstructed as jets with a large radius, which are called "large-R jet". The feature of substructure in the large-R jets, which is introduced as substructure variables, is useful to identify the top jets and reject quark/gluon-initiated jets. To maximize the discriminant power of the substructure variables, a deep neutral network (DNN) algorithm with a set of the substructure variables is used for the development of the tagging techniques, which can efficiently distinguish the top jets from the quark/gluon-initiated jets. The DNN top taggers are validated with the measurement of data efficiencies for the top jets and quark/gluon-initiated jets. The presence of the stop signals is tested by a fit to a representative kinematic observable after the selections are applied. In case no signal is found, the upper limit of the signal yields is evaluated, and then the lower limit of mass is considered.

We briefly introduce the theory of the Standard Model related to the unsolved problems and the theory of the MSSM in Chapter 2. The structure of the LHC and the ATLAS detector are described in Chapter 3. The samples and event reconstruction are in Chapter 4. A new method for the top-tagging is introduced in Chapter 5. The data analysis for the search for the stop using the full Run2 data of 139 fb^{-1} will be shown in Chapter 6. The ATLAS collaboration has published the new results at 139 fb^{-1} with an alternative method in the paper. The results with two different approaches, and the comparison with CMS results at 137 fb^{-1} of the full Run2 data are discussed in Chapter 7. Finally, all works are summarized in Chapter 8.

2 Theory

2.1 Brief introduction of the Standard Model

The Standard Model of particle physics includes three different gauge symmetries, which are denoted as $\mathrm{SU}(3)_C \times \mathrm{SU}(2)_L \times \mathrm{U}(1)_Y$. In the Standard Model, there are six quarks separated into the up-type and the down-type, and three generations of each pair of the up-type and the down-type quarks. There are also six leptons classified into three generations. These particles are spin $1/2$ fermions and also have their own anti-particles. In addition, there are also particles, which are bosons with spin-0 or spin-1. A photon γ is a particle, which propagates the electromagnetic force. The $W^{\pm}$ and Z are spin-1 bosons, which propagate the weak force, and the $W^{\pm}$ bosons only interact with left-handed particles. The gluons are massless bosons with spin 1, which propagate the strong force. The last one is the Higgs boson with spin 0, which makes the other particles massive. All particles are summarized in the Standard Model section of Figure 3 (left).

2.1.1 Symmetry transformation

To describe the behavior of the particles, the conservation law must be obeyed. The conservation law is given by some physical invariance. The symmetry transformations based on the invariance are represented by changes between different states. This is important for describing the dynamics of the particles. The infinitesimal changes of continuous transformations provide the description of the transformations by using the unitary or anti-unitary operator U with the identity and infinitesimal transformation:

$$\mathrm{U} = I + i\delta\xi G, \tag{1}$$

where I is the identity operator, and $\delta\xi$ indicates an infinitesimal change of a parameter. G is an operator which is the generator of the symmetry transformation.

2.1.2 Gauge theory

Gauge theory can describe physics with the global symmetry and local symmetry. For example, in the case of the isospin of a proton and a neutron, the symmetry transformation of isospin affects all the protons and neutrons in the universe. The

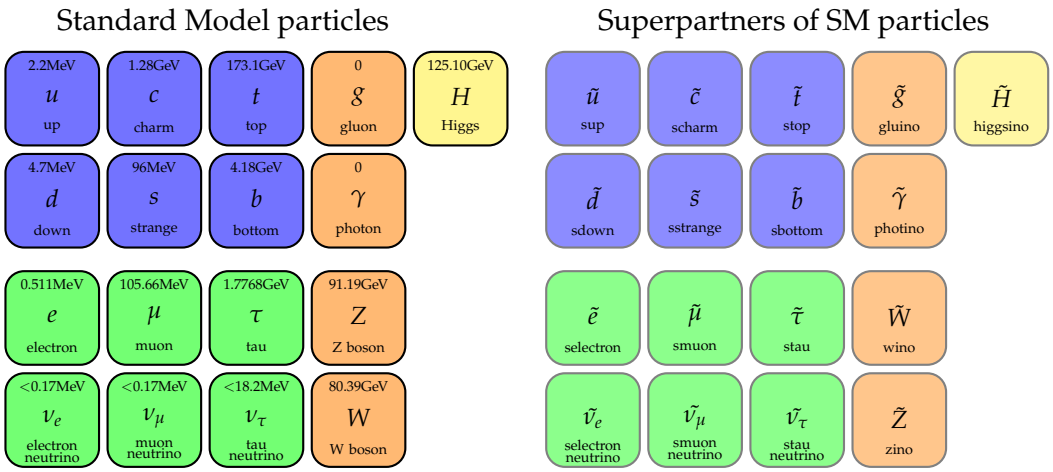

Figure 3: The elementary particles of the Standard Model (left) and their superpartners (right) in the supersymmetry theory.

symmetry is called global symmetry. However, the physics which we are dealing with changes locally. The effect from an event cannot propagate out of the space-time of the light cone (causality). This means the transformations can only happen independently. This kind of symmetry is called local symmetry. The first gauge theory with local symmetry is Maxwell's theory. The vector potential $\boldsymbol{A}$ and electrical potential V can be expressed by the form similar to the Eq. (1) with a gauge field,

$$\boldsymbol{A}' = \boldsymbol{A} + \nabla f, \quad V' = V - \frac{\partial f}{\partial t}. \tag{2}$$

In quantum field theory, the gauge theory can be built with an abelian group or a non-abelian group, expressed using the commutation relation of the generators as:

$$[T^i, T^j] = i f_{ijk} T^k, \tag{3}$$

where T represents the generators, and f_{ijk} is known as the structure constant. If f_{ijk}=0, the T belongs to the abelian group. For example, in quantum electrodynamics (QED), the generator of U(1) symmetry transformation is abelian. The symmetry transformation happens in the charge field. If f_{ijk} is not zero, the T is non-abelian. For example, the weak interaction has non-abelian SU(2) symmetry for the weak isospin. In addition, the generators which have SU(3) symmetry transformations in the color space in quantum chromodynamics (QCD) are also non-abelian.

2.1.3 Spontaneous symmetry breaking of electroweak theory

The electroweak theory is a theory for the unification of electromagnetic and weak interaction [4]. The gauge symmetry is $SU(2)_L \times U(1)_Y$. To introduce the gauge theory into the weak interaction, the gauge boson of weak interaction must be massive since the range of the interaction is short. On the other hand, the gauge boson for the photon should be massless. Since the properties of electromagnetic and weak interactions differ from each other at a low energy scale, the local symmetry of the electroweak must be broken. The Higgs mechanism is involved in the spontaneous symmetry breaking, making the vacuum expectation value of the Higgs field non-zero. The symmetry transformation cannot remain invariant. The $SU(2)_L \times U(1)_Y$ breaks into $U(1)_{em}$. In addition, the masses of fermions are also given by the broken symmetry. The Higgs fields are defined as one doublet scalar fields ϕ. The Higgs potential is introduced as a formula as:

$$V(\phi) = +\mu^2\phi^\dagger\phi + \lambda(\phi^\dagger\phi)^2, \tag{4}$$

where μ^2 is the mass parameter, and λ is the Higgs self-coupling. To minimize the $\langle 0|\phi|0\rangle$, we can consider two conditions for μ^2. For $\mu^2 > 0$, the vacuum expectation value $\nu = 0$, which is not what we expect for the symmetry breaking. For $\mu^2 < 0$, the vacuum expectation value is not zero and can be calculated from the Fermi coupling constant $v^2 = (\sqrt{2}G_F)^{-1} = (246\ \text{GeV})^2$. Then, we can have the Higgs mass M_H from the vacuum expectation value and the Higgs self-coupling.

$$M_H^2 = 2v^2\lambda. \tag{5}$$

2.1.4 Naturalness of Higgs mass

In the previous section, the Higgs mass is obtained at the tree level. Now, we consider Higgs bare mass m_H with one-loop precision before the renormalization [5],

$$m_H^2 = M_H^2 - 2g^2\left\{(1-n)(\frac{1}{2} + \frac{1}{4c_w^2}) - \frac{3}{4}\frac{M_H^2}{M_W^2} + \sum_f \frac{m_f^2}{M_W^2}\right\}\frac{\Lambda^2}{16\pi^2}, \tag{6}$$

where n is the number of the poles, g is the coupling constant, m_f is the mass of the fermion, Λ is the cut-off energy scale, M_W is the W mass, and c_w is the $\cos\theta_w$. The second term of the RHS is from the one-loop contribution and depends on the cut-off scale. This is known to cause a quadratic divergence, which is mainly contributed

from the integral of the propagators containing the poles. The renormalization also needs to have the cut-off dependence to match the Higgs mass obtained from the experimental results.

2.2 Supersymmetry

Supersymmetry is a spacetime symmetry which transforms fermionic (bosonic) fields into bosonic (fermionic) fields by using fermionic generators (Q, $Q^\dagger$) of supersymmetry transformations under the usual bosonic spacetime coordination, x^μ, and the four fermionic superspace, θ and $\theta^\dagger$ (two-component spinor for each). The generators are also known as supercharges. The anticommutation relations of the generators with two different Dirac spinors, α and β, form as:

$$\begin{aligned} \{Q_\alpha, Q^\dagger_{\dot{\alpha}}\} &= -2\sigma^\mu_{\alpha\dot{\alpha}} P_\mu, \\ \{Q_\alpha, Q_\beta\} = 0, \{Q^\dagger_{\dot{\alpha}},\ Q^\dagger_{\dot{\beta}}\} &= 0, \end{aligned} \tag{7}$$

where σ is the Pauli matrix, and P_μ is a four-vector momentum operator. The first line of Eq. (7) shows the transformation of the spacetime. Those new particles are superpartners of the Standard Model particles. The spin of the superpartner is different by a half. The spin half fermions become spin-0 bosons while the spin-1 gauge bosons become spin-$\frac{1}{2}$ gauge fermions. For example, a top quark in the Standard Model has its own superpartner, which is called the scalar top or the stop. The elementary particles predicted in supersymmetry are shown in Figure 3 (right).

2.2.1 Minimal supersymmetric Standard Model (MSSM)

In the MSSM, only the simple symmetry $\mathcal{N} = 1$, which means there is only one set of the supercharges, is used. There are two types of representations, chiral and vector supermultiplets. A chiral supermultiplet contains one complex scalar field ϕ, one two-component chiral fermionic field Φ, and a complex scalar auxiliary field F. A vector supermultiplet contains a spin 1 vector gauge boson field A^a_μ, a two-component Weyl fermion gaugino λ^a, and a real scalar auxiliary field D. The auxiliary fields make the closure of the supersymmetry off-shell.

The Higgs sector in the Standard Model is a single doublet field, which is mentioned in section 2.1.3. In the MSSM, the two doublet Higgs fields, H_u and H_d, are required for the holomorphic property of the superpotential. The H_u couples only to

the up-type quarks and the H_d to the down-type quarks, and charged lepton. Therefore, the superpotential for the quark and lepton masses in the MSSM is expressed as:

$$W = \epsilon_{\alpha\beta}[\bar{u}y_u QH_u - \bar{d}y_d QH_d - \bar{e}y_d LH_d + \mu H_u H_d], \tag{8}$$

where $\bar{u}$, $\bar{d}$, $\bar{e}$ are the up-type quark superfield, down-type quark superfield, and charged lepton superfield, respectively. The $\epsilon_{\alpha\beta}$ corresponds to the weak isospin with indexes. The y_u, y_d, and y_e are the Yukawa couplings. The Yukawa matrices determine the mass and CKM mixing angles of the quarks and leptons if the H_u and H_d have their vacuum expectation value. The Yukawa couplings in supersymmetry are required to be the same as the couplings in the Standard Model.

2.2.1.1 R-parity conservation

In supersymmetry, additional renormalizable terms violate the baryon number B and lepton number L, which causes the short lifetime of protons. To eliminate the violations, a new symmetry is introduced in the supersymmetry called R-parity, which is expressed as:

$$R = (-1)^{3(B-L)+2s}, \tag{9}$$

where s is the spin of the particle. The R-parity is defined to be +1 for particles in Standard Model and -1 for their superpartners. This property is important for the existing of the lightest supersymmetry particles (LSPs). In the MSSM, the R-parity is conserved. Therefore, the supersymmetry particles must be produced in pair, and the final states contain a pair of the LSPs. The LSPs are also considered as candidates for the dark matters since they are massive, and weakly interact with the Standard Model particles. In this thesis, the R-parity conservation is assumed.

2.2.1.2 Soft supersymmetry breaking

Since the supersymmetry particles are not observed so far, the supersymmetry must be broken. The Higgs mass term in the MSSM is non-negative. This causes a minimum at $H_u^0 = H_d^0 = 0$ if a supersymmetry-breaking squared-mass soft term is not

included. The soft Lagrangian given in Ref. [6] is expressed as:

$$\begin{aligned}\mathcal{L}_{soft} = &-\frac{1}{2}(M_3\tilde{g}\tilde{g} + M_2\tilde{W}\tilde{W} + M_1\tilde{B}\tilde{B} + c.c.) \\ &- (\tilde{\bar{u}}\boldsymbol{a_u}\tilde{Q}H_u - \tilde{\bar{d}}\boldsymbol{a_d}\tilde{Q}H_d - \tilde{\bar{e}}\boldsymbol{a_e}\tilde{L}H_d + c.c.) \\ &- \tilde{Q}^\dagger \boldsymbol{m}^2_{\boldsymbol{Q}}\tilde{Q} - \tilde{L}^\dagger \boldsymbol{m}^2_{\boldsymbol{L}}\tilde{L} - \tilde{\bar{u}}\boldsymbol{m}^2_{\bar{\boldsymbol{u}}}\tilde{\bar{u}}^\dagger - \tilde{\bar{d}}\boldsymbol{m}^2_{\bar{\boldsymbol{d}}}\tilde{\bar{d}}^\dagger - \tilde{\bar{e}}\boldsymbol{m}^2_{\bar{\boldsymbol{e}}}\tilde{\bar{e}}^\dagger \\ &- m^2_{H_u}H^*_u H_u - m^2_{H_d}H^*_d H_d - (bH_uH_d + c.c.).\end{aligned} \tag{10}$$

All the quantities in $\mathcal{L}_{soft}$ have the radiative corrections, which result in the cut-off dependence and can be renormalized. The M_3, M_2, and M_1 are the gluino, wino, and bino mass terms, respectively. The $\boldsymbol{a_u}$, $\boldsymbol{a_d}$, and $\boldsymbol{a_e}$ are 3x3 matrices corresponding to the Yukawa couplings and usually assumed to be proportional to the Yukawa couplings. The gluino cannot mix with the other particles in the MSSM due to the color octet. The other gauginos and higgsino with the same electrical charge can mix together. There are two mixed charged supersymmetry particles called charginos $\chi^\pm$ and four neutral mixed particles called neutralinos χ^0. The above quantities depend on the $tan\beta = \langle H_u \rangle \,/\, \langle H_d \rangle$, which is also a key variable in the experiments. The $tan\beta$ is also constrained by the Yukawa couplings and thus can be between $\sim$1 and 60.

The symmetry can be broken only if either the F term or the D term is not zero. For the D term breaking, a Fayet-Iliopoulos term is needed to be added into the Lagrangian. However, this breaks gauge invariance, and the mass terms of the squarks and sleptons disappear. The D term breaking mechanism is still unclear now. On the other hand, the F term breaking is called O'Raifeartaigh model. The supersymmetry breaking is also considered as a hidden sector. If it couples to visible sector directly, the gauge has no mass since there are no scalar-gaugino-gaugino couplings, and some predictions are already ruled out by experiments. Hence, there must be some mediating interactions between the hidden sector and the visible sector. If the mediating interaction is flavor-blind, the parameters in the MSSM have relations as follows:

$$\begin{gathered}\boldsymbol{m}^2_{\boldsymbol{Q}} = m^2_Q\mathbf{1},\ \boldsymbol{m}^2_{\bar{\boldsymbol{u}}} = m^2_{\bar{u}}\mathbf{1},\ \boldsymbol{m}^2_{\bar{\boldsymbol{d}}} = m^2_{\bar{d}}\mathbf{1},\ \boldsymbol{m}^2_{\boldsymbol{L}} = m^2_L\mathbf{1},\ \boldsymbol{m}^2_{\bar{\boldsymbol{e}}} = m^2_{\bar{e}}\mathbf{1}, \\ \boldsymbol{a_u} = A_{u0}\boldsymbol{y_u},\ \boldsymbol{a_d} = A_{d0}\boldsymbol{y_d},\ \boldsymbol{a_e} = A_{e0}\boldsymbol{y_e}.\end{gathered} \tag{11}$$

There are different mechanisms of the soft breaking, such as, gravity mediated symmetry breaking, gauge mediated symmetry breaking (GMSB), and anomaly mediated symmetry breaking (AMSB).

2.2.1.3 Higgs mass in the MSSM

From the contributions of the superpotential of Eq. (8), the soft Lagrangian in the Eq. (10), and Kähler D terms, the scalar Higgs potential is expressed as:

$$\begin{aligned} V_{Higgs} = & \frac{g^2 + g'^2}{8}(H_d^\dagger H_d - H_u^\dagger H_u)^2 + \frac{g^2}{2}|H_d^\dagger H_u|^2 + |\mu|^2(H_d^\dagger H_d + H_u^\dagger H_u) \\ & + (m_{H_d}^2 H_d^\dagger H_d + m_{H_u}^2 H_u^\dagger H_u) - (bH_u H_d + h.c.), \end{aligned} \tag{12}$$

where b is a complex parameter. The Higgs potential in the MSSM is much more complicated than the Higgs potential in the Standard Model. Owing to two doublet Higgs fields, the Higgs bosons have two mass states, M_h and M_H. The M_h is generally referred to as the smaller mass. The M_h at tree level is given by:

$$\left(M_h^{(0)}\right)^2 = \frac{1}{2}\left(M_A^2 + M_Z^2 - \sqrt{(M_A^2 - M_Z^2)^2 + 4M_A^2 M_Z^2 sin^2(2\beta)}\right), \tag{13}$$

where M_A^2 is $b(tan\beta + cot\beta)$. The M_h is smaller than M_Z even if the decoupling limit of $M_A \gg M_Z$ is considered, which causes the large difference of the Higgs mass between the prediction at tree level and the observation. Hence, the radiative corrections are needed, which is explained below.

2.2.2 Problems in the Standard Model

2.2.2.1 Hierarchy problem

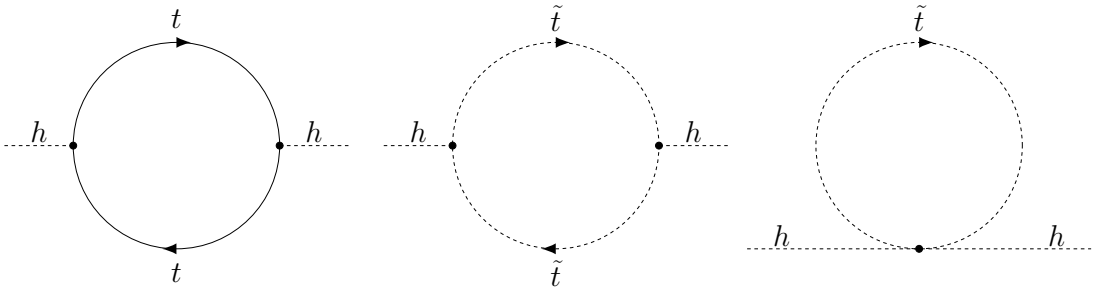

(a) (b)

Figure 4: The Higgs self-energy contributed from the (a) top loop and (b) scalar top quark loop in the MSSM.

As discussed in the section of the Standard Model, the cut-off dependence of the mass is unnatural. In the MSSM, thanks to the contributions of the supersymmetry particles at the loop level, the divergence of the Higgs bare mass can be reduced

before the renormalization. Since the Yukawa coupling of the top quark is largest among the other quarks, the contribution from the stop is also larger than the other squarks. The divergence contributed from top quarks (see Figure 4 (a)) can be cancelled out by introducing the scalar top quark loops (see Figure 4 (b)). The mass difference between tree level and 1-loop level is given by:

$$\Delta M_h^2 \sim \frac{3}{4\pi^2}\frac{m_t^4}{v^2}\left[\ln\frac{m_{\tilde{t}}^2}{m_t^2} + \frac{X_t^2}{m_{\tilde{t}^2}}(1 - \frac{X_t^2}{12m_{\tilde{t}^2}})\right], \tag{14}$$

where $X_t = a_t - \mu cot\beta$ is the stop mixing parameter.

2.2.2.2 Unification of coupling constants

In the Standard Model, the different forces are described in the different symmetries. These symmetries also can be considered as subgroups of a larger symmetry. In the grand unification theory, a SU(5) or SO(10) is used to unify the strong and electroweak interactions. Figure 5 shows the inverse of the running gauge coupling α^{-1}. The energy scale for the grand unification is up to 10^{15} GeV. In the Standard Model, the coupling constants $\alpha(\mathrm{SU}(3))$ and $\alpha(\mathrm{SU}(2))$ become weaker, and the $\alpha(\mathrm{U}(1))$ becomes stronger as the energy scale increases. However, the unification of coupling constants will not be seen in the Standard Model. With the supersymmetry, only the $\alpha(\mathrm{SU}(3))$ becomes weaker, and both the $\alpha(\mathrm{SU}(2))$ and the $\alpha(\mathrm{U}(1))$ become stronger as the energy scale increases. The unification can be possible around the GUT (Grand Unification Theory) scale.

2.2.2.3 Dark matter

The presence of dark matter is strongly believed from the cosmological studies. In the early studies on the galaxy clusters and the galactic rotation curves, there must be missing mass in the space. Someone may argue that the mass can be from known matters, which cannot be detected from the earth. Thanks to the fitting results of the cosmic microwave background (CMB) according to the Λ CDM predictions, the abundance of the interstellar deuterium can be correctly estimated, which can constrain the baryonic matter in the universe. According to the recent results with the data of baryon acoustic oscillations from the Planck project, the universe is made of $26.06\pm0.30\%$ of the cold dark matter [7]. In this thesis, we are interested in the candidates of supersymmetry particles, which belong to the weakly interacting massive

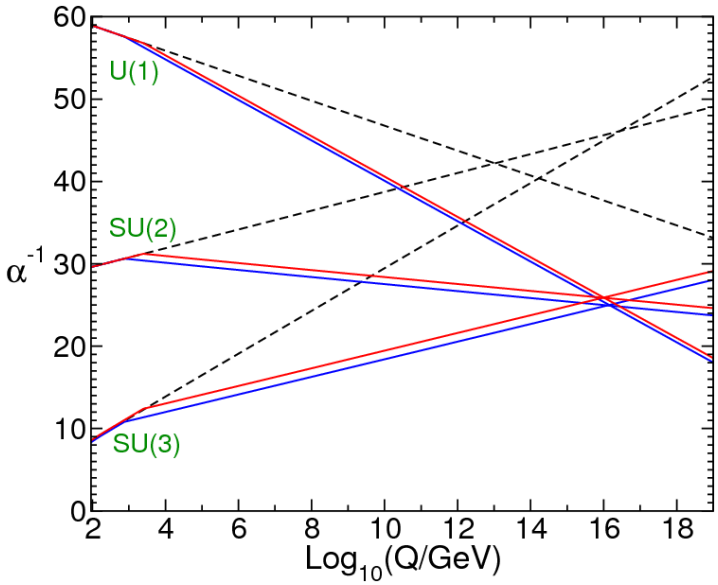

Figure 5: $\alpha^{-1}(Q)$ with two-loop radiative corrections as a function of the energy scale [6]. The dashed line is the inverse of the coupling constants in the SM. The blue and red lines show the constants, which are from the masses of sparticles at 750 GeV and 2.5 TeV, respectively.

particles (WIMPs). The WIMPs weakly interact with other particles, so it is hard to detect. With R-parity conservation, the LSPs may match the properties, which are required for the dark matter. The detectable mass states of the LSP can be the mixing states of the superpartners of the gauge bosons. The search for the LSP is model-dependent since a different soft symmetry breaking model predicts a different LSP. The LSP in the GMSB is the gravitino and the wino in the AMSB.

2.3 Properties of scalar top quarks

Due to the chirality, the stop sector has a right-handed stop $\tilde{t}_{\mathrm{R}}$ and a left-handed stop $\tilde{t}_{\mathrm{L}}$. The $\tilde{t}_{\mathrm{R}}$ and $\tilde{t}_{\mathrm{L}}$ can mix together, which causes that the $\tilde{t}_{\mathrm{R}}$ and $\tilde{t}_{\mathrm{L}}$ are not the mass eigenstates of the stop. The Lagrangian of the stop mass is as follows:

$$\mathcal{L} = -\begin{pmatrix} \tilde{t}_L^* & \tilde{t}_R^* \end{pmatrix} \boldsymbol{m}_{\tilde{\boldsymbol{t}}}^2 \begin{pmatrix} \tilde{t}_L \\ \tilde{t}_R \end{pmatrix}, \tag{15}$$

where

$$\boldsymbol{m}_{\tilde{\boldsymbol{t}}}^2 = \begin{pmatrix} m_{\mathrm{Q}_3}^2 + m_t^2 + \Delta_{\bar{u}_L} & v(a_t^* sin\beta - \mu y_t cos\beta) \\ v(a_t sin\beta - \mu^* y_t cos\beta) & m_{\bar{u}_3}^2 + m_t^2 + \Delta_{\bar{u}_R} \end{pmatrix}. \tag{16}$$

The top mass m_t, the Δ from the electroweak symmetry breaking, and the Yukawa coupling y_t in the Standard Model contribute to the stop mass. The a_t from the soft

breaking sector, the vacuum expectation value (VEV) v of H_d, and β from $tan\beta$ in the MSSM also contribute to the stop mass. The mass eigenstates can be obtained from the mixing of $\tilde{t}_L$, and $\tilde{t}_R$ with the mixing angle $\theta_{\tilde{t}}$:

$$\begin{pmatrix} \tilde{t}_1 \\ \tilde{t}_2 \end{pmatrix} = \begin{pmatrix} cos\theta_{\tilde{t}} & -sin\theta_{\tilde{t}} \\ sin\theta_{\tilde{t}} & cos\theta_{\tilde{t}} \end{pmatrix} \begin{pmatrix} \tilde{t}_L \\ \tilde{t}_R \end{pmatrix}, \tag{17}$$

where the stop with the smaller mass is assigned as $\tilde{t}_1$ and the one with the larger mass is $\tilde{t}_2$.

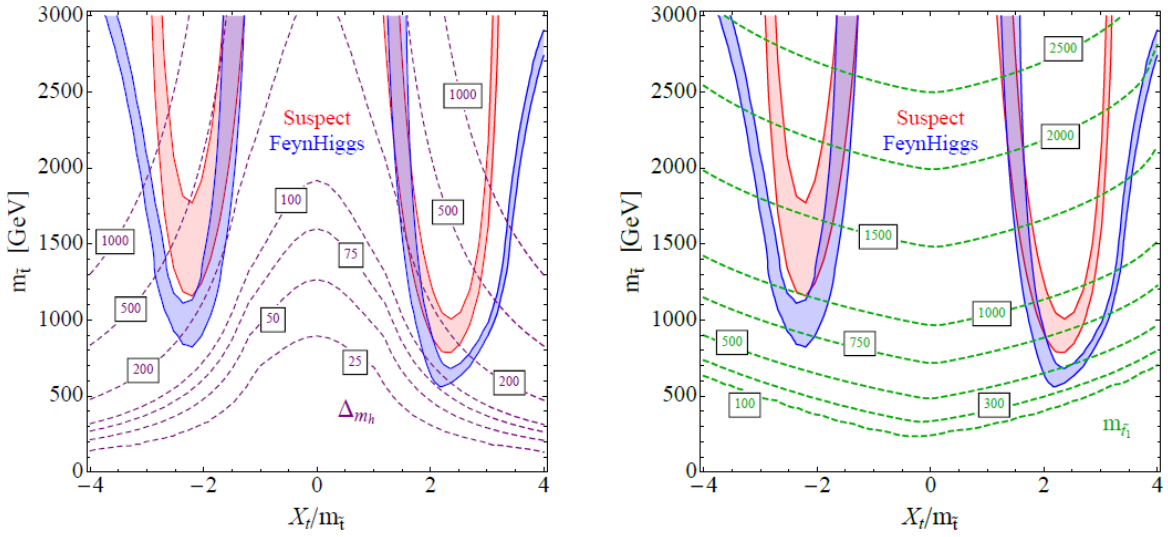

Figure 6: The contours show (Left) the fine tuning of the Higgs mass Δm_h (purple dash line) and (Right) lightest stop mass $m_{\tilde{t}_1}$ (green dash line) as a function of the stop mixing parameter X_t within the Higgs mass 124∼126 GeV by using simulation software, Suspect (Red) and FeynHiggs (Blue), at tanβ = 20 in the MSSM [8].

Figure 6 shows the results obtained by Lawrence et al. [8], who studied the relations of Higgs mass and the mixing of the stops. The X_t is the stop mixing parameter. The zero means there is no mixing between $\tilde{t}_R$ and $\tilde{t}_L$. Two public programs, Suspect and FeynHiggs, are used in this thesis. The calculations include radiative corrections up to the two-loop level. The Higgs mass is derived under the decoupling limit. If the mixing of the stop is not considered, the stop mass will not be below 3 TeV. The mass scale of 3 TeV or higher will not be reachable at LHC. However, the mass of $\tilde{t}_1$ can be 300−500 GeV if $X_t = \sqrt{6}$. This mass scale will allow us to search at LHC of $\sqrt{s}$ = 13 TeV.

In this thesis, the simplified model [10, 11] is used for the search for the stop. In the simplified model, we do not need to scan the large set of MSSM parameters. The mass spectrum of the SUSY particles is more important, and the parameters can be largely reduced. The gluino mass is assumed to be much higher than the stop mass.

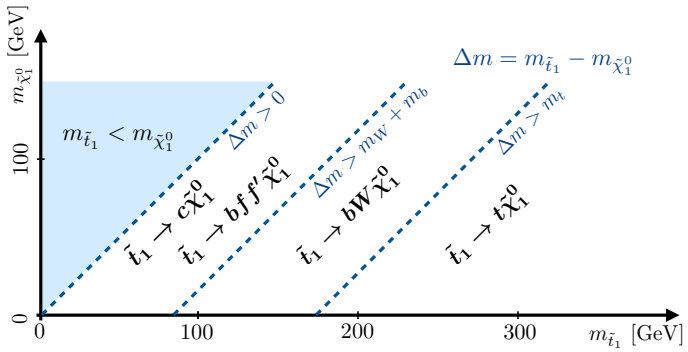

Figure 7: Decay channels with respect to the mass regions [9]. Two-body decay, $\tilde{t}_1 \to t\tilde{\chi}_1^0$, occurs in $\Delta m(\tilde{t}_1,\tilde{\chi}_1^0) > m_t$. Three-body decay, $\tilde{t}_1 \to bW\tilde{\chi}_1^0$, occurs in $m_W + m_b < \Delta m(\tilde{t}_1,\tilde{\chi}_1^0) < m_t$. Four-body decay, $\tilde{t}_1 \to bff'\tilde{\chi}_1^0$, occurs in $\Delta m(\tilde{t}_1,\tilde{\chi}_1^0) < m_W + m_b$.

The decay channels of the $\tilde{t}_1$ where the lightest neutralino $\tilde{\chi}_1^0$ is directly produced from the $\tilde{t}_1$ decay are shown in Figure 7. Depending on the mass difference between the $\tilde{t}_1$ and $\tilde{\chi}_1^0$ ($\Delta m(\tilde{t}_1,\tilde{\chi}_1^0)$), the decay channels can be classified into two-body, three-body, and four-body decays. If the $\Delta m(\tilde{t}_1,\tilde{\chi}_1^0)$ is larger than the top mass, the decay channel is the two-body decay. If the $\Delta m(\tilde{t}_1,\tilde{\chi}_1^0)$ is between top mass and W mass, the decay channel is the three-body decay. Finally, if the $\Delta m(\tilde{t}_1,\tilde{\chi}_1^0)$ is smaller than the W mass, the decay channel is the four-body decay. The $m_{\tilde{t}}$ smaller than $m_{\tilde{\chi}_1^0}$ is forbidden. In this thesis, we aim for the two-body decays with large $\Delta m(\tilde{t}_1,\tilde{\chi}_1^0)$, where the top quarks have high p_{T} and decay hadronically.

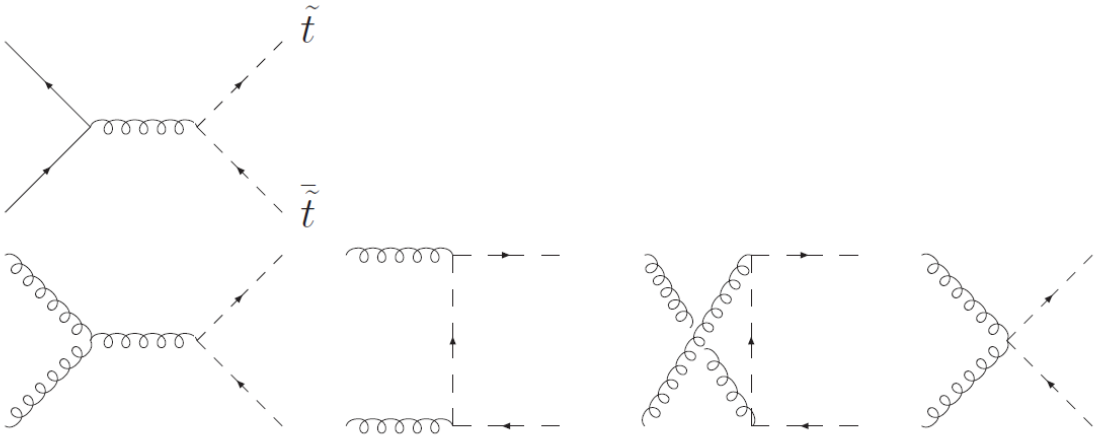

Figure 8: Feynman diagrams for the stop production via quark-antiquark annihilation (first row) and gluon-gluon fusion (second row) at leading order [12].

The pair production of the stops via $q\bar{q}$ and gg are considered in the calculation of the cross section. Other processes are suppressed by the higher order of the strong coupling. The cross section at leading order mainly depends on the stop mass since light squarks do not appear in the Feynman diagrams as shown in Figure 8. In

the higher order calculation, the gluinos and light squarks appear in the loop so the gluino mass and light squark mass affect the stop production. In addition, stop mixing parameter and other stop mass ($m_{\tilde{t}_2}$) also appear in high order calculation.

3 LHC and ATLAS detector

3.1 Large Hadron Collider

The Large Hadron Collider (LHC) [13] is a circular collider with 27 km in circumference, at the mean depth of 137 m across the France-Swiss border. The beam pipes are installed in the tunnel which was built for the Large Electron-Position (LEP) collider [14]. The proton or the lead ion beams go in the counter-rotating direction in two different beam pipes for the collision. With the high energy of the collisions, it allows us explore the physics at the TeV scale. The magnet system is a critical technology for the circulation of the beams. There are mainly two types of magnets, dipole and quadrupole magnets. These magnets are made of the NbTi Rutherford cables. The magnets provide 8 T field at the temperature below 2 K. The superfluid helium is used in the cryostat system. The energy of the proton beam is 7 TeV in the design. In the Run2 (2015-2018), the beam energy is only up to 6.5 TeV due to a limitation of available magnetic field.

The protons from a bottle of hydrogen gas are accelerated by the radio frequency in the series of accelerators, as shown in Figure 9. The protons are accelerated in Linac2, and the proton beam energy is up to 50 MeV. After the acceleration in Linac2, the beam energy is increased to 1.4 GeV in Proton Synchrotron Booster (PSB). The PSB also acts as the transition to convert the RF harmonics from the Linac2 to Proton Synchrotron (PS) where the beam energy is increased up to 25 GeV. The beam energy is further increased to 450 GeV in the Super Proton Synchrotron (SPS) and injected to the LHC. The proton beams are accelerated in the RF cavities of the LHC. After the beam energy reaches 6.5 TeV, the proton beams are used in the collisions.

The instantaneous luminosity of the ideal head-on collision of the Gaussian beams [16] is defined as:

$$L = \frac{N_1 N_2 f N_b}{4\pi\sigma_x\sigma_y}, \tag{18}$$

where N_1 and N_2 are the number of the particles in one bunch, f is the revolution frequency, and N_b is the number of bunches in the ring. σ_x,σ_y are the parameters described in Gaussian profiles. The additional terms are required to describe the real machines. The instantaneous luminosity has been achieved up to 2×10^{34} cm^{2}s^{-1} at the interaction points of the ATLAS detector and the CMS detector. The instantaneous luminosity in Run2 data taking exceeds the designed instantaneous luminosity

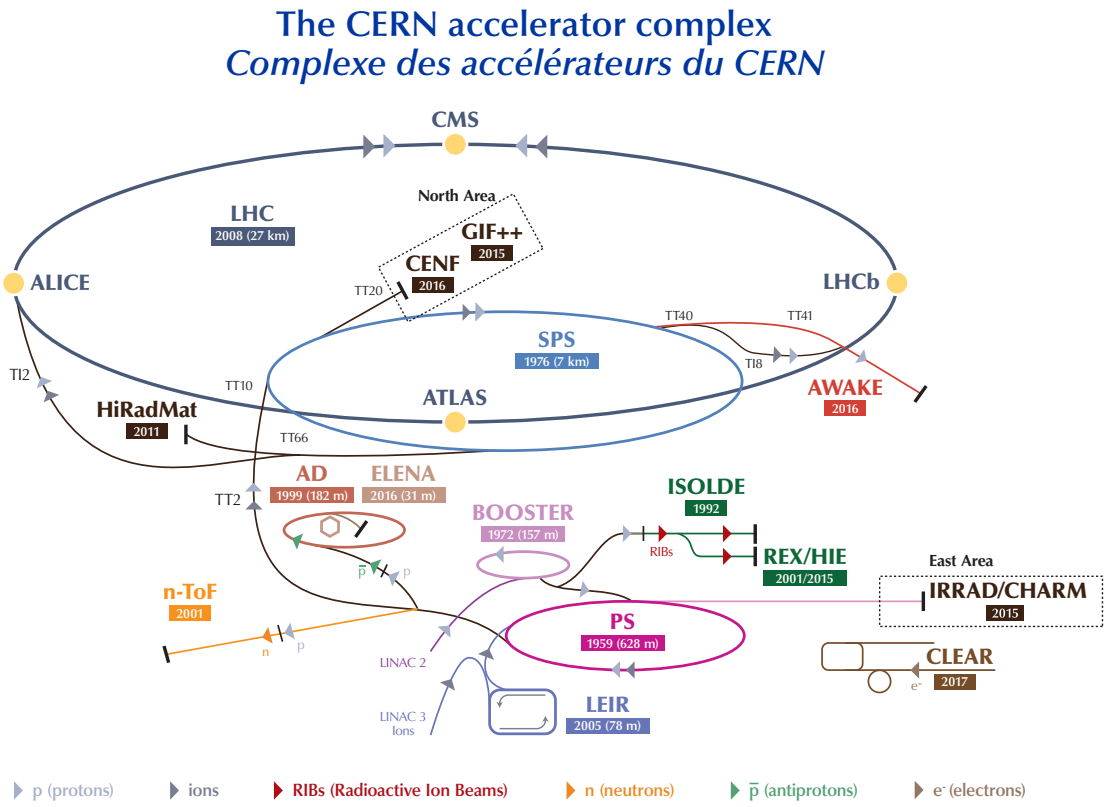

LHC - Large Hadron Collider // SPS - Super Proton Synchrotron // PS - Proton Synchrotron // AD - Antiproton Decelerator // CLEAR - CERN Linear Electron Accelerator for Research // AWAKE - Advanced WAKefield Experiment // ISOLDE - Isotope Separator OnLine // REX/HIE - Radioactive EXperiment/High Intensity and Energy ISOLDE // LEIR - Low Energy Ion Ring // LINAC - LINear ACcelerator // n-ToF - Neutrons Time Of Flight // HiRadMat - High-Radiation to Materials // CHARM - Cern High energy AcceleRator Mixed field facility // IRRAD - proton IRRADiation facility // GIF++ - Gamma Irradiation Facility // CENF - CErn Neutrino platForm

Figure 9: Accelerator complex at CERN [15].

of 1.0×10^{34} cm^{2}s^{-1}. The standard filling scheme of the LHC is 2808 bunches per ring. Each bunch contains $\sim 10^{11}$ protons in the dimension around 16 μm in width and few centimeters in length of the interaction point of ATLAS experiment.

3.2 ATLAS detector overviews

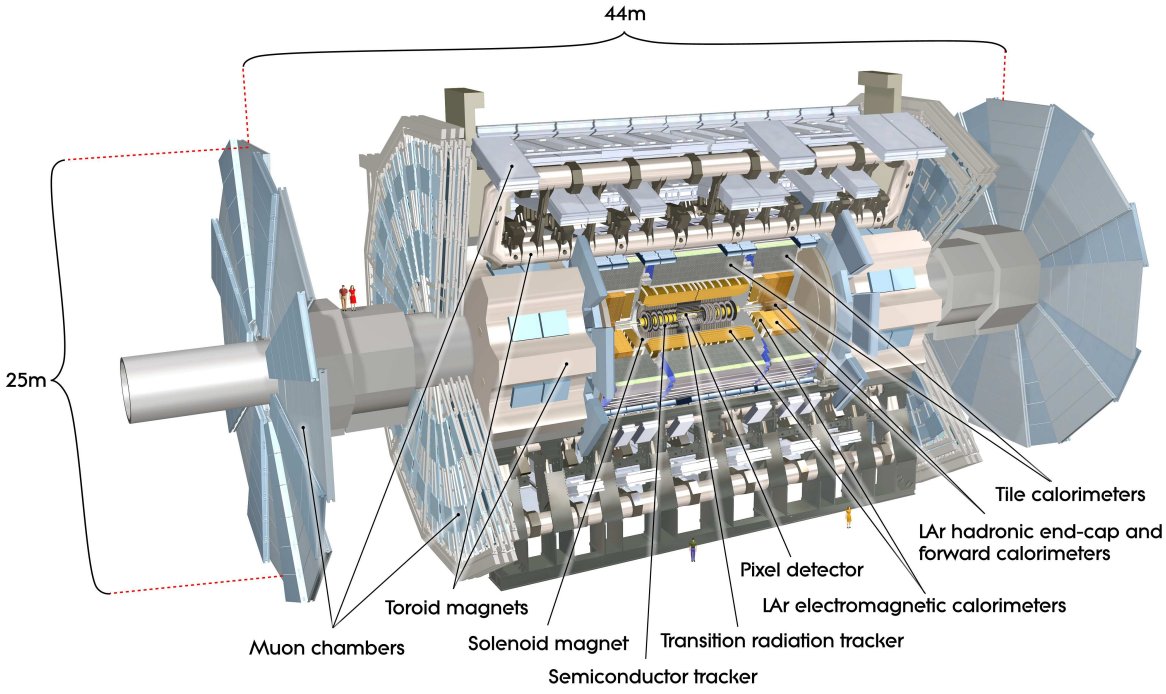

Figure 10: The cut-away view of the ATLAS detector [17].

The ATLAS (A Toroidal LHC ApparatuS) detector [18] is located at the point 1 of the LHC. Figure 10 shows the overviews of the ATLAS detector. The ATLAS detector is designed to have the 4π coverage and comprises several sub-detectors for a wide spectrum of physics processes. The magnet system makes the trajectories of the charged particles bent so that the momentum and electric charge can be measured. The detectors consist of the inner detector, the calorimeter, and the muon spectrometer from the inside to the outside. All three sub-systems consist of one barrel part and two end-cap parts.

3.3 Coordinate system

The directions and position in the ALTAS detector can be described in the xyz coordinate system. The origin (0,0,0) is defined at the center of the ATLAS detector. The z-axis is defined along the beam pipe. The positive z side is called A-side, and the

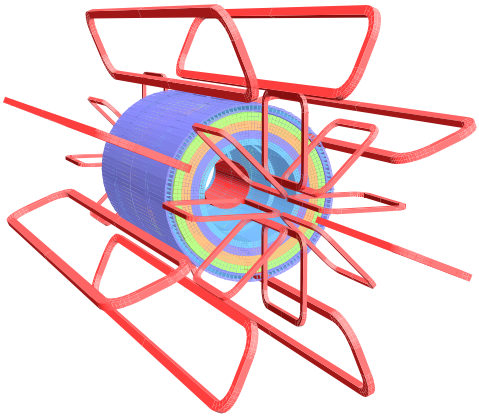

Figure 11: The geometry of the magnet systems (red) [18]. The tile calorimeter is also modelled.

negative z side is called C-side. The positive y-axis is defined in a vertical direction, pointing upwards. The positive x-axis points to the center of the LHC from the center of the ATLAS detector.

The magnitude of the momentum in the x-y plane is referred to as the transverse momentum. The azimuthal angle ϕ is defined with respect to the x-axis. Instead of the polar angle θ, the rapidity y is used in the hadron collider experiment:

$$y = \frac{1}{2}\ln\left(\frac{E + p_z}{E - p_z}\right), \tag{19}$$

where E denotes the energy of particles and p_z denotes the momentum along the z-axis. This quantity is very useful in high energy physics since the difference in rapidity is Lorentz invariant. For the massless objects, the pseudo-rapidity is used to approximate rapidity and defined as:

$$\eta = -\ln\left(\tan\frac{\theta}{2}\right). \tag{20}$$

It is useful since the pseudo-rapidity is directly calculated from the polar angle. To describe the angular separation of two objects, the ΔR is defined in the $\eta - \phi$ plane as:

$$\Delta R = \sqrt{(\Delta\eta)^2 + (\Delta\phi)^2}, \tag{21}$$

where $\Delta\eta = \eta_1 - \eta_2$, and $\Delta\phi = \phi_1 - \phi_2$.

3.4 Magnet system

There are one solenoid and three toroid magnet systems in the ATLAS detector. The location of the magnets is pointed out in Figure 11. The superconductors are used in the magnets. The whole magnet systems are contained in the cylindrical space with the 22 m in diameter and 26 m in length. The energy stored in the system is 1.6 GJ. The solenoid magnet with 2.46 m in diameter and 5.8 m in length the surrounds the inner detector and provides 2 T axial field. Three toroids around the calorimeters are arranged with an eight-fold azimuthal symmetry. A Barrel toroid with an inner diameter of 9.4 m and 25.3 m in axial length in the muon detectors provides $\sim$0.5 T magnetic field, and two end-cap toroids with 5.0 m in axial length also provide $\sim$1 T magnetic field.

3.5 Inner detector

The inner detector (ID) [19] provides a reconstruction of tracks of charged particles and vertices from the reconstructed tracks. The momentum can be determined from the curvature of the trajectories. The coverage is over the pseudo-rapidity range of $|\eta| < 2.5$. The inner detector is inside the solenoid magnet system and consists of three sub-detectors, pixel detector close to the beam pipe, silicon micro-strip tracker (SCT) in the middle and transition radiation tracker (TRT) in the outermost layers. Figure 12 shows the r-z cross-section views of the inner detector. Insertable B-Layer detector (IBL) [20] was installed during a long shutdown in 2014 before the Run2 to enhance the tracking performance and efficiency of b-tagging. The overall inner detector is 2.3 m in diameter and 7m in z-direction.

3.5.1 Pixel detector

The pixel detector consists of 1456 barrel modules and 288 disk modules. Four layers of pixel modules are in the barrel regions and three layers in the end-cap region. A pixel sensor [21] has a 256 μm thick n-bulk. The nominal pixel size is 50 μm(ϕ direction) $\times$ 400 μm (z-direction). The n^+ implants are embedded on the readout side, and the p-n junction is on the back size. The n^+-in-n design allows the operation even if the type inversion occurs. Each sensor module is composed of 47232 pixel sensors. The sensors are arranged in 144 columns and 328 rows. In the barrel region, 13 modules are mounted on each stave. The operation temperature is maintained

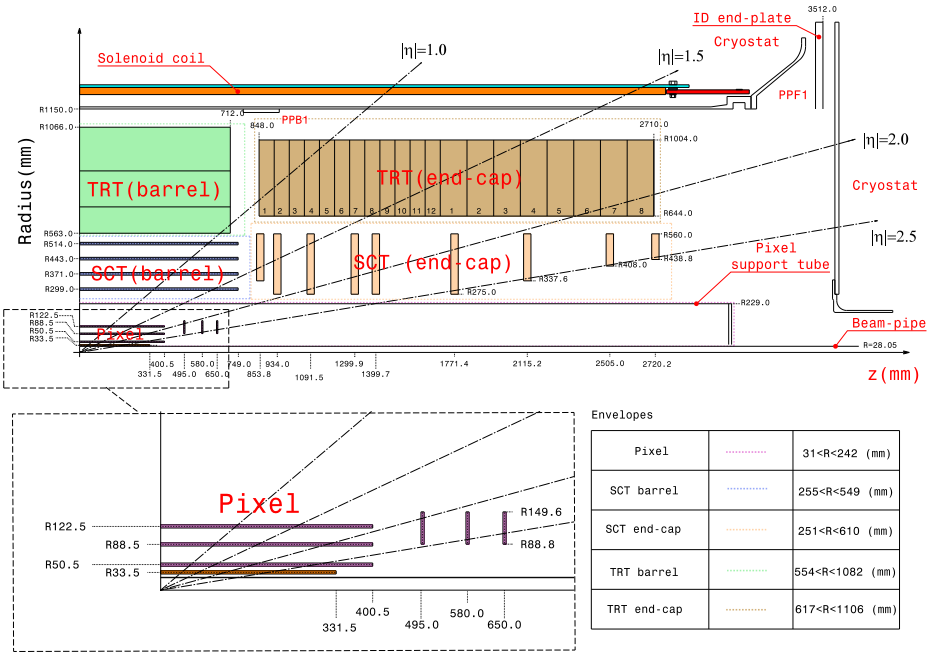

Figure 12: The r-z cross-section views of the position of a quadrant of all inner detectors (upper panel) and the pixel detector (lower left panel). The table shows the distance range of each sub-detector in r-axis.

within $-5\sim-10$ °C to suppress the annealing effect and the noise.

The IBL is the innermost layer of the pixel detector and consists of 14 carbon fiber staves. The addition of the IBL improves the track resolution [20]. Two different pixel sensors are used in each stave. 8 planar sensors are placed in the central region, and 4 full 3D sensors are placed on two sides of the stave. The design of the planar sensor is similar to the original design for the pixel detector but has several improvements. The 3D sensors have a better tolerance to a high fluence of the non-ionizing particles.

3.5.2 Silicon micro-strip tracker (SCT)

The SCT consists of 2112 barrel modules assembled in 4 layers in the barrel region [22], and 1976 end-cap modules assembled in 18 disks in the end-cap region [23]. The sensors of SCT are made by classical single-sided p-in-n technology. A barrel module contains four sensors. On each end, two sensors are connected in a daisy chain to form 768 strips of approximately 12 cm in length. On the other side, the identical sensors are glued back-to-back. The two identical sensors on both sides are aligned with a stereo angle of 4 mrad. Each module is mounted at an angle of 11° to the tangent to the cylinder in the inner two layers and 11.5° in the outer two layers. There are three different types of end-cap modules with trapezoidal sensors.

The modules with daisy-chained sensors are used in the outer and middle rings. The modules with one sensor on each side are used in the inner rings. All end-cap modules are similar to barrel modules. Two identical sensors are glued back-to-back.

3.5.3 Transition radiation tracker (TRT)

The TRT also consists of barrel modules and end-cap modules in the total coverage up to $|\eta| < 2.0$. The gas for the ionization is flowed in the straws. The radiators made by the polypropylene are placed outside of the straw. The length of straws is 144 cm in barrel modules and 37 cm in end-cap modules. The tube wall is made in the multilayer, including a layer of aluminium as the cathode. The gold-plated tungsten wires with the diameter of 31 μm kept at ground potential are in the center of the straws.

For the barrel part, total of 96 modules are assembled into three layers of rings from the inside to the outside. Each ring contains 32 modules. For the end-cap module [24], the straws placed radially in a wheel with layers. Between straw layers, layers of 15 μm thick polypropylene foils are filled. There are two different sets of wheels. The set close to the barrel contains 12 wheels. Each wheel has 8 layers of straws spaced by 8 mm. The outer set contains eight wheels. Each wheel has 8 layers of straws spaced by 15 mm.

The standard gas mixture is 70% Xe, 27% CO_2, and 3% O_2. During Run2, as the gas leak in some modules was large, the gas mixture of 70% Ar, 27% CO_2, and 3% O_2 is used instead. Although argon gas has much lower efficiency to be ionized by TR photons, the tracking capacity is similar to the xenon gas.

3.6 Calorimetry

The calorimeters have wide coverage in the range of $|\eta| < 4.9$ and are designed to measure the energy of both neutral and charged particles. Two different technologies are used in the calorimeters. The liquid argon calorimeters [25] provides the measurements of particles like electrons, positrons, photon, and hadronic particles. The tile calorimeters [26][27] provide the measurements of hadronic particles. The Liquid argon calorimeters (LAr) is located in the inner side of tile calorimeters in the range of $|\eta| < 1.7$, as shown in Figure 10.

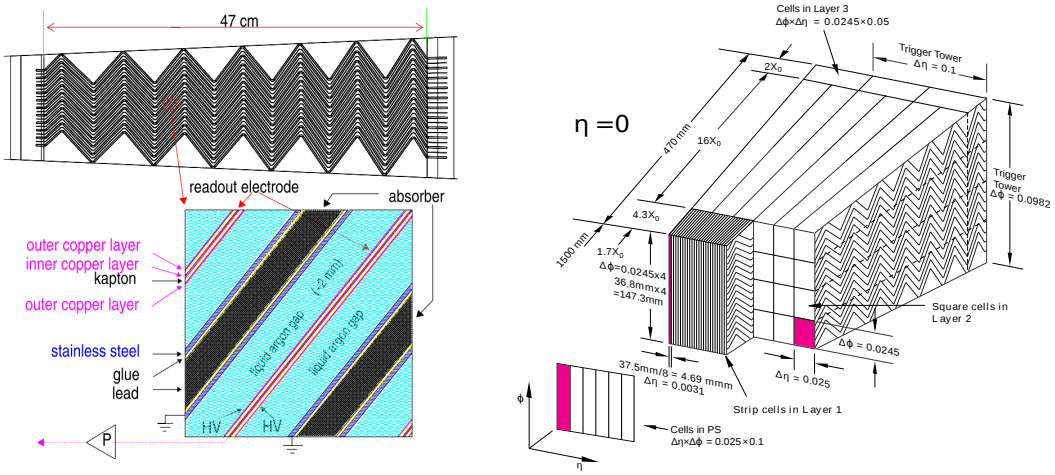

(a) (b)

Figure 13: (a) Accordion structure of electrode plates and absorber plates. The lower figure shows the details of the layers of plates and liquid argon gaps [28]. (b) A schematic of cells in accordion electrons divided into three layers [29].

3.6.1 Liquid argon calorimeter (LAr)

The particle through the liquid argon causes the ionization of argon atoms. The free electrons drift in the electrical field. Since liquid argon needs low temperature and good thermal insulation, the barrel part of the electromagnetic calorimeter (EMB) is sealed inside of the barrel cryostat. Three sub-systems, an electromagnetic end-cap calorimeter (EMEC), a hadronic end-cap calorimeter (HEC), and a forward calorimeter (FCal) [30] are in the end-cap cryostat for both sides. The EMB cover the range of $|\eta| < 1.475$. The EMEC covers the range of $1.375 < |\eta| < 3.2$. The HEC covers in the range of $1.5 < |\eta| < 3.2$. The FCal provides the coverage in the range of $3.1 < |\eta| < 4.9$.

3.6.1.1 Barrel electromagnetic calorimeter (EMB) and end-cap electromagnetic calorimeter (EMEC)

The absorbers in the calorimeters are lead plates glued between the two sheets of the stainless steel. The electrodes are three-layer copper-polyimide (Kapton) printed circuit boards [31]. Both absorbers and electrodes are bent in an accordion geometry to provide full coverage of absorbers and active material in the path of the particle. The cylindrical detector is made of the absorbers interleaved with the electrodes and the honeycomb spacer for the 2mm LAr gap (see Figure 13 (a)). The accordion-shaped electrodes are divided into three layers: the front layer, the middle layer, and the back layer (see Figure 13 (b)). The presamplers (PS) [32] are in front of the

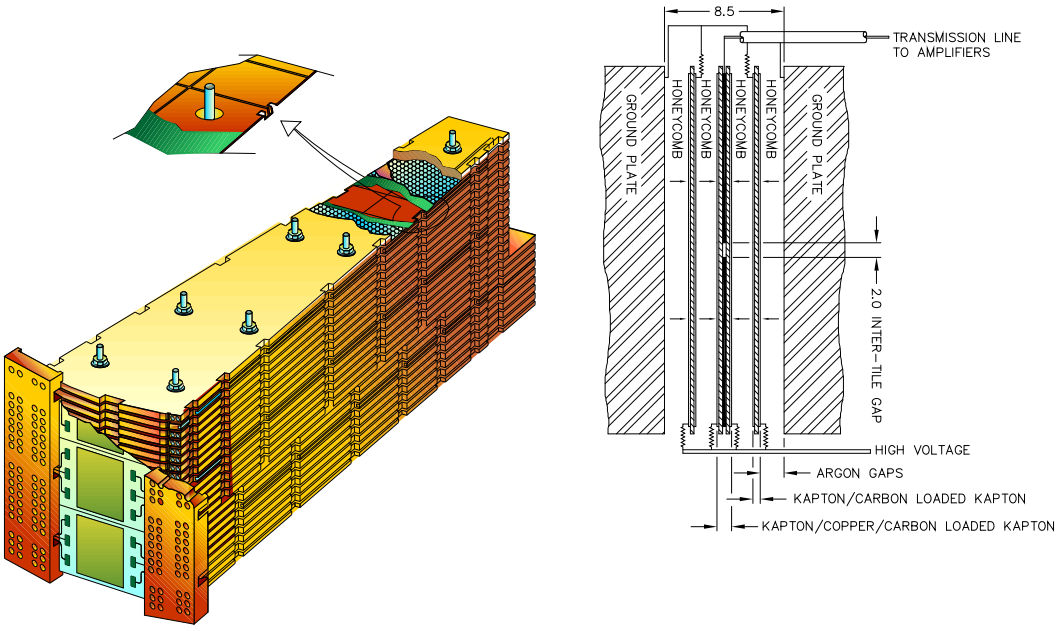

(a) (b)

Figure 14: (a) Cutout view of a HEC module [18]. (b) A schematic of the electrodes in the gap between copper plates [18].

electromagnetic calorimeters in the range of $|\eta| < 1.8$ for the improvement of the energy resolution. Except for the transition region between EMB and EMEC, the cells in the front layer have the finest granularity in η direction of the EMB ($\eta \times \phi = 0.003 \times 0.1$) but variable sizes in the EMEC to provide γ/π^0 separation. The cells in the middle layer have the medium granularity in η direction ($\eta \times \phi = 0.025 \times 0.025$ in EMB and EMEC). The cells in the back layers have the largest granularity ($\eta \times \phi = 0.05 \times 0.025$ in EMB and EMEC).

3.6.1.2 Hadronic end-cap calorimeter (HEC)

The hadronic end-cap calorimeter provides the measurements for the energy of hadronic particles. The absorbers in the hadronic end-cap calorimeter are the copper plates instead of the lead plates. Front wheels (HEC1) and rear wheels (HEC2) are on each side of the end-cap. Each wheel is composed of 32 modules (see Figure 14 (a)). Except for the front and rear copper plates which have only half of the thicknesses, the thicknesses of the copper plates in the HEC1 and the HEC2 are 25 mm and 50 mm, respectively. The copper plates are bolted together by the stainless steel tie rods and the annular spacers on the tie rods to maintain the 8.5 mm gap between two copper plates (see Figure 14 (b)). Three electrode boards are arranged in the 8.5 mm

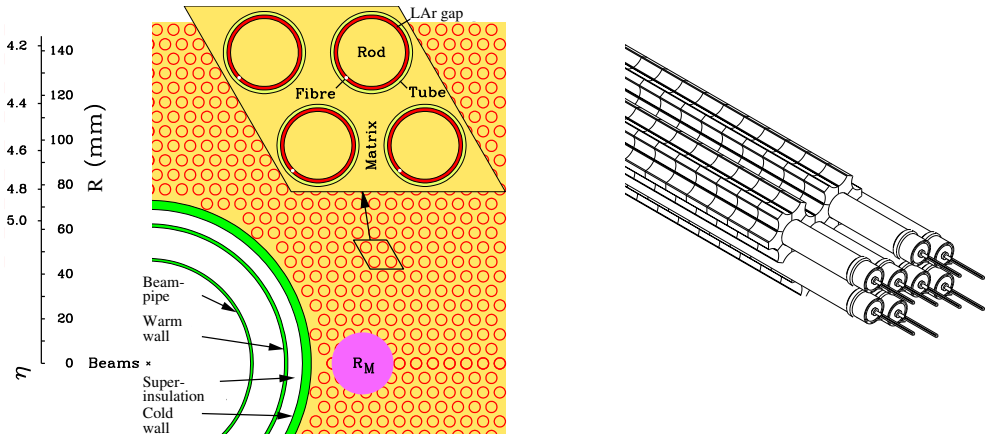

(a) (b)

Figure 15: (a) The array structure of anode rods, cathode tubes, and the LAr gaps in the FCal1 module [18]. The magenta disk represents the Molière radius. (b) The array of electrodes and the tungsten alloy slugs surrounded for the hadronic forward calorimeters [18].

gap between copper plates and separated by honeycomb spacers. The honeycomb spacers maintain the LAr gap of 1.8 mm between boards. The middle board contains a layer of the copper as a read-out electrode.

3.6.1.3 Forward calorimeter (FCal)

The FCal modules are surrounded by the end-cap cryostats. Three modules on each side are named as FCal1, FCal2, and FCal3 from the module close to the interaction point. The FCal1 is designed as an electromagnetic calorimeter, and the FCal2 and FCal3 are hadronic calorimeters. The electrode rods for the readout are parallel to the beam pipe and placed in the copper tube with PEEK fiber wrapped. The gap between the copper tube and rod is filled with the LAr. Since the FCal modules are close to the beam pipe, the high rate of the ionization is expected. To reduce the accumulation of the charge, the LAr gaps of the FCal1, FCal2, and FCal3 are smaller than the nominal LAr gap ($\sim$2 mm), and they are 0.269 mm, 0.376 mm, and 0.508 mm, respectively. For the FCal1, the material used in the rods and the matrix of the absorbers are the same. The absorbers are copper plates with holes for the electrodes, as shown in Figure 15 (a). For the FCal2 and FCal3, the rods are made by pure tungsten, but the absorber slugs (see Figure 15 (b)) are made by the tungsten alloy (97% tungsten, 2% nickel, and 1% iron).

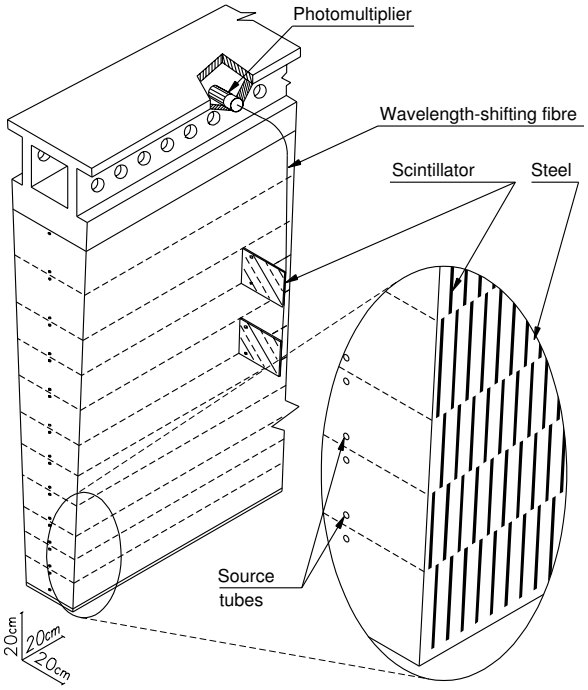

Figure 16: A schematic of the structure of absorbers and scintillators in a tile calorimeter module [18].

3.6.2 Tile calorimeter

The tile calorimeter [27, 33] consists of steel plates as the absorber and polystyrene tiles as the scintillator. The scintillator is inserted in the pockets which are formed between the master plates with trapezoidal shape divided by steel tiles, as shown in Figure 16. The scintillators are connected to the wavelength shifting fibers which guide the light to the PMTs in the girder. The modules are installed side by side to form a cylinder.

3.7 Muon spectrometer

The muon spectrometer (MS) contains the barrel part and end-cap part. The muon spectrometer covers the pseudorapidity range of $|\eta| < 2.7$. There are two purposes of the muon spectrometers. First, the precision momentum measurements are measured by the precision tracking chambers, which are the Monitored Drift Tube (MDT) and the Cathode-Strip Chamber (CSC). Second, the trigger chambers provide muon tracking information to the L1 trigger system. The Resistive Plate Chambers (RPC) and the Thin Gap Chambers (TGC) are the trigger chambers.

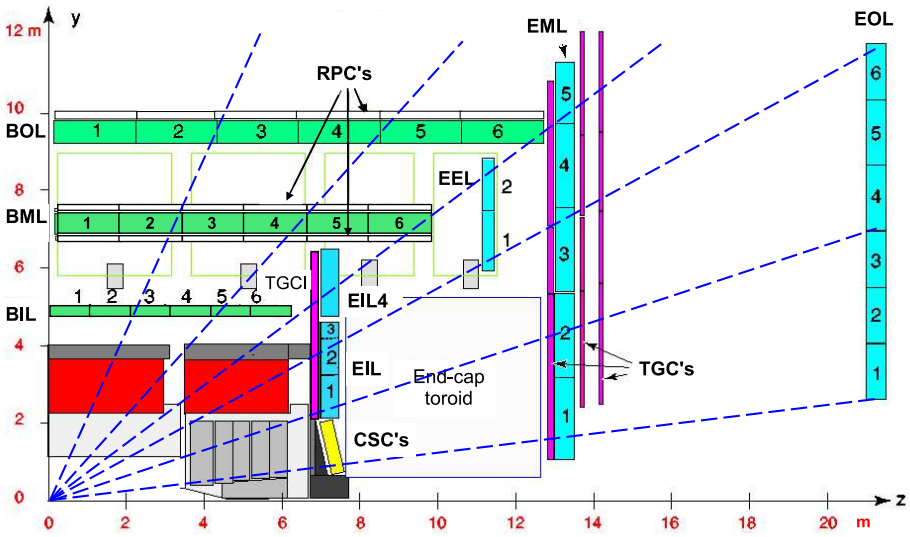

Figure 17: The schematic of r-z cross-section view of the muon spectrometer [18]. The dash lines show the muon trajectories with the infinite momentum.

3.7.1 Precision tracking chambers

3.7.1.1 Monitored Drift Tube (MDT)

The cathode of the sensor is the aluminium tube with an inner diameter of 30 mm. The gold-plated tungsten-rhenium wire (97% W and 3% Re) with a diameter of 50 μm is the anode at the center of the aluminium tube, which is the cathode. The tube is filled with 3 bara of Ar gas with a mixture of 93% Ar, 7% CO_2, and a few hundred ppm of water vapor. The HV is applied between the anode and the cathode. When the muon passes through the tube, the gas molecules are ionized, and the electron avalanche occurs. The drift time of the electrons is up to 700 ns. The read-out electronics is connected at the opposite end of the HV supply.

The MDT chambers are designed in three layers in the barrel region and three layers in the end-cap region and cover in a range of $|\eta| < 2.7$. The layout of an MDT chamber used in the barrel region is shown in Figure 17. The chambers are rectangular in the barrel region but trapezoidal in the end-cap region. There are two groups of multi-layers in each chamber. In the innermost layer of chambers, there are four tube layers for each group. In the middle and outer layers, three tube layers are used. The four-tube-layer structure is used to enhance the performance of the pattern recognition.

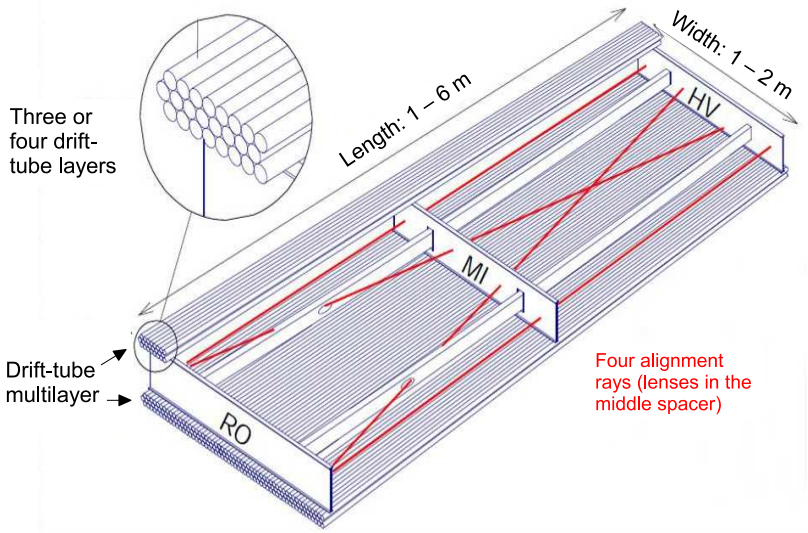

Figure 18: The schematic of a module of Monitored Drift Tubes [18]. Four alignment rays are used for monitoring the internal geometry. RO and HV mean the side of connection of readout electronics and the side for applying high voltage.

3.7.1.2 Cathode-Strip Chamber (CSC)

The CSC is located in the ATLAS small wheel behind the end-cap cryostats. The CSC covers the pseudorapidity range of $2.0 < |\eta| < 2.7$. In this region, the counting rate is over the limit of 150 Hz/cm^2 for the MDT. The rate of CSC can deal with up to 1000 Hz/cm^2.

The CSC contains multiple anode wires and cathode strips, as shown in Figure 19. The wires which are the same material used in the MDT are in the radial direction of the ATLAS detector. There are two types of the cathode planes in a CSC. First, the cathode strips lie in the direction orthogonal to the anode wires. This setup is targeting the space resolution of the η direction. Second, the cathode strips are in the same direction of the wires to enhance the resolution of the ϕ direction. There are also the small and the large chambers. The anode pitches are 5.3 mm in the small chambers and 5.6 mm in the large chambers. The strip width is 1.5 mm in the small chambers and 1.6 mm in the large chambers. The inter-strip gaps are the same. It is 0.25 mm. The gas mixture for the ionization is 80% Ar and 20% CO_2.

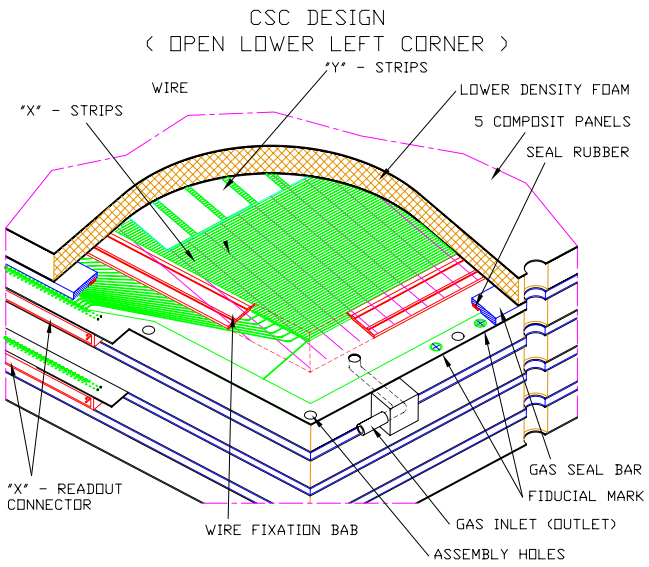

Figure 19: The cutoff views of the CSC design [18].

3.7.2 Trigger chambers

3.7.2.1 Resistive Plate Chambers (RPC)

The three layers of the RPC at the radius 7 m, 8 m 10 m from the interaction point are in the barrel region and cover in the range of $|\eta| < 1.05$. There are two units in a layer. Each unit contains two gas volumes for the discharge. The plate is made of phenolic-melaminic plastic laminate glued with graphite layers as electrodes. The gas mixture of 94.7% $C_2H_2F_2$, 5% isobutane, and SF_6 as the high resistive insulator is flushed through the gas volume. 9.8 kV is applied to the electrodes with 2mm gap.

3.7.2.2 Thin Gap Chambers (TGC)

The TGC is installed in the end-cap region for the muon trigger and compensation of the measurement of the MDT in azimuthal coordinate. TGC consists of multiple wires with a diameter of 50 μm in the middle of 2.8 mm gap. Wire pitch is 1.8 mm. The wall of the gap is coated with a graphite layer. The ionizing gas mixture of 55% CO_2 and 45% n-pentane is flushed through the gas volume. The high voltage is applied on the wire, and the graphite layer is grounded.

The outer ring of the TGC covers the range of $1.05 < |\eta| < 1.92$. The inner ring of the TGC covers the range of $1.92 < |\eta| < 2.4$. The outer ring consists of one layer of triplet modules and two layers of the doublet modules to form a seven-layer

structure. The inner ring of TGC only consists of one layer of double modules. The honeycomb paper is used for the separation of the chambers.

3.8 Forward Detector for Luminosity measurement

The LUCID-2 detector (LUminosity measurement using Cerenkov Integrating Detector) [34] provides the main measurement of the instantaneous luminosity and the integrated luminosity for the p-p scattering. The LUCID-2 is the upgraded version of the LUCID detector described in the ATLAS detector paper [18]. The PMT with quartz window as Cherenkov medium is used. Four groups of 5 PMTs surround the beam pipe at 14 m of both A-side and C-side. For each group, there is one MODIFIED detector with reduced acceptance ($\phi = 7$ mm but $\phi = 10$ mm for the nominal one), one LED detector for the calibration with LED signals, one BI detector for the calibration with ^{207}Bi sources, and one SPARE detector with the same configuration of the LED detector.

3.9 Trigger and Data Acquisition (TDAQ)

The trigger and data acquisition system plays an important role in the collider experiments. Only the data with interesting phase space is collected. The useful data is identified online by the trigger system and stored to be analyzed offline. Trigger system at ATLAS consists of the hardware-based Level-1 trigger (L1) and the software-based high level trigger (HLT) (see Figure 20).

3.9.1 Level-1 trigger

The decision of the L1 trigger are made by the Central Trigger Processor (CTP). The CTP receives the signals from the L1 calorimeter (L1Calo) trigger, L1 muon (L1Muon) trigger, L1 topological (L1Topo) trigger for the identified objects, signals from the Minimum Bias Trigger Scintillators (MBTS), LUCID-2, and zero-degree calorimeters (ZDC) [36].

The L1Calo trigger receives the signals from the calorimeters. The preprocessor system digitizes and calibrates the analog signals from front-end boards and passes the outputs to the Cluster Processor (CP) and Jet/Energy-sum Processor (JEP) in parallel. The clusters of trigger towers are identified by the preprocessor system.

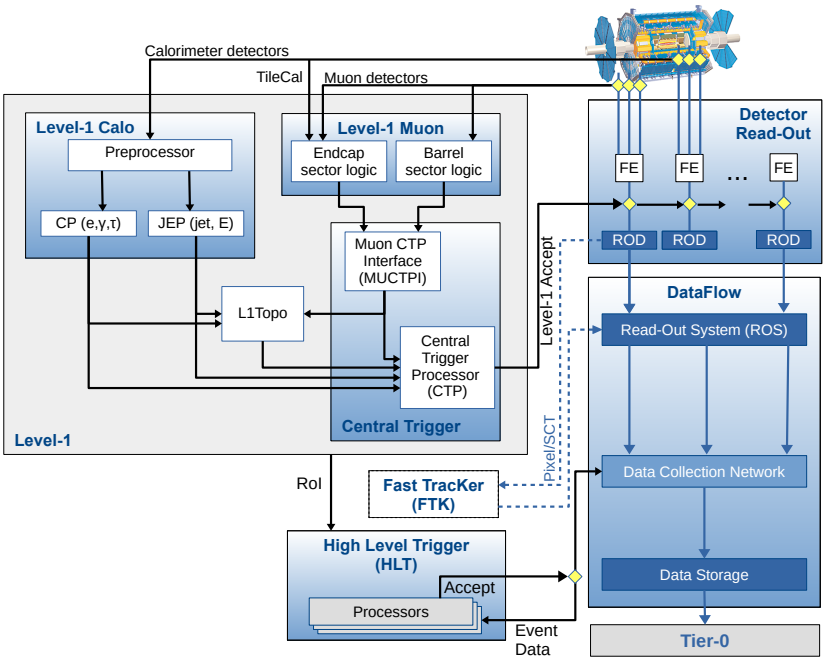

Figure 20: The schematics of the ATLAS TDAQ system in Run 2 with L1 trigger, HLT, and read-out data flow [35]. The Fast Tracker project was closed in 2019 due to the lack of person power.

The CP system identifies the electron, photon, and τ candidates. The JEP system identifies the jet candidates and produces the $E_{\mathrm{T}}^{\mathrm{miss}}$. The L1Muon trigger identifies the muon candidates by using the hits in the RPCs and TGCs if the coincidence of the hits satisfies the logic. The L1Topo trigger combines the geometry and kinematics of the identified objects from the L1Calo or L1Muon systems. The rate of Level-1 trigger reduces to the rate up to the maximum of 100 kHz from the bunch crossing rate of about 40 MHz. The latency of the process is less than 2.5 μs. The readout of the front-end electronics is sent to ReadOut Drivers (ROD) for the initial processing and formatting. The data is buffered in the ReadOut System (ROS).

3.9.2 High level trigger

The software based high level trigger is the second stage of the trigger systems and composed of the computer farm of about 40,000 Processing Units. The HLT receives the Region of Interests from the L1 trigger. The data rate is further reduced to 1.2 kHz after the HLT. The events accepted by the HLT are sent to the permanent storage for the offline analysis and exported to the Tier-0 facility at CERN's computing center.

4 Samples and event reconstruction

For the search for the stops, with the R-parity conservation, the stops are produced in pair in the events. For both stops, the two-body decay channel, $\tilde{t}_1 \to t\tilde{\chi}_1^0$, where $t \to bW \to bqq'$, is the target in this thesis. That is, the $\Delta m(\tilde{t}_1, \tilde{\chi}_1^0)$ is larger than m_t in this region. The final state contains four light quark jets, two b quark jets, and missing transverse momentum.

4.1 Data and Monte Carlo simulation

4.1.1 Data selections and triggers

The full ATLAS Run2 data collected in 2015-2018 with 33.7 of the average number of interactions per bunch crossing $\langle\mu\rangle$ at $\sqrt{s} = 13$ TeV in the p-p collision is used in this analysis. Figures 21 (a) and 21 (b) summarize the data collection in the full Run2. The data is reprocessed offline for the use of physical analysis. All data is recorded in lumi blocks (one lumi block is 1 min). The final integrated luminosity of selected data is 139 ± 2 fb^{-1} [38].

The events which pass the $E_{\mathrm{T}}^{\mathrm{miss}}$ triggers for the high $E_{\mathrm{T}}^{\mathrm{miss}}$ requirement in signal regions and control regions or the single lepton triggers for the control regions [39] are used. The used triggers in the ATLAS Run2 change between data years and are summarized in Tables 1 and 2, where the names include hardware-based first-level triggers (L1) and software-based high-level triggers (HLT).

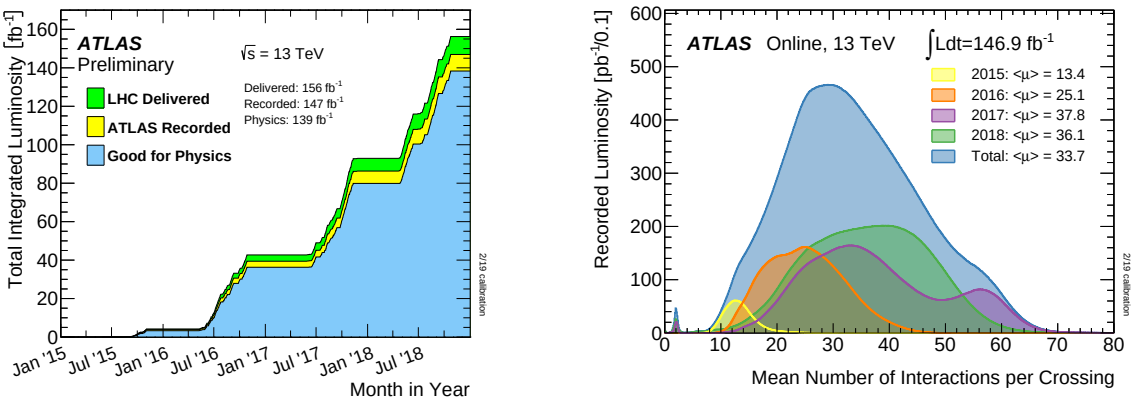

(a) (b)

Figure 21: (a) Integrated luminosity and (b) $\langle\mu\rangle$ distribution during all the Run2 period [37].

Table 1: Lowest unprescaled missing transverse energy trigger chains used for 2015, 2016, 2017, and 2018 0- and 1-lepton selections [40].

Trigger chain names	2015	2016	2017	2018
HLT_xe70_mht	✓			
HLT_xe90_mht_L1XE50 (A-D3)		✓		
HLT_xe100_mht_L1XE50 (D4-F1)		✓		
HLT_xe110_mht_L1XE50 (F2-end)		✓		
HLT_xe110_pufit_L1XE55 (B1-D5)			✓	
HLT_xe110_pufit_L1XE50 (D6-end)			✓	
HLT_xe110_pufit_xe70_L1XE50 (B-C5)				✓
HLT_xe110_pufit_xe65_L1XE50 (C6-end)				✓

Table 2: Lowest unprescaled single lepton trigger chains used for 2015, 2016, 2017, and 2018 2- and 3-lepton selections [41][42]. A logical OR is performed between the various chains for a given year.

Trigger chain names	2015	2016	2017	2018
HLT_e24_lhmedium_L1EM20VH	✓			
HLT_e26_lhtight_nod0_ivarloose		✓	✓	✓
HLT_e60_lhmedium	✓			
HLT_e60_lhmedium_nod0		✓	✓	✓
HLT_e120_lhloose	✓			
HLT_e140_lhloose_nod0		✓	✓	✓
HLT_mu20_iloose_L1MU15	✓			
HLT_mu26_ivarmedium		✓	✓	✓
HLT_mu40	✓			
HLT_mu50		✓	✓	✓

- Condition of the first level trigger (L1)

In L1 trigger, for example, "L1XE50" in Table 1 represents the met trigger with a threshold of 50 GeV. "L1MU15" in Table 2 represents the muon trigger with a threshold of 15 GeV. "EM" means the energy calculation is from electromagnetic calorimeters. The H denotes the veto of hadronic calorimeters for the electron candidates. The absorption length depends on η for the material in front of the calorimeters. V denotes the compensation of the effect by varying E_{T} as a function of η.

- Condition of the high level trigger (HLT)

Table 2 summaries the trigger chains with the HLT following the L1. The names of particle type are "xe" for the $E_{\mathrm{T}}^{\mathrm{miss}}$, "e" for the electrons and "mu" for the muons. For the $E_{\mathrm{T}}^{\mathrm{miss}}$ triggers [40], the number in the trigger names shows the transverse energy, and three algorithms are used for the reconstruction of the $E_{\mathrm{T}}^{\mathrm{miss}}$. First, the most basic algorithm, "cell", is to sum over all the calorimeter cells with the energy larger than two times of the noise level. Second, a "mht" algorithm means the $E_{\mathrm{T}}^{\mathrm{miss}}$ is calculated from the sum of all R=0.4 jets by using the anti-kt algorithm without the calibration. Third, a "pufit" algorithm represents a fit to the signals below E_T thresholds for the pile-up. The signals above the E_T threshold are corrected by using the fit results. For example, "HLT_xe110_pufit_xe65" denotes $E_{\mathrm{T}}^{\mathrm{miss}}$ threshold of 110 GeV in the "pufit" algorithm and 65 GeV in the "cell" algorithm. Figure 22 shows the efficiencies of the $E_{\mathrm{T}}^{\mathrm{miss}}$ triggers. For the electron triggers [41], the number shows the p_{T} of the electron. The "lhloose", "lhmedium", and "lhtight" denote working points of the likelihood discriminant of the multivariate techniques. The "nod0" means the impact parameter d_0 and its significance are not included in the selections. The "ivarloose" is an additional requirement for the track-only isolation for the electrons. In muon triggers [42], the HLT_mu26_ivarmedium is designed to select low p_{T} muon with the loose isolation. The trigger rate is in control, and the efficiency remains high. The HLT_mu20_iloose_L1MU15 is the lowest unprescaled version in 2015.

4.1.1.1 Monte Carlo simulation

A Monte Carlo (MC) method is used for the simulation of expected background and signal samples. The nominal MC background samples are all produced by the full ATLAS detector simulation modelled by GEANT4 [43], and some systematics

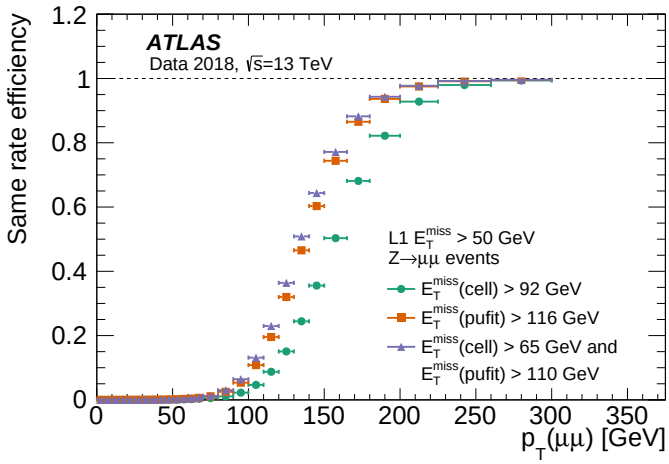

Figure 22: Trigger efficiency in the 2018 data of $Z\rightarrow \mu\mu$ events as a function of offline $E_{\mathrm{T}}^{\mathrm{miss}}$ [40]. Three different HLT algorithms, the "cell" algorithm alone, the "pufit" algorithm, and the combination of the "cell" algorithm and "pufit" algorithm, are shown.

samples and signal samples are produced by the ATLFAST-II [44]. For the ATLFAST-II, the electromagnetic and hadronic showers are parametrized in the longitudinal and lateral shower shapes in the calorimeters.

The real data contains multiple pp collisions, which are called pile-up, in one bunch crossing. To simulate such pileup conditions, the MC samples are produced for matching the pileup condition of the data. The pileup events are added with overlaid minimum bias interactions generated by using PYTHIA 8 [45, 46] with A3 set of tuned parameters [47] and NNPDF2.3 LO PDF set [48].

Tables 3 and 4 summarize the generators, PDF, tunes for underlying events (UE), and the order of the perturbative calculations for the cross-sections of all MC nominal samples used in the study of the stop analysis and DNN top taggers in Chapter 5. The stop signal samples are generated with MADGRAPH5_aMC@NLO 2.6.2 [49] at the next-to-leading order (NLO) in QCD. The parton showering and the hadronization are simulated in PYTHIA 8, and the decay of c-hadrons and b-hadrons is modeled using EVTGEN 1.6.0 [50]. The mixing of $\tilde{t}_{\mathrm{L}}$ and $\tilde{t}_{\mathrm{R}}$ is set to the maximum in the signal samples. Each signal sample has its own pair of the stop mass and neutralino mass. Figure 23 shows the signal samples in the $m_{\tilde{t}}$-$m_{\tilde{\chi}_1^0}$ plane. The Z/W+jets and diboson samples are generated by using SHERPA 2.2.1 [51] with NLO NNPDF2.3 set for up to two jets at NLO and up to four jets at LO and the parton showering at NLO level for the first and second jet and LO for the third and fourth jet. The $t\bar{t}W/Z$, tZ, tWZ, and $t\bar{t}H$ are generated by using MG5_aMC@NLO 2.3.3 (MG5_aMC@NLO 2.3.3 for $t\bar{t}H$) interfaced to PYTHIA 8.230 (PYTHIA 8.212 for tWZ) with A14 set of tuned

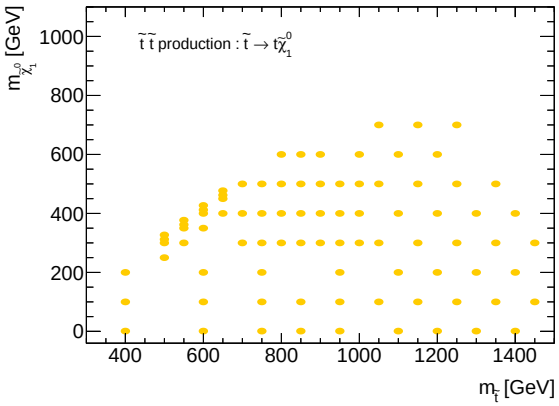

Figure 23: Signal samples in the the $m_{\tilde{t}}$-$m_{\tilde{\chi}_1^0}$ plane. Orange circles represent signal mass points.

parameters and NLO NNPDF3.0 set. Both $t\bar{t}$ and single top samples are generated by using Powheg-Box v2 [52] interfaced to PYTHIA 8.230 with A14 set of tuned parameters and NNLO NNPDF3.0 set. Alternative $t\bar{t}$ samples are generated by using POWHEG interfaced to HERWIG 7 with H7UE tune [53] and aMC@NLO [49] interfaced to PYTHIA 8 with the A14 tune for the alternative parton showering and generator. Finally, multijet samples are generated by using PYTHIA 8.230 with LO NNPDF2.3 set and A14 tune.

For MC samples used in DNN top tagger studies (see Chapter 5), $Z' \to t\bar{t}$ events with inclusive final state are generated by using PYTHIA 8 with A14 set of tunable parameters and LO NNPDF2.3 PDF set. The resonant mass is set to 2 TeV, and the cross-section is reweighed to flat distribution in the 200 GeV $< p_{\mathrm{T}} <$ 3 TeV. γ+jet samples are generated by SHERPA 2.1.1 with NLO CT10 set. $V\gamma$ samples with $V \to qq'$ states are generated by SHERPA 2.1.1 with LO CT10 set. $t\bar{t}$+γ samples are generated by MG5_aMC@NLO 2.2.3 interfaced to PYTHIA 8 with A14 set of tunable parameters and LO NNPDF2.3 set.

Table 3: Overview of the nominal simulated samples used in the stop analysis.

Process	ME event generator	ME PDF	PS and hadronisation	UE tune	Cross-section calculation
Z+jets, W+jets	SHERPA 2.2.1	NNPDF3.0 NNLO	SHERPA	Default	NNLO [54]
$t\bar{t}Z$, $t\bar{t}W$	MG5_aMC@NLO 2.3.3	NNPDF3.0 NLO	PYTHIA 8.230	A14 [48]	NLO [49, 55]
tZ	MG5_aMC@NLO 2.3.3	NNPDF3.0 NLO	PYTHIA 8.230	A14	NLO [49]
tWZ	MG5_aMC@NLO 2.3.3	NNPDF3.0 NLO	PYTHIA 8.212	A14	NLO [49, 55]
$t\bar{t}H$	MG5_aMC@NLO 2.2.3	NNPDF3.0 NLO	PYTHIA 8.230	A14	NLO [49]
$t\bar{t}$	Powheg-Box v2	NNPDF3.0 NNLO	PYTHIA 8.230	A14	NNLO+NNLL [56, 57, 58, 59, 60, 61]
Single top	Powheg-Box v2	NNPDF3.0 NNLO	PYTHIA 8.230	A14	NNLO+NNLL [62, 63, 64]
Diboson	SHERPA 2.2.1-2.2.2	NNPDF3.0 NNLO	SHERPA	Default	NLO [49, 65]
Multijet	PYTHIA 8.230	NNPDF2.3 LO	PYTHIA 8.230	A14	NLO [66]
Stop signal	MG5_aMC@NLO 2.6.2	NNPDF2.3 NLO	PYTHIA 8.230	A14	NNLO [67, 68, 12, 69]

Table 4: Overview of the nominal simulated samples used in DNN top taggers.

Process	ME event generator	ME PDF	PS and hadronisation	UE tune	Cross-section calculation
V+jets ($V = W/Z$)	SHERPA 2.2.1	NNPDF3.0 NNLO	SHERPA	Default	NNLO
	SHERPA 2.1.1	CT10 NLO [70]	SHERPA	Default	NNLO
$t\bar{t}$	Powheg-Box v2	NNPDF3.0 NNLO	PYTHIA 8.230	A14	NNLO+NNLL
Single top	Powheg-Box v2	NNPDF3.0 NNLO	PYTHIA 8.230	A14	NNLO+NNLL
Diboson	SHERPA 2.2.1	NNPDF3.0 NNLO	SHERPA	Default	NLO
Multijet	PYTHIA 8.230	NNPDF2.3 LO	PYTHIA 8.230	A14	NLO
γ+jet	SHERPA 2.1.1	CT10 NLO	SHERPA	Default	NLO [49]
$V\gamma$	SHERPA 2.1.1	CT10 NLO	SHERPA	Default	NLO [49]
$t\bar{t}\gamma$	MG5_aMC@NLO 2.3.3	NNPDF2.3 LO	PYTHIA 8.212	A14	NLO [49]
$Z' \to t\bar{t}$	PYTHIA 8.230	NNPDF2.3 LO	PYTHIA 8.230	A14	NLO [49]

4.2 Event reconstruction

In this section, the definitions of physical objects used in this thesis are introduced: electrons, muons, taus, jets, and $E_{\mathrm{T}}^{\mathrm{miss}}$. In our interested events, the final states are jets and $E_{\mathrm{T}}^{\mathrm{miss}}$, and the leptons are vetoed.

4.2.1 Track reconstruction

Charged particles pass through the inner detector and produce signals in each layer of sensors. The trajectories of the charged particles are reconstructed as tracks. The reconstruction of tracks is performed in three stages [71]:

- Clusterization

Charge particles usually produce signals in multiple pixel sensors of each layer. These signals are clustered into clusters. The positions of the clusters are referred to three-dimensional "space-points".

- Iterative combinatorial track finding

Track finding starts from tracks seeds, which are sets of three space-points. To distinguish the track quality, the purity of tracks is introduced by categorizing the space-points in SCT-only, pixel-only or mixed detectors. A combinatorial Kalman filter [72] is used to reconstruct the preliminary tracks in the pixel and SCT detectors. Very high efficiency for the track reconstruction is achieved but there are also track candidates with the space-points, which overlaps with other track candidates or are incorrectly assigned.

- Ambiguity solving

The quality of track candidates is determined by introducing a "track score". The track score of a track candidate depends on the weight of assigned clusters and holes in the expected trajectory of the track. A χ^2 fit for each track is also considered in the track score. After the score is calculated, the track candidates with bad scores are rejected, but the rest of track candidates also need to satisfy the following minimum criteria:

- $p_{\mathrm{T}} > 500$ MeV, $|\eta| < 2.5$,
- $|d_0| < 2$ mm, $|\Delta z_0 \sin\theta| < 3$ mm,
- Number of silicon clusters ≥ 7,
- Number of shared modules ≤ 1,

  (The shared module is defined as the $N_{Pix}^{shared} + N_{SCT}^{shared}/2$. N_{Pix}^{shared} is the number of pixel clusters shared by multiple tracks. N_{SCT}^{shared} is the number of SCT clusters shared by multiple tracks)
- Number of holes in silicon detectors ≤ 2,
- Number of holes in the pixel detector ≤ 1.

The d_0 and z_0 denote the transverse and longitudinal impact parameters with respect to the beam-line position and the primary vertex (see the next section). The transverse impact parameters are defined as the shortest distance between the tracks and the reference in the x-y plane. The longitudinal impact parameters are defined as the distance projected in the z-axis between the reference and the point with the shortest distance in the x-y plane.

4.2.2 Primary vertex

Event data of a bunch-crossing contains multiple inelastic pp interactions which can be reconstructed as the primary vertices. The additional interactions are usually soft-QCD interactions which are considered as pile-up events. The number of the interactions per bunch crossing follows a Poisson distribution with the mean value $\langle\mu\rangle$, which can be estimated by using the instantaneous luminosity. Primary vertices are constructed by fitting the track information of charged particles. The selected tracks have to pass the stage of ambiguity solving with the following minimum criteria:

- $p_{\mathrm{T}} > 500$ MeV,
- $|d_0| < 4$ mm, $\sigma(\mathrm{d}_0) < 4$ mm, $\sigma(\mathrm{z}_0) < 10$ mm,
- Number of silicon clusters ≥ 9,
- Number of SCT clusters ≥ 4,

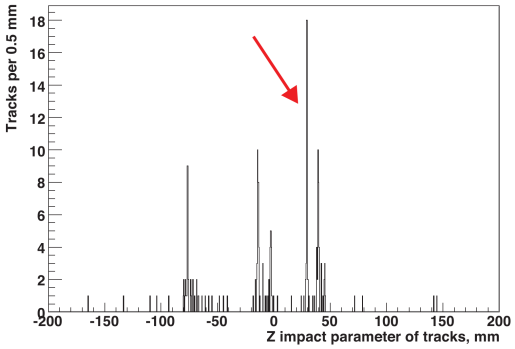

Figure 24: Distribution of the longitudinal impact parameter of the reconstructed tracks in the simulated $H(130) \to 4\ell$ events [73]. Signal primary vertex is marked with a red arrow.

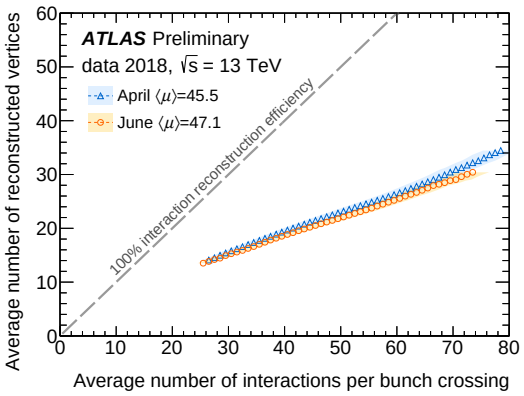

Figure 25: Performance of the reconstruction of primary vertices shown as a function of the average number of interactions per bunch crossing with 2018 data. The grey line shows 100% efficiency of the reconstruction.

- Number of holes in the pixel detector = 0,

where the definitions of d_0 and z_0 are different from the previous section, which denote the transverse and longitudinal impact parameters with respect to the center of the luminous region. $\sigma(d_0)$ and $\sigma(z_0)$ are the corresponding uncertainties.

The vertex seeds are identified by an iterative vertex finding algorithm [73]. The global maximum of the number of tracks in the z-direction is selected as a vertex seed (see Figure 24). The adaptive vertex fitting algorithm [74] is used to fit the position of the vertex seed and tracks around the seed by the χ^2 method. The tracks with the deviation of more than 7 σ are removed and used for the construction of the new vertex seeds. Figure 25 shows the average number of reconstructed primary vertices as a function of $\langle\mu\rangle$. The interactions, which can be estimated from the instantaneous luminosity, are not fully reconstructed as the primary vertices. A hard-scattering vertex is defined from a primary vertex with the highest sum of p_T^2 of the tracks.

4.2.3 Electron

Electrons are reconstructed in the range of $|\eta| < 2.47$, where the inner detector is available. Electrons pass through the inner detector and reach the calorimeter leave hits in the inner detector, and energy deposits in the calorimeter. The clusters of calorimeter cells are found by the topological-clustering algorithm [75]. The tracks are reconstructed in three steps: pattern recognition, ambiguity resolution, and TRT

extension. The reconstructed tracks are matched with the clusters by requiring the $|\eta_{cluster} - \eta_{track}| < 0.05$ and one of two selections of $-0.1 < \Delta\phi < 0.05$ and $-0.1 < \Delta\phi_{res} < 0.05$. $\Delta\phi$ and $\Delta\phi_{res}$ are calculated as $-q \times (\phi_{cluster} - \phi_{track})$ where q is the sign of the charge of the particle, and the momentum of the track is rescaled to the energy of the matched topo-cluster for $\Delta\phi_{res}$. The energy loss due to the path in the inner detector is estimated by the Gaussian Sum Filter [76], and the correction is applied to the clusters. The tracks with no pixel hit and associated with the conversion tracks from the photon conversion reconstruction [77] are considered as the electrons from the conversion of a photon.

Electron identification is performed by the likelihood ratio method. The several variables corresponding to the information of the calorimeters and tracking are considered in the PDF of the likelihood function. The detail of the variables can be found in Table 5.

Electron isolation is calculated by the "E_T cone" observable ($E^{isol}_{T,cone}$) based on the calorimeter energy cluster and the "p_{T} cone" observable (p^{isol}_{T}) based on the tracks to estimate the activity in the vicinity of the electron candidates. For E_T cone, the energy contributed from other clusters in the vicinity is summed in the range of $\Delta R < 0.2$ with the leakage and pile-up corrections. For p_{T} cone, the p_{T} of the surrounding charged particle is summed. The cone in the inner detector is chosen to be the smaller one due to the small size of sensors. The cone varies with p_{T} and has the upper limit of 0.2. The energy thresholds are optimized in the bins of η and E_T.

The energy and efficiency calibrations are performed with the samples of $J/\psi \to ee$ and $\mathrm{Z} \to ee$. $J/\psi \to ee$ samples are used in the derivation of scale factors[1] in the low p_{T} region (4.5 GeV$\sim$ 20 GeV). Z samples are used in the high p_{T} range ($>$ 15 GeV).

Baseline electrons are reconstructed in the range of $|\eta| < 2.47$ and have the $p_{\mathrm{T}} >$ 4.5 GeV. The identification has to pass *LooseAndBLayer* criteria with the track-to-vertex association ($|z_0 \sin\theta| < 0.5$ mm) applied. The *LooseAndBLayer* criteria have a requirement of the likelihood discriminant, at least two hits in the pixel detector, a hit in the IBL and total seven hits in the pixel and silicon strip detectors. The *baseline* electrons are used in the requirement of lepton-veto to define the signal regions.

The definitions of *signal* electrons are based on the *baseline* electrons and used for the control regions. *Tight* identification criteria, which is a tighter selection of

[1]The scale factors are the ratios of the energy (efficiency) in data to the energy (efficiency) in MC.

Table 5: Variables used for the likelihood discriminant [78].

Type	Name	Description
Hadronic leakage	R_{had1}	Ratio of E_T in the first layer of the hadronic calorimeter to E_T of the EM cluster (used in $\|\eta\| < 0.8$ or $\|\eta\| > 1.37$)
	R_{had}	Ratio of E_T in the hadronic calorimeter to E_T of the EM cluster (used in $0.8 < \|\eta\| < 1.37$)
Third layer of EM calorimeter	f_3	Ratio of the energy in the third layer to the total energy in the EM calorimeter (used in $E_T < 80$ GeV and $\|\eta\| < 2.37$)
Second of layer of EM calorimeter	w_{η^2}	Lateral shower width, $\sqrt{(\sum E_i \eta_i^2)/(\sum E_i) - ((\sum E_i \eta_i)/(\sum E_i))^2}$, where E_i is the energy of the cell i with the pseudorapidity η and the sum of energy is calculated within a window of 3×5 cells
	R_ϕ	Ratio of the total energy in a window of 3×3 cells to the total energy in a window of 3×7 cells
	R_η	Ratio of the total energy in a window of 3x7 cells to the total energy in a window of 7×7 cells
First layer of EM calorimeter	E_{ratio}	Ratio of the difference between the maximum energy deposit and secondary energy deposit in the cluster to sum of maximum and secondary energy
	f_1	Ratio of the energy in the first layer to the total energy in the EM calorimeter
Track conditions	d_0	Transverse impact parameter with respect to the beam line
	$\|d_0/\sigma(d_0)\|$	Significance of transverse impact parameter
	$\Delta p/p$	Momentum loss divided by the momentum in a track. Momentum loss is defined as the difference between the perigee and the last measurement point
TRT	eProbabilityHT	Likelihood probability based on transition radiation in the TRT
Track-cluster matching	$\Delta\eta_1$	$\Delta\eta$ between the first layer of the cluster and the extrapolated track
	ϕ_{res}	q$\Delta\phi$ where q sign of electric charge and $\Delta\phi$ between the second layer of the cluster and momentum-rescaled track

the likelihood discriminant, without the requirement of a hit in the IBL are further applied. In addition, the *Fix (Loose)* isolation, which passes $E^{isol}_{\mathrm{T},cone}/p_{\mathrm{T}} < 0.20$ and $p^{isol}_{\mathrm{T},var}/p_{\mathrm{T}} < 0.15$, is also required. The track-to-vertex association, d_0 significance $(d_0/\sigma_{d_0}) < 5$, is also applied.

4.2.4 Muon

The reconstruction of muons is available in the range of $|\eta| < 2.7$, where the muon spectrometer has coverage, and are based on several reconstruction methods [79]. A combined (CB) muon is reconstructed from the refit of tracks in both ID and MS. The hits in the MS can be added or removed in the refit process to improve the fit quality. A segment-tagged (ST) muon is reconstructed from a track in the ID and an associated local track in a segment of the CSC or the MDT. A calorimeter-tagged (CT) muon is reconstructed from a track in the ID and the associated deposited energy in the calorimeters with the minimum-ionizing particle. An extrapolated (ME) muon is reconstructed from a track in the MS and a loose requirement of the interaction points and is used in the range of $2.5 < |\eta| < 2.7$.

For CB tracks, the requirements of significance of a ratio of the charge and momentum (q/p significance), the absolute value of p_{T} difference in the ID and the MS divided by CB muon p_{T} (ρ'), and normalized χ^2 fit are applied to guarantee a good quality in the fit. Several thresholds are defined for different working points.

The track-based isolation and calorimeter-based isolation are considered in the muon isolation. The track-based isolation variable, $p_{\mathrm{T}}^{varcone30}$, depends on a variable cone size $\Delta R = min(10\,\mathrm{GeV}/p^{\mu}_{\mathrm{T}}, 0.3)$ with $p^{\mu}_{\mathrm{T}} > 1$ GeV. The method of calorimeter-based isolation is the same as the electron isolation. The variable, $E_{\mathrm{T}}^{varcone20}$, is used to estimate the activity in the range of $\Delta R < 0.2$.

The $\mathrm{Z} \to \mu\mu$ and $J/\psi \to \mu\mu$ are used for the calibration of the transverse momentum and the efficiencies. The p_{T} range of the calibration is available down to 4 GeV.

Baseline muons are reconstructed in the range of $|\eta| < 2.7$ and have $p_{\mathrm{T}} > 4$ GeV. The identification has to pass the *Medium* criteria. *Medium* muons are identified by using the CB and ME tracks. More than or equal to 3 hits in at least two MDTs layers are required in CB tracks except for the $|\eta| < 0.1$ where at least one MDT layer but no more than one hole in the MDT layers are accepted in the CB tracks. For ME tracks,

hits in at least three MDT/CSC layers are required in the $2.5 < |\eta| < 2.7$. The $|z_0 \sin\theta|$ < 0.5 mm is also applied.

Signal muons have to pass the same criteria of the *baseline* muon. In addition, the isolation working point is required to be *FixedCutLoose* (FCLoose), which satisfies $p_{\mathrm{T}}^{varcone30}/p_{\mathrm{T}}^{\mu} < 0.15$, $p_{\mathrm{T}}^{varcone20}/p_{\mathrm{T}}^{\mu} < 0.30$. The track-to-vertex association, d_0 significance < 3, is also applied.

BadMuon is also defined to veto a muon with a significantly bad momentum resolution. For the combined muon, the fit is performed with hits in the inner detector and muon spectrometer. The misalignment between two sub-detectors may not properly be taken into account. If muons satisfy

$$\frac{[\sigma(q/p)/(q/p)]_{ID}}{[\sigma(q/p)(q/p)]_{CB}} < 0.8 \text{ or } \frac{[\sigma(q/p)/(q/p)]_{MS}}{[\sigma(q/p)(q/p)]_{CB}} < 0.8, \tag{22}$$

which indicates that the resolution of the combined muon is much worse than the resolution in the inner detector and muon spectrometer, the muons are labelled as BadMuon. This kind of reconstructed muons causes a non-negligible impact on the analysis. The events with the "BadMuon" muons are vetoed.

"Cosmic muons" are defined to satisfy $|d_0| > 0.2$ mm, $|z_0| > 1$ mm or $|\sigma(q/p)/(q/p)| >$ 0.2. The events with cosmic muons are vetoed.

4.2.5 Jet

Jets are reconstructed in two stages. First, the signals of calorimeter cells are clustered by using the topological-clustering algorithm [75]. Second, the topo-clusters are clustered into jets by using the anti-k_t algorithm [80].

- **Topo-clusters**

A calorimeter cell with the absolute energy above 4σ of cell noise is treated as a seed. The expansion of a seed is performed to build a cluster if the energy of neighborhood cells exceeds 2σ of the cell noise, but the expansion stops in the neighborhood cells with no more than zero σ of the cell noise. A negative energy of the cells is possible since the cell signals are collected in the bipolar shape with a pedestal level sustaining for several bunch crossings. The negative energy can be caused by the pile-up and the electronic noise and used in the clustering to cancel the contribution of the out-of-time pile-up. A cluster with two or more local maximums is split into

clusters to keep the jet substructure and high quality of $E_{\mathrm{T}}^{\mathrm{miss}}$ reconstruction.

To deal with the nature of showering and the signal loss due to the strategy of clustering, there are three corrections of the energy applied for the cell signals. First, the cell signals are weighted with different scales, which are considered during the reconstruction of topo-clusters for the different types of the showering. The electromagnetic scale (EM scale) is set the weight to 1 since the electromagnetic showering directly responds to the ionization of the argon. The local cluster weighting (LCW) is applied if the signals are from the hadronic showering. Second, the reconstruction of clusters may not contain whole energy of particles creating a single shower. The out-of-cluster correction is taken into account that the signals is not in the neighborhood cells, and the shared signals are from other clusters. Third, the dead material correction is to compensate for the energy deposits in the dead material in front of calorimeters or in the calorimeters.

- **Small-R jets**

The topo-clusters with the EM scale correction are further reclustered to the R = 0.4 jets by the anti-k_t algorithm. The jet p_{T} is required to be larger than 20 GeV and in the range of $|\eta| < 2.8$. The jet needs to be associated with the hard-scattering vertex. The JETVERTEXTAGGER (JVT) algorithm [81] is used to veto jets from pile-up vertices. The multivariate discriminant of the associated tracks with $|\eta| < 2.5$ is used in the JVT. The JVT requirements are applied for the jets with $p_{\mathrm{T}} < 120$ GeV due to the low rate of pile-up jets with $p_{\mathrm{T}} > 120$ GeV. The efficiency with JVT > 0.59 ($|\eta| < 2.4$) and JVT > 0.11 ($2.4 < |\eta| < 2.5$) is 89 (95) % at 20 (60) GeV.

The jets can be originated from in non-collision background or the noise in the cells of the calorimeters [82], which are called fake jets. The relations between energy depositing in the calorimeters and the energy from the tracks and the quality of cell signals, for example, the pulse shape in comparison with the reference, in the calorimeters are used as the discriminant for the signal jets and the fake jets. The jets which do not pass the criteria are tagged as bad jets.

- **Large-R jets**

The topo-clusters with LCW scale correction are further reclustered to reconstruct jets with radius R = 1.0 by the anti-k_t algorithm. The jets are called large-R jets. The clusters inside a large-R jet, which are called "constitutes", are reclustered to R = 0.2 "subjets" by using k_t algorithm. The grooming technique called "trimming" [83] is applied to the large-R jets to reduce the effect of the pileup and soft radiations. If an R = 0.2 subjet inside a large-R jet has p_{T} smaller than 5% of large-R jet p_{T}, the subjet is removed from the jet. The large-R jets are required in the range of $|\eta| < 2.0$.

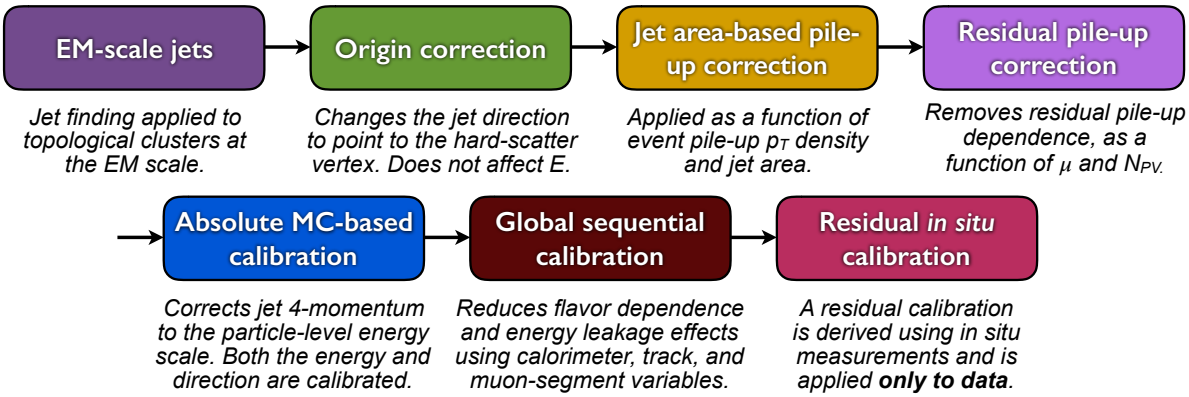

Figure 26: Full calibration stages for the jet energy scale in the small-R jets [84].

- **Jet energy calibration**

Figure 26 summarizes all the stages in the small-R jet calibration. The reconstructed small-R jets need to be calibrated for energy based on truth information and the location of hard-scattering vertex, which is often shifted from the center of the detector. The jet axis is also corrected with respect to the hard-scattering vertex.

The pile-up correction is one of the most important corrections in the jet calibration. The MC samples are used for the pile-up estimation. The pile-up contribution of jet p_{T} is derived by using the jet area estimated from the ghost-association [85] and multiplying the jet area by the p_{T} density of pile-up. There is still a residual pile-up contribution after the aforementioned correction is performed. The residual pile-up is corrected as a function of the number of primary vertices and $\langle\mu\rangle$.

Next, jets need to be calibrated to the energy in the truth particle level (truth particles which contribute energy deposits in the detector). The reconstructed jets are compared to truth jets for the estimation of p_{T} response. The truth jets are defined with the stable truth particles with $c\tau > 10$ mm. The muons and neutrinos are not included in the truth jets. The p_{T} response is derived as a function of η since the transition of detector structure causes biases on the jet reconstruction.

The global sequential calibration (GSC) further includes the information of muon spectrometers and associated tracks to improve the jet energy resolution.

Finally, the p_{T} correction derived with data events (in-situ calibration) is also needed as the detector description used in the MC is not perfect. The four methods [84, 86] are used to calibrate the jet p_{T}. The Z/γ+jet in low p_{T} range and multijet balance in high p_{T} range are used for the jet in the central region. The p_{T} of a recoiled jet is corrected by the well-calibrated physical objects. For the η-calibration, the well-calibrated jet in the central region is used to calibrate the jets in higher η region. The relative small-R jet responses for the in-situ calibration are shown in Figure 27.

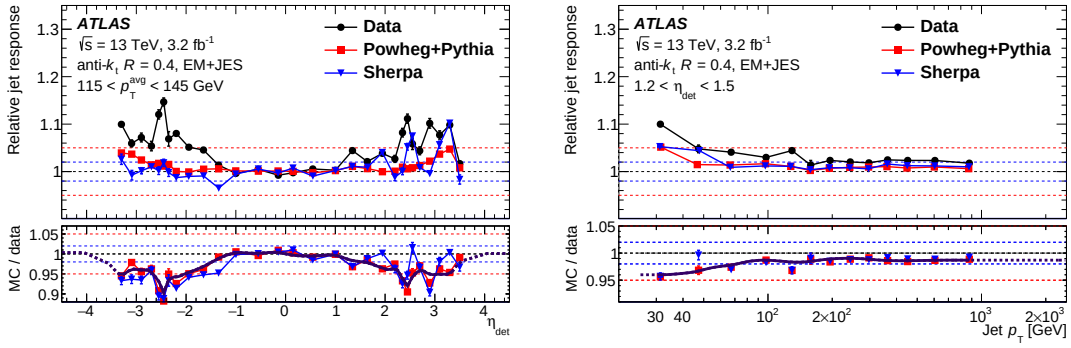

(a) (b)

Figure 27: Relative jet response of small-R jets as a function of (a) η in 115 GeV $< p_{\mathrm{T}}^{avg} <$ 145 GeV and (b) p_{T} in $1.2 < \eta_{det} < 1.5$ [84]. $p_{\mathrm{T}}^{\mathrm{avg}}$ is the average p_{T} between a reference jet and a probed jet in the η-calibration. The lower panel shows the ratios for the in-situ calibration smoothed by using the sliding Gaussian kernel.

For the large-R jets, the pile-up correction and GSC are not applied, but the MC-based and in-situ calibrations are applied. The methods of the in-situ calibration are similar to the calibration for the small-R jets. The relative large-R jet responses for the in-situ calibration are shown in Figure 28.

- **Large-R jet mass** (m^{comb})

For a jet including the decay products of a massive particle, the decay products may spread in a comparable scale of the granularity of the calorimeter cells. Combined mass (m^{comb}) benefits from the measurement of energy in the calorimeter and the finer angular resolution of tracking. The m^{comb} is the combination of the calo mass (m^{calo}) and track-assisted mass (m^{TA}) and defined as:

$$m^{comb} = \frac{\sigma_{calo}^{-2}}{\sigma_{calo}^{-2} + \sigma_{TA}^{-2}} m^{calo} + \frac{\sigma_{TA}^{-2}}{\sigma_{calo}^{-2} + \sigma_{TA}^{-2}} m^{TA}. \tag{23}$$

The calo mass is defined with the energy and momentum of the clusters as:

$$m^{calo} = \sqrt{(\sum_{i \in \text{jet}} E_i)^2 - (\sum_{i \in \text{jet}} \overrightarrow{p_i})^2}. \tag{24}$$

The track-assisted mass is defined with the ratio of the calo p_{T} and track p_{T} times track mass (m^{track}) as:

$$m^{TA} = \frac{p_{\mathrm{T}}^{calo}}{p_{\mathrm{T}}^{track}} m^{track}, \tag{25}$$

where p_{T}^{calo} is the transverse momentum of the large-R jet, and m^{track} and p_{T}^{track} are the invariant mass and the transverse momentum from four-vector sum of all associated tracks in a jet. Both m^{calo} and m^{TA} are calibrated with truth jet mass after the jet

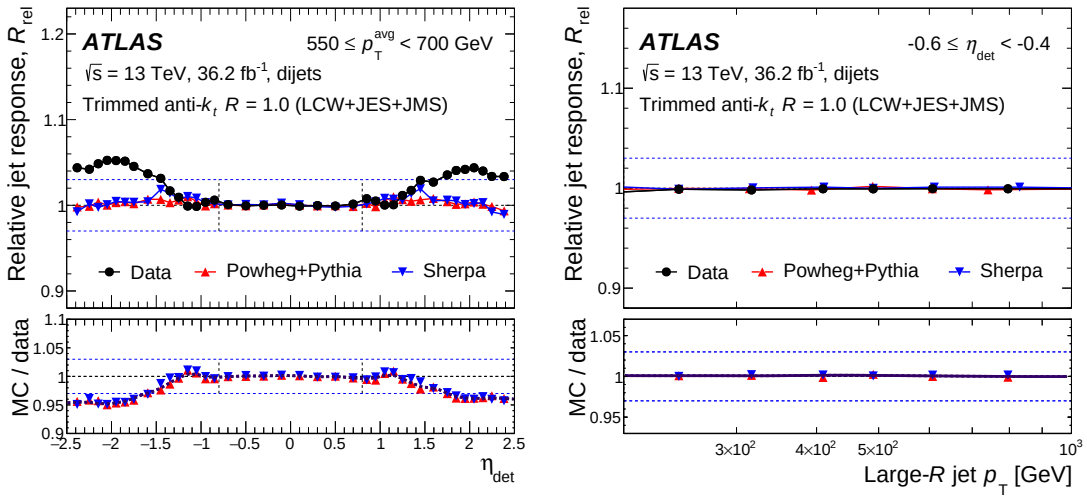

(a) (b)

Figure 28: Relative jet response of large-R jets as a function of (a) η in 550 GeV $\leq p_{\mathrm{T}}^{avg} <$ 700 GeV and (b) p_{T} in -0.6 $\leq \eta_{det} <$ -0.4 [86]. $p_{\mathrm{T}}^{\mathrm{avg}}$ is the average p_{T} between a reference jet and a probed jet in the η-calibration. The lower panel shows the ratios for the in-situ calibration smoothed by using the sliding Gaussian kernel.

energy scale is applied. The σ_{calo} and σ_{TA} are the resolutions of the m^{calo} and m^{TA} obtained from the correction of jet mass between the truth jets and reconstructed jets.

4.2.6 VR Track jets

Variable Radius (VR) track jets are used only in the calibration of top taggers. VR track jets are reconstructed from the tracks identified in the inner detector by the anti-k_t algorithm. The track candidates must pass minimum criteria but with no requirements on the transverse impact parameter. The VR track jets are also required to be originated from the hard-scattering vertex by using $|\Delta z_0 \sin\theta| < 3$ mm. The radius of the VR track jets depends on the jet p_{T} [87]:

$$R \to R_{eff}(p_{\mathrm{T}}) = max\left\{R_{min}, min\left[\frac{\rho}{p_{\mathrm{T}}}, R_{max}\right]\right\}, \tag{26}$$

where the parameter ρ is used to optimize the performance and set to 30 GeV. R_{min} and R_{max} are the range for the variation of the radius and set to 0.2 and 0.4, respectively. The VR track jets are required to satisfy $p_{\mathrm{T}} > 5$ GeV and $|\eta| < 2.5$.

4.2.7 Flavor tagging

The b-tagging is applied to small-R jets and VR track jets. The b-tagging algorithm is performed in two levels [88] with the properties of the tracks.

At the first level, three types of low-level algorithms are performed. Tracks matching with a small-R jet by requiring a ΔR as a function of the jet p_{T} (0.45 for p_{T} = 20 GeV and 0.26 for jet p_{T} = 150 GeV) or tracks in the VR track jets are used in all algorithms. IP2D and IP3D algorithms are based on the impact parameters. The IP2D uses the signed significance of the transverse impact parameter of the tracks to construct the likelihood functions. The IP3D uses both the signed significance of the transverse and longitudinal impact parameters. The likelihood ratios of b-jet to light jet or c-jet are built for the discriminant. The secondary vertex tagging algorithm (SV1) [89] uses each pair of tracks to reconstruct the vertex by the χ^2 method. The likelihood ratio between b-jet and other jets is also used in this algorithm. Finally, the topological multi-vertex algorithms, JetFitter [90], uses tracks to reconstruct the secondary vertices, which provides the topological variables to construct the likelihood functions for the b-tagging.

At the second level, a high-level MV2 algorithm which is a Boosted Decision Tree (BDT) algorithm is used with the output of three low-level algorithms. The weight of the BDT output is the final discriminant, as shown in Figure 29. The cut on the output weights is optimized for different cut-based working points of the efficiencies. Alternative DL1 algorithm based on a deep feed-forward neural network (NN) is also used for the second level. The working points of DL1 b-tagging are also optimized based on the weight of the output.

The b-tagged small-R jets with MV2 selections in the stop analysis are required to be in the range of $|\eta| < 2.5$ and $p_{\mathrm{T}} > 20$ GeV. A 77% efficiency of the selections derived from the b-jets from $\mathrm{t} \to Wb$ are used in the search for the stop. The background rejections derived from the inversion of the efficiencies are 110 for light jets and 5 for charm jets. The b-tagged VR track jets with a 77% efficiency of DL1 selections are used in the calibration of top taggers. The scale factors from the efficiency calibration are derived from the $\mathrm{t\bar{t}}$ MC events.

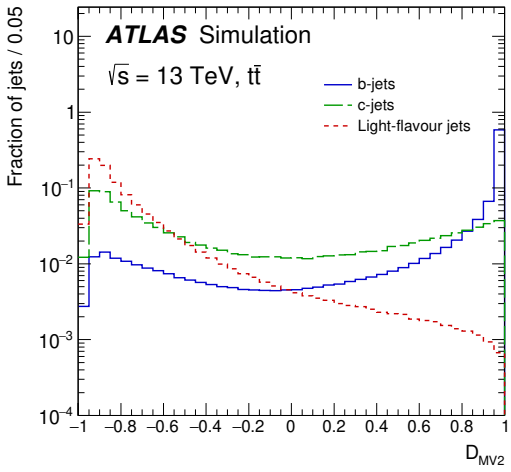

Figure 29: Distribution of the output of the MV2 algorithm for the small-R jets from b-jets, c-jets and light jets in the $t\bar{t}$ simulated events.

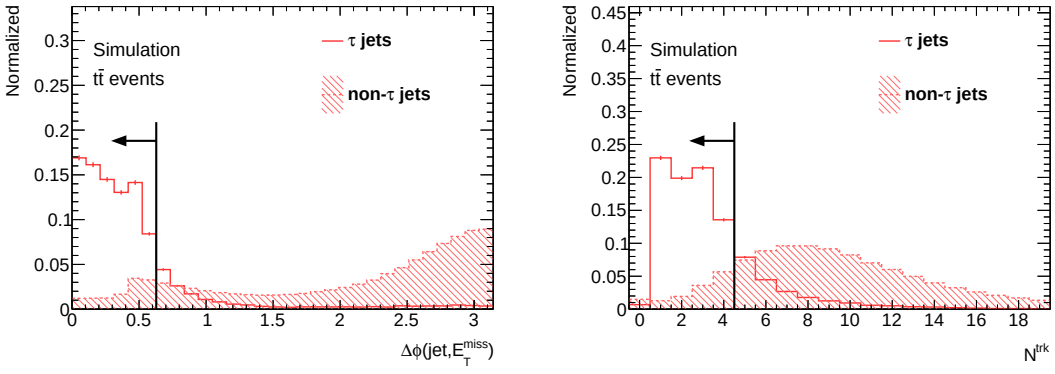

(a) (b)

Figure 30: Distributions of (a) $\Delta\phi(E_{\mathrm{T}}^{\mathrm{miss}},\mathrm{jet})$ and (b) the number of tracks N^{trk} for the τ jets and non-τ jets in the particle level in the $t\bar{t}$ events selected by using the preselections in Table 10. The black arrows show the cut values for the hadronic tau candidates.

4.2.8 Hadronic tau

Hadronic taus are also considered in the search for the stop since they can be reconstructed as jets. The hadronic tau candidates are selected from the small-R jets with no b-tagging in the range of $|\eta| < 2.5$ and associated with four tacks or fewer. The candidates also need to satisfy $\Delta\phi(E_{\mathrm{T}}^{\mathrm{miss}},\mathrm{jet}) < \pi/5$ for the events with $W \to \tau\nu$. Figure 30 shows the distributions of the $\Delta\phi(E_{\mathrm{T}}^{\mathrm{miss}},\mathrm{jet})$ and the number of tracks for the τ jets and non-τ jets with cut values for the identification of hadronic tau candidates.

4.2.9 Overlap removal

Muons, electrons, and jets are independently reconstructed. This can cause that the same low-level reconstructed objects may be identified as the different physical objects. To prevent the possible overlapping physical objects, the procedures of overlap removal are applied in order after each kind of objects is defined. The ΔR between objects are used as the metric. The b-tagging working point in the overlap removal is 85% to remove the electrons more aggressively. The hadronic taus and large-R jets, which are considered in the optimization of signal regions are not used in the overlap removal.

- **Electron-jet**

The energy of electrons depositing in the calorimeters may also be reconstructed as a jet. If a non-b-tagged jet matches with an electron within $\Delta R < 0.2$, the jet is removed. To preserve the semi-leptonic b-jets which may also produce the electrons, if an electron matches with a b-tagged jet within $\Delta R < 0.04 + 10\,\text{GeV}/p_{\text{T}}^{\text{electron}}$ or $\Delta R < 0.4$, the electron is removed.

- **Muon-jet**

The $\pi^{\pm}$ and $K^{\pm}$ in the hadronic showering may produce the muons in-flight, which is identified as a muon in the reconstruction stage. Also, as above, in the electron-jet, a b-jet may also produce a muon. A muon with very high energy may produce the electromagnetic showering in the calorimeters and is misidentified as a jet. To remove the overlapping, if a non-b-tagged jet with the number of tracks smaller than three matches with a muon within $\Delta R < 0.2$, the jet is removed. If a b-jet matches with a muon within $\Delta R < 0.04 + 10\,\text{GeV}/p_{\text{T}}^{\text{muon}}$ or $\Delta R < 0.4$, the muon is removed.

4.2.10 $E_{\text{T}}^{\text{miss}}$ and object-based $E_{\text{T}}^{\text{miss}}$ significance

The imbalance of the vector sum of the transverse energy of objects is defined as the missing transverse energy ($E_{\text{T}}^{\text{miss}}$) [91]. The $E_{\text{T}}^{\text{miss}}$ in the direction along x-axis and y-axis is defined as:

$$E_{x(y)}^{miss} = -(E_{x(y)}^{\mu} + E_{x(y)}^{e} + E_{x(y)}^{jet} + E_{x(y)}^{soft,TST}), \tag{27}$$

A photon is not reconstructed as a photon object but treated as a jet in the calculation. The well-reconstructed objects like electrons, muons, and jets are considered as the hard terms. The hard terms also need to pass the overlap removal. The tracks or the energy deposits in the calorimeters which do not match the hard terms are included in the soft term called Track-based soft term (TST). TST can remove the out-of-time pile-up in the calorimeters, but the neutral particles are not included in the soft term.

Since the large $E_{\mathrm{T}}^{\mathrm{miss}}$ significance[2] cannot be explained by the momentum resolution of hard terms which produce the imbalance of the transverse momentum and such large $E_{\mathrm{T}}^{\mathrm{miss}}$ significance can be produced by invisible particles in the detector, object-based $E_{\mathrm{T}}^{\mathrm{miss}}$ significance [92] is introduced. This variable is based on the likelihood ratio of the probability of non-zero true $E_{\mathrm{T}}^{\mathrm{miss}}$ to the probability of zero true $E_{\mathrm{T}}^{\mathrm{miss}}$. The significance can be written as:

$$S = \sqrt{\frac{|E_{\mathrm{T}}^{\mathrm{miss}}|^2}{\sigma_L^2(1-\rho_{LT}^2)}}\,, \tag{28}$$

with the relatively total longitudinal resolution (σ_L) and the correlation factor between total longitudinal and transverse relative resolution (ρ_{LT}^2) of all the objects.

[2] $E_{\mathrm{T}}^{\mathrm{miss}}$ significance is defined as $E_{\mathrm{T}}^{\mathrm{miss}}/\sqrt{\sigma_{E_{\mathrm{T}}^{\mathrm{miss}}}}$.

5 DNN top taggers and their calibration

The reconstruction of boosted objects becomes more important as the mass of interest of the stop search goes higher. In the final state of the production of a top and a neutralino from the stop with no lepton, it is possible to fully reconstruct top quark decay products into a large-R jet. A multivariate Deep neural network (DNN) algorithm is used to identify boosted objects reconstructed by using large-R jets. This is called a DNN top tagger.

The top taggers are trained with the Monte Carlo simulation samples. The truth information of the large-R jets needs to be defined for both signal jets which are from top decay and background jets which are quark or gluon-initiated jets (q/g jets) to develop top taggers. Large-R jet labeling is introduced in Section 5.1. Variables used in the development as the inputs of the taggers to distinguish signal jets from background jets are explained in Section 5.2. A network model of DNN is described in Section 5.3. The performance of top taggers is calibrated with signal jets and background jets in data. The results of the scale factors are shown in Section 5.4.

5.1 Large-R jet labeling

The size of the spread of the decay products (ΔR) follows the relation of p_{T} and mass of the parent particle:

$$\Delta R \approx \frac{2m}{p_{\mathrm{T}}}. \tag{29}$$

When the mass is fixed, the ΔR becomes smaller as the p_{T} goes higher. Figure 31 shows the study on the containment of a top decay at the truth level. When the top p_{T} is higher than 500 GeV, the large-R jet containing all the decay products dominates. In the p_{T} range of 200 GeV $< p_{\mathrm{T}} <$ 500 GeV, the qb and qq are the dominant components. Below 200 GeV, the single b or single q becomes dominating. To define a top in the jet at reconstruction level, the following criteria are required. First, the R = 1 truth jet and large-R jet need to pass a criterion of $\Delta R(J_{reco}, J_{truth}) <$ 0.75. Second, a top needs to pass the criterion of $\Delta R(top, J_{truth}) < 0.75$ [94]. Then, a jet satisfies these criteria is labeled as "inclusive top." A jet labeled as "contained top" needs to pass, in addition to those, the selection of the truth jet mass larger than 140 GeV and one b-hadron in the jet with the ghost-association [85]. These criteria

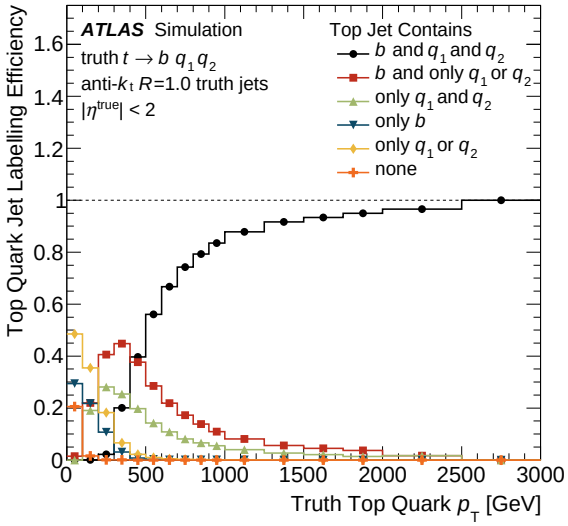

Figure 31: Ratio of the containment of top quark decay products in a matched anti-k_t R = 1.0 truth jet with respect to the top p_{T} [93].

are generator-independent[3] and can be applied to the samples generated from the different generators.

5.2 Variables

The topology of topo-clusters inside a large-R jet is called "substructure". The jet substructure efficiently distinguish signal jets from the background jets since the top decay produces separated constituents, corresponding to $t \to bqq'$, while a quark or a gluon produces a single dense constituent surrounded by the soft radiation in a jet. Many studies show how to use the variable to describe the substructure. There are 13 jet substructure variables used as the inputs of the DNN algorithm. Table 6 summaries all the variables.

Except for p_{T} and combined mass m^{comb}, other 11 variables are explained as follows:

(i) N-subjettiness and its ratio

The N-subjettiness is defined as a function of the sum over p_{T} of all the constituents multiplied by ΔR between constituents and the closest subjet among the

[3] SHERPA does not contain the truth information of W bosons in truth level. It is not possible to label a large-R jet based on the truth level partons. The ghost-associated b-hadron can be applicable for all the MC samples.

Table 6: Summary of the variables used as the input of the DNN algorithm. β angular exponent is set to 1.

Observables	variables	Reference
Jet kinematics	p_{T}, $\mathrm{m}^{\mathrm{comb}}$	[95]
N-subjettiness and its ratio	τ_1, τ_2, τ_3, τ_{21}, τ_{32}	[96, 97]
Energy correlation ratios	e_3, C_2, D_2	[98, 99, 100]
Splitting scales	$\sqrt{d_{12}}$, $\sqrt{d_{23}}$	[101, 102]
W reconstruction	Q_w	[103]

leading N subjets (defined in Chapter 4.2.5):

$$\tau_N^\beta = \sum_i p_{\mathrm{T}i} min\{\Delta R_{1,i}^\beta, \Delta R_{2,i}^\beta, \cdots, \Delta R_{N,i}^\beta\}, \tag{30}$$

where β is the angular weighting exponent analogous to the parameter in angularities [104]. β = 1 is found to contribute to the identification of the boosted objects [97]. The jets with $\tau_N \approx 0$ are considered as jets with N (or fewer) subjets since all the constituents are aligned with one of the leading N subjets. On the other hand, the jets with large τ_N represent at least N+1 subjets in the jets since some constituents distribute away from the selected subjets. Figure 32 shows all the N-subjetttness variables used as inputs. q/g jets from multijet events distribute in low τ_2 and τ_3 but high τ_1. Top jets have high τ_1 and τ_2 but low τ_3. Therefore, the τ_2 shows good discrimination between top jets and q/g jets.

The N-subjettiness ratios are defined as:

$$\tau_{21} = \frac{\tau_2}{\tau_1}, \qquad \tau_{32} = \frac{\tau_3}{\tau_2}, \tag{31}$$

which further enhance the discrimination.

(ii) Energy correlation function ratios

An energy correlation function (ECF) is a function of p_{T} of the subjet and ΔR between subjets within leading N subjets:

$$e_2^\beta = \sum_{1 \le i < j \le N} z_i z_j \Delta R_{ij}^\beta \tag{32}$$

and

$$e_3^\beta = \sum_{1 \le i < j < k \le N} z_i z_j z_k \Delta R_{ij}^\beta \Delta R_{jk}^\beta \Delta R_{ik}^\beta \tag{33}$$

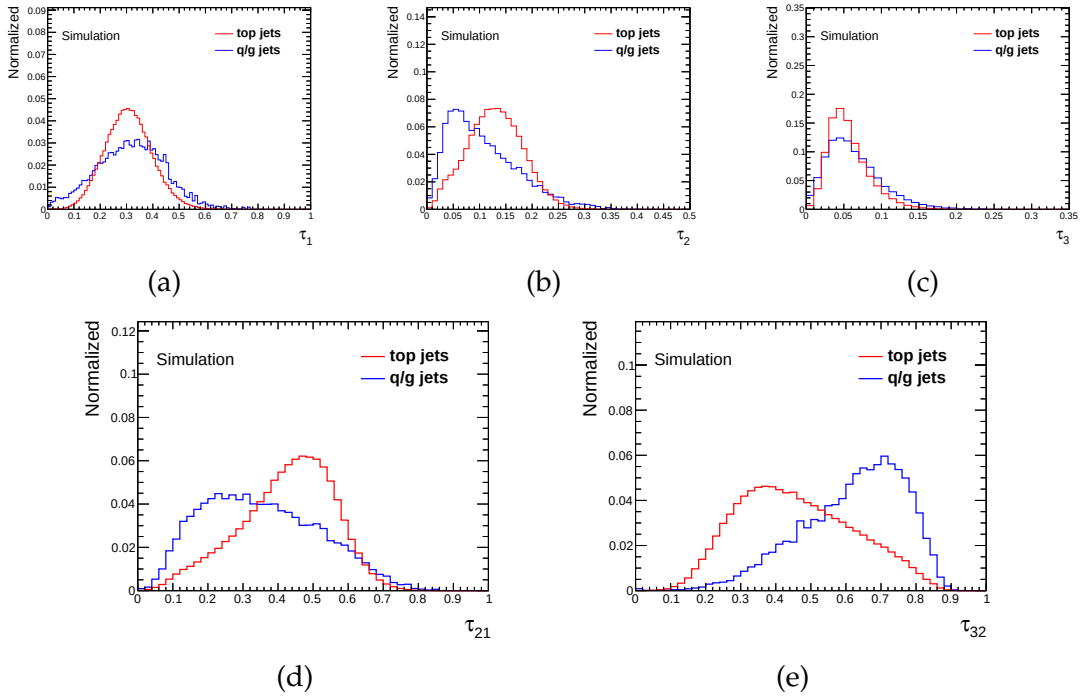

Figure 32: Comparison of shapes of (a) τ_1, (b) τ_2, (c) τ_3, (d) τ_{21}, and (e) τ_{32} in large-R jets with simulated $t\bar{t}$ samples (red) and multijet samples (blue). The contained top definition is used for the identification of top jets. Angular weighting exponent, β, is set to 1. The truth jet mass is required within 140 GeV $<$ mass $<$ 200GeV.

with

$$z_i = \frac{p_{\mathrm{T,i}}}{\sum_{j \in N} p_{\mathrm{T,j}}}, \tag{34}$$

where β is the angular exponent. The C_2 and D_2 is defined as:

$$C_2^{\beta} = \frac{e_3^{\beta}}{(e_2^{\beta})^2}, \quad D_2^{\beta} = \frac{e_3^{\beta}}{(e_2^{\beta})^3}. \tag{35}$$

The energy correlations are similar to the N-subjettiness. As a result, the energy correlations like e_{n+1} are close to zero in the jets with n subjets, which is also the case in the N-subjettiness. Those variables show good separations of jets from QCD and Z bosons [105]. This is also the case in top quarks, as shown in Figure 33 (a) (b) (c).

(iii) k_t Splitting Scales

The splitting scales ($\sqrt{d_{ij}}$) are used in the k_t jet algorithm. It is defined as:

$$\sqrt{d_{ij}} = \sqrt{min(p_{\mathrm{T},i}^2, p_{\mathrm{T},j}^2)\frac{R_{ij}^2}{R^2}}, \tag{36}$$

with the reclustered jet radius R (R = 0.2 inside large-R jets) and $p_{\mathrm{T},i}$ of subjets.

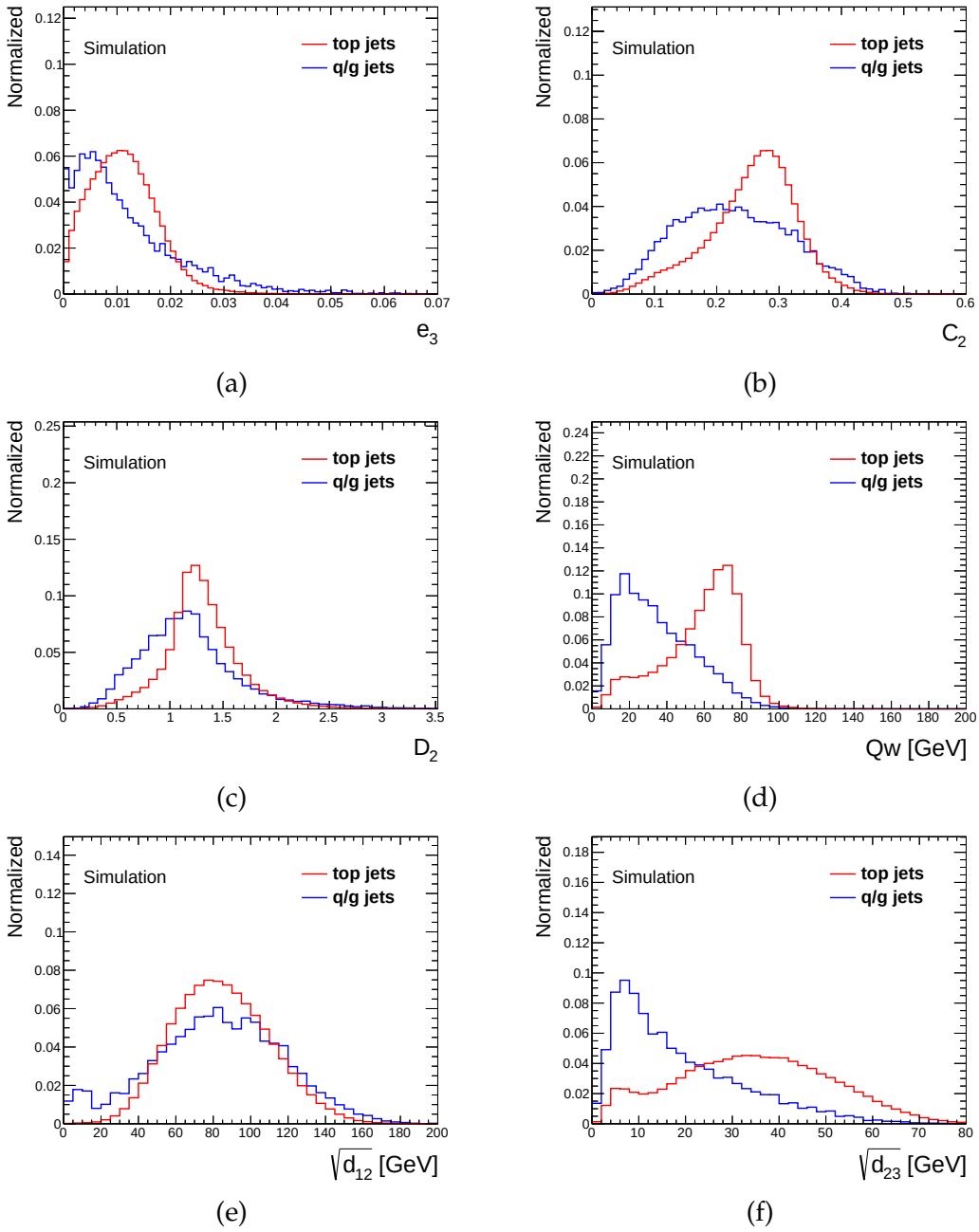

Figure 33: Comparison of shapes of (a) e_3, (b) C_2, (c) D_2, (d) Q_w, (e) $\sqrt{d_{12}}$, and (f) $\sqrt{d_{12}}$ in large-R jets with simulated $t\bar{t}$ samples (red) and multijet samples (blue). The contained top definition is used for the identification of top jets. Angular weighting exponent, β, is set to 1. The truth jet mass is required within 140 GeV $<$ mass $<$ 200GeV.

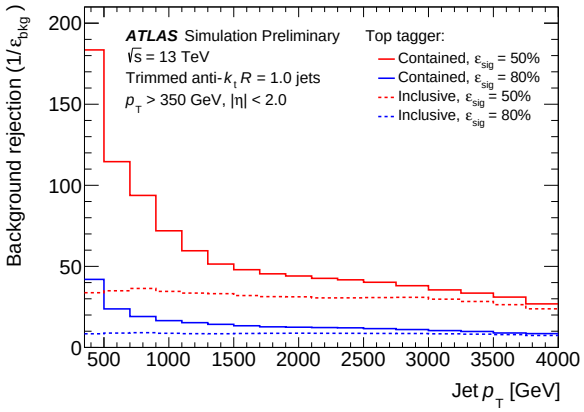

Figure 34: Background rejections as a function of jet p_{T} for the contained and inclusive top taggers with both 50% and 80% efficiencies in multijet events [109]. Rejection is defined as the inversion of tagging efficiencies on background jets.

Figures 33 (e) and 33 (f) show the distributions of top and multijet samples. More discrimination power is observed in splitting scales between subleading and third jets.

(iv) W reconstruction

The subjets reconstructed by using the k_t jet algorithm are paired to reconstruct the invariant mass of two subjets. The minimum mass is defined as the Q_w. The peak around W mass is observed in top jets, as shown in Figure 33 (d).

5.3 Network model of the taggers

The deep neural network is a fully-connected feedforward neural network trained in the Keras framework [106] with the Theano backend [107] and Adam optimizer [108]. The detail of the DNN algorithm is described in Table 7. The jets passing $m^{comb} > 40$ GeV and $N^{const} \geq 3$ are used in the training. The input of jet truth p_{T} is ranged from 200 GeV to 4 TeV. The truth p_{T} is reweighted into a flat distribution to remove the bias of kinematics between the signal and background samples. The efficiency of the taggers is determined by the cut value of the DNN output as a function of p_{T}. The taggers with 80% and 50% efficiencies of top-tagging in both definitions of the contained top and inclusive top are developed in the ATLAS. Figure 34 shows the background rejections of four taggers in multijet events.

Table 7: Parameters and architecture used in the training of the top taggers [93].

	DNN top taggers
Software	Keras 1.0.8 [106] with Theano backend [107], lwtnn 2.0 [110]
Layer type	Dense
Number of hidden layers	5
Architecture	18, 16, 14, 10, 5
Activation function	Rectified linear unit (ReLU)
Optimizer	Adam [108]
Learning	0.00005
L1 regulariser	0.001
NN weight initialization	Glorot uniform
Batch size	200
Batch normalization	✓
Number of epochs	100 with early stopping

5.4 Calibration of the taggers

The top-tagging algorithm is trained using MC simulation, but it is calibrated using data and MC to evaluate the deviation of efficiencies between the data and MC. The scale factors of signal and background for the individual tagger are introduced for quantifying the deviations. The signal scale factors are derived in the events with the high purity of the semi-leptonic $t\bar{t}$ events. The background scale factors are derived in two different event selections. A set of selections that enhances γ+jet fraction is used for the low jet p_{T} region. The selections to enhance the multijet fraction is used for the high jet p_{T} region. Baseline large-R jets used in the calibration are required to satisfy $p_{\mathrm{T}} > 200$ GeV, $|\eta| < 2.0$, and $m^{comb} > 40$ GeV.

5.4.1 Region definitions

The selections for semi-leptonic $t\bar{t}$ events are defined in Table 8. Only events containing exactly one muon and at least one large-R jet are used. A small-R jet is required to be close to the muon for the b-jet from leptonic decay of the top quark. A b-tagged VR track jet is also required to be in the leading large-R jet for the rejection of the jets from W bosons. The requirement of $E_{\mathrm{T}}^{\mathrm{miss}}$ is to select events with neutrinos. For the events with low $E_{\mathrm{T}}^{\mathrm{miss}}$, the selection on the transverse mass of the muon and $E_{\mathrm{T}}^{\mathrm{miss}}$ can reduce the events with the significant mismeasurements of jet energies. The data/MC distributions of important variables are shown in Figure 35. This method covers the p_{T} range from 350 GeV to 1000 GeV. The scale factors and uncertainties are extrapolated from the last bin for the jet with 1000 GeV $< p_{\mathrm{T}} <$ 3000 GeV due to low

Table 8: Selections for the $t\bar{t}$ events with one muon.

Variables	
Trigger	single muon trigger
N^{muon} ($p_{\text{T}} > 30$ GeV)	1
N^{electron} ($p_{\text{T}} > 25$ GeV)	0
$E_{\text{T}}^{\text{miss}}$	>20 GeV
$E_{\text{T}}^{\text{miss}}+m_{\text{T}}^{W}$	> 60 GeV
$N^{\text{small-}R\text{ jet, }p_{\text{T}}>25\text{ GeV, }\Delta R(\text{jet,muon})<1.5}$	≥ 1
$N^{\text{large-}R\text{ jet, }p_{\text{T}}>200\text{ GeV}}$	≥ 1
$N^{b\text{-tagged VR track jet}}$	≥ 1
$\Delta R(\text{leading large-}R\text{ jet, }b\text{-tagged VR jet})$	< 1.0

statistics in high p_{T} range.

To cover the full range of the jet p_{T}, two selections of γ+jet and multijet events are required, as shown in Table 9. A photon in the γ+jet events also needs to satisfy $p_{\text{T}} > 155$ GeV and the loose isolation for the region of high efficiencies in the single photon trigger. At least one large-R jet is required for the jet calibration in the γ+jet events. A leading large-R jet with $p_{\text{T}} > 500$ GeV is required in the multijet events duo to the high efficiencies of the single large-R jet trigger. Additional large-R jets are considered as objects recoiled from the leading large-R jet. Due to the limited statistics of the data events, the scale factors derived from γ+jet samples cover the leading large-R p_{T} range from 350 GeV to 500 GeV, and the multijet region covers the range from 500 GeV to 2500 GeV. Figures 36 and 37 show the data and MC distributions of both regions. The significant deviations of PYTHIA γ+jet samples are due to a bug in the MC production, which results in the overestimation of the modelling uncertainties.

Table 9: Definition of γ+jet region and multijet region.

Variables	γ+jet	multijet
Trigger	single photon	single large-R jet
$N^{\text{large-}R\text{ jet}}$	≥ 1	≥ 2
$N^{\text{large-}R\text{ jet, }p_{\text{T}}>500\text{ GeV}}$	-	≥ 1
$N^{\text{photon, }p_{\text{T}}>155\text{ GeV}}$	≥ 1	-

5.4.2 Scale factors

- **Signal scale factors**

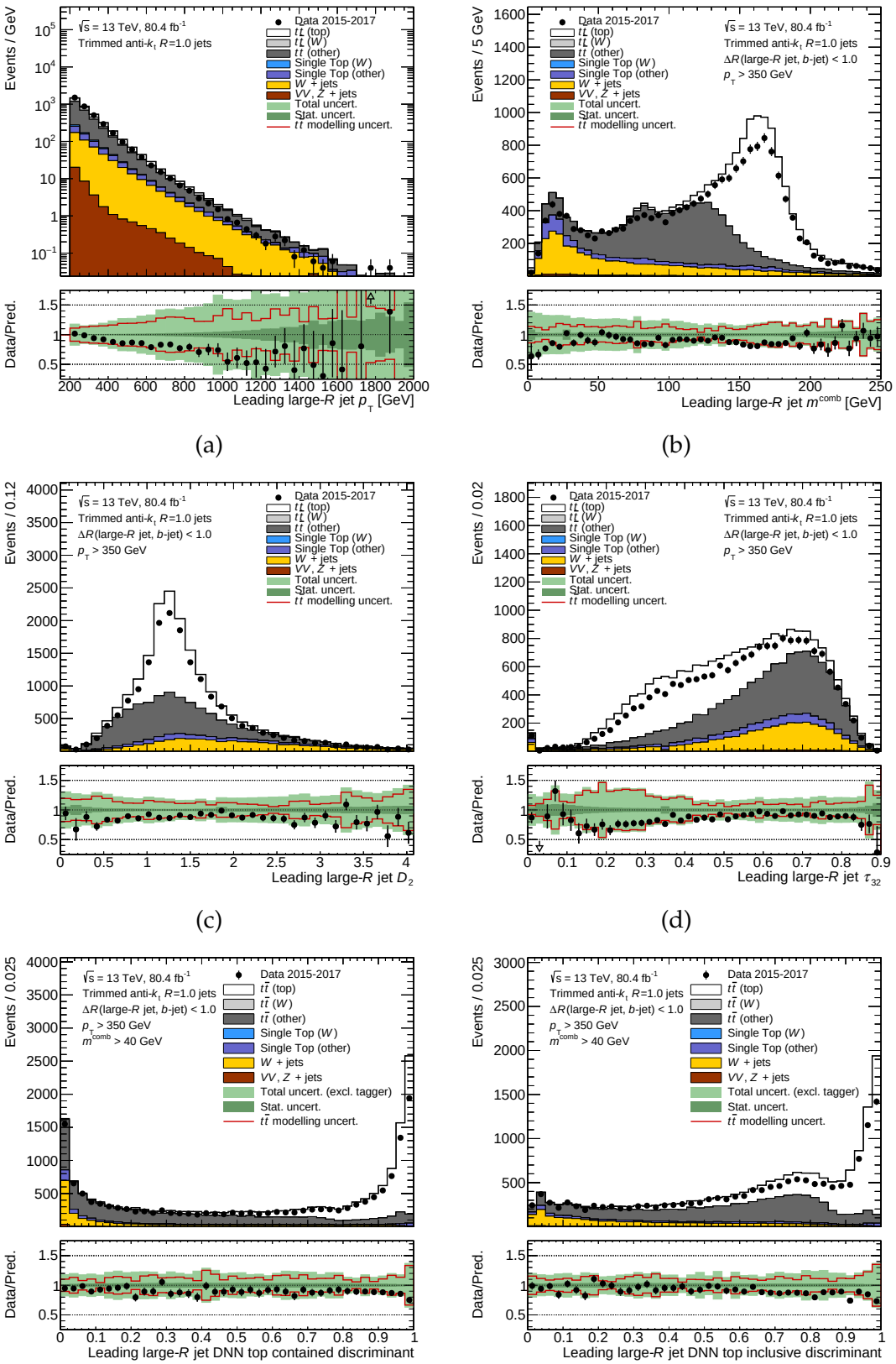

Figure 35: Distributions of leading large-R jet (a) p_T, (b) combine mass, (c) D_2, (d) τ_{32}, (e) DNN discriminant for the 80% contained top tagger, and (f) DNN discriminant for the 80% inclusive top tagger in $t\bar{t}$ event selections for both data and MC predictions.

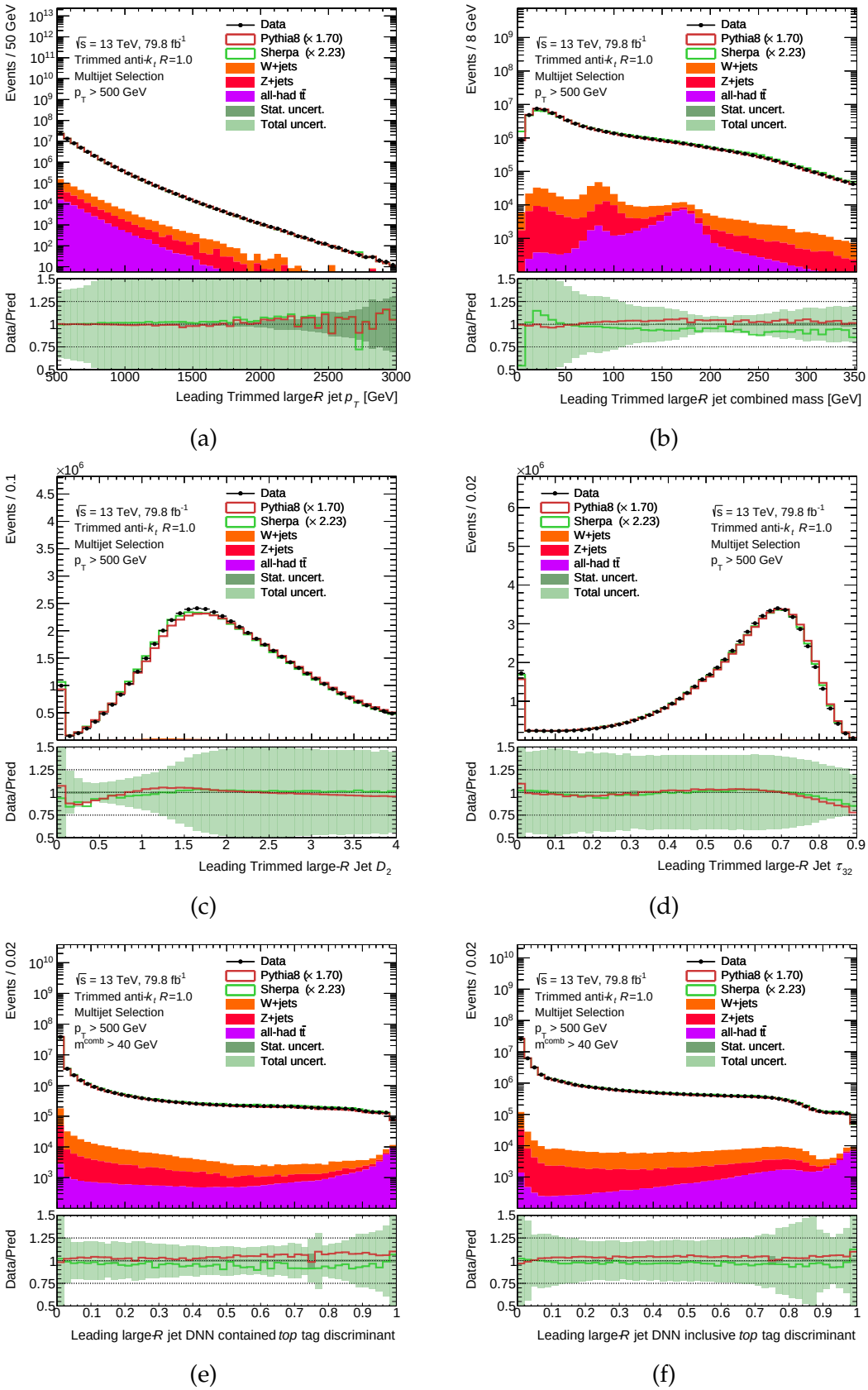

Figure 36: Distributions of (a) p_{T}, (b) mass, (c) D_2, (d) τ_{32}, (e) DNN discriminant for the 80% contained top tagger, and (f) DNN discriminant for the 80% inclusive top tagger of the leading large-R jets in multijet selection for both data and MC predictions. The ratios to the SHERPA and PYTHIA are the scale factor to the yields from $N^{data} - N^{V+jets} - N^{\mathrm{t\bar{t}}}$.

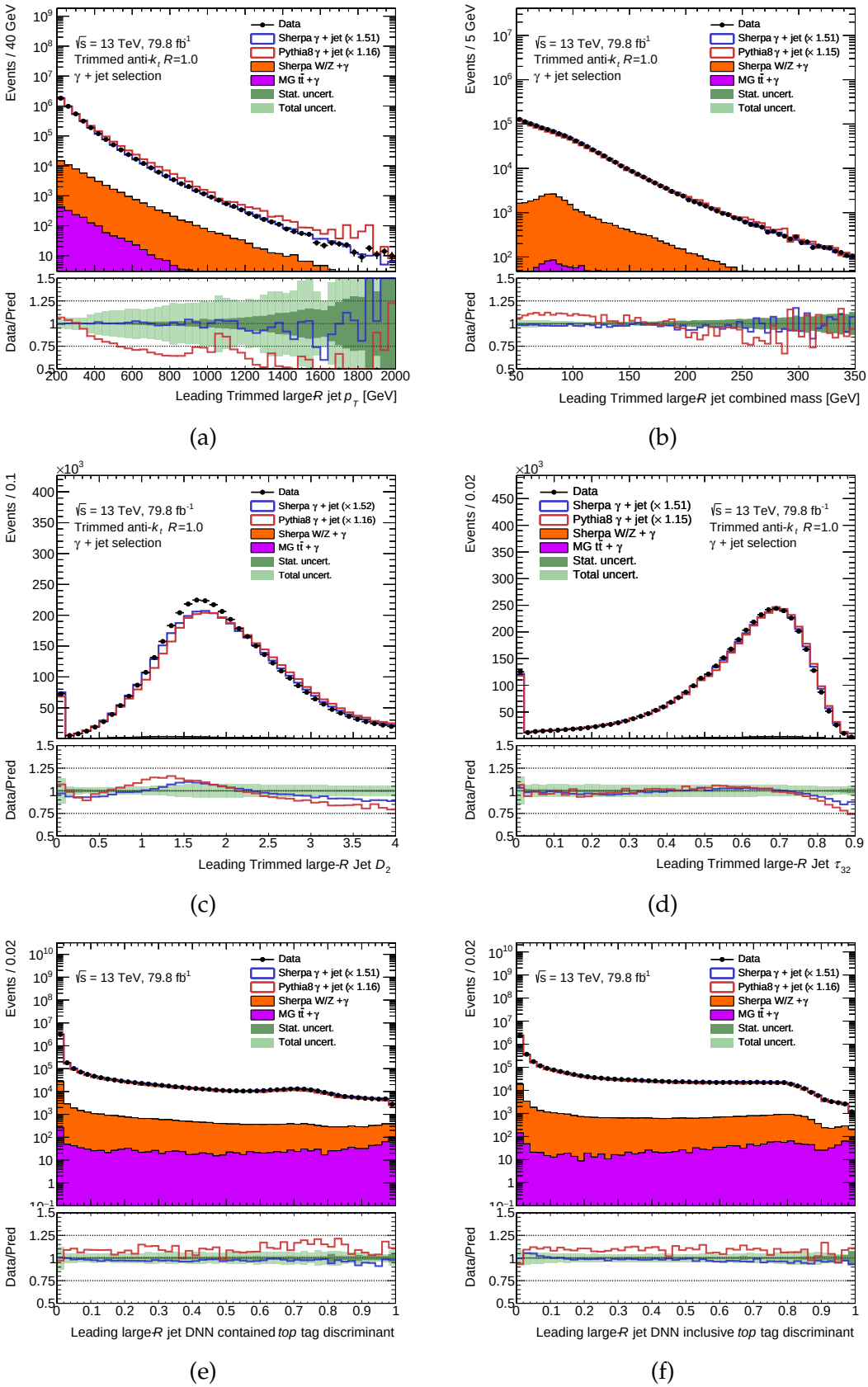

Figure 37: Distributions of (a) p_{T}, (b) mass, (c) D_2 and (d) τ_{32}, (e) DNN discriminant for the 80% contained top tagger, and (f) DNN discriminant for the 80% inclusive top tagger in the γ+jet selections for both data and MC predictions. The ratios next to the SHERPA and PYTHIA are the scale factor to the yields from $N^{data} - N^{V\gamma} - N^{\mathrm{t\bar{t}}\gamma}$.

The signal jets which satisfy truth top labels (either contained tops or inclusive tops) are from not only in $t\bar{t}$ events but also the single top events with a hadronic decay top. The jets with no truth top definitions in $t\bar{t}$ events or single top events are treated as non-$t\bar{t}$ backgrounds. To derive the scale factors, the MC efficiency of $t\bar{t}$ events in the p_{T} bin i is defined as:

$$\epsilon_i^{MC} = \frac{N_{i,signal}^{passed}}{N_{i,signal}^{Total}}. \tag{37}$$

The large-R jets tagged as top candidates are put in a pass category. If they are not tagged, they are put in a fail category. The simultaneous fit between pass and fail categories is performed in each p_{T} bin independently by using the χ^2 method. The data efficiencies are defined as:

$$\epsilon_i^{data} = \frac{N_{i,fitted\ signal}^{passed}}{N_{i,fitted\ signal}^{Total}}, \tag{38}$$

where the number of fitted signal events are used. Hence, the scale factor for the p_{T} bin i is defined as:

$$SF_i = \frac{\epsilon_i^{data}}{\epsilon_i^{MC}}. \tag{39}$$

- **Background scale factors**

The scale factors are derived as a function of p_{T} and $\ln(m^{comb}/p_{\mathrm{T}})$ to reduce the scale factor uncertainties along with the top mass due to the correlation between jet p_{T} and mass. The MC efficiencies in each p_{T}-$\ln(m^{comb}/p_{\mathrm{T}})$ bin are defined as:

$$\epsilon_{MC} = \frac{N_{dijet/\gamma+jet}^{tagged}}{N_{dijet/\gamma+jet}^{total}}. \tag{40}$$

The data efficiencies are derived from the data events subtracted by other minor physics process using MC samples,

$$\epsilon_{data} = \frac{N_{data}^{tagged} - N_{MC,others}^{tagged}}{N_{data}^{total} - N_{MC,others}^{total}}. \tag{41}$$

The scale factor is defined as a ratio of ϵ^{data} to ϵ^{MC}.

5.4.3 Systematic uncertainties on the scale factor estimation

Several theoretical and experimental uncertainties are considered for the uncertainties of scale factors. The theoretical uncertainties include the uncertainties of the prediction estimated by using a few different generators for the physics processes and the varying the scales of parameters. The experimental uncertainties are uncertainties of the detector response dependent on the truth objects. The major sources of the uncertainties are described as follows:

- **Jet energy scale uncertainties for large-R jets**

  The uncertainties on the jet energy scale (JES) from the jet response are needed to be considered. The R_{trk} method [111] is used to derive the large-R jet uncertainties. The double ratio of the response of the jet moment in data and MC prediction is used, and the response is defined as the ratio of the calorimeter to the matched track jet.

- **Background modelling**

  The modelling uncertainties used in multijet and γ+jet events vary the background scale factors. Alternative SHERPA samples for the multijet events and PYTHIA samples for the γ+jet events is used to derive the uncertainties of background modelling that accounts for the effect on the different generators and parton showering.

- **$t\bar{t}$ modelling**

  The uncertainties of hard-scattering, parton showering, and QCD radiation are considered in the $t\bar{t}$ modelling. The alternative samples of POWHEG interfaced to HERWIG 7 are used for the derivation of uncertainties of the parton showering. The samples of aMC@NLO with the same showering configuration as the nominal samples are used to determine the uncertainties of the hard-scattering. The uncertainties of initial/final state radiation are derived by varying the renormalization scale (μ_R) for strong coupling at m_Z, the factorization scale (μ_F) for the parton density function [112], and the parameters for the initial state radiation.

- **Flavor-tagging uncertainties**

  The uncertainties of both theoretical and experimental uncertainties are considered in the calibration of the DL1 b-tagging algorithm. There are nuisance parameters of the uncertainties provided from the calibration with true b-jets, c-jets, and light jets and the extrapolation to high p_{T} for true b-jets and c-jets.

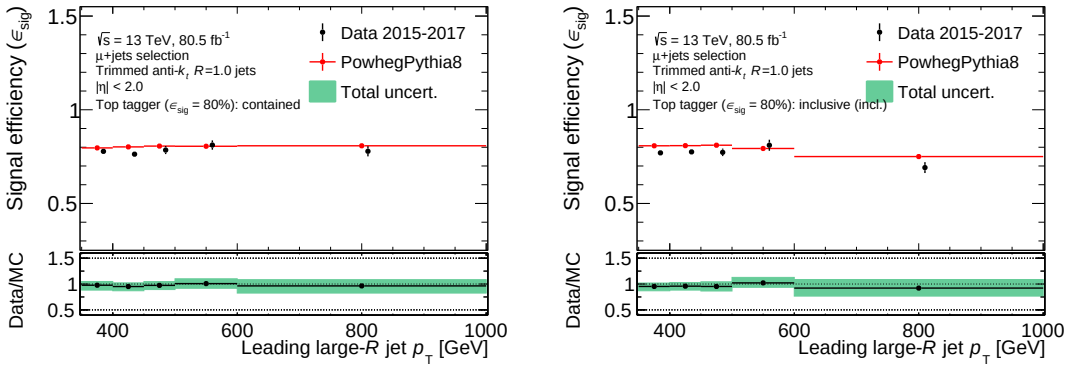

(a) (b)

Figure 38: Signal efficiencies and scale factors (lower panel) of DNN (a) contained top tagger and (b) inclusive top tagger with 80% efficiencies are derived as a function of large-R jet p_{T}. The total uncertainties are evaluated in the quadratic sum.

5.4.4 Results

Figure 38 shows the results of the scale factors of DNN top taggers. JES uncertainties for large-R jets and $t\bar{t}$ modelling uncertainties are the dominated uncertainties of the scale factors. The scale factors are consistent with 1 within total uncertainties which are around 6∼16%. The results show a good modelling of the signal jets in the MC samples.

Figure 39 shows the background scale factors and total JES uncertainties, which are the dominated uncertainties, in the two-dimensional plane. The empty bins are filled by the average of their neighbors. The 2D Gaussian smoothing is applied to the scale factors and the uncertainties to reduce the fluctuation of statistics among bins. The high scale factor uncertainties of $\sim$ 80% in the low $\ln(m^{comb}/p_{\mathrm{T}})$ of Figure 39 (c) and are mainly from the one variation of JES uncertainties, although the variation contributes only $\sim$ 8% shift in the large-R p_{T}. This has been verified by checking the event migration. By shifting in p_{T}, mass or both of p_{T} and mass, it is found that the trained taggers are sensitive to the changing in m^{comb}/p_{T}, which results in propagated uncertainties become very high. For the DNN algorithm with 80% efficiency on tagging contained top, the uncertainties are up to 80% in the low mass region but the less than 20% around the true top mass in the range $p_{\mathrm{T}} < 1$ TeV. The scale factors are around $0.9 \sim 1.1$.

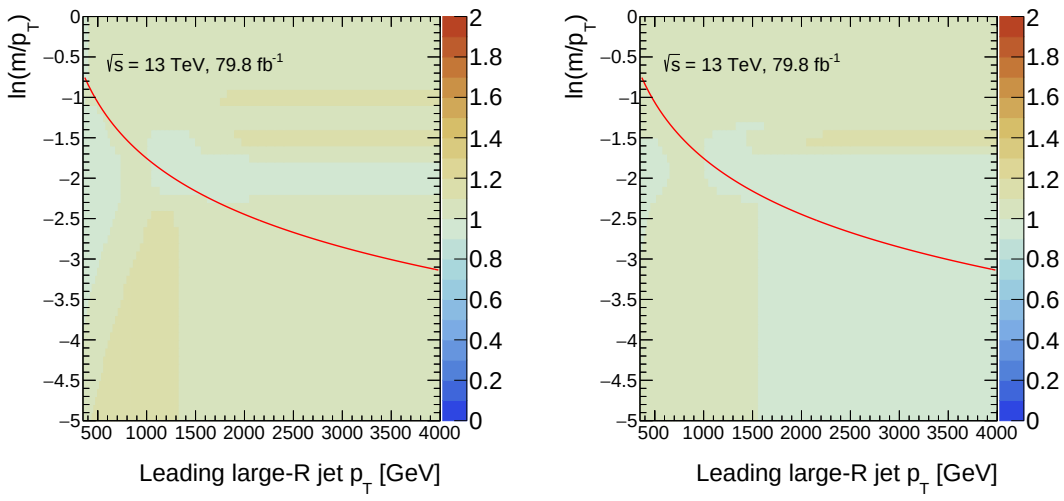

(a)

(b)

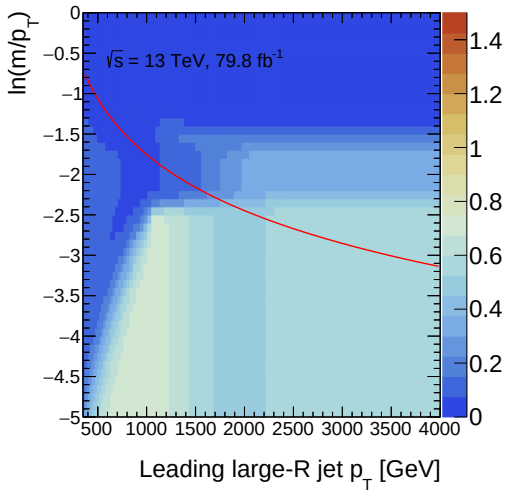

(c)

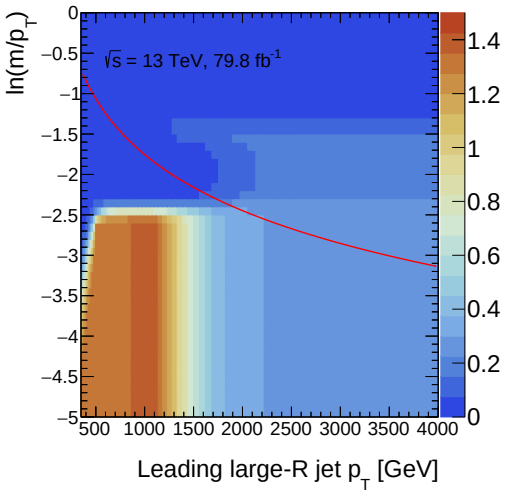

(d)

Figure 39: Background scale factors of (a) contained top tagger and (b) inclusive top tagger with 80% efficiencies and uncertainties of the scale factors propagated from JES uncertainties with (c) contained top tagger, and (d) inclusive top tagger with 80% efficiencies as a function of p_{T} and $\ln(m^{comb}/p_{\mathrm{T}})$. "1" in uncertainty means a 100% uncertainty of a scale factor. The red lines indicate the top mass.

6 Data analysis and results

6.1 Analysis overviews

The events are preliminary selected by using preselections based on the feature of stop signals. After the event selections are applied by using the signal signatures, further selections are considered to enhance the purity of stop signals and increase the search sensitivity. Signal regions (SRs) are defined for the phase space expected to contain more stop signals and less SM backgrounds to maximize the sensitivities of the search for the stop.

The backgrounds in the SRs need to be correctly estimated by introducing the control regions (CRs) for each background process. By selecting a CR dominated by a given background process and contaminated with the negligible signal, we can control the background by comparing with the data sample in the CR. The topology in the CRs is as close as possible to the topology in SRs. We can assume the same behavior between the SRs and the CRs to apply the extrapolation from the CRs to the SRs. The validation regions (VRs) are used to validate the background estimations from CRs. The VRs are defined in the phase space close to the SRs and have relatively low signal contamination. The presence of the signal can be examined by using a simultaneous fit to the SRs and CRs.

The preselections are introduced in Section 6.2. The definitions of SRs are introduced in Section 6.3. The CRs and VRs are introduced in Section 6.4 for background estimations. The statistical method and fit configurations are explained in Section 6.6. The fit results are presented in Section 6.7.

6.2 Preselections

A stop ($\tilde{t}$) decays into a top quark and a neutralino ($\tilde{\chi}_1^0$), and our target channel is the channel in which the top quark decays hadronically. There are two unknown masses, $m_{\tilde{t}}$ and $m_{\tilde{\chi}_1^0}$, in this channel. The decay topology and the optimal search strategy depend on the $\Delta m(\tilde{t}_1,\tilde{\chi}_1^0)$. In the region of medium to high $\Delta m(\tilde{t}_1,\tilde{\chi}_1^0)$, the final state is characterized by the existence of multiple small-R jets, large-R jets, b-tagged jets, high $E_{\mathrm{T}}^{\mathrm{miss}}$ and zero lepton. The large-R jets with DNN top taggers are a key for the top-tagging, which are used in the definition of signal regions.

The preselections for the topology signatures are defined in Table 10. The first five selections are required for all the regions in this analysis. The GoodRunLists is the list of the recorded data with good conditions of detector operations. The events affected by the noise of the detector signals or the incomplete information are removed in Event Cleaning. Bad jets and bad muons (Chapter 4.2) are also removed from the events. The requirement of the primary vertex is to ensure the hard-scattering in the events. Since the channel for the search is defined in the zero lepton, the QCD backgrounds also need to be carefully taken into account. The $E_{\mathrm{T}}^{\mathrm{miss}} > 250$ GeV, $\min[\Delta\phi(j_{1-4}, E_{\mathrm{T}}^{\mathrm{miss}})] > 0.4$, and object-based $E_{\mathrm{T}}^{\mathrm{miss}}$ significance > 5 suppress the QCD background. Figures 40 (a), 40 (b), and 40 (c) are the N$-$1 plots[4] for $\min[\Delta\phi(j_{1-4}, E_{\mathrm{T}}^{\mathrm{miss}})]$, object-based $E_{\mathrm{T}}^{\mathrm{miss}}$ significance and $E_{\mathrm{T}}^{\mathrm{miss}}$. Owing to the selections of three variables, the multijet background (orange in Figure 40) is below 2% of total SM background in the event selections. The $\mathrm{N}_{\mathrm{jets}} \geq 4$ (the number of small-R jets in Figure 40 (e)), p_{T}^{j2} (subleading small-R jet p_{T} in Figure 40 (f)), and p_{T}^{j4} (4th leading small-R jet p_{T}) are required to satisfy the criteria in the table for the rejection of the backgrounds and retaining signal events. The $\mathrm{N}_{b\text{-jet}} \geq 1$ (Figure 40 (d)) is also used for the rejection of the backgrounds with no b quarks. The dominant backgrounds that remain after these preselections are $\mathrm{t\bar{t}Z}$, Z+jets, and $\mathrm{t\bar{t}}$. Diboson, single top, and W+jets are minor backgrounds.

Table 10: Definition of preselections based on the common signal signatures and event cleaning

Variables	Preselection
GoodRunLists	✓
Event Cleaning	✓
Bad jet veto	✓
Bad muon veto	✓
N_{PV}	≥ 1
baseline ℓ	0
$E_{\mathrm{T}}^{\mathrm{miss}}$ trigger	✓
$E_{\mathrm{T}}^{\mathrm{miss}}$	> 250 GeV
$\min[\Delta\phi(j_{1-4}, E_{\mathrm{T}}^{\mathrm{miss}})]$	> 0.4
Object-based $E_{\mathrm{T}}^{\mathrm{miss}}$ sig.	> 5
$\mathrm{N}_{\mathrm{jets}}$	≥ 4
$p_{\mathrm{T}}^{j_2}$	> 80 GeV
$p_{\mathrm{T}}^{j_4}$	> 40 GeV
$\mathrm{N}_{b\text{-jet}}$	≥ 1

[4]N-1 means all selections are applied except for the selections shown in the plots.

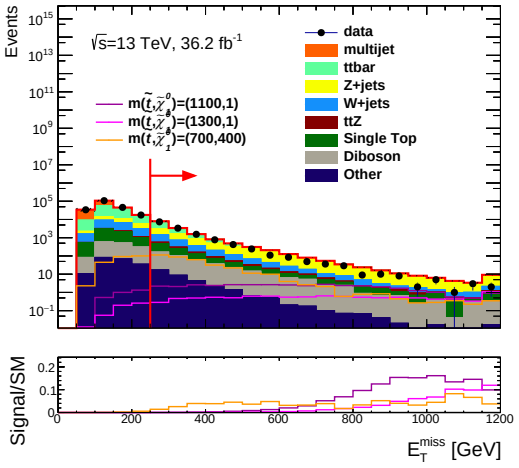

(a) $E_{\mathrm{T}}^{\mathrm{miss}}$

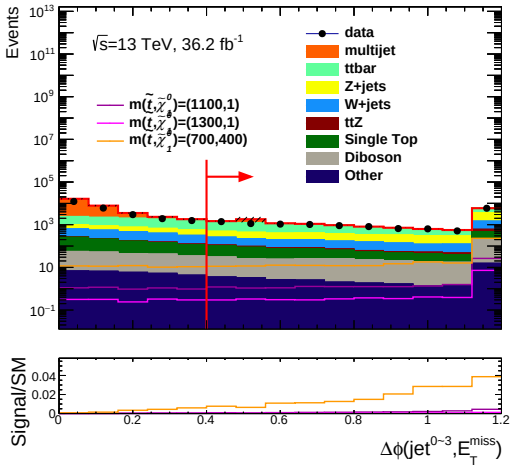

(b) $\min[\Delta\phi(j_{1-4}, E_{\mathrm{T}}^{\mathrm{miss}})]$

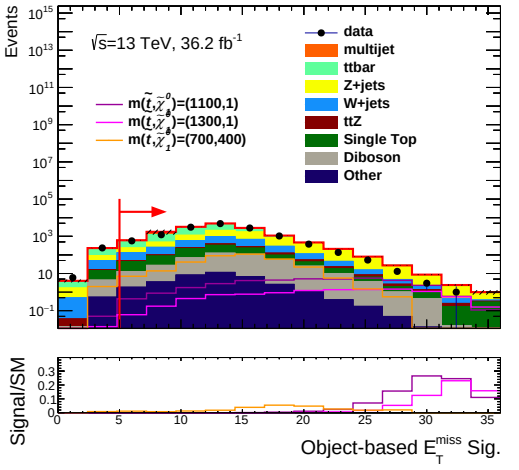

(c) Object-based $E_{\mathrm{T}}^{\mathrm{miss}}$ sig.

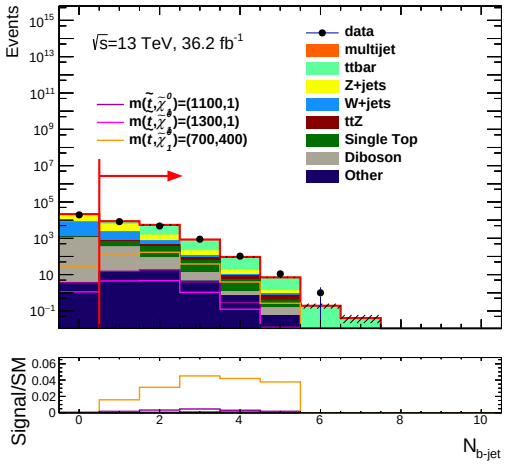

(d) $\mathrm{N}_{b\text{-jet}}$

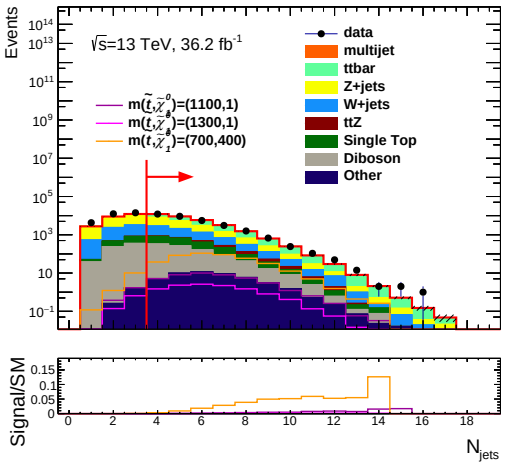

(e) $\mathrm{N}_{\mathrm{jets}}$

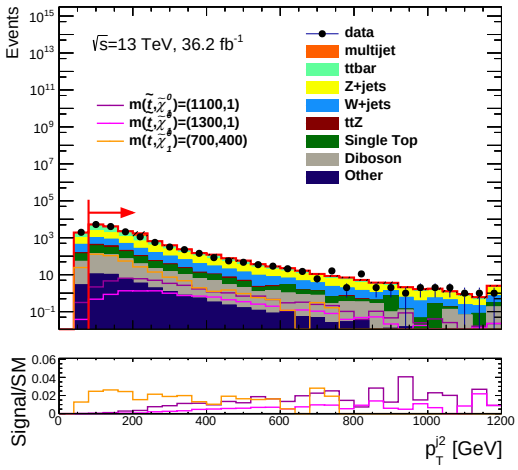

(f) p_{T}^{j2}

Figure 40: Data/MC N-1 plots for the preselections. N-1 means the all selections are applied except for the selections shown in the plots. The last bin contains the events in overflow bin. The lower panel shows the ratios of signals of $(m_{\tilde{t}}, m_{\tilde{\chi}_1^0})$ = (700,400) GeV (orange), (1100,1) GeV (purple), and (1300,1) GeV (pink) to the total SM prediction.

6.3 Signal region definitions

To characterize the properties of the signal with varying $\Delta m(\tilde{t}_1,\tilde{\chi}_1^0)$ values, the benchmark points of signals ($m_{\tilde{t}}$, $m_{\tilde{\chi}_1^0}$) = (1300,1) GeV, (1100,1) GeV, and (700,400) GeV are used. Two signal points, ($m_{\tilde{t}}$, $m_{\tilde{\chi}_1^0}$) = (1300,1) GeV and (1100,1) GeV, are chosen for the large $\Delta m(\tilde{t}_1,\tilde{\chi}_1^0)$ regions, and one signal point, ($m_{\tilde{t}}$, $m_{\tilde{\chi}_1^0}$) = (700,400) GeV, is for the medium $\Delta m(\tilde{t}_1,\tilde{\chi}_1^0)$. (1100,1) GeV is the point close to the exclusion limit of ATLAS results at 36 fb^{-1} [113]. (1300, 1) GeV and (700,400) GeV are expected to be close to the limit boundaries at 139 fb^{-1}.

The m_{T2} algorithm [114, 115] is used to reconstruct the stop transverse mass. In general, the m_{T2} is expressed as:

$$m_{T2}(m_{\mathrm{t}},m_{\tilde{\chi}_1^0},\vec{t_1},\vec{t_2},\vec{\not{p}}_T) = \min_{\vec{p}_1+\vec{p}_2=\vec{\not{p}}_T}\{\max[M_T(m_t,\vec{t_1};m_{\tilde{\chi}_1^0},\vec{p_1}),m_T(m_t,\vec{t_2};m_{\tilde{\chi}_1^0},\vec{p_2})]\}, \quad (42)$$

where the transverse mass m_T is defined as:

$$m_T(m_{\mathrm{t}},\vec{t};m_{\tilde{\chi}_1^0},\vec{p}) = \sqrt{m_{\mathrm{t}}^2+m_{\tilde{\chi}_1^0}^2+2\sqrt{m_{\mathrm{t}}^2+|\vec{t}|^2}\sqrt{m_{\tilde{\chi}_1^0}^2+|\vec{p}|^2}-2\vec{t}\cdot\vec{p}}. \quad (43)$$

m_{t} and $m_{\tilde{\chi}_1^0}$ represent top and neutralino mass, respectively. $\vec{t}_{(1/2)}$ is the transverse momentum of the top quark, and $\vec{p}_{(1/2)}$ is the transverse momentum of the neutralinos. $\vec{\not{p}}_T$ is the $E_{\mathrm{T}}^{\mathrm{miss}}$ vector. A top candidate is reconstructed by a vector sum of a b-tagged jet and one or two small-R light jets treated as a W boson. For only one b-tagged jet in an event, the second b-tagged jet is selected from a light jet with the highest b-tagging weight. The optimal combination of jets for two top candidates is decided by the minimization of χ^2-like function:

$$\chi^2 = \frac{(m_{W,1}-m_W^{true})^2}{m_W^{true}}+\frac{(m_{top,1}-m_{top}^{true})^2}{m_{top}^{true}}+\frac{(m_{W,2}-m_W^{true})^2}{m_W^{true}}+\frac{(m_{top,2}-m_{top}^{true})^2}{m_{top}^{true}}. \quad (44)$$

The true masses of the W boson and top quark are set to 80.4 GeV and 173.2 GeV, respectively. The neutralino mass is set to 1 GeV. The m_{T2} based on the top candidates selected by the aforementioned χ^2-like function is expressed as the m_{T2,χ^2}. The m_{T2,χ^2} shows good separation of the signal points at large $\Delta m(\tilde{t}_1,\tilde{\chi}_1^0)$ ((1100,1)
GeV and (1300,1) GeV) and medium $\Delta m(\tilde{t}_1,\tilde{\chi}_1^0)$ ((700,400) GeV), as shown in Figure 41. At the boundary of 450 GeV, the signal point with medium $\Delta m(\tilde{t}_1,\tilde{\chi}_1^0)$ and

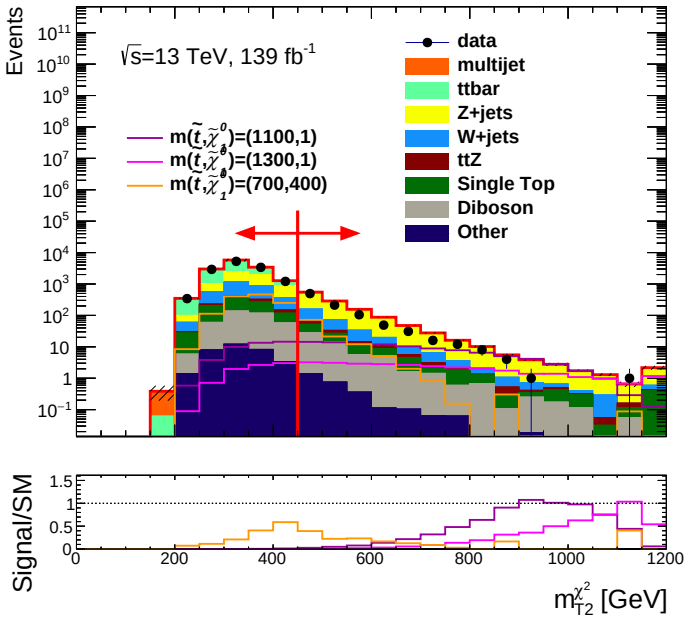

Figure 41: m_{T2,χ^2} distribution after the event selections with signal samples, ($m_{\tilde{t}}$, $m_{\tilde{\chi}_1^0}$) = (700,400) GeV, ($m_{\tilde{t}}$, $m_{\tilde{\chi}_1^0}$) = (1100,1) GeV, and ($m_{\tilde{t}}$, $m_{\tilde{\chi}_1^0}$) = (1300,1) GeV, at 139 fb^{-1}. The ratio of ($m_{\tilde{t}}$, $m_{\tilde{\chi}_1^0}$) = (700,400) GeV is multiplied by 3. "Other" includes tZ, tWZ, t$\bar{\mathrm{t}}W$, and t$\bar{\mathrm{t}}H$. Lower panel shows ratios of individual signals to total SM predictions.

the signal points with large $\Delta m(\tilde{t}_1,\tilde{\chi}_1^0)$ are separated according to the optimal signal significance. The signal of medium $\Delta m(\tilde{t}_1,\tilde{\chi}_1^0)$ with the upper cut of m_{T2,χ^2} has better signal significance than those without the upper cut. Owing to this behavior of the signals, we define the signal region A (SRA) in large $m_{\mathrm{T2},\chi^2} > 450$ GeV region and the signal region B (SRB) in $m_{\mathrm{T2},\chi^2} < 450$ GeV region.

The SRA has a highly boosted topology since the top quark is boosted due to the large $\Delta m(\tilde{t}_1,\tilde{\chi}_1^0)$. Figures 42 show the correlation between the maximal ΔR of the daughter quarks (two quarks from W and one b quark) from the hadronically decaying top and the p_{T} of top quark. The top quarks produced in the (1300,1) GeV sample tend to have higher p_{T}, and the ΔR of the final state particles becomes smaller.

The top candidates from the DNN contained top tagger, and the inclusive top tagger are used to categorize the signal regions. All the signal regions are required to contain at least one contained top candidate due to higher background reduction. Three categories, TT, TW, and T0, are designed to cover the possible topologies of the second top candidate to maximize the acceptance of the signals. "T" denotes the contained top. "W" denotes the inclusive top, which is not identified as a contained

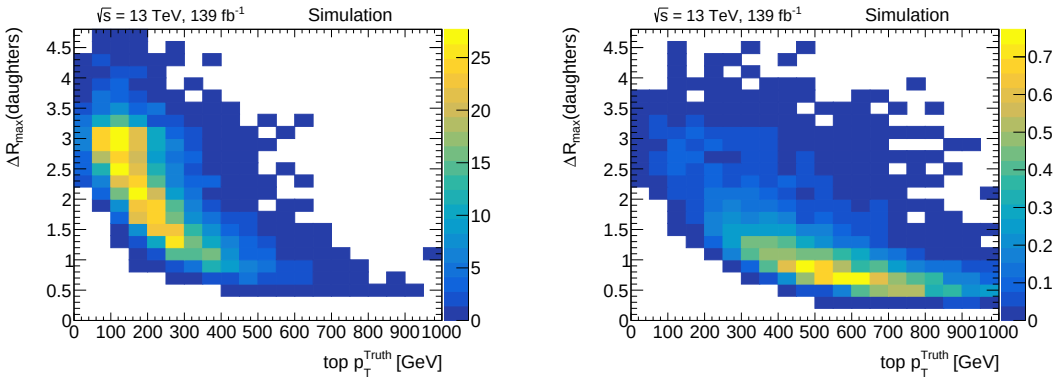

(a) (b)

Figure 42: The correlation plots of maximal ΔR of quarks from top decay and top truth p_{T} for the signal samples of (a) ($m_{\tilde{t}}$, $m_{\tilde{\chi}_1^0}$) = (700,400) GeV and (b) ($m_{\tilde{t}}$,$m_{\tilde{\chi}_1^0}$) = (1300,1) GeV.

top. "0" denotes that no second top candidate is identified.

The signal regions are also categorized by the number of the b-tagged jets to maximize the sensitivity. Two categories, one for exactly one b-tagged jet and the other one for two or more than two b-tagged jets, are defined. The high background rejection of the DNN top tagger enables us to use only one b-tagged jet region that contributes to the sensitivity of the search.

6.3.1 Signal region A ($m_{\mathrm{T2},\chi^2} > 450$ GeV)

Table 11 shows the definitions of all six signal regions categorized by the top candidates and the number of b-tagged jets, which are optimized with the object based $E_{\mathrm{T}}^{\mathrm{miss}}$ significance. The $E_{\mathrm{T}}^{\mathrm{miss}}$ is expected to be higher in the boosted regions so that the cut value of object-based $E_{\mathrm{T}}^{\mathrm{miss}}$ significance is large. For the cut value optimization, Figure 43 shows the N$-$1 plots with the expected discovery significance $Z_{0,A}$ based on the profiled likelihood ratio test and Asimov approximation [116]:

$$Z_{0,A} = \sqrt{q_{0,A}} = \sqrt{2((s+b)\ln\left[\frac{(s+b)(b+\sigma_b^2)}{b^2+(s+b)\sigma_b^2}\right] - \frac{b^2}{\sigma_b^2}\ln\left[1+\frac{\sigma_b^2 s}{b(b+\sigma_b^2)}\right]}, \quad (45)$$

where s denotes the total signal yield, b denotes the total background yield, and σ_b^2 denotes the uncertainty of the total background. The lower panel of the plots shows the significance calculated by integrating signal and background yields from the rightmost bin to the current bin. The cut values are optimized with the significance and the statistics to maximize the sensitivity. Tables 12 and 13 show the expected

Table 11: Definitions of the signal region A in addition to the event selections in Table 10

Variables	SRATT		SRATW		SRAT0	
m_{T2,χ^2}	>450 GeV					
$N_{\mathrm{DNNFCtop80}}$	≥ 2		1		1	
Excl. $N_{\mathrm{DNNInctop80}}$	-		≥ 1		0	
$N_{b\text{-jet}}$	≥ 2	1	≥ 2	1	≥ 2	1
Object-based $E_{\mathrm{T}}^{\mathrm{miss}}$ sig.	>20	>22	>20	>22	>28	>28
τ veto	✓					

Table 12: Signal region A with the number of b-tagged jets greater than or equal to 2 at 139 fb^{-1}. "Other" includes tZ, tWZ, t$\bar{\mathrm{t}}W$, and t$\bar{\mathrm{t}}H$. The relative ratios of each background to the total background are shown in parentheses.

Regions	SRATT-2b	SRATW-2b	SRAT0-2b
Z+jets	0.14 ± 0.12 (17.3%)	0.53 ± 0.15 (24.2%)	1.24 ± 0.27 (46.8%)
t$\bar{\mathrm{t}}Z$	0.45 ± 0.25 (56.2%)	0.80 ± 0.26 (36.1%)	0.50 ± 0.27 (19.0%)
t$\bar{\mathrm{t}}$	0.07 ± 0.11 (8.8%)	0.34 ± 0.36 (15.5%)	0.11 ± 0.12 (4.2%)
W+jets	0.04 ± 0.03 (5.1%)	0.17 ± 0.09 (7.9%)	0.41 ± 0.15 (15.4%)
single top	0.06 ± 0.04 (7.2%)	0.28 ± 0.09 (12.6%)	0.32 ± 0.17 (12.2%)
diboson	0.00 ± 0.00 (0.0%)	0.02 ± 0.00 (0.8%)	0.05 ± 0.05 (1.9%)
others	0.04 ± 0.03 (5.4%)	0.07 ± 0.02 (3.1%)	0.01 ± 0.01 (0.4%)
Total SM	0.81 ± 0.40	2.21 ± 0.49	2.65 ± 0.57
$(m_{\tilde{t}},m_{\tilde{\chi}_1^0})$=(700,400)	0.00 ± 0.00	0.18 ± 0.19	0.00 ± 0.00
$(m_{\tilde{t}},m_{\tilde{\chi}_1^0})$=(1100,1)	4.75 ± 1.86	4.87 ± 1.22	4.25 ± 1.01
$(m_{\tilde{t}},m_{\tilde{\chi}_1^0})$=(1300,1)	2.01 ± 0.74	1.79 ± 0.51	1.96 ± 0.50

yields of the signals and backgrounds. The main backgrounds are t$\bar{\mathrm{t}}Z$ and Z+jets.

6.3.2 Signal region B ($m_{\mathrm{T2},\chi^2} < 450$ GeV)

To enhance the background rejection in the SRB, more variables are considered. The $\Delta R(b_1, b_2)$ is ΔR between the two b-tagged jets with the highest b-tagged weights. This variable is used to remove the b-tagged jets from gluon-splitting, which is expected to have small $\Delta R(b_1, b_2)$. The criteria of $m_{\mathrm{T}}^{b,\mathrm{min}}$ and $m_{\mathrm{T}}^{b,\mathrm{max}}$ aim to reduce the semi-leptonic decay of the t$\bar{\mathrm{t}}$ events. If an unidentified lepton exists, the lepton is expected to be merged into the $E_{\mathrm{T}}^{\mathrm{miss}}$. The transverse mass of the b-tagged jet and the $E_{\mathrm{T}}^{\mathrm{miss}}$ can be considered as the transverse mass of a top. The formula of transverse

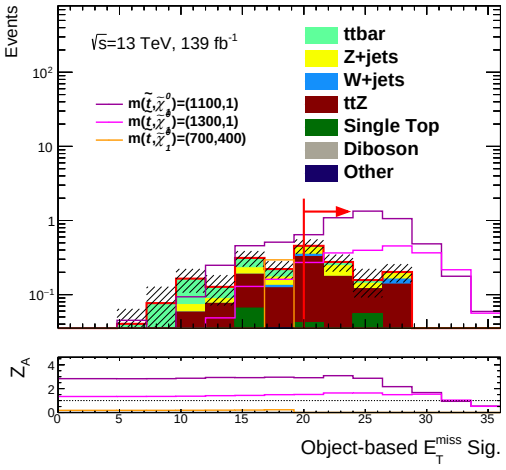

(a) SRATT-2b

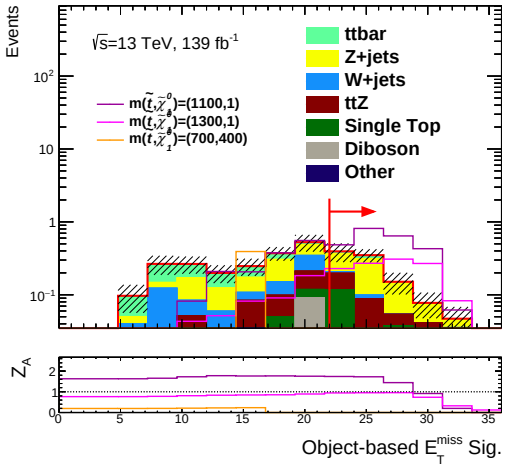

(b) SRATT-1b

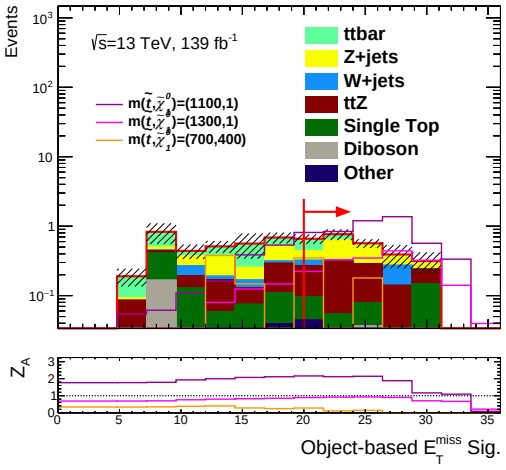

(c) SRATW-2b

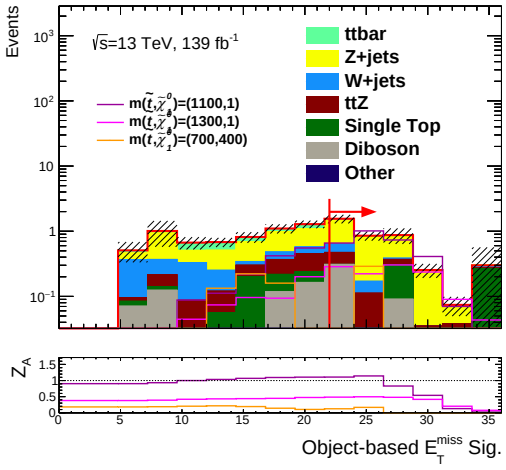

(d) SRATW-1b

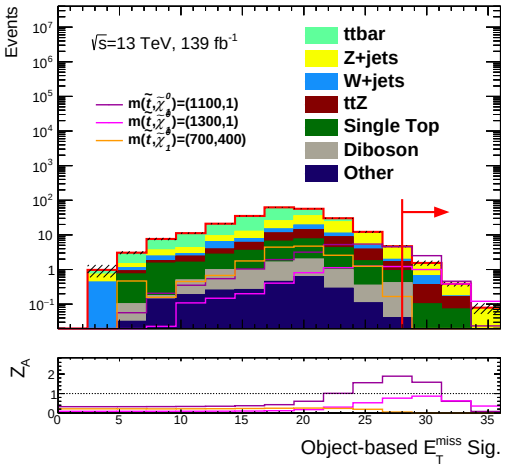

(e) SRAT0-2b

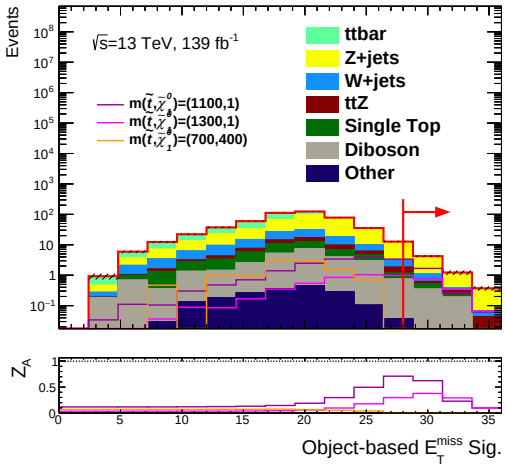

(f) SRAT0-1b

Figure 43: N−1 plots of object-based $E_{\mathrm{T}}^{\mathrm{miss}}$ significance for the signal region A with the cut value where the red arrows indicate. Full selections are applied except for the object-based $E_{\mathrm{T}}^{\mathrm{miss}}$ significance at 139 fb^{-1}. "Other" includes tZ, tWZ, t$\bar{\mathrm{t}}W$, and t$\bar{\mathrm{t}}H$. Signal samples, ($m_{\tilde{t}}$, $m_{\tilde{\chi}_1^0}$) = (700,400) GeV, ($m_{\tilde{t}}$, $m_{\tilde{\chi}_1^0}$) = (1100,1) GeV, and ($m_{\tilde{t}}$, $m_{\tilde{\chi}_1^0}$) = (1300,1) GeV are shown in the plots.

Table 13: Yields of the signal region A with one b-tagged jet at 139 fb^{-1}. "Other" includes tZ, tWZ, t$\bar{t}W$, and t$\bar{t}H$. The relative ratios of each background to the total background are shown in parentheses.

Regions	SRATT-1b	SRATW-1b	SRAT0-1b
Z+jets	0.35 ± 0.22 (42.8%)	1.38 ± 0.41 (46.1%)	3.87 ± 1.05 (61.2%)
t$\bar{t}Z$	0.21 ± 0.09 (25.8%)	0.33 ± 0.13 (11.5%)	0.47 ± 0.36 (7.5%)
t$\bar{t}$	0.06 ± 0.07 (7.1%)	0.15 ± 0.13 (4.9%)	0.25 ± 0.12 (4.0%)
W+jets	0.04 ± 0.02 (4.6%)	0.24 ± 0.12 (8.0%)	0.81 ± 0.44 (13.0%)
single top	0.12 ± 0.07 (14.8%)	0.51 ± 0.13 (17.1%)	0.33 ± 0.46 (5.3%)
diboson	0.01 ± 0.01 (1.1%)	0.32 ± 0.16 (10.6%)	0.53 ± 0.10 (8.5%)
others	0.03 ± 0.02 (3.8%)	0.05 ± 0.01 (1.7%)	0.03 ± 0.01 (0.5%)
Total SM	0.82 ± 0.32	3.00 ± 0.60	6.25 ± 1.88
($m_{\tilde{t}}$,$m_{\tilde{\chi}_1^0}$)=(700,400)	0.00 ± 0.00	0.29 ± 0.07	0.00 ± 0.00
($m_{\tilde{t}}$,$m_{\tilde{\chi}_1^0}$)=(1100,1)	2.39 ± 0.93	2.74 ± 0.81	2.83 ± 0.78
($m_{\tilde{t}}$,$m_{\tilde{\chi}_1^0}$)=(1300,1)	1.14 ± 0.56	1.16 ± 0.32	1.51 ± 0.38

Table 14: Definitions of the signal region B in addition to the event selections in Table 10

Variables	SRBTT		SRBTW		SRBT0	
m_{T2,χ^2}			< 450 GeV			
$\mathrm{N}_{\mathrm{DNNFCtop80}}$	≥ 2		1		1	
Excl. $\mathrm{N}_{\mathrm{DNNInctop80}}$	-		≥ 1		0	
$\mathrm{N}_{b\text{-jet}}$	≥ 2	1	≥ 2	1	≥ 2	1
$\Delta R\,(b_1, b_2)$	> 1.4	-	> 1.4	-	> 1.4	-
$m_{\mathrm{T}}^{b,\mathrm{min}}$	> 200 GeV	> 200 GeV	> 200 GeV	-	> 150 GeV	-
$m_{\mathrm{T}}^{b,\mathrm{max}}$	-		-		> 150 GeV	-
Object-based $E_{\mathrm{T}}^{\mathrm{miss}}$ sig.	> 12	> 12	> 12	> 12	> 20	> 20
τ veto			✓			

mass is as follows:

$$m_T^{b,min/max} = \sqrt{2p_{\mathrm{T}}^{\mathrm{b}} E_{\mathrm{T}}^{\mathrm{miss}} \left(1 - \cos\left(\max / \min[\Delta\phi(b, E_{\mathrm{T}}^{\mathrm{miss}})]\right)\right)}. \tag{46}$$

The four variables, including object-based $E_{\mathrm{T}}^{\mathrm{miss}}$ significance, are considered in the optimization of the sensitivities (see the cut value in Figures 44 and 45). The definitions of six regions are summarized in Table 14. Tables 15 and 16 show expected yields of the signal and backgrounds. The main backgrounds are t$\bar{t}$ and Z+jets.

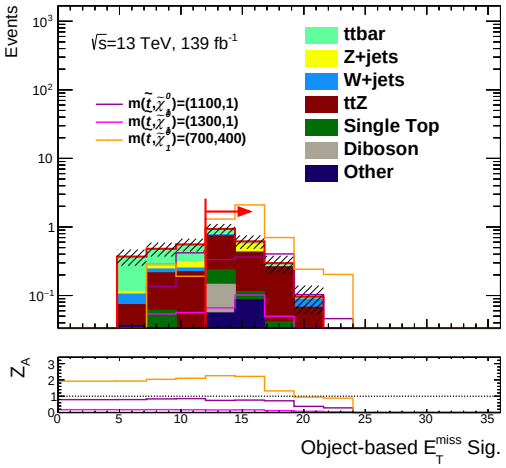

(a) SRBTT-2b

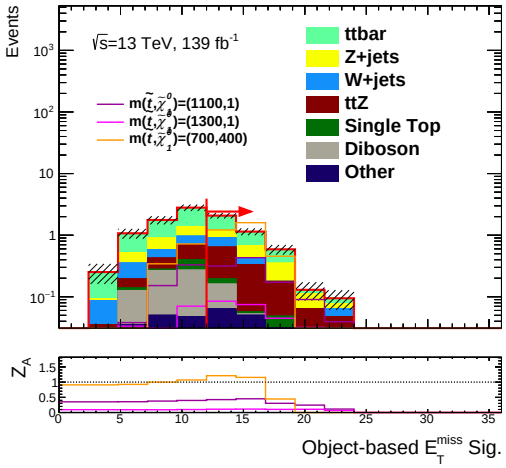

(b) SRBTT-1b

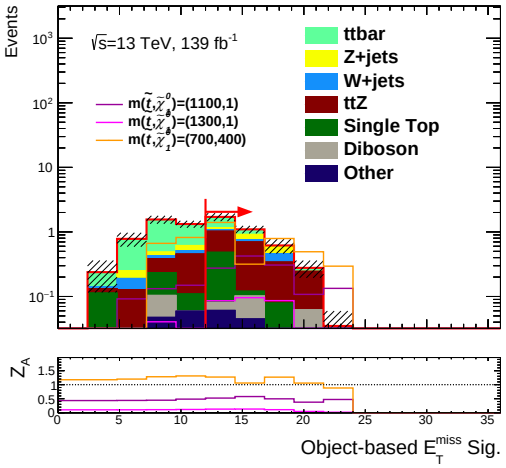

(c) SRBTW-2b

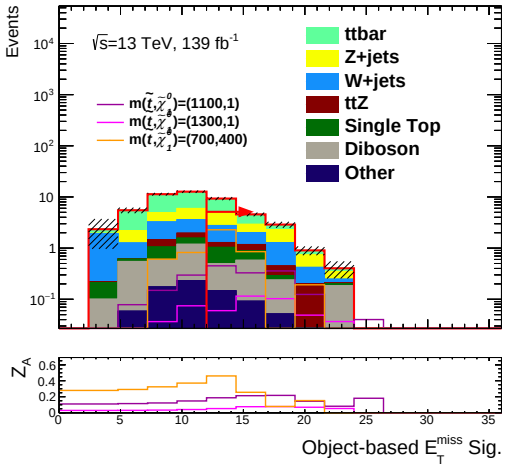

(d) SRBTW-1b

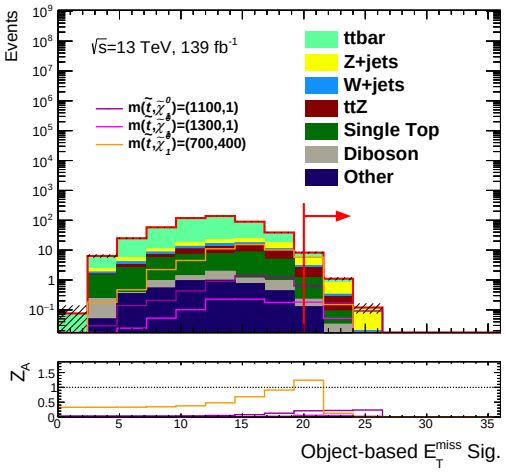

(e) SRBT0-2b

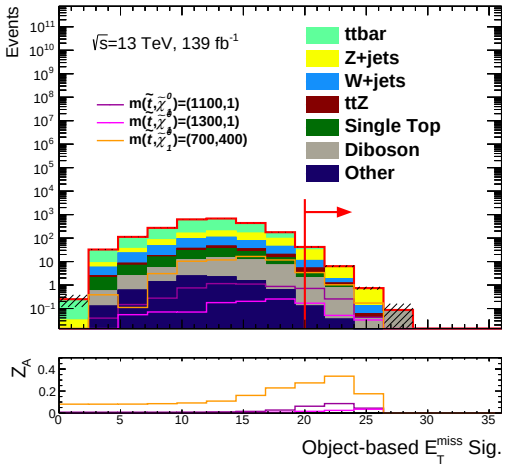

(f) SRBT0-1b

Figure 44: N−1 plots of object-based $E_{\mathrm{T}}^{\mathrm{miss}}$ significance for the signal region B with the cut value where the red arrows indicate. Full selections are applied except for the object-based $E_{\mathrm{T}}^{\mathrm{miss}}$ significance. "Other" includes tZ, tWZ, t$\bar{\mathrm{t}}W$, and t$\bar{\mathrm{t}}H$. Signal samples, $(m_{\tilde{t}}, m_{\tilde{\chi}_1^0})$ = (700,400) GeV, $(m_{\tilde{t}}, m_{\tilde{\chi}_1^0})$ = (1100,1) GeV, and $(m_{\tilde{t}}, m_{\tilde{\chi}_1^0})$ = (1300,1) GeV are shown in the plots.

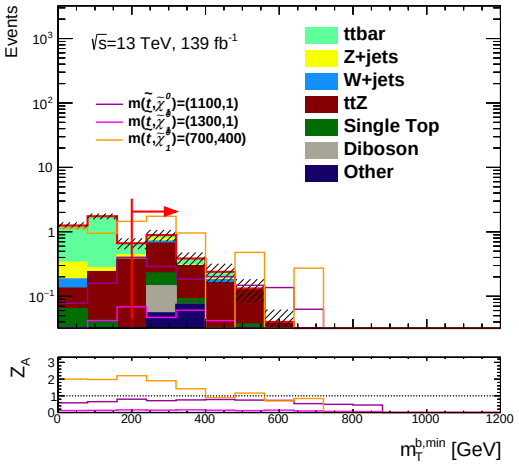

(a) SRBTT-2b $m_{\mathrm{T}}^{b,\mathrm{min}}$

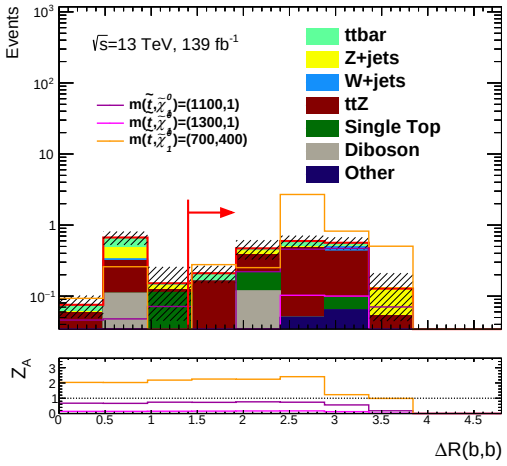

(b) SRBTT-2b $\Delta R\,(b_1, b_2)$

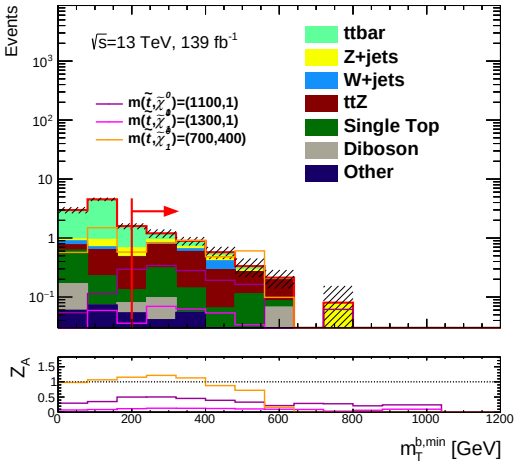

(c) SRBTW-2b $m_{\mathrm{T}}^{b,\mathrm{min}}$

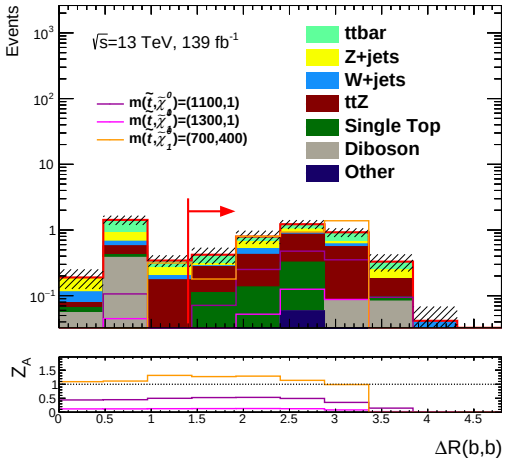

(d) SRBTW-2b $\Delta R\,(b_1, b_2)$

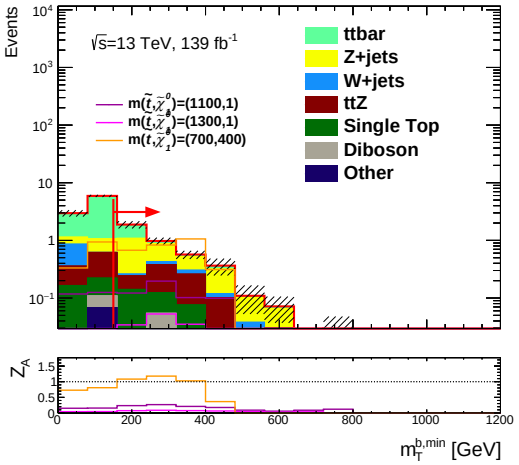

(e) SRBT0-2b $m_{\mathrm{T}}^{b,\mathrm{min}}$

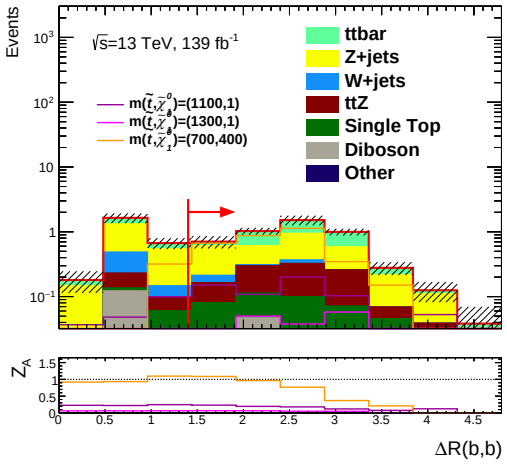

(f) SRBT0-2b $\Delta R\,(b_1, b_2)$

Figure 45: N−1 plots of $\Delta R\,(b_1, b_2)$ and $m_{\mathrm{T}}^{b,\mathrm{min}}$ for the signal region B with the cut value where the red arrows indicate. Full selections are applied except for the $\Delta R\,(b_1, b_2)$ (right side) or $m_{\mathrm{T}}^{b,\mathrm{min}}$ (left side). "Other" includes tZ, tWZ, t$\bar{\mathrm{t}}W$, and t$\bar{\mathrm{t}}H$. Signal samples, ($m_{\tilde{t}}$, $m_{\tilde{\chi}_1^0}$) = (700,400) GeV, ($m_{\tilde{t}}$, $m_{\tilde{\chi}_1^0}$) = (1100,1) GeV and ($m_{\tilde{t}}$, $m_{\tilde{\chi}_1^0}$) = (1300,1) GeV are shown in the plots.

Table 15: Yields in the signal region B with the number of b-tagged jet greater than or equal to 2 at 139 fb^{-1}. "Other" includes tZ, tWZ, t$\bar{t}W$, and t$\bar{t}H$. The relative ratios of each background to the total background are shown in parentheses.

Regions	SRBTT-2b	SRBTW-2b	SRBT0-2b
Z+jets	0.10 ± 0.04 (5.4%)	0.19 ± 0.11 (5.3%)	1.01 ± 0.36 (25.9%)
t$\bar{t}Z$	1.10 ± 0.29 (57.2%)	1.58 ± 0.41 (44.6%)	0.72 ± 0.38 (18.5%)
t$\bar{t}$	0.25 ± 0.29 (13.2%)	0.78 ± 0.53 (22.2%)	1.59 ± 0.35 (40.8%)
W+jets	0.07 ± 0.03 (3.5%)	0.23 ± 0.09 (6.6%)	0.14 ± 0.12 (3.5%)
single top	0.14 ± 0.03 (7.5%)	0.48 ± 0.30 (13.5%)	0.36 ± 0.15 (9.3%)
diboson	0.09 ± 0.03 (4.7%)	0.14 ± 0.04 (3.9%)	0.03 ± 0.04 (0.8%)
others	0.16 ± 0.04 (8.5%)	0.13 ± 0.03 (3.8%)	0.04 ± 0.04 (0.9%)
Total SM	1.92 ± 0.50	3.53 ± 0.77	3.09 ± 0.84
($m_{\tilde{t}}$,$m_{\tilde{\chi}_1^0}$)=(700,400)	4.55 ± 1.89	3.30 ± 1.57	3.17 ± 2.11
($m_{\tilde{t}}$,$m_{\tilde{\chi}_1^0}$)=(1100,1)	1.25 ± 0.52	1.25 ± 0.41	0.62 ± 0.19
($m_{\tilde{t}}$,$m_{\tilde{\chi}_1^0}$)=(1300,1)	0.24 ± 0.11	0.30 ± 0.10	0.17 ± 0.05

Table 16: Yields of the signal region B with one b-tagged jet at 139 fb^{-1}. "Other" includes tZ, tWZ, t$\bar{t}W$, and t$\bar{t}H$. The relative ratios of each background to the total background are shown in parentheses.

Regions	SRBTT-1b	SRBTW-1b	SRBT0-1b
Z+jets	0.60 ± 0.45 (13.7%)	3.41 ± 1.18 (20.5%)	8.63 ± 1.65 (40.8%)
t$\bar{t}Z$	0.97 ± 0.34 (21.5%)	0.90 ± 0.29 (5.4%)	1.27 ± 0.45 (6.0%)
t$\bar{t}$	2.12 ± 1.48 (48.7%)	6.89 ± 2.64 (41.5%)	5.35 ± 1.64 (25.3%)
W+jets	0.37 ± 0.18 (8.5%)	3.41 ± 1.18 (20.5%)	3.62 ± 2.19 (17.1%)
single top	0.08 ± 0.03 (1.9%)	0.92 ± 0.67 (5.6%)	0.61 ± 0.75 (2.9%)
diboson	0.10 ± 0.02 (2.3%)	1.11 ± 0.47 (6.7%)	1.60 ± 0.58 (7.6%)
others	0.14 ± 0.04 (3.3%)	0.30 ± 0.04 (1.8%)	0.06 ± 0.02 (0.3%)
Total SM	4.35 ± 1.88	16.62 ± 3.13	21.14 ± 3.70
($m_{\tilde{t}}$,$m_{\tilde{\chi}_1^0}$)=(700,400)	3.27 ± 1.12	3.33 ± 1.54	3.64 ± 1.32
($m_{\tilde{t}}$,$m_{\tilde{\chi}_1^0}$)=(1100,1)	1.05 ± 0.47	1.32 ± 0.38	0.80 ± 0.27
($m_{\tilde{t}}$,$m_{\tilde{\chi}_1^0}$)=(1300,1)	0.26 ± 0.14	0.36 ± 0.12	0.18 ± 0.05

6.4 Background estimations

The background estimation using Monte Carlo simulation may be imprecise due to possible mismodelling in the simulation. To correctly estimate the background in signal regions, the control regions of individual background components are defined and used to account for the discrepancies between the data and the simulation.

From Tables 12, 13, 15, and 16, we can conclude that there are three main backgrounds, $t\bar{t}Z$, Z+jets, and $t\bar{t}$. The control regions are defined to be orthogonal to the signal regions, and the phase space of control regions is chosen as close as possible to the signal regions. Three floating parameters, $\mu_{t\bar{t}Z}$, μ_Z, and $\mu_{t\bar{t}}$, are introduced as the normalization factors of $t\bar{t}Z$, Z+jets, and $t\bar{t}$, respectively. The normalization factors are determined by the simultaneous fit to all the control regions with the data (see Background-only fit in Chapter 6.6).

To validate the background estimations, the validation regions are also defined as close as possible to the signal regions. The normalization factors are applied to correct the background yields in the validation regions and the corrected background yields are compared with the data to confirm the fit results.

Figure 46 summarizes the control regions and validation regions by the number of b-tagged jets and the number of leptons. The $t\bar{t}Z$, Z+jets, and $t\bar{t}$ backgrounds in all the plots shown in this chapter are normalized with the normalization factors from the background-only fit, which is discussed in Chapter 6.7.

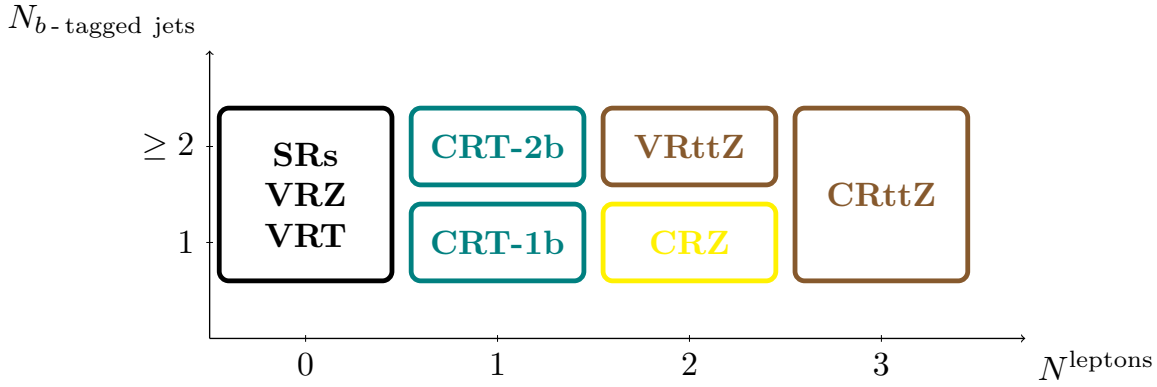

Figure 46: Region definitions in the plane with a vertical axis of the number of b-tagged jets and a horizontal axis of the number of leptons. The SRs are the signal regions. The VRZ and VRT are the validation regions of Z+jets and $t\bar{t}$, respectively. The CRT-1b and CRT-2b are $t\bar{t}$ control regions defined in only one b-tagged region and ≥ 2 b-tagged region, respectively. The CRZ is a Z+jets control region. The VRttZ and CRttZ are a validation region and a control region for the $t\bar{t}Z$, respectively.

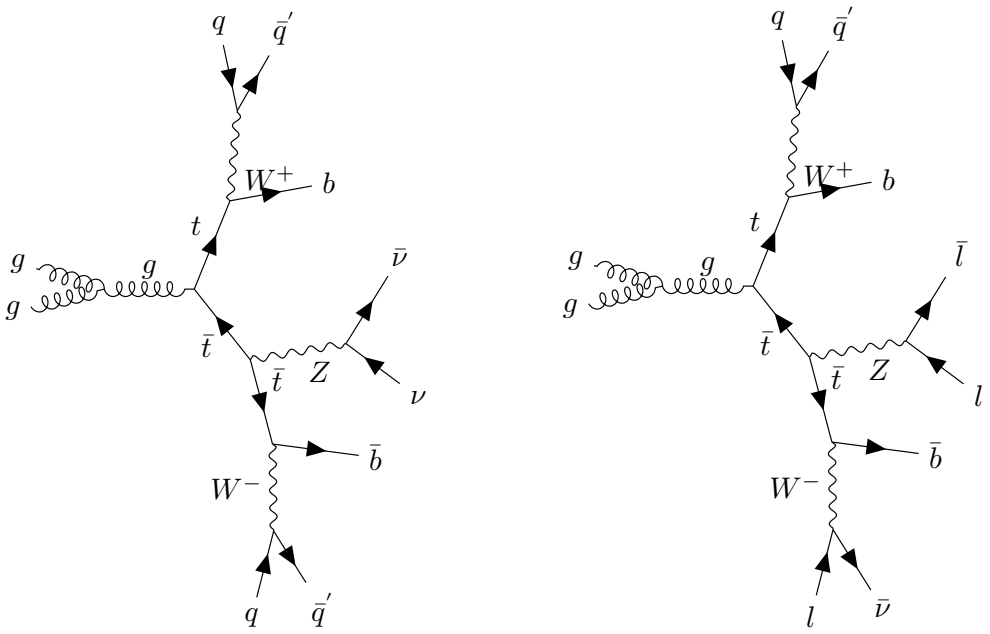

Figure 47: Diagrams of $t\bar{t}Z$ decay chains with (a) zero lepton and (b) three leptons.

6.4.1 Control regions

6.4.1.1 $t\bar{t}Z$ control region (CRttZ)

The $t\bar{t}Z$ events with $Z \to \nu\nu$ and fully hadronic $t\bar{t}$ in the signal regions result in the final states with high $E_{\mathrm{T}}^{\mathrm{miss}}$ and zero lepton. The $t\bar{t}Z$ is the main background in the TT2b and TW2b regions and sub-dominant background in the TT1b region. Figure 47 (a) shows the diagram of the dominant channel of $t\bar{t}Z$ in the signal region. The control region of $t\bar{t}Z$ is defined by using three lepton region in which $t\bar{t}Z$ process dominates (see Figure 47 (b)). To emulate the topology in the signal regions, the two opposite-sign same-flavor leptons are required and the mass of two leptons should be in the mass window of Z boson ($81\mathrm{GeV} < m(\ell,\ell) < 101\mathrm{GeV}$). The $E_{\mathrm{T}}^{\mathrm{miss}}$ in three lepton region is treated as a jet p_{T}. The extra one lepton is also treated as a jet. Therefore, the selection variables relative to jets, $\mathrm{N_{jets}}$ and jet p_{T}, contain the $E_{\mathrm{T}}^{\mathrm{miss}}$ and lepton p_{T}. The definition of variables is listed in Table 17. The number of DNN top tagged jets, which reduces the data statistics significantly, is not considered in the definition of the control region. For the boosted topologies in the $t\bar{t}Z$ control region, the p_{T} and mass selections of leading Large-R jet are needed. Figure 48 shows the post-fit plots for some variables. No significant mismodelling is found.

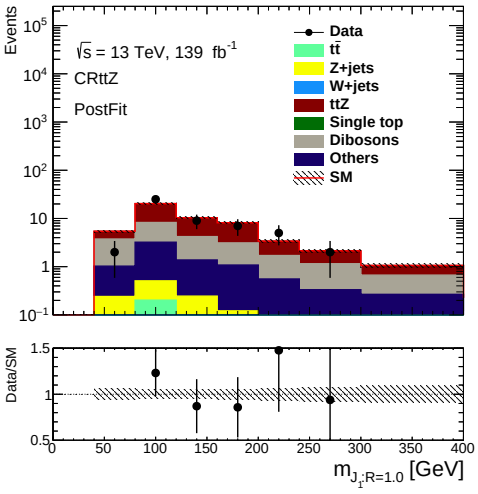

(a) Leading large-R jet mass

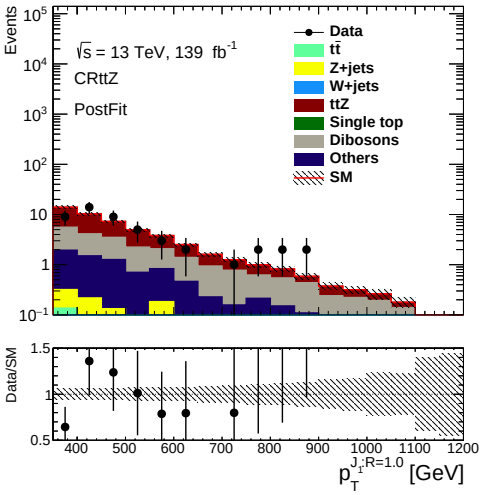

(b) Leading large-R jet p_{T}

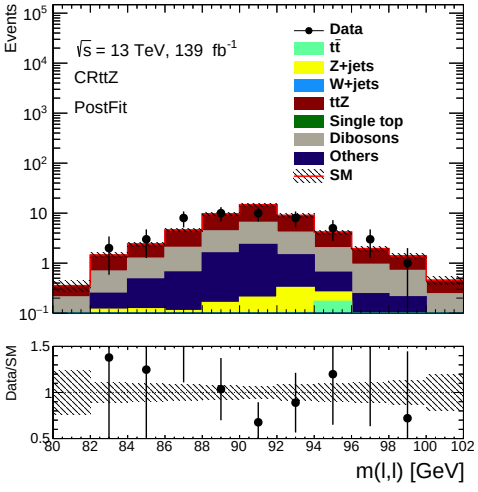

(c) $m(\ell,\ell)$

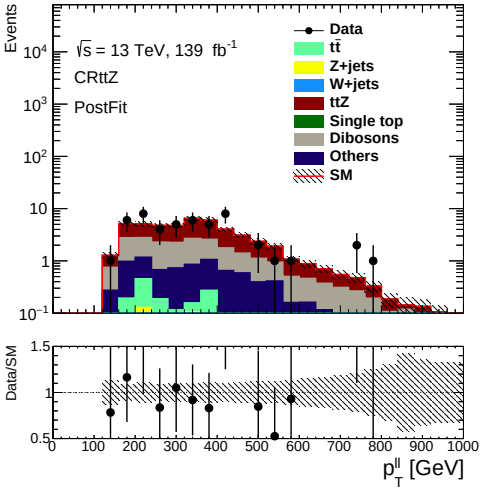

(d) $p_{\mathrm{T}}^{\ell\ell}$

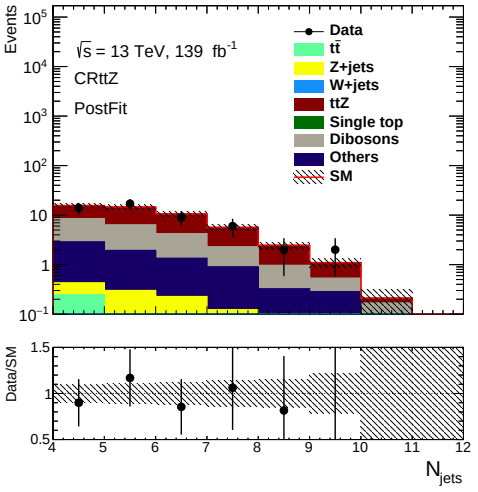

(e) $\mathrm{N}_{\mathrm{jets}}$

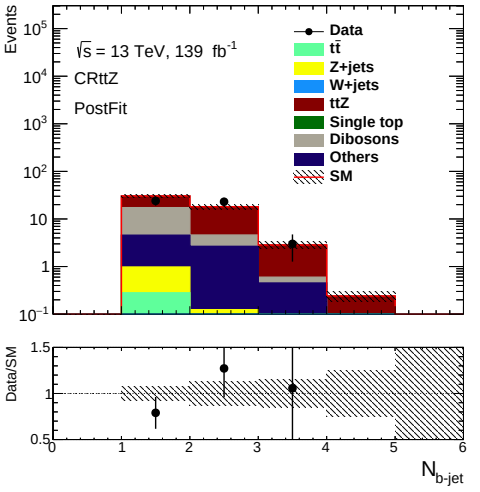

(f) $\mathrm{N}_{b\text{-jet}}$

Figure 48: Post-fit plots for the $\mathrm{t\bar{t}Z}$ control region. $\mu_Z = 0.93 \pm 0.12$, $\mu_{\mathrm{t\bar{t}Z}} = 0.77 \pm 0.22$, and $\mu_{\mathrm{t\bar{t}}} = 0.83 \pm 0.04$ are applied to Z+jets, $\mathrm{t\bar{t}Z}$, and $\mathrm{t\bar{t}}$, respectively. The shaded area in the lower panel shows total uncertainties including systematic and statistical uncertainties.

Table 17: Definitions of $t\bar{t}Z$ control region in three lepton region.

Variables	CRttZ
signal ℓ	3, 2 with same flavor / sum of charge=± 1
additional baseline ℓ	0
single lepton trigger	✓
$m(\ell,\ell)$	[81,101] GeV
N_{jets}	≥ 4 ($E_{\text{T}}^{\text{miss}}$included)
$p_{\text{T}}^{j_2}$	> 80 GeV
$p_{\text{T}}^{j_4}$	> 40 GeV
Leading p_{T}^{ℓ}	> 27 GeV
Third p_{T}^{ℓ}	> 20 GeV
$E_{\text{T}}^{\text{miss}}$	-
$N_{b\text{-jet}}$	≥ 1
$N_{\text{DNNFCtop80}}$	-
Leading Large-R jet p_{T}	> 350 GeV
Leading Large-R jet mass	> 40 GeV
$p_{\text{T}}^{\ell\ell}$	> 150 GeV

6.4.1.2 Z+jets control region (CRZ)

The control region of Z+jets is defined in a region with two lepton events. The events are selected using a single muon or single election triggers. The two opposite-sign same flavor (OSSF) leptons are required. The leading lepton p_{T} is required to be larger than 27 GeV. The mass of two leptons is in the mass window between 81 GeV and 101 GeV. The muons or electrons from Z bosons are treated like the neutrinos from Z bosons. Therefore, the p_{T} of the dilepton system is used for $E_{\text{T}}^{\text{miss}'} = |\vec{p}_{\text{T}}^{\ell\ell}| = |\vec{p}_{\text{T}}^{\ell^+} + \vec{p}_{\text{T}}^{\ell^-}|$ in the Z+jets control region. The Z+jets with two leptons has no true $E_{\text{T}}^{\text{miss}}$ since all the final states are detectable in the ATLAS detector. The upper cut of $E_{\text{T}}^{\text{miss}}$ is required to reduce the other background contamination. The requirement of Z+jets control region is in Table 18. The only-one b-tagged jet makes CRZ orthogonal to the $t\bar{t}Z$ validation region. Figure 49 shows post-fit plots for some variables. The data and MC predictions are in agreement after the normalization factors are applied.

6.4.1.3 $t\bar{t}$ control region (CRT)

The $t\bar{t}$ control region is defined to be dominated by $t\bar{t}$ events with a lepton (see Figure 50) since the fully-hadronic $t\bar{t}$ is removed by requiring high $E_{\text{T}}^{\text{miss}}$. Most of

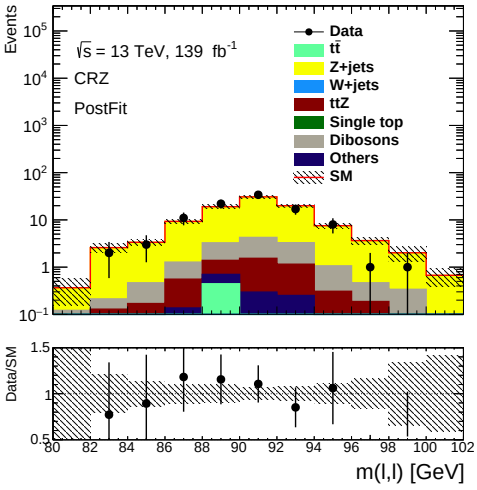

(a) $m(\ell,\ell)$

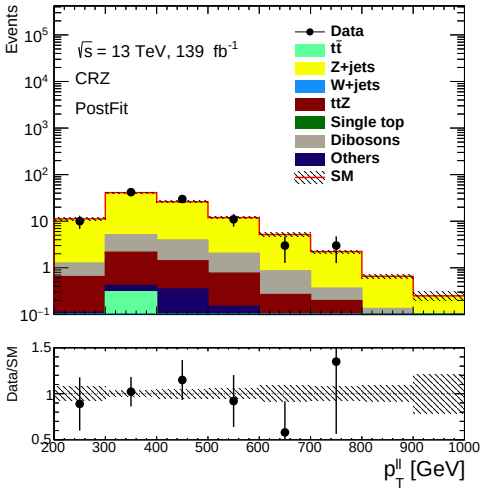

(b) $p_{\mathrm{T}}^{\ell\ell}$ ($E_{\mathrm{T}}^{\mathrm{miss}\prime}$)

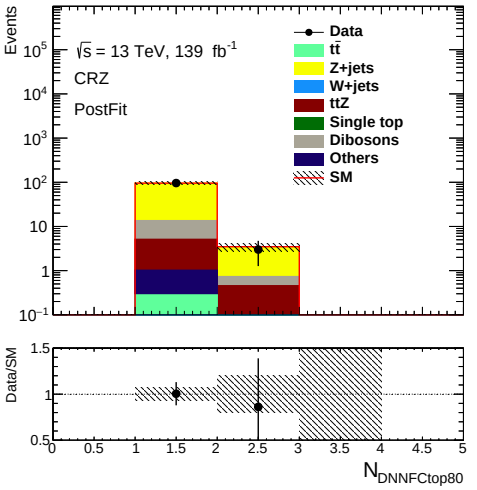

(c) $\mathrm{N}_{\mathrm{DNNFCtop80}}$

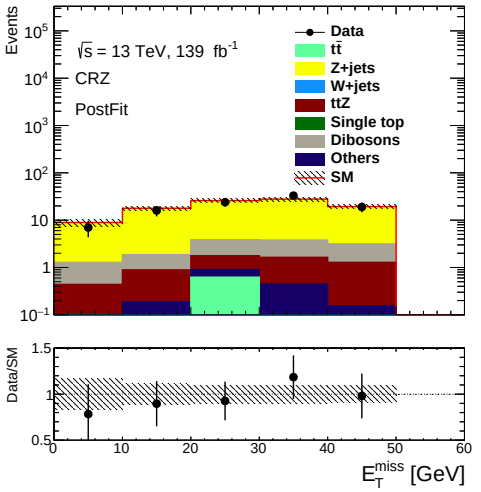

(d) $E_{\mathrm{T}}^{\mathrm{miss}}$

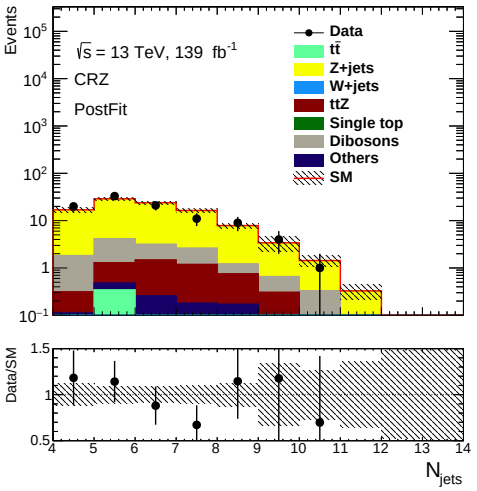

(e) $\mathrm{N}_{\mathrm{jets}}$

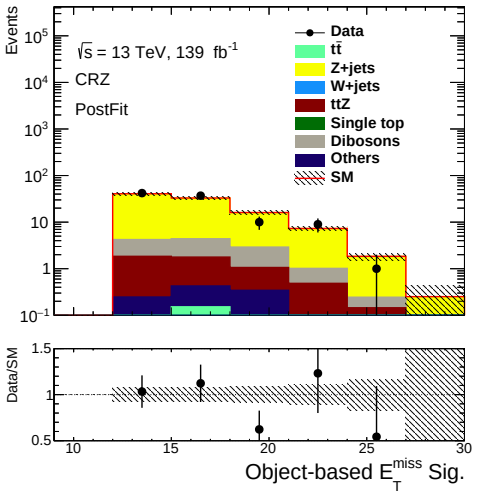

(f) Object-based $E_{\mathrm{T}}^{\mathrm{miss}}$ sig.

Figure 49: Post-fit plots for the Z control region. $\mu_Z = 0.93 \pm 0.12$, $\mu_{\mathrm{t\bar{t}Z}} = 0.77 \pm 0.22$, and $\mu_{\mathrm{t\bar{t}}} = 0.83 \pm 0.04$ are applied to Z+jets, $\mathrm{t\bar{t}}Z$, and $\mathrm{t\bar{t}}$, respectively. The shaded area in the lower panel shows total uncertainties including systematic and statistical uncertainties.

Table 18: Definitions of Z+jets control region in two lepton region.

Variables	CRZ
single lepton trigger	✓
signal ℓ	2, same flavor / opposite sign
additional baseline ℓ	0
Leading p_{T}^{ℓ}	>27 GeV
Subleading p_{T}^{ℓ}	>20 GeV
$m(\ell,\ell)$	[81,101] GeV
$\min\left\|\Delta\phi\left(\mathrm{jet}^{1-4}, E_{\mathrm{T}}^{\mathrm{miss}'}\right)\right\|$	>0.4
$E_{\mathrm{T}}^{\mathrm{miss}'}$	>250 GeV
$E_{\mathrm{T}}^{\mathrm{miss}}$	<50 GeV
$\mathrm{N}_{\mathrm{jets}}$	≥ 4
$p_{\mathrm{T}}^{j_2}$	>80 GeV
$p_{\mathrm{T}}^{j_4}$	>40 GeV
$\mathrm{N}_{b\text{-jet}}$	1
$\mathrm{N}_{\mathrm{DNNFCtop80}}$	≥ 1
Object-based $E_{\mathrm{T}}^{\mathrm{miss}'}$ sig.	>12

W bosons decay into a τ and a neutrino in signal regions where the τ has p_{T} lower than 20 GeV since the tau-veto is also required in the signal regions. In the $\mathrm{t\bar{t}}$ control region, the $E_{\mathrm{T}}^{\mathrm{miss}}$ trigger is used. One baseline lepton is required. The lower bound of the baseline lepton p_{T} is very low (4.5 GeV for muons and 5 GeV for electrons). The p_{T} of muons or electrons is required to be lower than 20 GeV so that muons or electrons in the control region can mimic τs in the signal regions. The definitions of the $\mathrm{t\bar{t}}$ control region are in Table 19. To account for the effect due to the requirement of a different number of b-tagged jets in the signal regions, the 1b and 2b regions are defined. Figures 51 and 52 show the post-fit plots for the variables. The fit works well, and no significant mismodelling is found.

6.4.2 Validation regions

6.4.2.1 $\mathrm{t\bar{t}}Z$ validation region (VRttZ)

The $\mathrm{t\bar{t}}Z$ is the main background in SRAs but it is difficult to find a $\mathrm{t\bar{t}}Z$ validation region with high statistics of $\mathrm{t\bar{t}}Z$ in the zero lepton final states. Therefore, the $\mathrm{t\bar{t}}Z$ validation region is finally defined with two lepton events (see Table 20). The single lepton trigger is used. The OSSF leptons with the dilepton mass falling in the window (81 GeV $< m(\ell,\ell) <$ 101 GeV) are required to select events with a Z boson. The number of

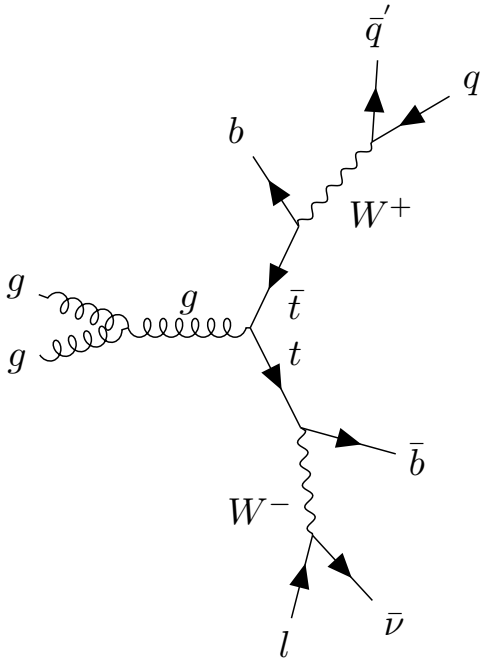

Figure 50: Diagram of semi-leptonic $t\bar{t}$.

Table 19: Definitions of $t\bar{t}$ control region with one lepton. CRT-1b and CRT-2b are defined in the region with only one b-tagged jet and more than two b-tagged jets.

Variables	CRT-1b	CRT-2b
$E_{\mathrm{T}}^{\mathrm{miss}}$trigger	✓	
baseline ℓ	1	
p_T^{ℓ}	< 20 GeV	
$\mathrm{N}_{\mathrm{jets}}$	≥ 4	
$p_{\mathrm{T}}^{j_2}$	> 80 GeV	
$p_{\mathrm{T}}^{j_4}$	> 40 GeV	
$\mathrm{N}_{\mathrm{DNNFCtop80}}$	≥ 1	
$m_{\mathrm{T}}\left(\ell, E_{\mathrm{T}}^{\mathrm{miss}}\right)$	< 120 GeV	
Object-based $E_{\mathrm{T}}^{\mathrm{miss}}$ sig.	> 12	
$\Delta R\left(b_1, b_2\right)$	-	> 1.4
$\mathrm{N}_{b\text{-jet}}$	1	≥ 2

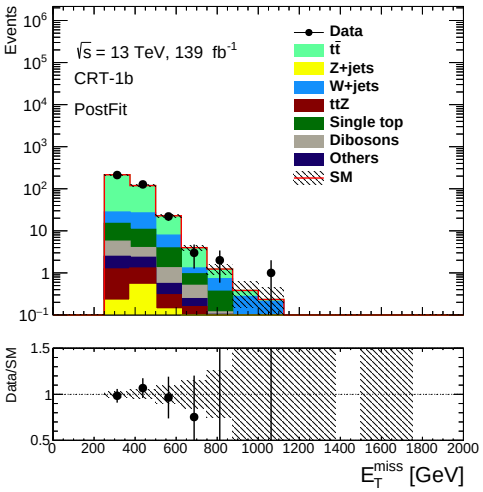

(a) $E_{\mathrm{T}}^{\mathrm{miss}}$

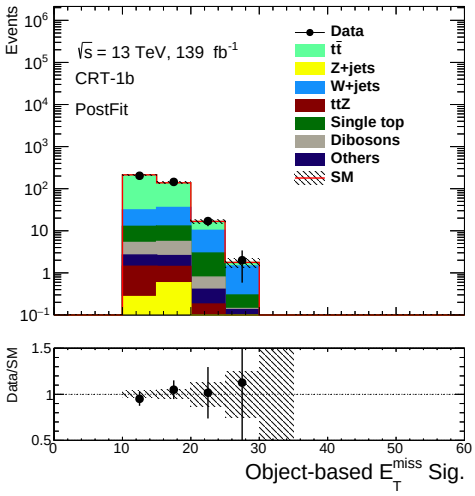

(b) Object-based $E_{\mathrm{T}}^{\mathrm{miss}}$ sig.

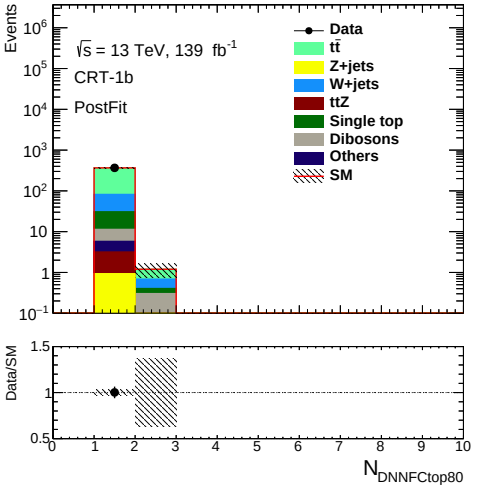

(c) $\mathrm{N}_{\mathrm{DNNFCtop80}}$

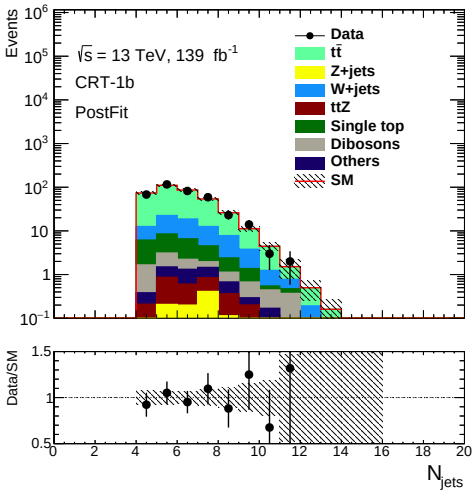

(d) $\mathrm{N}_{\mathrm{jets}}$

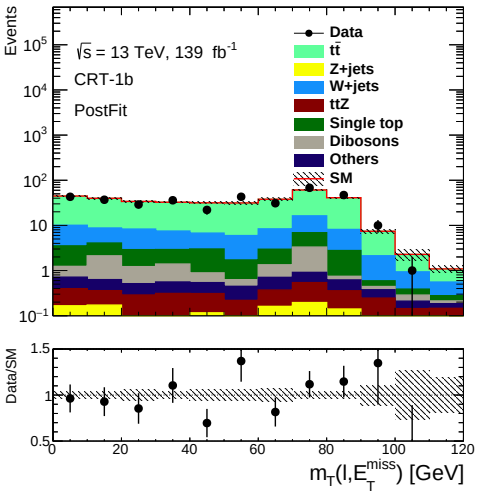

(e) $m_{\mathrm{T}}\left(\ell, E_{\mathrm{T}}^{\mathrm{miss}}\right)$

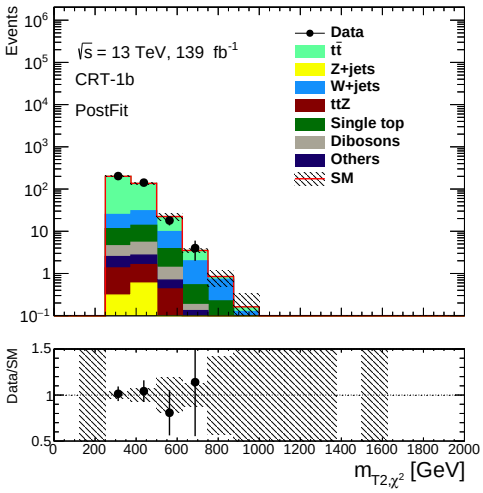

(f) m_{T2,χ^2}

Figure 51: Post-fit plots for the $\mathrm{t\bar{t}}$ control region with one b-tagged jet. μ_Z = 0.93 $\pm$ 0.12, $\mu_{\mathrm{t\bar{t}Z}}$ = 0.77 $\pm$ 0.22, and $\mu_{\mathrm{t\bar{t}}}$ = 0.83 $\pm$ 0.04 are applied to Z+jets, $\mathrm{t\bar{t}}Z$, and $\mathrm{t\bar{t}}$, respectively. The shaded area in the lower panel shows total uncertainties including systematic and statistical uncertainties.

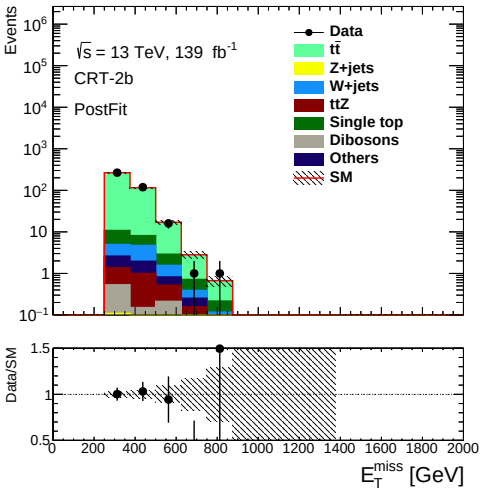

(a) $E_{\mathrm{T}}^{\mathrm{miss}}$

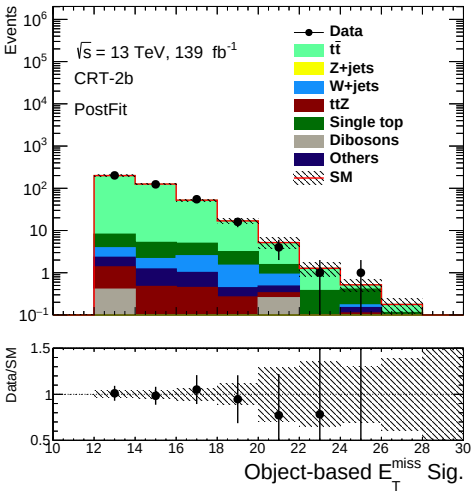

(b) Object-based $E_{\mathrm{T}}^{\mathrm{miss}}$ sig.

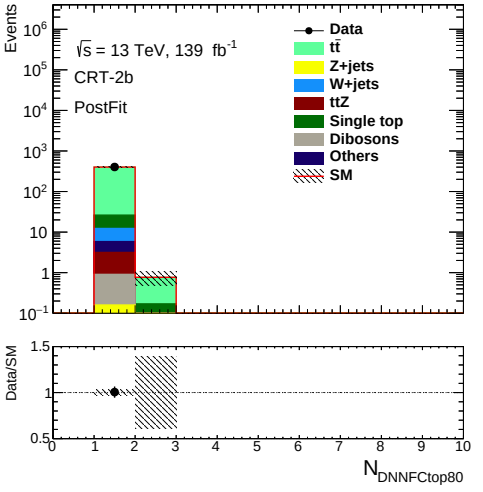

(c) $\mathrm{N}_{\mathrm{DNNFCtop80}}$

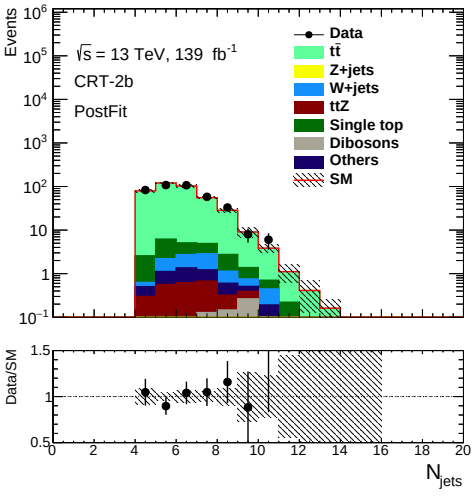

(d) $\mathrm{N}_{\mathrm{jets}}$

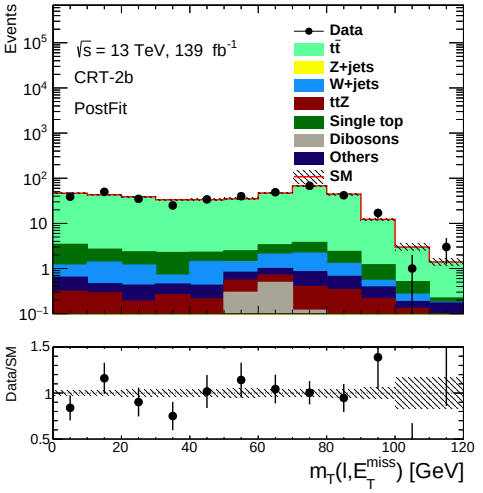

(e) $m_{\mathrm{T}}\left(\ell, E_{\mathrm{T}}^{\mathrm{miss}}\right)$

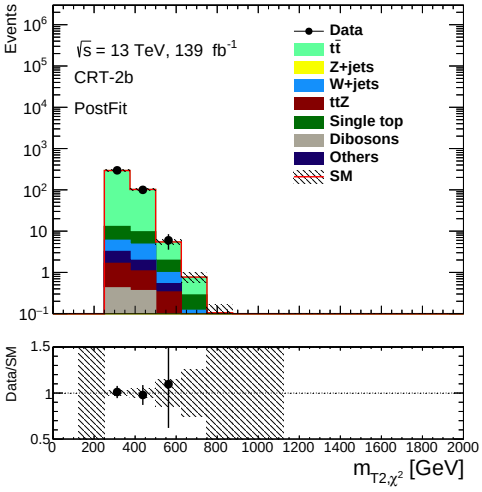

(f) m_{T2,χ^2}

Figure 52: Post-fit plots for the $\mathrm{t\bar{t}}$ control region with equal to or more than two b-tagged jet. $\mu_Z = 0.93 \pm 0.12$, $\mu_{\mathrm{t\bar{t}Z}} = 0.77 \pm 0.22$, and $\mu_{\mathrm{t\bar{t}}} = 0.83 \pm 0.04$ are applied to Z+jets, $\mathrm{t\bar{t}Z}$, and $\mathrm{t\bar{t}}$, respectively. The shaded area in the lower panel shows total uncertainties including systematic and statistical uncertainties.

Table 20: Definitions of $t\bar{t}Z$ validation region.

Variables	VRttZ
single lepton trigger	✓
signal ℓ	2, same flavor / opposite sign
additional baseline ℓ	0
Leading p_{T}^{ℓ}	> 27 GeV
Subleading p_{T}^{ℓ}	> 20 GeV
$m(\ell,\ell)$	[81,101] GeV
$\min \left\lvert \Delta\phi \left(\mathrm{jet}^{1-4}, E_{\mathrm{T}}^{\mathrm{miss}} \right) \right\rvert$	> 0.4
$E_{\mathrm{T}}^{\mathrm{miss}}$	< 50 GeV
$E_{\mathrm{T}}^{\mathrm{miss}'}$	> 150 GeV
$\mathrm{N}_{\mathrm{jets}}$	≥ 4
$p_{\mathrm{T}}^{j_2}$	> 80 GeV
$p_{\mathrm{T}}^{j_4}$	> 40 GeV
$\mathrm{N}_{b\text{-jet}}$	≥ 1
$\mathrm{N}_{\mathrm{DNNFCtop80}}$	≥ 1
Object-based $E_{\mathrm{T}}^{\mathrm{miss}'}$ sig.	> 5
$\Delta R\,(b_1, b_2)$	> 1.4

b-tagged jets ($N_{b\text{-jet}}$) is the key selection for the orthogonality with CRZ and increasing the purity of $t\bar{t}Z$. The $t\bar{t}Z$ validation region is still largely contaminated by the Z+jets. Figure 53 shows the post-fit plots of the variables. No significant deviation is found but the validation in the VRttZ is significantly affected by the Z+jet events.

6.4.2.2 Z+jets validation region (VRZ)

The two Z+jets validation regions are defined in Table 21 since the statistics is allowed to validate two different topologies of SRA and SRB. For the SRA, the validation region, VRZA, is designed in the zero top-tagged large-R jet, but the p_{T} and mass of large-R jet are required to mimic the boosted topologies. The VRZB for the SRB is defined in the inversion of $\Delta R\,(b_1, b_2)$ and largely contaminated by $t\bar{t}$. The validation in the VRZB is also affected by the $t\bar{t}$ events. Figures 54 and 55 show the post-fit plots of the variables. No significant deviation is found in the both regions.

6.4.2.3 $t\bar{t}$ validation region (VRT)

The $t\bar{t}$ validation region is defined in a region with zero lepton events. The $E_{\mathrm{T}}^{\mathrm{miss}}$ trigger is used. The inversion of object-based $E_{\mathrm{T}}^{\mathrm{miss}}$ significance is chosen for the high

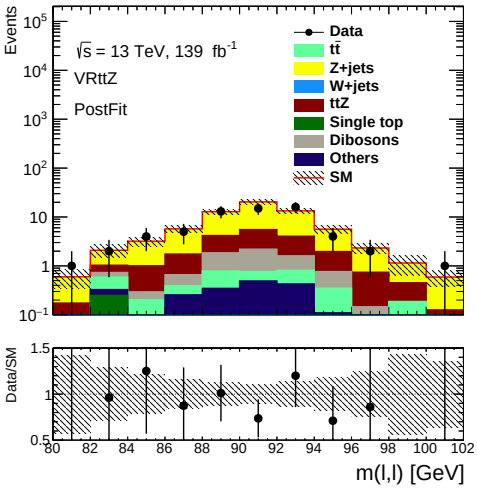

(a) $m(\ell,\ell)$

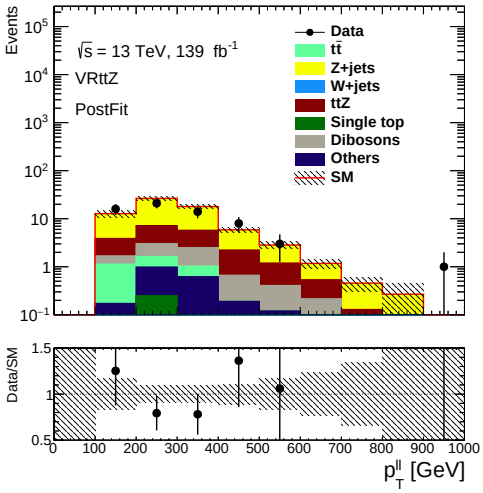

(b) $p_{\mathrm{T}}^{\ell\ell}$

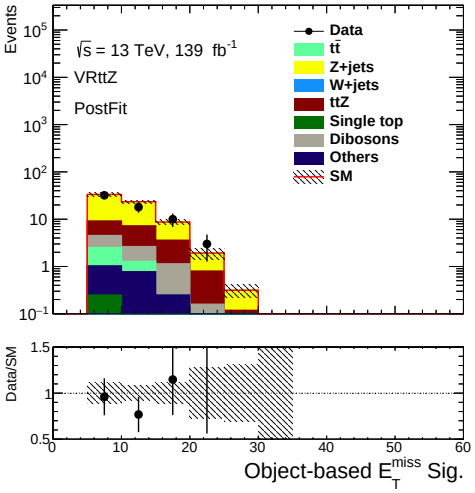

(c) Object-based $E_{\mathrm{T}}^{\mathrm{miss}}$ sig.

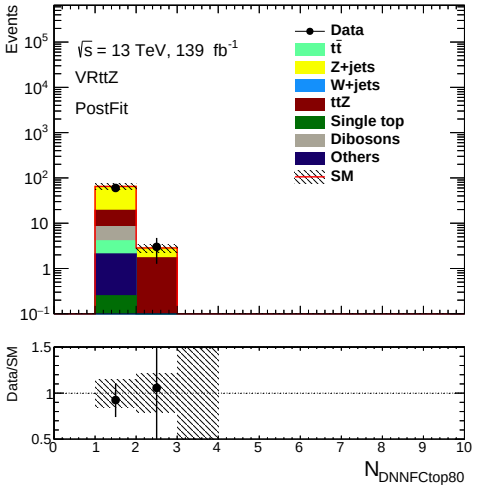

(d) $\mathrm{N}_{\mathrm{DNNFCtop80}}$

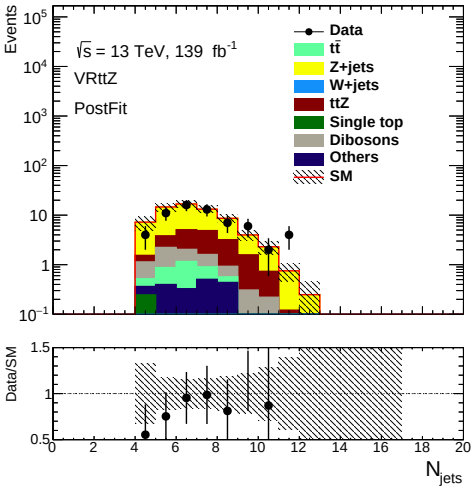

(e) $\mathrm{N}_{\mathrm{jets}}$

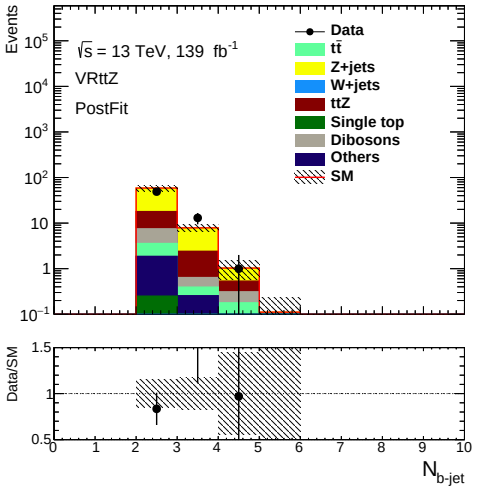

(f) $\mathrm{N}_{b\text{-jet}}$

Figure 53: Post-fit plots for the $\mathrm{t\bar{t}Z}$ validation region. $\mu_Z = 0.93 \pm 0.12$, $\mu_{\mathrm{t\bar{t}Z}} = 0.77 \pm 0.22$, and $\mu_{\mathrm{t\bar{t}}} = 0.83 \pm 0.04$ are applied to Z+jets, $\mathrm{t\bar{t}Z}$, and $\mathrm{t\bar{t}}$, respectively. The shaded area in the lower panel shows total uncertainties including systematic and statistical uncertainties.

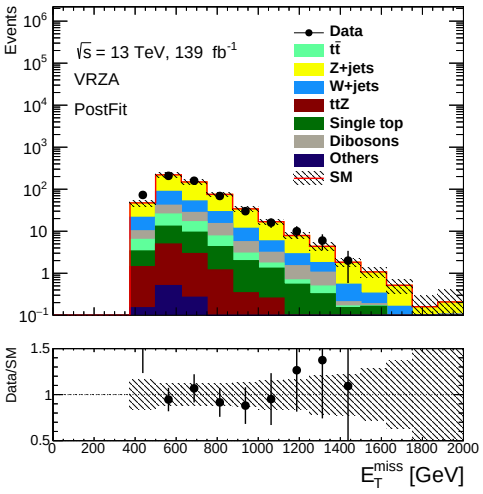

(a) $E_{\mathrm{T}}^{\mathrm{miss}}$

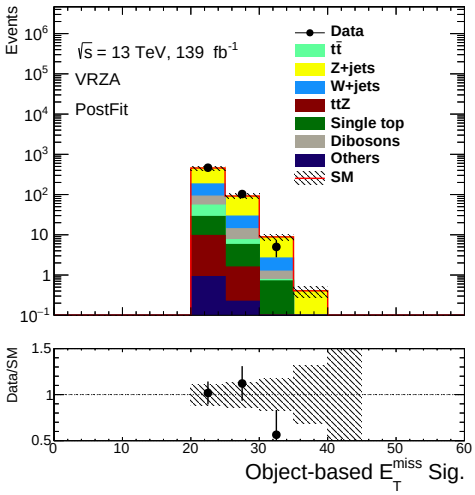

(b) Object-based $E_{\mathrm{T}}^{\mathrm{miss}}$ sig.

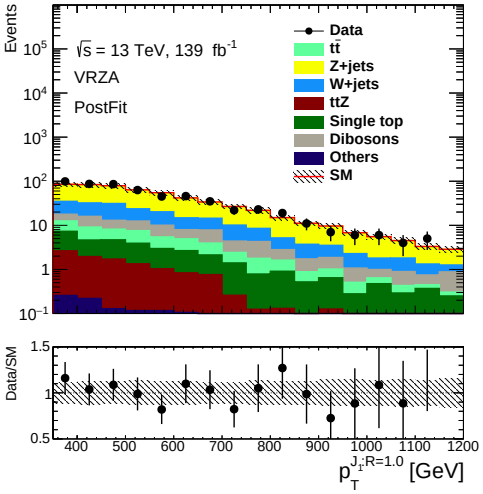

(c) Leading large-R jet p_{T}

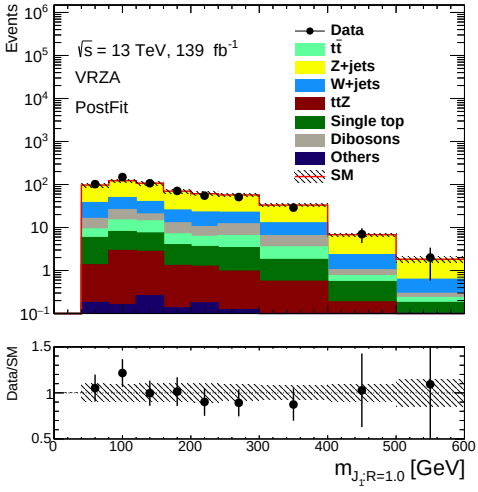

(d) Leading large-R jet mass

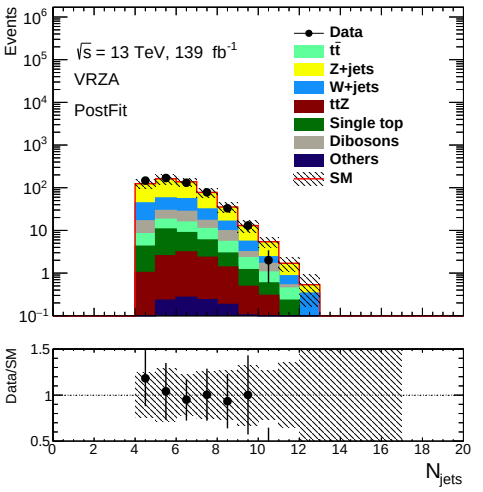

(e) $\mathrm{N}_{\mathrm{jets}}$

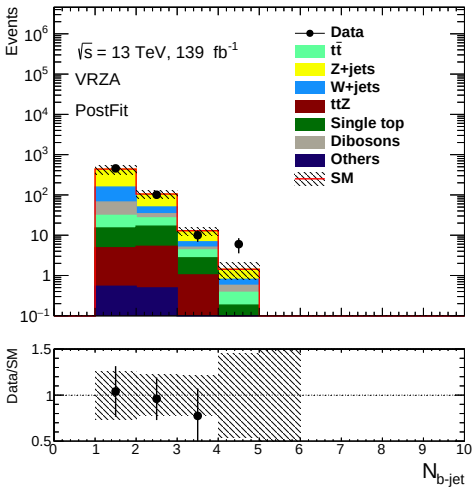

(f) $\mathrm{N}_{b\text{-jet}}$

Figure 54: Post-fit plots for the Z+jets validation region, corresponding to signal region A. $\mu_Z = 0.93 \pm 0.12$, $\mu_{\mathrm{t\bar{t}}Z} = 0.77 \pm 0.22$, and $\mu_{\mathrm{t\bar{t}}} = 0.83 \pm 0.04$ are applied to Z+jets, $\mathrm{t\bar{t}}Z$, and $\mathrm{t\bar{t}}$, respectively. The shaded area in the lower panel shows total uncertainties including systematic and statistical uncertainties.

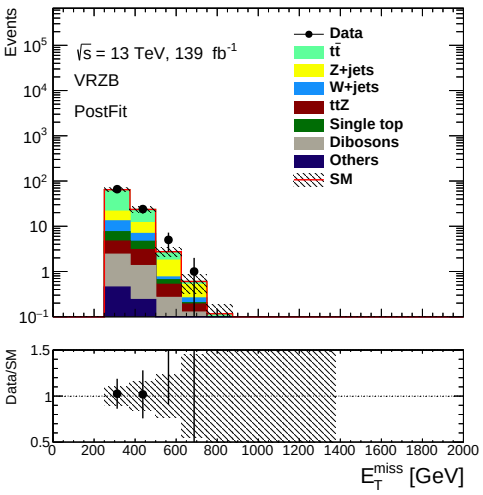

(a) $E_{\mathrm{T}}^{\mathrm{miss}}$

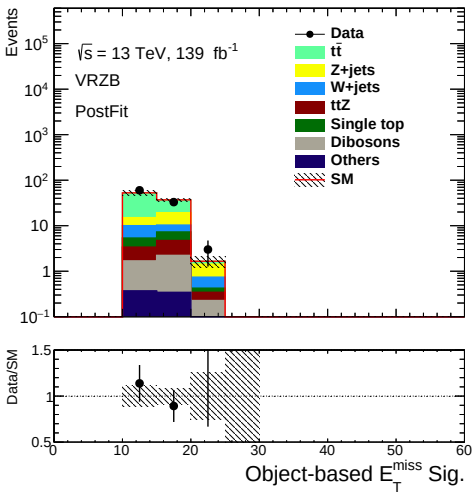

(b) Object-based $E_{\mathrm{T}}^{\mathrm{miss}}$ sig.

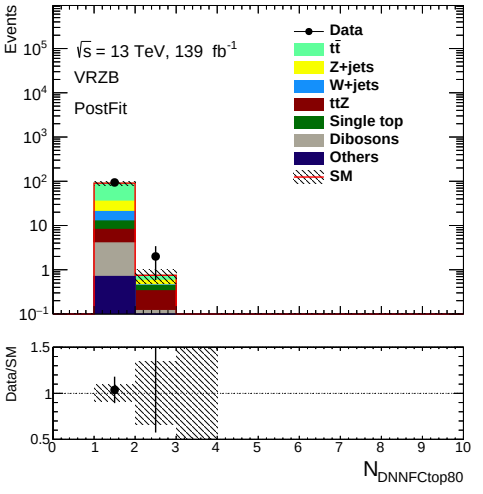

(c) $\mathrm{N}_{\mathrm{DNNFCtop80}}$

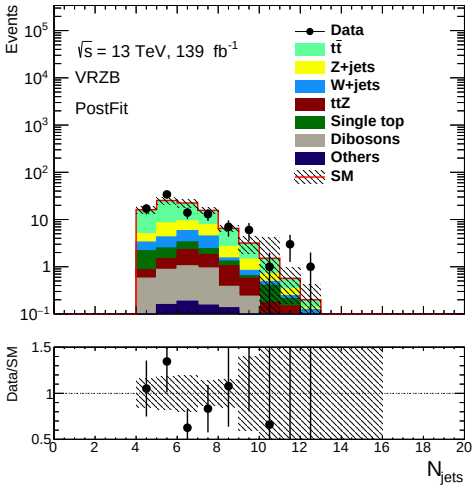

(d) $\mathrm{N}_{\mathrm{jets}}$

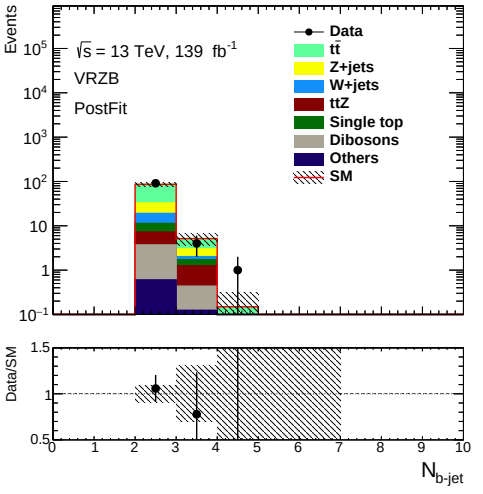

(e) $\mathrm{N}_{b\text{-jet}}$

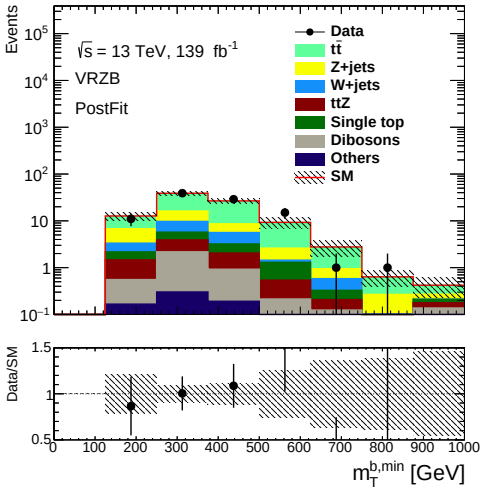

(f) $m_{\mathrm{T}}^{b,\mathrm{min}}$

Figure 55: Post-fit plots for the Z+jets validation region, corresponding to signal region B. $\mu_Z = 0.93 \pm 0.12$, $\mu_{\mathrm{t\bar{t}}Z} = 0.77 \pm 0.22$, and $\mu_{\mathrm{t\bar{t}}} = 0.83 \pm 0.04$ are applied to Z+jets, $\mathrm{t\bar{t}}Z$, and $\mathrm{t\bar{t}}$, respectively. The shaded area in the lower panel shows total uncertainties including systematic and statistical uncertainties.

Table 21: Definitions of Z+jets validation regions with zero lepton. VRZA and VRZB are the validation regions for SRA and SRB, respectively.

Variables	VRZA	VRZB
$E_{\mathrm{T}}^{\mathrm{miss}}$trigger	✓	
baseline ℓ	0	
$\mathrm{N}_{\mathrm{jets}}$	≥ 4	
$p_{\mathrm{T}}^{j_2}$	> 80 GeV	
$p_{\mathrm{T}}^{j_4}$	> 40 GeV	
$\min \left\lvert \Delta\phi \left(\mathrm{jet}^{1-4}, E_{\mathrm{T}}^{\mathrm{miss}} \right) \right\rvert$	> 0.4	
τ veto	✓	
m_{T2,χ^2}	> 450 GeV	< 450 GeV
$\mathrm{N}_{\mathrm{DNNFCtop80}}$	0	≥ 1
Object-based $E_{\mathrm{T}}^{\mathrm{miss}}$ sig.	> 20	> 12
$\Delta R\,(b_1, b_2)$	-	< 1.4
$\mathrm{N}_{b\text{-jet}}$	≥ 1	≥ 2
$m_{\mathrm{T}}^{b,\mathrm{min}}$	-	> 200 GeV
Leading Large-R jet p_{T}	> 350 GeV	-
Leading Large-R jet mass	> 40 GeV	-

purity of $\mathrm{t\bar{t}}$ events. Since the lower object-based $E_{\mathrm{T}}^{\mathrm{miss}}$ significance cut is used in the SRB, the selection of object-based $E_{\mathrm{T}}^{\mathrm{miss}}$ significance is between 5 and 12. The $\mathrm{N}_{\mathrm{DNNFCtop80}}$ and $\mathrm{N}_{b\text{-jet}}$ are required to be larger than or equal to one. Figure 56 shows the post-fit plots for the variables. No significant deviation is found.

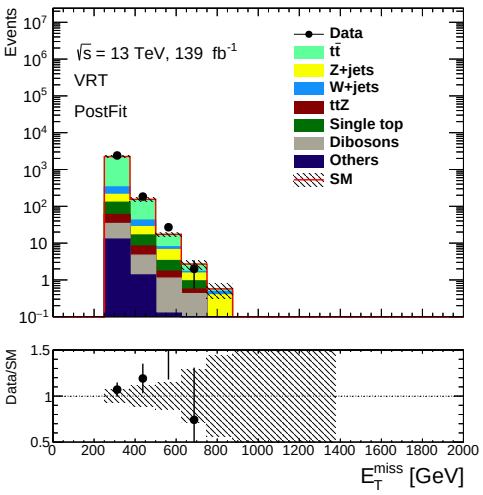

(a) $E_{\mathrm{T}}^{\mathrm{miss}}$

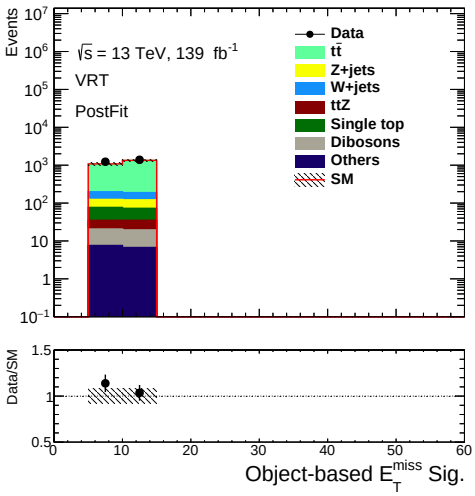

(b) Object-based $E_{\mathrm{T}}^{\mathrm{miss}}$ sig.

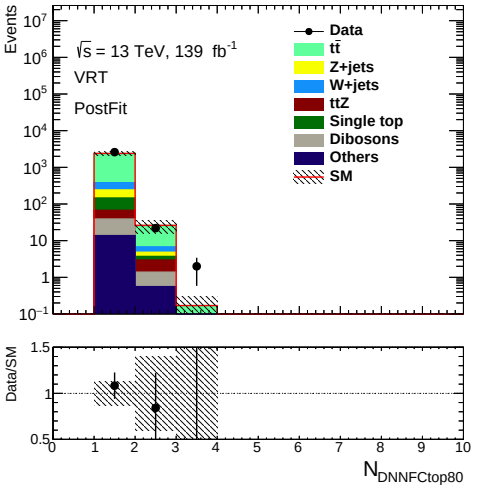

(c) $\mathrm{N_{DNNFCtop80}}$

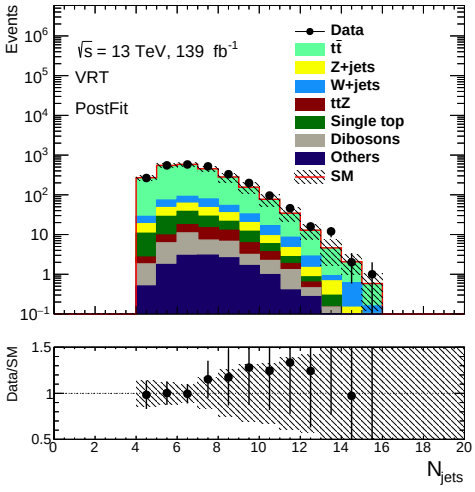

(d) $\mathrm{N_{jets}}$

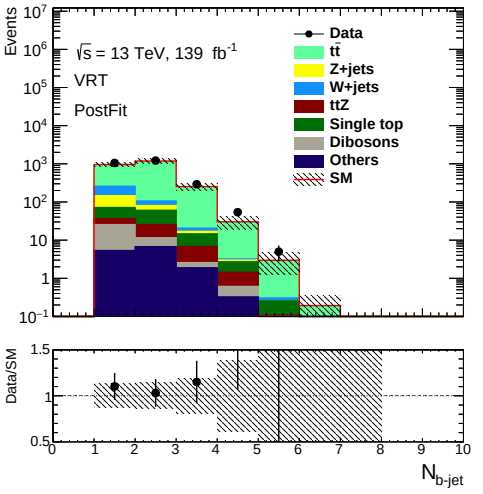

(e) $\mathrm{N}_{b\text{-jet}}$

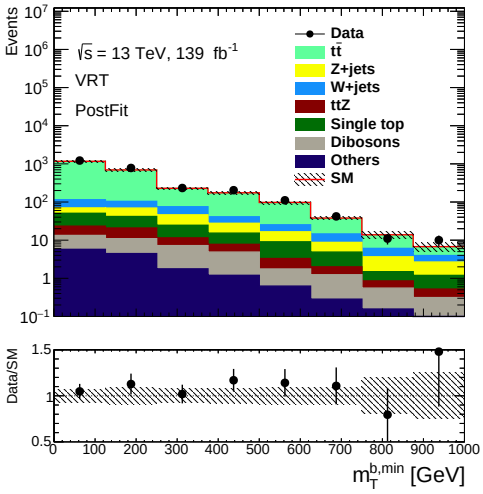

(f) $m_{\mathrm{T}}^{b,\mathrm{min}}$

Figure 56: Post-fit plots for the $\mathrm{t\bar{t}}$ validation region. $\mu_Z = 0.93 \pm 0.12$, $\mu_{\mathrm{t\bar{t}}Z} = 0.77 \pm 0.22$, and $\mu_{\mathrm{t\bar{t}}} = 0.83 \pm 0.04$ are applied to Z+jets, $\mathrm{t\bar{t}}Z$, and $\mathrm{t\bar{t}}$, respectively. The shaded area in the lower panel shows total uncertainties including systematic and statistical uncertainties.

Table 22: Definitions of $t\bar{t}$ validation region.

Variable	VRT
$E_{\mathrm{T}}^{\mathrm{miss}}$trigger	✓
baseline ℓ	0
$\mathrm{N}_{\mathrm{jets}}$	≥ 4
$p_{\mathrm{T}}^{j_2}$	> 80 GeV
$p_{\mathrm{T}}^{j_4}$	> 40 GeV
$\min \left\lvert \Delta\phi \left(\mathrm{jet}^{1-4}, E_{\mathrm{T}}^{\mathrm{miss}} \right) \right\rvert$	> 0.4
τ veto	✓
m_{T2,χ^2}	-
$\mathrm{N}_{\mathrm{DNNFCtop80}}$	≥ 1
Object-based $E_{\mathrm{T}}^{\mathrm{miss}}$ sig.	$[5, 12]$
$\mathrm{N}_{b\text{-jet}}$	≥ 1

6.5 Systematic uncertainties

Experimental uncertainties are those originating from the experiment, for example, the calibration of each physical object. Theoretical uncertainties are from the uncertainties of the simulation and the calculation, for example, the choice of the modelling, and cross section of signal and background processes.

6.5.1 Experimental uncertainties

- **Jet energy scale (JES) for small-R jets**

The uncertainties of jet energy scale originate from the jet energy calibration explained in Chapter 4.2.5 [84]. The uncertainties are derived as a function of p_{T} and η. Total 77 components of uncertainties are extracted from the 4 in-situ method, pile-up, jet-flavor, punch-through, fast simulation and single-particle response for the jets with p_{T} larger than 2 TeV [117]. The pile-up uncertainties originate from the MC mismodelling of N_{PV}, μ, ρ, and the dependence of residual p_{T}. The jet flavor accounts for the difference due to jets originating from light quarks, gluons, and b quarks. Strongly reduced scenario of the uncertainties is used, which reduces the full 77 nuisance parameters (NP) into 7 NPs only via an eigenvector decomposition [84, 118]. The uncertainties of the total SM predictions are 8$\sim$52% for the signal regions.

- **Jet energy resolution (JER) for small-R jets**

The jet energy resolution is parametrized by using the function of the relative

energy resolution in the calorimeters [117]. The function with p_{T} dependence is expressed as:

$$\frac{\sigma_{p_{\mathrm{T}}}}{p_{\mathrm{T}}} = \frac{N}{p_{\mathrm{T}}} \oplus \frac{S}{\sqrt{p_{\mathrm{T}}}} \oplus C, \tag{47}$$

where the first term in the right-hand side is the noise term, the second term is the stochastic term, and C is the constant term. JER measurement is derived by the dijet balance method [117]. The asymmetry of two leading jets forms the Gaussian distribution with the standard deviation as the JER. The noise term is derived by the random cone method to measure the fluctuation due to the pile-up. The JER uncertainties are obtained by the fit to JER measurement with the template of Eq. (47). The nuisance parameters are also reduced via the eigenvector decomposition. The uncertainties of the total SM predictions are 3∼36% for the signal regions.

- **JES for large-R jets and DNN top tagger uncertainties (Large-R jet + DNN)**

The jet energy scale for the large-R jets and the uncertainties of scale factors of DNN top taggers are already explained in Chapter 5. The propagated JES uncertainties of large-R jets after the DNN taggers are correlated with the original JES uncertainties for the large-R jets. The uncertainties of the total SM predictions are 14∼88% for the signal regions.

- **Jet vertex tagger**

The uncertainties are estimated from the calibration of the mis-tagged efficiencies on the pile-up jets with $Z \to \mu\mu$+jets events [81]. The difference of mis-tagged efficiencies between data and MC samples and the difference of hard-scatter efficiencies between two different simulation generators are included. The uncertainties of the total SM predictions are 5∼21% for the signal regions.

- ***b*-tagging**

Scale factors of the efficiencies between data and MC samples are applied to correct the efficiency of the b-tagging on the small-R jets [90]. The uncertainties of scale factors include the modelling uncertainties, JES uncertainties and other sources. The final nuisance parameters are reduced via eigenvector decomposition. The uncertainties of the total SM predictions are 3∼8% for the signal regions.

- $E_{\mathrm{T}}^{\mathrm{miss}}$ **soft-term resolution and scale**

The $E_{\mathrm{T}}^{\mathrm{miss}}$ uncertainty is derived from the hard components and soft term in Eq. (27) [91]. For the hard components, their uncertainties are propagated to the $E_{\mathrm{T}}^{\mathrm{miss}}$ uncertainty directly. On the other hand, the uncertainties of the soft term include

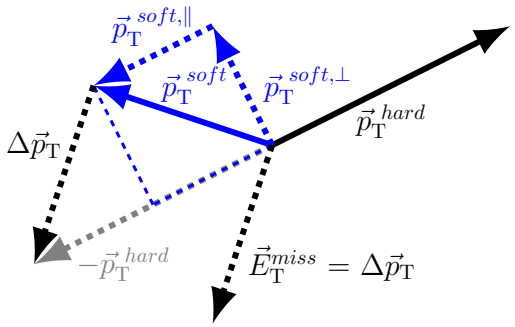

Figure 57: Projection of the soft term vector with respect to the vector sum of the hard terms [91].

the parallel scale, the parallel resolution and the transverse resolution. Figure 57 shows the definition of direction of the soft term [91]. The reference direction is defined in the direction of the vector sum of p_{T} of hard components. The data/MC difference in the $Z \to \ell\ell$ events are used as the uncertainties of the soft term. The uncertainties of the total SM predictions are 1∼20% for the signal regions. The $E_{\mathrm{T}}^{\mathrm{miss}}$ trigger uncertainties can be ignored due to high $E_{\mathrm{T}}^{\mathrm{miss}}$ requirement in the offline selection, where the efficiencies of $E_{\mathrm{T}}^{\mathrm{miss}}$ trigger are higher than 99%.

- **Lepton reconstruction and identification**

The electrons and muons are calibrated for the energy scale, energy resolution and efficiencies [78, 79]. The uncertainties are applied to backgrounds. The scale factors of lepton trigger and trigger uncertainties are also applied due to the control regions with leptons.

- **Pile-up reweighting**

The pile-up reweighting is the correction of an average number of interactions per bunch crossing $\langle\mu\rangle$ on the MC samples [119]. The $\langle\mu\rangle$ in the MC sample is rescaled by 1.03 to match the data. The uncertainties are accounted for the shifts in the nominal scale factor by changing the scale factors from 1.03 to 1.0 and 1.18.

6.5.2 Theoretical uncertainties

- ***Z/W*+jet modelling**

The Z/W+jet samples with Sherpa event generator are produced with a simplified scale prescription [120]. The matrix element matching (CKKW) provides the calculation for the overlap between jets from the matrix element and the parton shower. The nominal value is 20 GeV and varied to 15 GeV and 30 GeV. The renormalization

scale (renorm) for the running strong coupling constant, the factorization scale (fac) for the parton density functions, and the resummation scale(qsf) for the resummation of soft gluon emission are varied to 2 and 1/2 with respect to the nominal value. The uncertainties of the total SM predictions are 3∼20% for the signal regions. A 30% uncertainty is assigned to the extrapolation between the control regions and signal regions to account for the uncertainty associated with Z/W+heavy flavor jet modeling because the extrapolation relies on the number of *b*-tagged jets.

- $t\bar{t}$ **modelling**

The $t\bar{t}$ modelling can be referred to Chapter 5.4.3. The uncertainties of the total SM predictions are 2∼35% for the signal regions.

- **Single top modelling**

The single top production is dominated by the Wt process in the signal and control regions. There is an issue on the diagram of the NLO calculation. When the invariant mass of a *W* and an extra *b* at NLO is close to top mass, the interference to the $t\bar{t}$ events becomes significant. There are two methods, a diagram removal (DR) and diagram subtraction (DS) [121], to remove the effect on cross-section calculation. The DR is used as the baseline method for the simulation. The DS is used as an alternative sample for the estimation of the correction on the interference. The difference between DR and DS is considered as a single top modelling uncertainty. The uncertainties of the total SM predictions are 1∼17% for the signal regions.

- $t\bar{t}Z$ **modelling**

The 6 point variations in the factorization scale and renormalization scale and the Var3c envelope [48] are used for the evaluation of the parton shower and radiation uncertainties. The envelope of all difference is used in the fit. The uncertainties of the total SM predictions are 1∼19% for signal regions.

- **Signal uncertainties**

The variation of factorization scale for the PDF, renormalization scale for the strong coupling, merging scale between the matrix element and parton shower, and Var3c envelop are evaluated for the uncertainties. The uncertainties of signal yields are 5% for the SRA and 12% for the SRB.

- **Monte Carlo statistics**

The statistics of simulation events can affect the results significantly due to the limited computing power in some regions. The uncertainties of the total SM predictions are 26∼49% for the TT regions and 19∼30% for the other regions.

6.6 Statistical model

With the region definitions, event yields of signals and the individual background can be estimated. The statistical model of the analysis is built by using HistFactory [122]. The tool is developed based on the RooStats [123] and RooFit [124]. The minimization of the minus log-likelihood is performed by MINUIT, which is implemented in ROOT. In this analysis, each region is described as a single channel. The probability density function (PDF) in each region c (channel) is a Poisson distribution with expected events ν_c and observed events n_c, where the ν_c is described as:

$$\nu_c = \mu_{sig}\nu_c^{sig} + \sum_i \mu_{bkg,i}\nu_c^{bkg,i}, \tag{48}$$

where μ_{sig} is the signal strength, and $\mu_{bkg,i}$ is the normalization factor of a background process i. When we include the nuisance parameters and normalization factors, the likelihood template can be written into a formula as:

$$\boldsymbol{L}(\boldsymbol{n}, \boldsymbol{\theta}^0 | \mu_{sig}, \boldsymbol{\mu}_{bkg}, \boldsymbol{\theta}) = \prod_{c \in channels} \text{Pois}(n_c | \lambda_c(\mu_{sig}, \boldsymbol{\mu}_{bkg}, \boldsymbol{\alpha})) \cdot \prod_p G(\theta_p^0 | \theta_p), \tag{49}$$

where p denotes parameters, θ_p denotes nuisance parameters associated to the systematics and θ_p^0 is an auxiliary measurement used to constrain θ_p. The expectation value λ_c of the Poisson distribution is described as a function of signal strength, normalization factors of background processes and nuisance parameters. The $G(\theta_p^0|\theta_p)$ is the constraint term for other nuisance parameters by using the Gaussian function with a standard deviation $\Delta\theta = 1$.

6.6.1 Fit strategy

All the fit strategies are provided in the HistFitter framework [125]. Figure 58 summaries the procedures to get the upper limits on the cross section for the stop signal. Three types of fitting are used for different purposes. A background-only fit is performed for the validation of background estimations and unblinded results in the SRs. A model-dependent fit and a model-independent fit are used to evaluate the upper limits on the cross section if there is no significant excess in the unblinded results.

- **Background-only fit**

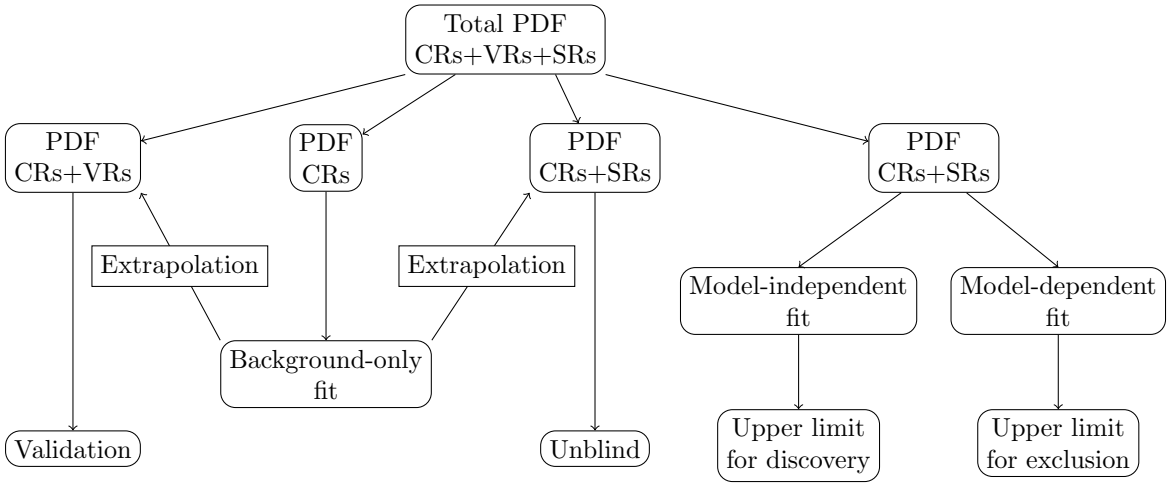

Figure 58: Overviews of the fit strategy for background estimations and the upper limits of the signals.

The dominant backgrounds in the SRs and VRs are estimated by the background-only fit in all the CRs. Only the likelihood models of all the CRs are included in the statistical model. The normalization factor of each background is set as a free parameter in the fit. The simultaneous fit among all the CRs is performed to take into account the contamination of other backgrounds in a certain CR which aims for high purity of a specific background sample.

The fitted normalization factors are applied to the VRs to check the fit results. If there is no significant mismodelling in the VRs, the fit results are considered to be validated, and the normalization factors are applied to the backgrounds in the SRs. The same fitted normalization factor of each dominant background is applied to the corresponding background obtained from MC samples in SRs.

The minor backgrounds in the SRs are estimated by using MC predictions, and the impacts due to constraints on the backgrounds in CRs are not considered since they are minor.

- **Model-dependent signal fit**

The signal model with the signal strength μ_{sig} and background models with normalization factors are included in the model-dependent signal fit. In case of no excess found in SRs, the model-dependent fit is used for the exclusion of a given signal model. In contrast, if the excess is found in SRs, the model-dependent fit can be used for measurement of the signal strength. The fit is performed in all the SRs and CRs simultaneously. The signal contamination in the CRs can be taken into account. Since

the multiple SRs are statistically independent, the combination of the SRs in the fit should provide a better expected exclusion sensitivity.

- **Model-independent signal fit**

For the search for new physics, upper limits of event yields or cross sections of any signal models are set in each SR. The model-independent fit is performed in only one signal region with all the CRs. In case of model-dependent signal fit, the signal can potentially spread across the multiple SRs. This is not considered for the case of model-independence. A dummy signal model is used in the fit to estimate the upper limit of the signal cross section (see Section 6.7.4). In this fit, no signal contamination in the CRs is assumed. The background-only hypothesis test is also performed for quantifying the significance of any observed excess of events in each SR.

6.6.2 Statistical test

For the search for new physics, we need to define what is known and what we want to know. The Standard Model processes are defined as a null hypothesis, H_0, and described as a background model. The new physics is defined as an alternative hypothesis, H_1, and described as a signal model. To quantify the agreement between data and the background hypothesis, we calculate the p-value based on the hypotheses to estimate the incompatibility of the observation in a certain region. A p-value is usually converted into a significance Z. For discovery of new physics, Z is required to be at least 5, which means $p = 2.87 \times 10^{-7}$. For an exclusion limit, $p = 0.05$ is often used, which is equivalent to Z = 1.64 for one sided test.

The parameter of interest, μ_{sig}, provides the key information for both hypotheses. The profiled likelihood ratio is usually used for quantifying the observation, and defined as:

$$\lambda(\mu_{sig}) = \frac{\boldsymbol{L}(\mu_{sig}, \hat{\hat{\boldsymbol{\theta}}})}{\boldsymbol{L}(\hat{\mu}_{sig}, \hat{\boldsymbol{\theta}})}, \tag{50}$$

where the quantity $\hat{\hat{\boldsymbol{\theta}}}$ denotes the value of nuisance parameter $\boldsymbol{\theta}$ with a given μ_{sig}, and the $\hat{\mu}$ and the $\hat{\boldsymbol{\theta}}$ are the maximum likelihood (ML) estimators, which maximize the likelihood function. The profiled likelihood ratio is a ratio of the conditional maximum likelihood to the maximum likelihood as a function of μ_{sig} with a value between 0 and 1. If the $\lambda(\mu_{sig})$ is close to 1, it implies that the data is consistent with signal plus background model with the given μ_{sig}. A natural logarithmic form is

usually used as a test statistic,

$$q_{\mu_{sig}} = -2\ln(\lambda(\mu_{sig})). \tag{51}$$

To quantify the observation in both null hypothesis and alternative hypothesis, the p-value from the probability density function of the test statistic is required. From Wald's work [126], the test statistic with a single parameter can be expressed as:

$$q_{\mu_{sig}} = -2\ln(\lambda(\mu_{sig})) \ = \frac{(\mu sig - \hat{\mu}_{sig})^2}{\sigma^2} + O(1/\sqrt{N}), \tag{52}$$

where the $\hat{\mu}_{sig}$ is a Gaussian distribution with a mean $\mu^{'}_{sig}$ and a standard deviation σ, and N denotes the data sample size. The second term can be ignored if the data sample size is large. Then, the PDF of the test statistic can be expressed as a non-central χ^2 function:

$$f(q_{\mu_{sig}};\Lambda) = \frac{1}{2\sqrt{q_{\mu_{sig}}}}\frac{1}{\sqrt{2\pi}}\times \\ \left[exp\left(-\frac{1}{2}(\sqrt{q_{\mu_{sig}}} + \sqrt{\Lambda})^2\right) + exp\left(-\frac{1}{2}(\sqrt{q_{\mu_{sig}}} - \sqrt{\Lambda})^2\right)\right], \tag{53}$$

where the non-centrality parameter Λ is defined as:

$$\Lambda = \frac{(\mu_{sig} - \mu^{'}_{sig})^2}{\sigma^2}. \tag{54}$$

For the case of $\mu_{sig} = \mu^{'}_{sig}$, the distribution becomes a χ^2 distribution and depends only on $q_{\mu_{sig}}$.

For the unknown Λ, Asimov data set [127] is defined for both signal regions and control regions in the assumption of the partial derivatives of likelihood function with respect to the nuisance parameters equal to zero. The profiled likelihood ratio from the Asimov data set can be used for the approximation of the Λ:

$$q_{\mu_{sig},A} = -2\ln\lambda_A(\mu_{sig}) \approx \frac{(\mu_{sig} - \hat{\mu}_{sig})^2}{\sigma^2} = \Lambda. \tag{55}$$

Then, σ is obtained from this expression.

There are two test statistics used in the analysis with the approximation from the Asimov data set: discovery and upper limit. q_0 is defined for the discovery, which

rejects the null hypothesis with $\mu_{sig} = 0$. The definition is as follows:

$$q_0 = \begin{cases} \hat{\mu}_{sig}^2/\sigma^2, & \hat{\mu}_{sig} \geq 0, \\ 0, & \hat{\mu}_{sig} < 0. \end{cases} \tag{56}$$

Only the positive signal is taken into account. The downward fluctuation of data below the background-only hypothesis is assumed as the effect from the systematic uncertainties.

$\tilde{q}_{\mu_{sig}}$ is defined for the upper limit by rejecting the $\hat{\mu}_{sig} > \mu_{sig}$ and models with $\mu_{sig} \geq 0$ by requiring maximum likelihood at 0 if $\hat{\mu}_{sig} < 0$. The definition of $\tilde{q}_u$ is expressed as:

$$\tilde{q}_{\mu_{sig}} = \begin{cases} \mu_{sig}^2/\sigma^2 + 2\mu_{sig}\hat{\mu}_{sig}/\sigma^2, & \hat{\mu}_{sig} < 0, \\ (\mu_{sig} - \hat{\mu}_{sig})^2/\sigma^2, & 0 \leq \hat{\mu}_{sig} \leq \mu_{sig}, \\ 0, & \hat{\mu}_{sig} > \mu_{sig}. \end{cases} \tag{57}$$

Figure 59 shows examples of q_0 and $\tilde{q}_{\mu_{sig}}$ distributions including the signal plus

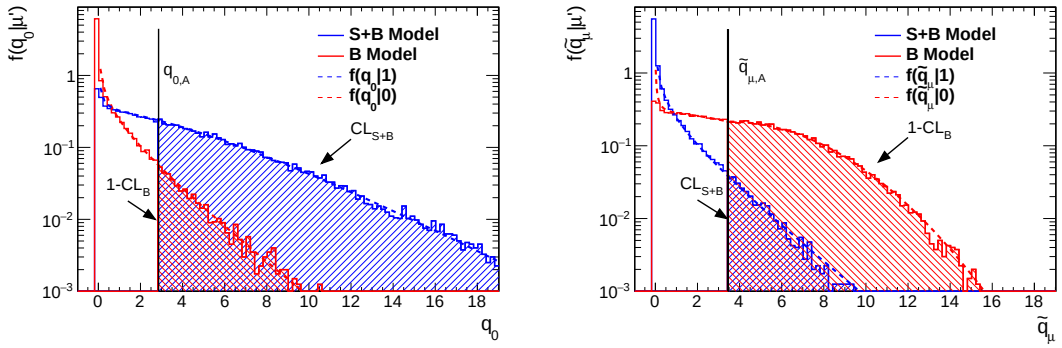

(a) (b)

Figure 59: Example of the probability density function of profiled likelihood ratio for (a) the discovery and (b) the upper limit with models background only (red) and signal plus background (blue). The black line shows the median value of $q_{0,A}$ and $\tilde{q}_{\mu,A}$ for the evaluation of p-values for the background only ($1 - \mathrm{CL_B}$) and for the signal plus background ($\mathrm{CL_{S+B}}$).

background model and background only model made by using the toy experiments generated by the Monte Carlo method, which are showed as the histograms. The approximated distributions from the Asimov data set are shown as dashed lines, which have good agreement with the distributions from the toy experiments. The p-values of the observation for both models (shaded area) are easily obtained from the non-central χ^2 function without consuming the large computing power.

The CL_S method [128] is used for the upper limit to prevent the exclusion in the alternative hypothesis with no or little sensitivity. The CL_S is defined as:

$$CL_S \equiv \frac{CL_{S+B}}{1 - CL_B}, \tag{58}$$

where the CL_{S+B} and $1 - CL_B$ can be referred in Figure 59. The one-sided p-value of the CL_S at 95% confidence level ($CL_S < 0.05$) is used to reject the alternative hypothesis.

6.7 Results

Signal regions, control regions and validation regions are defined as mentioned in the previous sections. All the experimental and theoretical systematic uncertainties are used in the statistical model of the likelihood function. Based on the fit configurations introduced in the previous section, all three types of fits have been performed.

6.7.1 Background-only fit

μ_Z, $\mu_{t\bar{t}Z}$, and $\mu_{t\bar{t}}$, which are the normalization factors of Z+jets, $t\bar{t}Z$, and $t\bar{t}$, are the floating parameters in the fit. Table 23 summaries the normalization factors of each dominated background. The statistics of data affect the uncertainties of the normalization factors in the $t\bar{t}Z$ control region since the yields are relatively low. Figure 60 summarizes the data and MC in both control regions and validation regions after the normalization factors are applied. There are no significant deviations between the data and MC predictions in all regions. The data and MC agreement in both 1b and 2b regions of $t\bar{t}$ control regions with only one normalization factor of $t\bar{t}$ indicates the normalization is not affected by the b-tagging.

Table 23: Floating parameters for the background-only fit with the initial value equal to 1 and final values.

Floating Parameter	Final Value
μ_Z	0.93 ± 0.12
$\mu_{t\bar{t}Z}$	0.77 ± 0.22
$\mu_{t\bar{t}}$	0.83 ± 0.04

The breakdown of dominant systematic uncertainties in background estimations is shown in Table 24 in the percentage of total systematic uncertainties. For

Table 24: Systematic uncertainties in percentage of the total SM predictions larger than 1 % within SRA and SRB. The floating normalization factors, $\mu_{t\bar{t}}$, $\mu_{t\bar{t}Z}$, and μ_Z are determined by simultaneous fit to all the control regions with data. The uncertainties are estimated by simultaneous fit to all the control regions and each signal region with normalization factors. Single top modelling is negligible after the fit.

	SRATT		**SRATW**		**SRAT0**		**SRBTT**		**SRBTW**		**SRBT0**	
$N_{b\text{-jet}}$	≥ 2	1	≥ 2	1	≥ 2	1	≥ 2	1	≥ 2	1	≥ 2	1
Total syst. unc.	50	40	21	21	21	29	28	41	23	18	21	16
$t\bar{t}$ modelling	12	6	12	3	2	1	12	27	11	10	5	4
$t\bar{t}Z$ modelling	15	7	5	1	8	3	5	2	3	<1	2	<1
Z modelling	4	6	4	7	7	10	1	1	1	1	4	6
W modelling	3	1	4	2	5	4	1	3	2	6	1	5
$\mu_{t\bar{t}}$	<1	<1	1	<1	<1	<1	1	3	1	2	2	1
$\mu_{t\bar{t}+Z}$	14	6	9	3	4	2	15	5	11	1	5	1
μ_Z	2	5	3	6	6	8	1	2	1	2	3	5
Small-R JER	21	9	3	7	9	23	8	9	5	5	13	12
Small-R JES	3	9	1	3	2	3	1	3	6	3	8	5
Large-R jet + DNN	32	29	3	5	5	10	13	26	11	10	4	3
b-tagging	3	1	4	3	5	2	4	3	3	2	4	2
E_T^{miss}soft term	2	1	1	1	3	3	<1	3	1	1	6	2
Lepton	4	5	3	4	5	7	3	3	2	3	4	3
Pile-up	<1	2	2	1	2	2	4	2	1	1	1	<1
MC statistics	18	17	11	15	11	6	12	10	9	5	8	4

the experimental uncertainties, the Large-R jet + DNN and JER for the small-R jets are dominant systematic uncertainties. The Large-R jet + DNN contributes to the uncertainties mostly in TT regions of both SRA and SRB (over 30% in SRATT). The JER for small-R jets is dominant in T0 regions and subdominant in TT regions. The Large-R jet + DNN in the Z+jets event is well controlled by the CRZ, which results in small uncertainties of the Large-R jet + DNN when the Z+jets dominates. For theoretical uncertainties, the $t\bar{t}Z$ uncertainty is dominant in the SRATT due to main backgrounds in SRATT. The $t\bar{t}$ modelling is non-negligible in most of the signal regions and dominant in SRBTT and SRBTW. The Z modelling does not affect the uncertainties significantly. The fit results in Figure 61 show the nuisance parameters belonging to the theoretical uncertainties of the main backgrounds, the dominant experimental uncertainties and normalization factors of $t\bar{t}$, $t\bar{t}Z$, and Z+jets. Most of the nuisance parameters show no significant deviation between pre-fit and post-fit except for the $t\bar{t}$ modelling due to two $t\bar{t}$ control regions with one normalization factor.

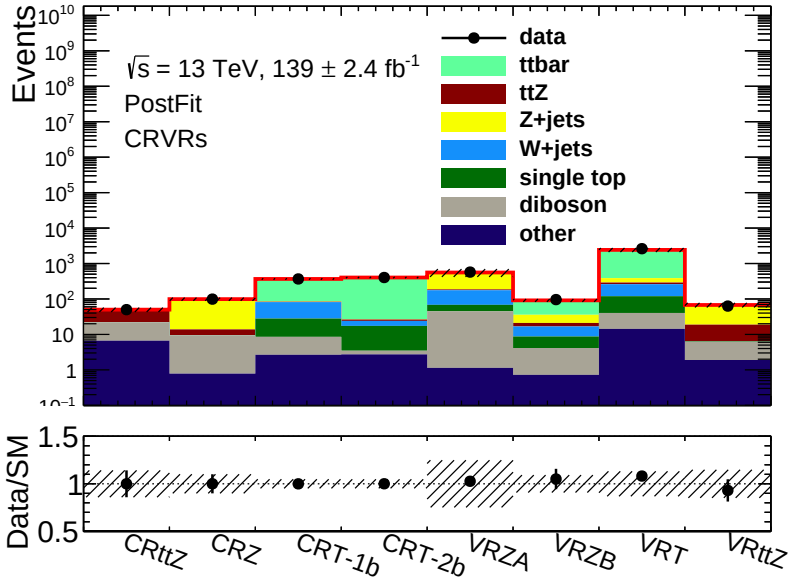

Figure 60: Summary plots for control regions and validation regions. All the SM backgrounds are included with the band of the total uncertainties.

6.7.2 Discussion of data in signal regions

Tables 26 and 27 show the yields after the normalization factors are applied. No excess is found in all the signal regions. Figure 62 summarizes all the signal regions. No events are observed in the SRATT2b and SRATT1b. The SM predictions

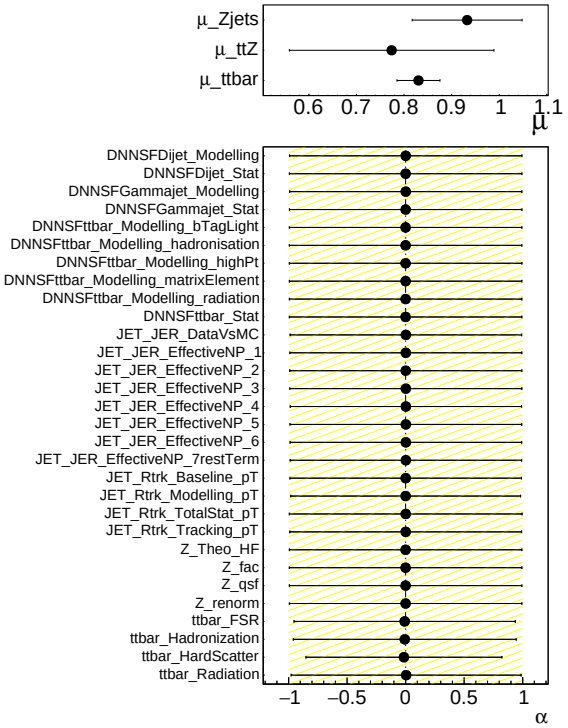

Figure 61: Results of fit parameters α and normalization factors μ of main backgrounds (upper panel) from the background-only fit to all control regions. $\alpha = (\theta - \theta^0)/\Delta\theta$, where θ^0 and $\Delta\theta$ are the initial mean values and standard deviations for individual parameters, and θ is final value after the fit. Only the nuisance parameters belong to main backgrounds with significant uncertainties and the normalization factors are shown. The details of the nuisance parameters can be found in Table 25. The $t\bar{t}Z$ modelling is not included in the background-only fit to all the control regions since the errors are assigned directly to $\mu_{t\bar{t}Z}$. The shaded area refers to the initial value of nuisance parameters, which are set to 0 ± 1.

Table 25: Nuisance parameters with major contributions of the systematic uncertainties.

Uncertainties	Parameters	Description
Jet energy resolution	JET_JER_EffectiveNP_1 JET_JER_EffectiveNP_2 JET_JER_EffectiveNP_3 JET_JER_EffectiveNP_4 JET_JER_EffectiveNP_5 JET_JER_EffectiveNP_6 JET_JER_EffectiveNP_7restTerm JET_JER_DataVsMC	7 NPs including the uncertainties propagated from JES uncertainties and random cone method and 1 NP for the non-closure between the data and MC
Large-R jet + DNN	JET_Rtrk_Tracking_pT JET_Rtrk_TotalStat_pT JET_Rtrk_Modelling_pT JET_Rtrk_Baseline_pT	4 NPs for jet response from the R_{trk} method
	DNNSFttbar_Stat DNNSFttbar_Modelling_radiation DNNSFttbar_Modelling_matrixElement DNNSFttbar_Modelling_highPt DNNSFttbar_Modelling_hadronisation DNNSFttbar_Modelling_bTagLight	6 NPs for signal scale factors of DNN top tagger
	DNNSFGammajet_Stat DNNSFGammajet_Modelling DNNSFDijet_Stat DNNSFDijet_Modelling	4 NPs for background scale factors of DNN top tagger
$t\bar{t}$ modelling	ttbar_Radiation ttbar_HardScatter ttbar_Hadronization ttbar_FSR	Uncertainty in the initial state radiation Uncertainty in different generators Uncertainty in the parton showing Uncertainty in the final state radiation
Z+jets modelling	Z_ckkw Z_fac Z_qsf Z_renorm Z_Theo_HF	Uncertainty in the matrix element matching Uncertainty in the factorization scale Uncertainty in the resummation scale Uncertainty in the renormalization scale Uncertainty in the Z+heavy flavor jets

in the SRATW2b and SRAT02b are slightly higher than the observed events, but the SM predictions of SRATW1b and SRAT01b are in agreement with the data which have higher statistics than those in the SRATW2b and SRAT02b. This could be simply caused by the fluctuation of low statistics data. The SRB shows better agreement between data and SM predictions. Figure 63 shows the post-fit distributions of m_{T2,χ^2}, $\mathrm{N_{jets}}$, $m_{\mathrm{T}}^{b,\mathrm{min}}$, $E_{\mathrm{T}}^{\mathrm{miss}}$, $m_{\mathrm{T}}^{b,\mathrm{max}}$, and object-based $E_{\mathrm{T}}^{\mathrm{miss}}$ significance in SRATW1b, SRAT01b, SRBTW2b, SRBTW1b, SRBT02b, and SRBTT1b, respectively.

Table 26: Fit results for the SRA with background corrections, for an integrated luminosity of 139 fb^{-1}. The total uncertainties are shown. "Other" includes tZ, tWZ, $t\bar{t}W$, and $t\bar{t}H$.

Regions	SRATT2b	SRATW2b	SRAT02b	SRATT1b	SRATW1b	SRAT01b
Observed events	0	1	1	0	3	7
SM events	0.7 ± 0.3	1.9 ± 0.4	2.4 ± 0.5	0.7 ± 0.3	2.8 ± 0.6	5.8 ± 1.7
$t\bar{t}$ events	$0.1^{+0.1}_{-0.1}$	0.3 ± 0.2	$0.1^{+0.1}_{-0.1}$	$0.0^{+0.1}_{-0.0}$	0.1 ± 0.1	0.2 ± 0.1
$t\bar{t}Z$ events	0.4 ± 0.2	0.6 ± 0.3	0.4 ± 0.2	0.2 ± 0.1	0.3 ± 0.1	0.4 ± 0.3
W+jets events	0.0 ± 0.0	0.2 ± 0.1	0.4 ± 0.2	0.0 ± 0.0	0.2 ± 0.1	0.8 ± 0.4
Z+jets events	0.1 ± 0.1	0.5 ± 0.2	1.2 ± 0.3	0.3 ± 0.2	1.3 ± 0.4	3.6 ± 1.0
Single top events	0.1 ± 0.0	0.3 ± 0.1	0.3 ± 0.2	0.1 ± 0.1	0.5 ± 0.1	$0.3^{+0.4}_{-0.3}$
Diboson events	0.0 ± 0.0	0.0 ± 0.0	0.1 ± 0.0	0.0 ± 0.0	0.3 ± 0.2	0.5 ± 0.1
Other events	0.0 ± 0.0	0.1 ± 0.0	$0.0^{+0.0}_{-0.0}$	0.0 ± 0.0	0.1 ± 0.0	0.0 ± 0.0

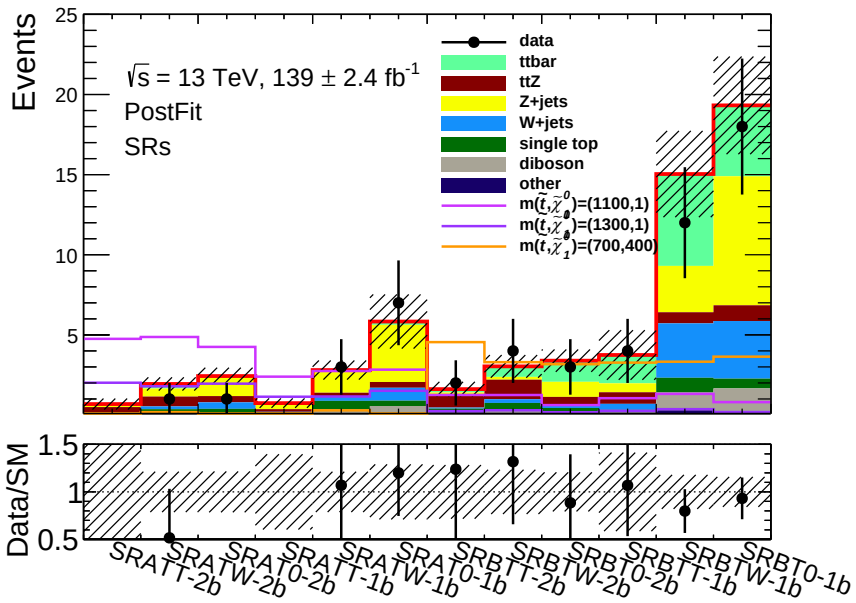

Figure 62: Summary plots for all the signal regions with data unblinded. All the SM backgrounds with the shaded band of the total uncertainties are included. ($m_{\tilde{t}}$,$m_{\tilde{\chi}_1^0}$) = (1300,1), ($m_{\tilde{t}}$,$m_{\tilde{\chi}_1^0}$) = (1100,1), and ($m_{\tilde{t}}$,$m_{\tilde{\chi}_1^0}$) = (700,400) are also shown.

Table 27: Fit results for the SRB with background corrections, for an integrated luminosity of 139 fb^{-1}. The total uncertainties are shown. "Other" includes tZ, tWZ, t$\bar{t}W$, and t$\bar{t}H$.

Regions	SRBTT2b	SRBTW2b	SRBT02b	SRBTT1b	SRBTW1b	SRBT01b
Observed events	2	4	3	4	12	18
SM events	1.6 ± 0.5	3.0 ± 0.7	3.4 ± 0.7	3.7 ± 1.5	15.0 ± 2.7	19.3 ± 3.0
t$\bar{t}$ events	$0.2^{+0.2}_{-0.2}$	0.7 ± 0.4	1.3 ± 0.3	1.8 ± 1.2	5.7 ± 2.2	4.4 ± 1.2
t$\bar{t}Z$events	0.8 ± 0.3	1.2 ± 0.5	0.6 ± 0.3	0.7 ± 0.3	0.7 ± 0.3	1.0 ± 0.4
W+jets events	0.1 ± 0.0	0.2 ± 0.1	0.1 ± 0.1	0.4 ± 0.2	3.4 ± 1.1	3.6 ± 2.1
Z+jets events	0.1 ± 0.0	0.2 ± 0.1	0.9 ± 0.4	0.6 ± 0.4	2.9 ± 1.0	8.1 ± 1.8
Single top events	0.1 ± 0.0	0.5 ± 0.3	0.4 ± 0.2	0.1 ± 0.0	0.9 ± 0.7	$0.6^{+0.7}_{-0.6}$
Diboson events	0.1 ± 0.0	0.1 ± 0.0	$0.0^{+0.0}_{-0.0}$	0.1 ± 0.0	1.1 ± 0.5	1.6 ± 0.6
Other events	0.2 ± 0.0	0.1 ± 0.0	0.0 ± 0.0	0.1 ± 0.0	0.3 ± 0.0	0.1 ± 0.0

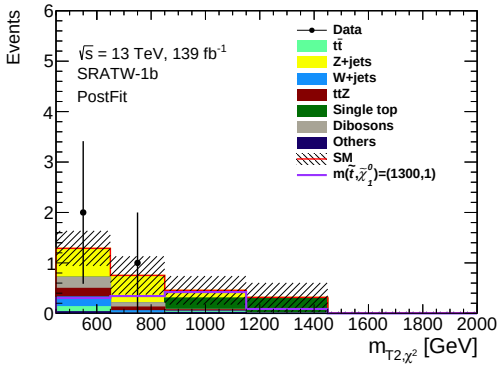

(a) m_{T2,χ^2} in SRATW1b

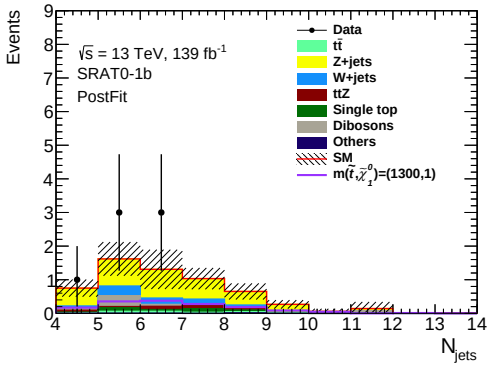

(b) $\mathrm{N_{jets}}$ in SRAT01b

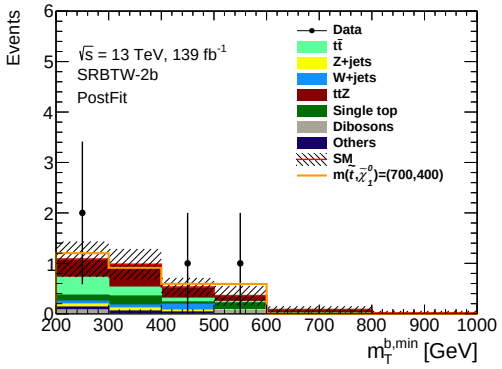

(c) $m_{\mathrm{T}}^{b,\mathrm{min}}$ in SRBTW2b

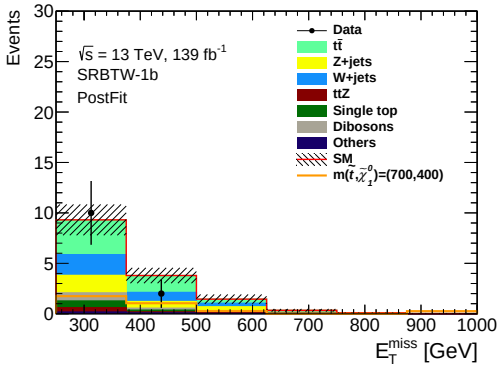

(d) $E_{\mathrm{T}}^{\mathrm{miss}}$ in SRBTW1b

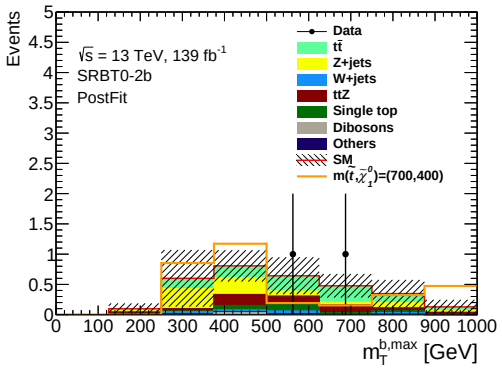

(e) $m_{\mathrm{T}}^{b,\mathrm{max}}$ in SRBT02b

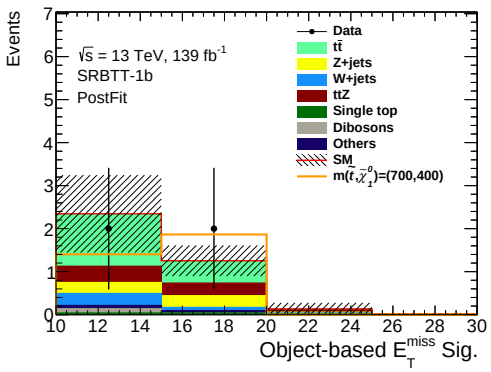

(f) Object-based $E_{\mathrm{T}}^{\mathrm{miss}}$ sig. in SRBTT1b

Figure 63: Post-fit plots for the signal regions. All the SM backgrounds are included with the band of the total uncertainties. $(m_{\tilde{t}},m_{\tilde{\chi}_1^0})$ = (1300,1) is shown in (a) and (b). $(m_{\tilde{t}},m_{\tilde{\chi}_1^0})$ = (700,400) is shown in (c), (d), (e), and (f).

6.7.3 Model-dependent signal fit

Since no significant excess from total SM predictions is found, a model-dependent signal fit is performed in each signal point of ($m_{\tilde{t}}$, $m_{\tilde{\chi}_1^0}$) to extract the lower limits on the masses. Although the results are changing in different signal models, the most relevant results are the benchmark point ($m_{\tilde{t}}$, $m_{\tilde{\chi}_1^0}$) = (1300,1) GeV. All control regions for $t\bar{t}Z$, $t\bar{t}$, and Z+jets and all signal regions (SRAs and SRBs) are included in PDFs for the total likelihood function. The breakdown of the systematic uncertainties is shown in Table 28. Comparing to Table 24 for the background-only fit, most of the dominant uncertainties remain the same. The uncertainty for μ_{sig} is large in SRATT2b due to the signal yield being large in the SRATT2b. The results of fit parameters for the model-dependent signal fit are shown in Figure 64. Slight deviations between pre-fit and post-fit are observed in the model-dependent signal fit since the data are not matched well the SM predictions.

Table 28: Systematic uncertainties in percentage of the total SM predictions larger than 1 % within SRA and SRB. The uncertainties are estimated by using simultaneous fit to the all signal regions and control regions in data and MC with fixed normalization factors ($\mu_{t\bar{t}}$, $\mu_{t\bar{t}Z}$, and μ_Z) from the background-only fit and floating μ_{sig}. The signal samples ($m_{\tilde{t}}$, $m_{\tilde{\chi}_1^0}$) = (1300,1) GeV is used as signal model. Single top modelling is negligible after the fit.

	SRATT		**SRATW**		**SRAT0**		**SRBTT**		**SRBTW**		**SRBT0**	
$N_{b\text{-jet}}$	≥ 2	1	≥ 2	1	≥ 2	1	≥ 2	1	≥ 2	1	≥ 2	1
Total syst. unc.	42	26	19	18	17	21	24	31	19	13	17	12
$t\bar{t}$ modelling	12	6	10	3	2	1	11	28	9	7	6	5
$t\bar{t}Z$ modelling	16	7	5	2	8	3	5	2	3	<1	2	1
Z modelling	5	8	5	9	9	13	1	1	1	1	5	7
W modelling	3	2	3	3	6	4	1	4	3	8	1	6
μ_{sig}	19	9	6	3	5	2	1	<1	1	<1	<1	<1
$\mu_{t\bar{t}}$	<1	<1	1	<1	<1	<1	1	3	1	2	2	1
$\mu_{t\bar{t}+Z}$	14	6	9	3	4	2	14	5	11	1	5	1
μ_Z	2	5	3	5	6	7	1	2	1	2	3	5
Small-R JER	19	8	3	6	9	20	8	9	5	5	12	10
Small-R JES	3	10	1	3	2	3	1	3	5	3	7	5
Large-R jet + DNN	20	15	3	3	5	8	8	15	7	5	4	3
b-tagging	3	2	4	4	5	2	4	3	4	2	4	2
E_T^{miss}soft term	2	1	1	1	3	3	<1	3	1	1	5	2
Lepton	4	5	3	4	5	6	3	3	2	2	4	3
Pile-up	<1	2	2	1	2	2	4	2	1	1	1	<1
MC statistics	6	8	7	10	7	5	11	9	8	5	8	4

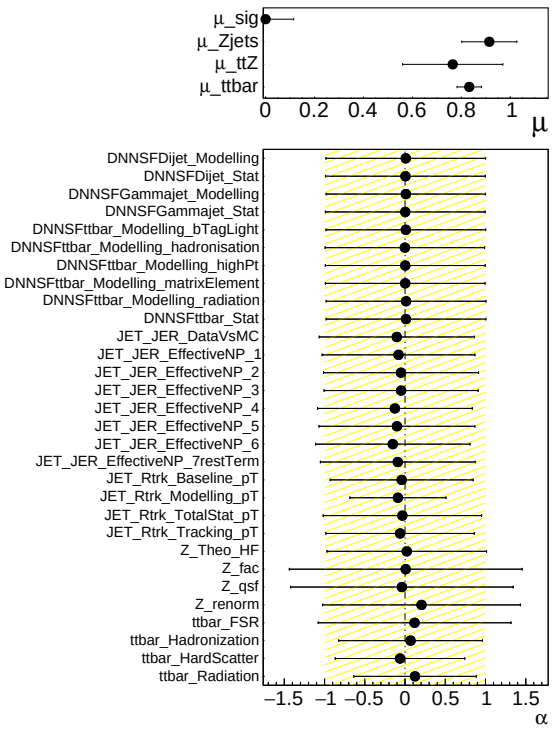

Figure 64: Results of fit parameters α and normalization factors μ of main backgrounds and a signal (upper panel) from the model-dependent signal fit to all control regions and signal regions with signal model ($m_{\tilde{t}}$,$m_{\tilde{\chi}_1^0}$) = (1300,1) GeV. $\alpha = (\theta - \theta^0)/\Delta\theta$, where θ^0 and $\Delta\theta$ are the initial mean values and standard deviations for individual parameters, and θ is final value after the fit. Only the nuisance parameters belong to main backgrounds with significant uncertainties and the normalization factors are shown. The details of the nuisance parameters can be found in Table 25. The $t\bar{t}Z$ modelling is not included in the model-dependent fit since the errors are assigned directly to $\mu_{t\bar{t}Z}$. The shaded area refers to the initial value of nuisance parameters, which are set to 0 ± 1.

6.7.4 Model-independent signal fit

By performing the model-independent signal fit, we can extract the probability of signals and the upper limit on the visible cross section for new physics. Since no signal model is considered, the fit is performed separately for each signal region. Table 29 shows the results of the fit. The visible cross section is defined as the product of the cross section, acceptance, and efficiency for the selection criteria used in the analysis. Four SRA regions in the top rows of the table show the lowest upper limits on the visible cross section, which is 0.02 fb^{-1}.

Table 29: 95% CL upper limits on the visible cross section ($\langle\epsilon\sigma\rangle^{95}_{\text{obs}}$) and on the number of signal events (S^{95}_{obs}) for each signal region. The third column (S^{95}_{exp}) shows the 95% CL upper limit on the number of signal events, given the expected number (and $\pm 1\sigma$ excursions on the expectation) of background events. The last two columns indicate the CL_B value, i.e. the confidence level observed for the background-only hypothesis, the discovery p-value ($p(s=0)$), and the significance (Z). The p-value is truncated to 0.5 if the data is less than the MC predictions.

Signal Region	$\langle\epsilon\sigma\rangle^{95}_{\text{obs}}$ [fb]	S^{95}_{obs}	S^{95}_{exp}	CL_B	$p(s=0)$ **(**Z**)**
SRATT2b	0.02	2.3	$3.0^{+2.0}_{-1.1}$	0.28	0.50 (0.00)
SRATW2b	0.02	3.3	$4.2^{+2.5}_{-1.4}$	0.29	0.50 (0.00)
SRAT02b	0.02	3.3	$4.5^{+2.5}_{-1.5}$	0.23	0.50 (0.00)
SRATT1b	0.02	2.3	$3.1^{+2.1}_{-1.1}$	0.26	0.50 (0.00)
SRATW1b	0.04	5.0	$4.9^{+2.7}_{-1.6}$	0.54	0.46 (0.11)
SRAT01b	0.06	8.0	$7.0^{+3.5}_{-2.2}$	0.63	0.35 (0.38)
SRBTT2b	0.03	4.4	$4.0^{+2.4}_{-1.4}$	0.58	0.39 (0.27)
SRBTW2b	0.04	6.0	$5.0^{+2.8}_{-1.7}$	0.66	0.31 (0.48)
SRBT02b	0.03	4.8	$5.2^{+2.8}_{-1.7}$	0.43	0.50 (0.00)
SRBTT1b	0.05	6.7	$6.5^{+3.0}_{-1.9}$	0.53	0.46 (0.10)
SRBTW1b	0.06	8.0	$10.0^{+4.6}_{-3.0}$	0.27	0.50 (0.00)
SRBT01b	0.08	10.9	$12.0^{+5.3}_{-3.6}$	0.41	0.50 (0.00)

7 Discussion

7.1 Exclusion limit

Exclusion limits with the DNN top taggers are shown in Figure 65 in the cross section as a function of $m_{\tilde{t}}$ at $m_{\tilde{\chi}_1^0}$ = 100 GeV and Figure 66 in the $m_{\tilde{t}}$-$m_{\tilde{\chi}_1^0}$ plane. The expected limit of $m_{\tilde{t}}$ is extended to ∼1300 GeV at low $m_{\tilde{\chi}_1^0}$. The observed limit with the DNN top tagger is extended to ∼1400 GeV. The expected (observed) limit of $m_{\tilde{\chi}_1^0}$ reaches up to 540 (610) GeV. The $m_{\tilde{t}}$ region below 400 GeV is not considered in the analysis since the mass region is already excluded in the previous ATLAS results at 36 fb^{-1} [3]. The deviation between expected limit and observed limit around $m_{\tilde{t}}$ = 1300-1400 GeV is due to the smaller number of observed events in the SRAs with respect to the background expectation.

7.2 Comparison with the results of reclustering method

The search for the scalar top quark in the boosted regions in the paper [129] is briefly introduced, and the results are compared to the results with DNN top tagger method obtained in this thesis. The paper shows the results of the four signal regions, SRA, SRB, SRC, and SRD. The SRC focuses on the compressed region of two-body and three-body decays (see Figure 7). The SRD covers the three-body and four-body decays. The SRA and SRB aim for the same mass region as this thesis (DNN top tagger method). The critical difference between this thesis and the paper is the method of top reconstruction. The reclustering jets are used in the paper.

7.2.1 Regions with the reclustering method

Due to different methods of top reconstruction, the design of the regions is also different. Here, we briefly summarize signal regions and top-tagging method used in the paper.

7.2.2 Signal regions

The reclustering is the alternative method of the top reconstruction used in the stop search in the final state with jets and $E_{\mathrm{T}}^{\mathrm{miss}}$ [3]. The decay products of hadronically

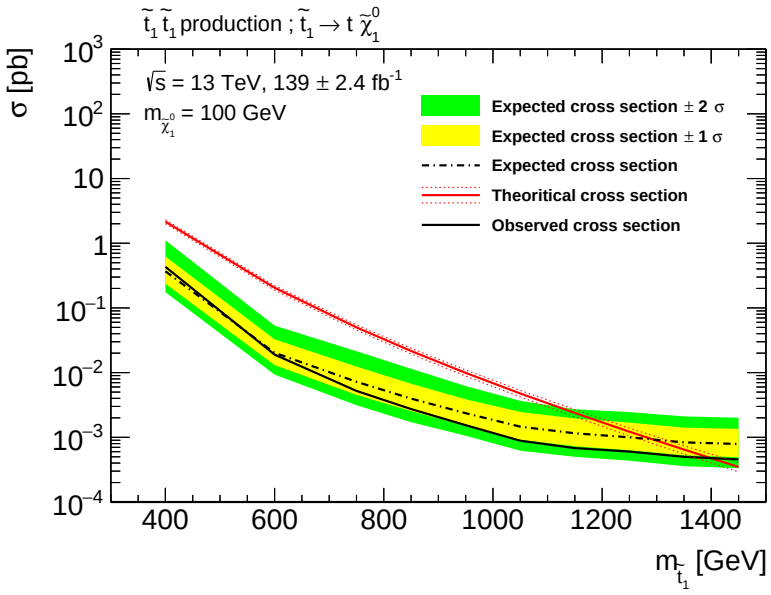

Figure 65: Observed (black solid line) and expected (black dot-dashed line) limits as a function of mass of the scalar top quarks on the production cross section at 95% confidence level with 139 fb^{-1}of full Run2 dataset. The theoretical cross sections are shown as the red line.

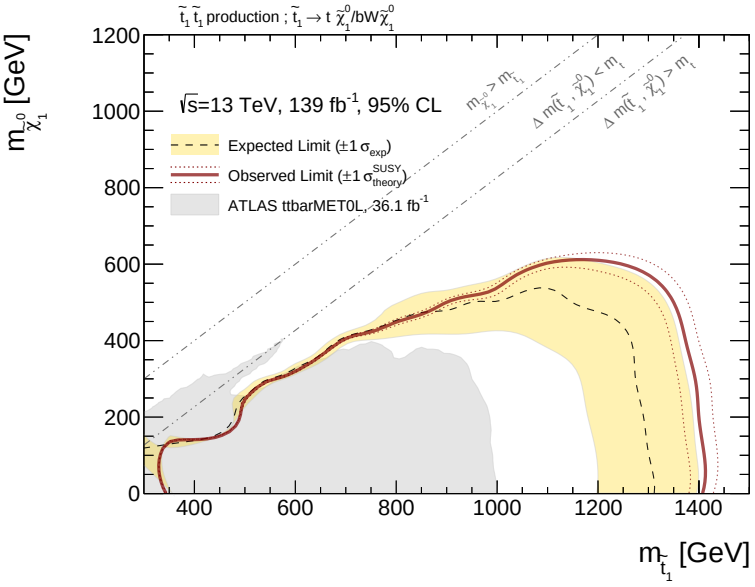

Figure 66: Observed (red line) and expected (black dash line) exclusion limit at 95% confidence level with 139 fb^{-1}of full Run2 dataset. $\pm 1\sigma$ of expected limit (yellow band) is also shown. Observed exclusion limit is also shown in grey area for the comparison. Grey dash-dotted lines indicate the mass regions of the two-body and three/four-body decays.

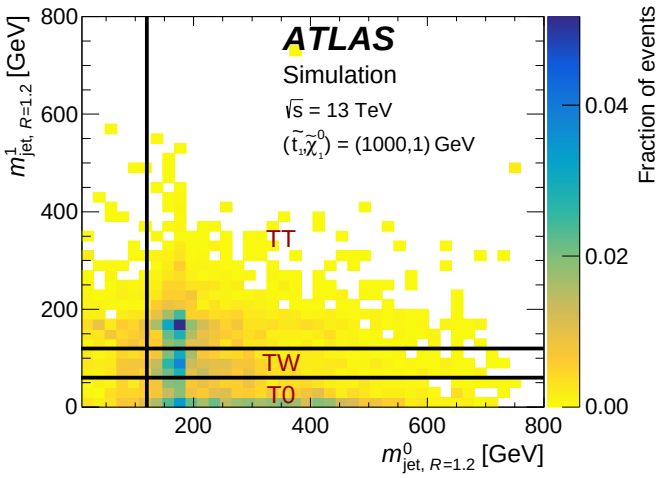

Figure 67: The categories of the signal regions based on the mass of leading R = 1.2 reclustered jets ($m^0_{\text{jet, } R=1.2}$) and subleading R = 1.2 reclustered jets ($m^1_{\text{jet, } R=1.2}$) [3]. The simulation sample of ($m_{\tilde{t}}$, $m_{\tilde{\chi}^0_1}$) = (1000,1) GeV is used and loose preselections are applied. The black line shows the mass requirements of the categories.

decaying top quarks can be mostly reconstructed using small-R jets. These small-R jets are reclustered into R = 1.2 and R = 0.8 jets separately by using the anti-k_t algorithm. No further grooming techniques are applied during the reclustering. The categories of the signal regions are based on the masses of the leading and subleading R = 1.2 reclustered jets. Figure 67 shows the two-dimensional mass distributions of the leading and subleading reclustered jets, with the three prominent populations visible in the mass plane (The leading jet and the subleading jet are defined as 0 and 1 in the paper with the 36 fb^{-1}data but they are defined as 1 and 2 in the paper with the 139 fb^{-1}data. Here, we use 1 and 2 for the leading jet and the subleading jet.). All the signal regions are defined by using the leading R = 1.2 jets with the jet mass larger than 120 GeV ($m^1_{\text{jet},R=1.2}>$ 120 GeV). The "TT" category, which means two top candidates, is defined by using subleading R = 1.2 reclustered jets with the mass $>$ 120 GeV. The "TW" category means one top candidate and one W candidate in the mass region of 60 GeV $<m^2_{\text{jet},R=1.2}<$ 120 GeV. Finally, the "T0", which means only one top candidate is found, is defined with $m^2_{\text{jet},R=1.2}<$ 60 GeV. Both SRA and SRB consist of these three categories but are separated by using the $m_{\text{T2},\chi^2}>$ 450 GeV for the SRA and $m_{\text{T2},\chi^2}<$ 450 GeV for the SRB. In SRA, the mass requirement of the R = 0.8 reclustered jet and b-tagged jet matched with the leading R = 1.2 reclustered jet by using $\Delta R < 1.2$ are additionally applied. The signal regions are optimized by using $\Delta R\,(b_1, b_2)$, $m_{\text{T}}^{b,\text{min}}$, $m_{\text{T}}^{b,\text{max}}$, and object-based $E_{\text{T}}^{\text{miss}}$ significance, which are also used in the DNN top tagger method. All the regions are defined in the region with more than two b-tagged jets. Other variables in Table 30 have been mentioned in the previous chapters.

Table 30: Definition of the SRA and SRB using the reclustered jets and other variables [129]. The dash line indicates no selection is applied.

Variable/SR	SRA-TT	SRA-TW	SRA-T0	SRB-TT	SRB-TW	SRB-T0
Trigger	$E_{\mathrm{T}}^{\mathrm{miss}}$					
$E_{\mathrm{T}}^{\mathrm{miss}}$	> 250 GeV					
$\mathrm{N}_{\mathrm{leptons}}$	exactly 0					
$\mathrm{N}_{\mathrm{jets}}$	≥ 4					
p_{T}^{2}	> 80 GeV					
p_{T}^{4}	> 40 GeV					
$\left\lvert\Delta\phi\left(\mathrm{jet}^{1-4}, E_{\mathrm{T}}^{\mathrm{miss}}\right)\right\rvert$	> 0.4					
$\mathrm{N}_{b\text{-jet}}$	≥ 2					
$m_{\mathrm{T}}^{b,\mathrm{min}}$	> 200 GeV					
τ-veto	✓					
$m_{\mathrm{jet},R=1.2}^{1}$	> 120 GeV					
$m_{\mathrm{jet},R=1.2}^{2}$	> 120 GeV	60–120 GeV	< 60 GeV	> 120 GeV	60–120 GeV	< 60 GeV
$m_{\mathrm{jet},R=0.8}^{1}$	> 60 GeV			–		
$j_{1}^{R=1.2}(b)$	✓			–		
$j_{2}^{R=1.2}(b)$	✓	–				
$\Delta R\,(b,b)$	> 1.0	–		> 1.4		
$m_{\mathrm{T}}^{b,\mathrm{max}}$	–			> 200 GeV		
Object-based $E_{\mathrm{T}}^{\mathrm{miss}}$ sig.	> 25			> 14		
m_{T2,χ^2}	> 450 GeV			< 450 GeV		

7.2.3 Performance comparison

Figure 68 (a) shows the top-tagging efficiencies of both reclustered jets and DNN contained top tagged jets as a function of leading large-R jet p_{T} in $p_{\mathrm{T}} > 350$ GeV. The leading large-R jets are selected by requiring ΔR (large-R jet labelled as a contained top, R = 1.2 reclustered jet) < 1.0. The reclustering method shows excellent efficiencies close to 100%. The efficiencies of the DNN contained top tagger are around 80% as expected. Figure 68 (b) shows the background rejection of both methods for the main background process of $Z\rightarrow \nu\nu$. The DNN contained top tagger has $\sim$5 times better background rejection than the reclustering method. The reclustering method has essentially no ability of rejecting background in high p_{T} range. This can explain why reclustering method has the signal efficiency of nearly 100%.

Based on the performance of two methods, most of the signal regions with reclustering method are defined with the tighter selections. The $m_{\mathrm{T}}^{b,\mathrm{min}}$, $m_{\mathrm{T}}^{b,\mathrm{max}}$, and

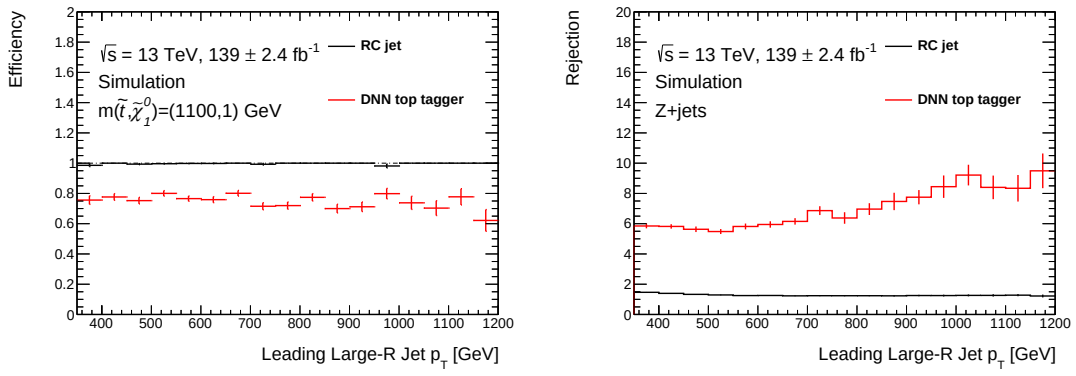

(a) (b)

Figure 68: Performance of the DNN contained top tagger and reclustered jet on (a) the signal efficiencies derived in the simulation sample of $(m_{\tilde{t}}, m_{\tilde{\chi}_1^0})$ = (1100,1) GeV and (b) the background rejection derived in the simulation samples of $Z \to \nu\nu$. A RC jet is referred to the a reclustered jet.

Table 31: Observed data and fitted SM yields of the reclustering method in SRAs and SRBs after the background-only fit [3]. The uncertainties include MC statistical uncertainties, the experimental uncertainties and theoretical uncertainties.

	SRA-TT	**SRA-TW**	**SRA-T0**	**SRB-TT**	**SRB-TW**	**SRB-T0**
Observed	4	8	11	67	84	292
Total SM	3.2 ± 0.5	5.6 ± 0.7	17.3 ± 1.7	46 ± 7	81 ± 7	276 ± 24
Z + jets	1.35 ± 0.28	3.2 ± 0.4	10.5 ± 1.3	15.6 ± 3.3	28.7 ± 3.4	117 ± 14
Single top	0.50 ± 0.31	0.59 ± 0.29	1.9 ± 0.8	3.5 ± 1.2	7.0 ± 3.0	31 ± 15
$t\bar{t}$	0.08 ± 0.07	0.16 ± 0.10	0.4 ± 0.4	10 ± 5	20 ± 6	72 ± 19
$t\bar{t}$+Z	1.05 ± 0.29	0.74 ± 0.17	1.50 ± 0.34	9.9 ± 1.9	12.5 ± 2.5	22 ± 4
W + jets	0.16 ± 0.07	0.53 ± 0.20	1.7 ± 0.6	4.9 ± 1.9	8 ± 4	22 ± 9
Other	0.080 ± 0.020	0.34 ± 0.24	1.32 ± 0.22	2.4 ± 0.4	4.7 ± 2.3	10.4 ± 1.3

$\Delta R\,(b_1, b_2)$ are not used in the SRA with the DNN top tagger method. The selections of object-based $E_{\mathrm{T}}^{\mathrm{miss}}$ significance with reclustering method are tighter than the selections with DNN top tagger method except for T0 regions. In addition, the regions with only one b-tagged jet can be used only for using the DNN top tagger method since only one b-tagged region has too many background events for the reclustering method.

7.2.4 Comparison of Results

The fit strategy is basically the same as the strategy mentioned in Chapter 6.6.1. The background-only fit estimates corrections of the normalization factors of backgrounds by using the simultaneous fit to all the control regions. The five floating normalization factors are set for Z+jets, $t\bar{t}Z$, $t\bar{t}$, single top, and W+jets for the fitting.

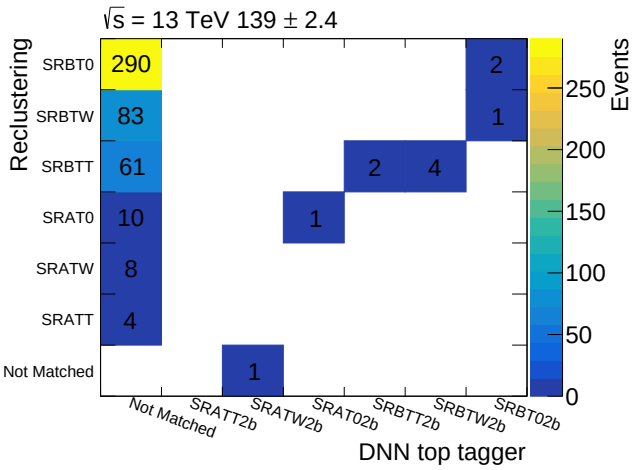

Figure 69: Comparison of the observed data between DNN top tagger method and reclustering method in the regions with ≥ 2 b-tagged jets. "Not matched" shows the events are found only in only one method.

Table 31 shows the observed data and fitted SM backgrounds after the background-only fit. No significant excess is found in the results except for the $\sim 1.9\sigma$ in the SRBTT. Comparing with the sensitivity for the signal ($m_{\tilde{t}}$,$m_{\tilde{\chi}_1^0}$) = (1300,1) GeV using the DNN top tagger method, the expected significance is improved by 14% with the DNN top tagger method if only the signal regions with at least two b-tagged jets are considered. Furthermore, the DNN top tagger method improves the expected significance by 27% over the reclustering method if signal regions with both one and at least two b-tagged jets are considered.

Figure 69 shows the correlation of observed data between the DNN top tagger method and reclustering method. Since no events are found in the SRATT2b, the SRATT2b bins are empty. Most of the events in DNN top tagger method can be found in the reclustering method except for one in the SRATW2b. The event in the SRATW2b contains the leading large-R jet being tagged as an inclusive top and the subleading large-R jet being as a tagged contained top. The leading large-R jet matches the leading reclustered jet with mass less than 120 GeV. Therefore, the event does not pass the criteria in the reclustering method. The data migration is found in the SRB. The TT goes to the TW, and the TW goes to T0. This is expected due to the tighter selections applied to the top candidates.

Figure 70 shows the exclusion limit in the $m_{\tilde{t}}$-$m_{\tilde{\chi}_1^0}$ plane with full Run2 139 fb^{-1}dataset for both reclustering method and DNN top tagger method. For the reclustering method, the yellow band and black dashed line are the expected limit with $\pm 1\sigma$ uncertainties. The expected and observed exclusion limits of $m_{\tilde{t}}$ are ex-

tended to ∼1250 GeV at low neutralino mass. The expected (observed) exclusion limit of $m_{\tilde{\chi}_1^0}$ is extended to ∼510 (490) GeV around $m_{\tilde{t}}$ = 1100 GeV. The expected exclusion area is largely improved for the results at 139 fb^{-1}. For the DNN top tagger method, the expected (observed) limit of $m_{\tilde{t}}$ at low neutralino mass is 50 (150) GeV higher than the reclustering method and the expected (observed) limit of $m_{\tilde{\chi}_1^0}$ is 30 (120) GeV higher in two-body region. It is clearly seen that the search at the boosted region can benefit from the DNN top tagger method. On the other hand, the region containing more resolved top signals benefits from the reclustering method with larger radius jets and loose selections. Such selections with the reclustering method will result in higher sensitivity in the region close to the compressed region below $m_{\tilde{t}}$ = 800 GeV.

Due to the excess in SRBTT with the reclustering method, the observed limit around ($m_{\tilde{t}}$,$m_{\tilde{\chi}_1^0}$) = (900,400) GeV is not excluded. However, the excess is not found in the DNN top tagger method, and the signal point is excluded by the DNN top tagger method.

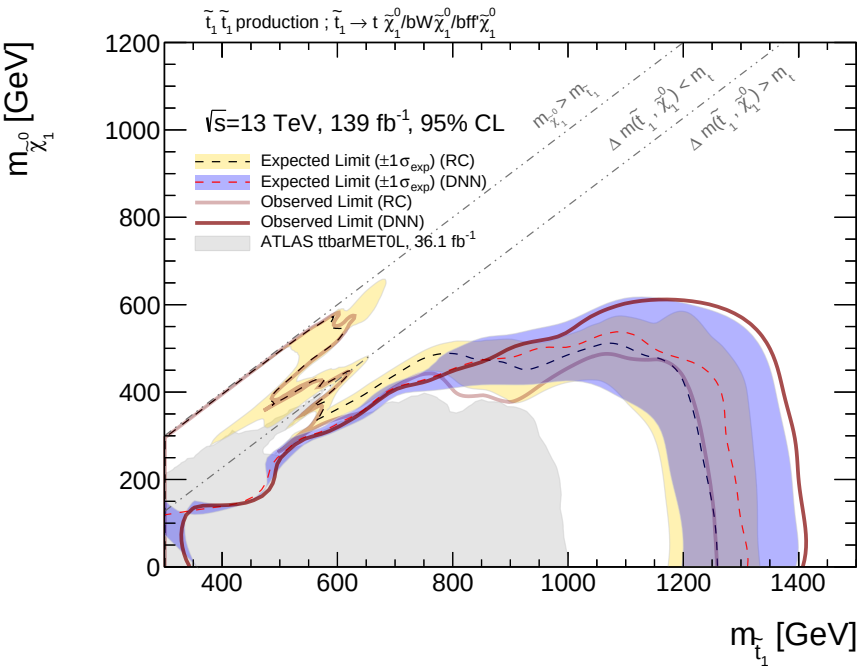

Figure 70: Observed and expected exclusion limit at 95% confidence level with 139 fb^{-1}of full Run2 dataset in the $m_{\tilde{t}}$-$m_{\tilde{\chi}_1^0}$ plane for both DNN top tagger method and reclustering method. "RC" represents the reclustering method and "DNN" represents the DNN top tagger method. The results of reclustering method include the search for a compressed region of two-body decay ($\Delta m(\tilde{t}_1,\tilde{\chi}_1^0) > m_t$) and three/four-body decay ($\Delta m(\tilde{t}_1,\tilde{\chi}_1^0) < m_t$). Both targeting regions are also sensitive to three-body decay. Observed exclusion limit is also shown in a grey area for the comparison.

7.3 Comparison with CMS results

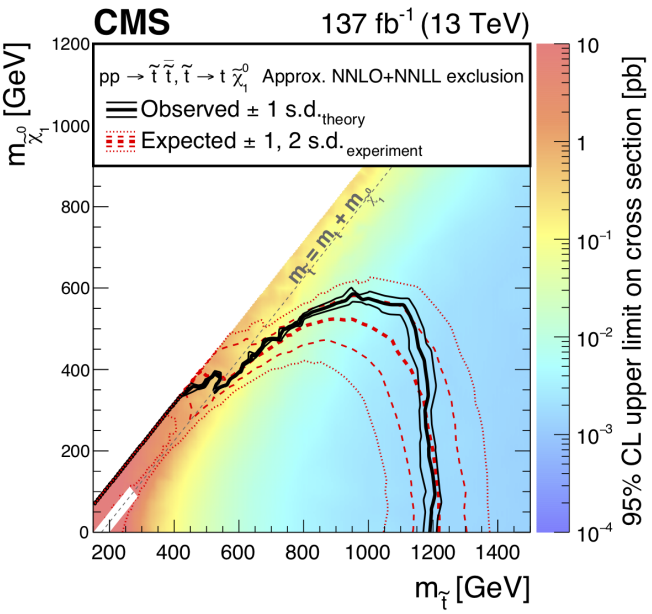

Figure 71: Observed and expected exclusion limit at 95% confidence level with 137 $\text{fb}^{-1}$of full Run2 dataset in the $m_{\tilde{t}}$-$m_{\tilde{\chi}_1^0}$ plane [130].

Figure 71 shows the exclusion contour of $m_{\tilde{t}}$ and $m_{\tilde{\chi}_1^0}$, where the scalar top quarks decay in the two-body and three-body, with 137 fb^{-1} of full Run2 data recorded by the CMS detector. The $m_{\tilde{t}}$ is excluded up to 1220 GeV for the expected limit and 1200 GeV for the observed limit. The $m_{\tilde{\chi}_1^0}$ is excluded up to 520 GeV for the expected limit and 580 GeV for the observed limit. CMS collaboration uses m_{T2} inclusive search for the SUSY particles including gluinos, light-flavor, bottom and top squarks. The m_{T2} is reconstructed by selecting the $E_{\text{T}}^{\text{miss}}$ and the two jets with the highest dijet invariant mass. Total 282 signal regions are categorized by the number of jets, the number of b-tagged jets, the scalar sum of jet p_{T} and m_{T2}. In the DNN top tagger method and reclustering method, we aggressively select boosted top candidates in SRA regions and SRB regions to get higher sensitivity at high $m_{\tilde{t}}$. However, CMS collaboration has better results near the compressed region, for example, the ($m_{\tilde{t}}$, $m_{\tilde{\chi}_1^0}$) = (700, 450) GeV, which is not excluded by either the DNN top tagger or reclustering method. In this region, the top quarks are not boosted so that the decay products may spread widely. The reconstruction of resolved top quarks can be a key for the improvement of the sensitivity.

In summary, CMS results show better limits in the compressed region near $\Delta m(\tilde{t}_1, \tilde{\chi}_1^0) \sim m_t$. The results of DNN top tagger method show better limits in high $m_{\tilde{t}}$ region, which is our target in this thesis.

7.4 Comparison with results in one/two-lepton final states

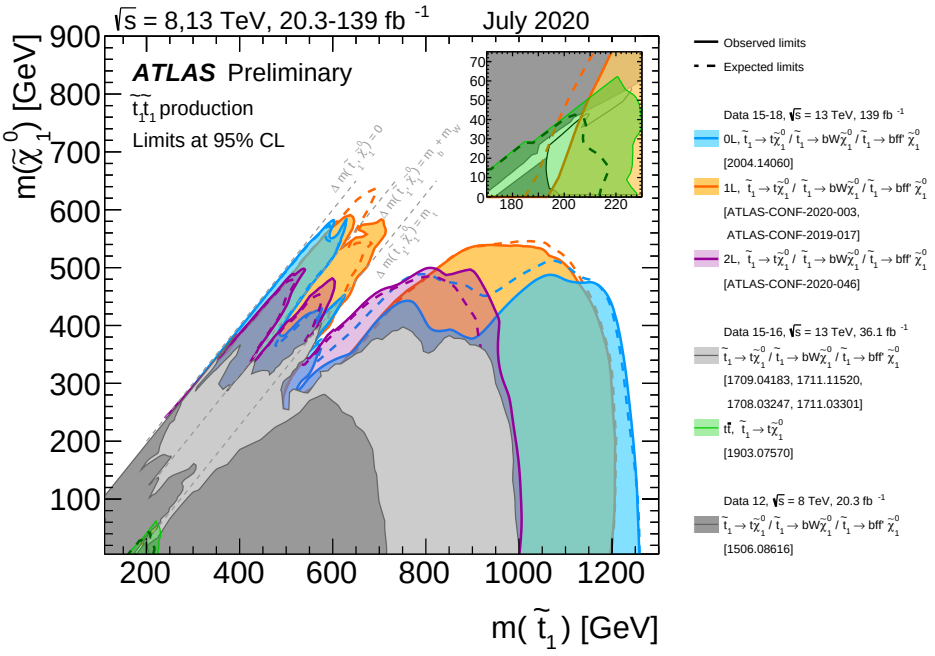

Figure 72: Observed and expected exclusion limit of all channels at 95% confidence level with 139 fb^{-1}of full Run2 dataset in the $m_{\tilde{t}}$-$m_{\tilde{\chi}_1^0}$ plane [131].

Figure 72 shows the exclusion contour of $m_{\tilde{t}}$ and $m_{\tilde{\chi}_1^0}$ with 139 fb^{-1} of full Run2 data recorded by the ATLAS detector. The expected (observed) limit of the stop mass is extended up to 970(1000) GeV for the two-lepton channel and 1200(1200) GeV for the one-lepton channel. In the analysis of two-lepton channel [132], the reconstruction of top candidates is not considered. Instead, the m_{T2} algorithm with the inputs of two leptons and $E_{\mathrm{T}}^{\mathrm{miss}}$ is used for the rejection of background leptonic decay of W bosons if the $E_{\mathrm{T}}^{\mathrm{miss}}$ is mainly contributed from neutrinos. In the one-lepton channel [133], two methods are used for the top reconstruction in the medium and high $\Delta m(\tilde{t}_1,\tilde{\chi}_1^0)$. First, the topness variable [134] is used for the rejection of dileptonic $\mathrm{t\bar{t}}$, which one of the two leptons is not identified. The variable is determined by minimizing the χ^2-like function based on the top mass and W boson mass. Second, the reslustered jets with a variable radius are used for the hadronic decay of top quarks, which the initial radius is 3.0. The larger radius can provide the reconstruction of top candidates with lower p_{T}. However, the identification of boosted top candidates shows better sensitivity in the high stop mass region since the limit of the stop mass in the zero-lepton channel is higher than the limit in the one-lepton channel.

In summary, the identification of boosted top candidates in the hadronic final states plays a key role in the search for the stop with the high mass.

8 Conclusion

A new method for the top reconstruction, DNN top tagger, has been introduced in the search for the scalar top quark with fully hadronic final states. This search is performed with an integrated luminosity of 139 fb^{-1} of $\sqrt{s}$ = 13 TeV proton-proton collision data acquired at the ATLAS. The direct pair production of the scalar top quarks is assumed in the signal scenario. A scalar top quark is expected to decay into a top and a neutralino. The target for the improvement is the boosted region with large $\Delta m(\tilde{t}_1,\tilde{\chi}_1^0)$. The number of the top quark candidates from the DNN top tagger provides good categorization to maximize the acceptance of the stop signals and reduce the backgrounds. The signal regions with high sensitivity are defined and optimized for the full Run 2 dataset. The main backgrounds in the signal regions are carefully estimated using the control regions defined for each main background and validated in the validation regions. The performance of top taggers is also validated by evaluating the top-quark tagging efficiency and background rejection using data enriched in hadronic top jets and background jets.

The comparison between the reclustering method used in the ATLAS paper and the DNN top tagger method used in this thesis is also presented. The reclustering method shows very high tagging efficiencies but low background rejections. The DNN top tagger method has the comparable tagging efficiencies (80%) with five times higher background rejections. The new method exploits the jet substructure variables and the deep learning algorithm to gain the background rejection, resulting in the restoration of the sensitivity in certain signal regions, otherwise dominated by the background. Owing to the improved background rejection, the signal regions with only 1 b-tagged jet are newly introduced to the search for the scalar top quark signals. As a result, the DNN top tagger method improves the 27% higher sensitivity over the reclustering method in the search for the scalar top quark in the boosted regions.

No significant excess is found in the stop search using the DNN top tagger method. Exclusion limits at 95% confidence level are evaluated as a function of $m_{\tilde{t}}$ and $m_{\tilde{\chi}_1^0}$. The exclusion of the $m_{\tilde{t}}$ is extended up to 1.4 TeV for the $m_{\tilde{\chi}_1^0}$ below 200 GeV. Model-independent limits are also derived for each signal region. The lowest cross section bound for new physics phenomena is down to 0.02 fb.

Reference

[1] M. Tanabashi et al. "Review of Particle Physics". *Phys. Rev. D* 98 (3 2018), p. 030001. DOI: 10.1103/PhysRevD.98.030001. URL: https://link.aps.org/doi/10.1103/PhysRevD.98.030001 (cit. on p. 7).

[2] Albert M Sirunyan et al. "Search for supersymmetry in proton-proton collisions at 13 TeV using identified top quarks". *Phys. Rev. D* 97.CMS-SUS-16-050, CERN-EP-2017-269 (2018), p. 012007. DOI: 10.1103/PhysRevD.97.012007. arXiv: 1710.11188 [hep-ex] (cit. on pp. 7, 8).

[3] Morad Aaboud et al. "Search for a scalar partner of the top quark in the jets plus missing transverse momentum final state at $\sqrt{s}$=13 TeV with the ATLAS detector". *JHEP* 12.CERN-EP-2017-162 (2017), p. 085. DOI: 10.1007/JHEP12(2017)085. arXiv: 1709.04183 [hep-ex] (cit. on pp. 7, 8, 120, 122, 124).

[4] Steven Weinberg. "A Model of Leptons". *Phys. Rev. Lett.* 19 (21 1967), pp. 1264–1266. DOI: 10.1103/PhysRevLett.19.1264 (cit. on p. 12).

[5] M. J. G. Veltman. "The Infrared - Ultraviolet Connection". *Acta Phys. Polon.* B12.Print-80-0851 (MICHIGAN) (1981), p. 437 (cit. on p. 12).

[6] Stephen P. Martin. "A Supersymmetry primer". FERMILAB-PUB-97-425-T (1997). [Adv. Ser. Direct. High Energy Phys.18,1(1998)], pp. 1–98. DOI: 10.1142/9789812839657_0001. arXiv: hep-ph/9709356 [hep-ph] (cit. on pp. 15, 18).

[7] Y. Akrami et al. "Planck 2018 results. I. Overview and the cosmological legacy of Planck" (2018). arXiv: 1807.06205 [astro-ph.CO] (cit. on p. 17).

[8] Lawrence J. Hall, David Pinner, and Joshua T. Ruderman. "A natural SUSY Higgs near 125 GeV". *Journal of High Energy Physics* 2012.4 (2012), p. 131. ISSN: 1029-8479. DOI: 10.1007/JHEP04(2012)131 (cit. on p. 19).

[9] ATLAS collaboration. "Search for direct top squark pair production in the 3-body decay mode with a final state containing one lepton, jets, and missing transverse momentum in $\sqrt{s} = 13$TeV pp collision data with the ATLAS detector". ATLAS-CONF-2019-017 (May 2019) (cit. on p. 20).

[10] Johan Alwall, Philip Schuster, and Natalia Toro. "Simplified Models for a First Characterization of New Physics at the LHC". *Phys. Rev. D* 79 (2009), p. 075020. DOI: 10.1103/PhysRevD.79.075020. arXiv: 0810.3921 [hep-ph] (cit. on p. 19).

[11] Claus Horn. "A Bottom-Up Approach to SUSY Analyses". *J. Phys. G* 36 (2009), p. 105005. DOI: 10.1088/0954-3899/36/10/105005. arXiv: 0905.4497 [hep-ex] (cit. on p. 19).

[12] Wim Beenakker et al. "Supersymmetric top and bottom squark production at hadron colliders". *JHEP* 08.CERN-PH-TH-2010-142, ITFA-2010-015, ITP-UU-10-17, NIKHEF-2010-016, TTK-10-33 (2010), p. 098. DOI: 10.1007/JHEP08(2010)098. arXiv: 1006.4771 [hep-ph] (cit. on pp. 20, 43).

[13] Lyndon Evans and Philip Bryant. "LHC Machine". *JINST* 3 (2008), S08001. DOI: 10.1088/1748-0221/3/08/S08001 (cit. on p. 22).

[14] CERN. "LEP Design Report: Vol.2. The LEP Main Ring". CERN-LEP-84-01 (June 1984) (cit. on p. 22).

[15] Esma Mobs. "The CERN accelerator complex - August 2018. Complexe des accélérateurs du CERN - Août 2018". OPEN-PHO-ACCEL-2018-005 (2018). General Photo. URL: http://cds.cern.ch/record/2636343 (cit. on p. 23).

[16] Werner Herr and B Muratori. "Concept of luminosity" (2006). DOI: 10.5170/CERN-2006-002.361. URL: https://cds.cern.ch/record/941318 (cit. on p. 22).

[17] Joao Pequenao. "Computer generated image of the whole ATLAS detector". 2008. URL: https://cds.cern.ch/record/1095924 (cit. on p. 24).

[18] G. Aad et al. "The ATLAS Experiment at the CERN Large Hadron Collider". *JINST* 3 (2008), S08003. DOI: 10.1088/1748-0221/3/08/S08003 (cit. on pp. 24, 25, 30–36).

[19] ATLAS collaboration. "ATLAS inner detector: Technical design report. Vol. 1". CERN-LHCC-97-16, ATLAS-TDR-4 (Apr. 1997) (cit. on p. 26).

[20] M. Capeans et al. "ATLAS Insertable B-Layer Technical Design Report". CERN-LHCC-2010-013, ATLAS-TDR-19 (Sept. 2010) (cit. on pp. 26, 27).

[21] G. Aad et al. "ATLAS pixel detector electronics and sensors". *JINST* 3 (2008), P07007. DOI: 10.1088/1748-0221/3/07/P07007 (cit. on p. 26).

[22] A. Abdesselam et al. "The barrel modules of the ATLAS semiconductor tracker". *Nucl. Instrum. Meth. A* 568.ATL-COM-INDET-2006-009, ATL-INDET-PUB-2006-005 (2006), pp. 642–671. DOI: 10.1016/j.nima.2006.08.036 (cit. on p. 27).

[23] A. Abdesselam et al. "The ATLAS semiconductor tracker end-cap module". *Nucl. Instrum. Meth. A* 575 (2007), pp. 353–389. DOI: 10.1016/j.nima.2007.02.019 (cit. on p. 27).

[24] E. Abat et al. "The ATLAS TRT end-cap detectors". *JINST* 3 (2008), P10003. DOI: 10.1088/1748-0221/3/10/P10003 (cit. on p. 28).

[25] ATLAS collaboration. "ATLAS liquid argon calorimeter: Technical design report". CERN-LHCC-96-41 (Dec. 1996) (cit. on p. 28).

[26] ATLAS collaboration. "ATLAS tile calorimeter: Technical design report". CERN-LHCC-96-42 (Dec. 1996) (cit. on p. 28).

[27] J. Abdallah et al. "The Production and Qualification of Scintillator Tiles for the ATLAS Hadronic Calorimeter". ATL-COM-TILECAL-2007-026, ATL-TILECAL-PUB-2007-010 (Dec. 2007) (cit. on pp. 28, 32).

[28] G. Aad et al. "Drift time measurement in the ATLAS liquid argon electromagnetic calorimeter using cosmic muons". *J. Phys. Conf. Ser.* 293 (2011), p. 012050. DOI: 10.1088/1742-6596/293/1/012050 (cit. on p. 29).

[29] I. Wingerter-Seez. "Particle Physics Instrumentation". *Proceedings, 2nd Asia-Europe-Pacific School of High-Energy Physics (AEPSHEP 2014): Puri, India, November 04–17, 2014*. 2017, pp. 295–314. DOI: 10.23730/CYRSP-2017-002.295. arXiv: 1804.11246 [physics.ins-det] (cit. on p. 29).

[30] A. Artamonov et al. "The ATLAS forward calorimeters". *JINST* 3 (2008), P02010. DOI: 10.1088/1748-0221/3/02/P02010 (cit. on p. 29).

[31] Bernard Aubert et al. "Development and construction of large size signal electrodes for the ATLAS electromagnetic calorimeter". *Nucl. Instrum. Meth. A* 539.CERN-PH-EP-2004-019 (2005), pp. 558–594. DOI: 10.1016/j.nima.2004.11.005 (cit. on p. 29).

[32] M.L Andrieux et al. "Construction and test of the first two sectors of the ATLAS barrel liquid argon presampler". *Nucl. Instrum. Meth. A* 479 (2002), pp. 316–333. DOI: 10.1016/S0168-9002(01)00943-3 (cit. on p. 29).

[33] J. Abdallah et al. "Mechanical construction and installation of the ATLAS tile calorimeter". *JINST* 8 (2013), T11001. DOI: 10.1088/1748-0221/8/11/T11001 (cit. on p. 32).

[34] G. Avoni et al. "The new LUCID-2 detector for luminosity measurement and monitoring in ATLAS". *Journal of Instrumentation* 13.07 (2018), P07017–P07017. DOI: 10.1088/1748-0221/13/07/p07017 (cit. on p. 36).

[35] Georges Aad et al. "Operation of the ATLAS trigger system in Run 2". CERN-EP-2020-109 (July 2020). arXiv: 2007.12539 [physics.ins-det] (cit. on p. 37).

[36] Peter Jenni, Marzio Nessi, and Markus Nordberg. *Zero Degree Calorimeters for ATLAS*. Tech. rep. CERN-LHCC-2007-001. LHCC-I-016. Geneva: CERN, 2007. URL: https://cds.cern.ch/record/1009649 (cit. on p. 36).

[37] ATLAS collaboration. *LuminosityPublicResultsRun2*. https://twiki.cern.ch/twiki/bin/view/AtlasPublic/LuminosityPublicResultsRun2 (cit. on p. 38).

[38] ATLAS collaboration. "Luminosity determination in pp collisions at $\sqrt{s} = 13$ TeV using the ATLAS detector at the LHC". ATLAS-CONF-2019-021 (June 2019) (cit. on p. 38).

[39] Morad Aaboud et al. "Performance of the ATLAS Trigger System in 2015". *Eur. Phys. J. C* 77.CERN-EP-2016-241 (2017), p. 317. DOI: 10.1140/epjc/s10052-017-4852-3. arXiv: 1611.09661 [hep-ex] (cit. on p. 38).

[40] Georges Aad et al. "Performance of the missing transverse momentum triggers for the ATLAS detector during Run-2 data taking". *JHEP* 08.CERN-EP-2020-050 (2020), p. 080. DOI: 10.1007/JHEP08(2020)080. arXiv: 2005.09554 [hep-ex] (cit. on pp. 39–41).

[41] G. Aad et al. "Performance of electron and photon triggers in ATLAS during LHC Run 2". *The European Physical Journal C* 80.1 (2020). ISSN: 1434-6052. DOI: 10.1140/epjc/s10052-019-7500-2 (cit. on pp. 39, 40).

[42] Georges Aad et al. "Performance of the ATLAS muon triggers in Run 2". *JINST* 15.CERN-EP-2020-031 (2020), P09015. DOI: 10.1088/1748-0221/15/09/p09015. arXiv: 2004.13447 [hep-ex] (cit. on pp. 39, 40).

[43] S. Agostinelli et al. "Geant4 - a simulation toolkit". *Nuclear Instruments and Methods in Physics Research Section A: Accelerators, Spectrometers, Detectors and Associated Equipment* 506.3 (2003), pp. 250–303. DOI: 10.1016/S0168-9002(03)01368-8 (cit. on p. 40).

[44] ATLAS collaboration. "The simulation principle and performance of the ATLAS fast calorimeter simulation FastCaloSim". ATL-PHYS-PUB-2010-013, ATL-COM-PHYS-2010-838 (Oct. 2010) (cit. on p. 41).

[45] Torbjörn Sjöstrand, Stephen Mrenna, and Peter Z. Skands. "PYTHIA 6.4 Physics and Manual". *JHEP* 05 (2006), p. 026. DOI: 10.1088/1126-6708/2006/05/026 (cit. on p. 41).

[46] Torbjörn Sjöstrand, Stephen Mrenna, and Peter Z. Skands. "A Brief Introduction to PYTHIA 8.1". *Comput. Phys. Commun.* 178 (2008), pp. 852–867. DOI: 10.1016/j.cpc.2008.01.036 (cit. on p. 41).

[47] ATLAS collaboration. "The Pythia 8 A3 tune description of ATLAS minimum bias and inelastic measurements incorporating the Donnachie-Landshoff diffractive model". ATL-PHYS-PUB-2016-017 (Aug. 2016) (cit. on p. 41).

[48] ATLAS collaboration. "ATLAS Pythia 8 tunes to 7 TeV datas". ATL-PHYS-PUB-2014-021 (Nov. 2014) (cit. on pp. 41, 43, 104).

[49] J. Alwall et al. "The automated computation of tree-level and next-to-leading order differential cross sections, and their matching to parton shower simulations". *JHEP* 07 (2014), p. 079. DOI: 10.1007/JHEP07(2014)079 (cit. on pp. 41–43).

[50] D.J. Lange. "The EvtGen particle decay simulation package". *Nucl. Instrum. Meth. A* 462 (2001). Ed. by S. Erhan, P. Schlein, and Y. Rozen, pp. 152–155. DOI: 10.1016/S0168-9002(01)00089-4 (cit. on p. 41).

[51] T. Gleisberg et al. "Event generation with SHERPA 1.1". *JHEP* 02.FERMILAB-PUB-08-477-T, SLAC-PUB-13420, ZU-TH-17-08, DCPT-08-138, EDINBURGH-2008-30, IPPP-08-69, MCNET-08-14 (2009), p. 007. DOI: 10.1088/1126-6708/2009/02/007. arXiv: 0811.4622 [hep-ph] (cit. on p. 41).

[52] Simone Alioli et al. "A general framework for implementing NLO calculations in shower Monte Carlo programs: the POWHEG BOX". *JHEP* 06.DESY-10-018, SFB-CPP-10-22, IPPP-10-11, DCPT-10-22 (2010), p. 043. DOI: 10.1007/JHEP06(2010)043. arXiv: 1002.2581 [hep-ph] (cit. on p. 42).

[53] Johannes Bellm et al. "Herwig 7.0/Herwig++ 3.0 release note". *Eur. Phys. J.* C76.4 (2016), p. 196. DOI: 10.1140/epjc/s10052-016-4018-8 (cit. on p. 42).

[54] Stefano Catani et al. "Vector boson production at hadron colliders: a fully exclusive QCD calculation at NNLO". *Phys. Rev. Lett.* 103 (2009), p. 082001. DOI: 10.1103/PhysRevLett.103.082001. arXiv: 0903.2120 [hep-ph] (cit. on p. 43).

[55] ATLAS collaboration. "Modelling of rare top quark processes at $\sqrt{s}$ = 13 TeV in ATLAS". ATL-PHYS-PUB-2020-024 (Sept. 2020) (cit. on p. 43).

[56] Michał Czakon, Paul Fiedler, and Alexander Mitov. "Total Top-Quark Pair-Production Cross Section at Hadron Colliders Through $\mathcal{O}(\alpha_S^4)$". *Phys. Rev. Lett.* 110.CERN-PH-TH-2013-056, TTK-13-08 (2013), p. 252004. DOI: 10.1103/PhysRevLett.110.252004. arXiv: 1303.6254 [hep-ph] (cit. on p. 43).

[57] Michal Czakon and Alexander Mitov. "NNLO corrections to top pair production at hadron colliders: the quark-gluon reaction". *JHEP* 01.CERN-PH-TH-2012-286 (2013), p. 080. DOI: 10.1007/JHEP01(2013)080. arXiv: 1210.6832 [hep-ph] (cit. on p. 43).

[58] Michal Czakon and Alexander Mitov. "NNLO corrections to top-pair production at hadron colliders: the all-fermionic scattering channels". *JHEP* 12.CERN-PH-TH-2012-181 (2012), p. 054. DOI: 10.1007/JHEP12(2012)054. arXiv: 1207.0236 [hep-ph] (cit. on p. 43).

[59] Peter Bärnreuther, Michal Czakon, and Alexander Mitov. "Percent Level Precision Physics at the Tevatron: First Genuine NNLO QCD Corrections to $q\bar{q} \to t\bar{t} + X$". *Phys. Rev. Lett.* 109.CERN-PH-TH-2012-092 (2012), p. 132001. DOI: 10.1103/PhysRevLett.109.132001. arXiv: 1204.5201 [hep-ph] (cit. on p. 43).

[60] Matteo Cacciari et al. "Top-pair production at hadron colliders with next-to-next-to-leading logarithmic soft-gluon resummation". *Phys. Lett.* B710.CERN-PH-TH-2011-277, TTK-11-54 (2012), pp. 612–622. DOI: 10.1016/j.physletb.2012.03.013. arXiv: 1111.5869 [hep-ph] (cit. on p. 43).

[61] Michal Czakon and Alexander Mitov. "Top++: A Program for the Calculation of the Top-Pair Cross-Section at Hadron Colliders". *Comput. Phys. Commun.* 185.CERN-PH-TH-2011-303, TTK-11-58 (2014), p. 2930. DOI: 10.1016/j.cpc.2014.06.021. arXiv: 1112.5675 [hep-ph] (cit. on p. 43).

[62] Nikolaos Kidonakis. "Next-to-next-to-leading-order collinear and soft gluon corrections for t-channel single top quark production". *Phys. Rev.* D83 (2011), p. 091503. DOI: 10.1103/PhysRevD.83.091503. arXiv: 1103.2792 [hep-ph] (cit. on p. 43).

[63] Nikolaos Kidonakis. "Two-loop soft anomalous dimensions for single top quark associated production with a W^- or H^-". *Phys. Rev.* D82 (2010), p. 054018. DOI: 10.1103/PhysRevD.82.054018. arXiv: 1005.4451 [hep-ph] (cit. on p. 43).

[64] Nikolaos Kidonakis. "NNLL resummation for s-channel single top quark production". *Phys. Rev.* D81 (2010), p. 054028. DOI: 10.1103/PhysRevD.81.054028. arXiv: 1001.5034 [hep-ph] (cit. on p. 43).

[65] ATLAS collaboration. "Multi-Boson Simulation for 13 TeV ATLAS Analyses". ATL-PHYS-PUB-2017-005 (May 2017) (cit. on p. 43).

[66] ATLAS collaboration. "Multijet simulation for 13 TeV ATLAS Analyses". ATL-PHYS-PUB-2019-017 (2019) (cit. on p. 43).

[67] Wim Beenakker et al. "NNLL-fast: predictions for coloured supersymmetric particle production at the LHC with threshold and Coulomb resummation". *JHEP* 12.MS-TP-16-17, NIKHEF-2016-037, TTK-16-28 (2016), p. 133. DOI: 10.1007/JHEP12(2016)133. arXiv: 1607.07741 [hep-ph] (cit. on p. 43).

[68] W. Beenakker et al. "Stop production at hadron colliders". *Nucl. Phys. B* 515.RAL-TR-97-056, DESY-97-214, CERN-TH-97-177 (1998), pp. 3–14. DOI: 10.1016/S0550-3213(98)00014-5. arXiv: hep-ph/9710451 (cit. on p. 43).

[69] Wim Beenakker et al. "NNLL resummation for stop pair-production at the LHC". *JHEP* 05.MS-TP-16-01, TTK-16-01, NIKHEF-2016-002 (2016), p. 153. DOI: 10.1007/JHEP05(2016)153. arXiv: 1601.02954 [hep-ph] (cit. on p. 43).

[70] Hung-Liang Lai et al. "New parton distributions for collider physics". *Phys. Rev. D* 82.MSUHEP-100707, SMU-HEP-10-10 (2010), p. 074024. DOI: 10.1103/PhysRevD.82.074024. arXiv: 1007.2241 [hep-ph] (cit. on p. 43).

[71] M. Aaboud et al. "Performance of the ATLAS Track Reconstruction Algorithms in Dense Environments in LHC Run 2". *Eur. Phys. J. C* 77.CERN-EP-2017-045 (2017), p. 673. DOI: 10.1140/epjc/s10052-017-5225-7. arXiv: 1704.07983 [hep-ex] (cit. on p. 44).

[72] R. Fruhwirth. "Application of Kalman filtering to track and vertex fitting". *Nucl. Instrum. Meth. A* 262.HEPHY-PUB-87-503 (1987), pp. 444–450. DOI: 10.1016/0168-9002(87)90887-4 (cit. on p. 44).

[73] G. Piacquadio, Kirill Prokofiev, and A. Wildauer. "Primary vertex reconstruction in the ATLAS experiment at LHC". *J. Phys. Conf. Ser.* 119 (2008), p. 032033. DOI: 10.1088/1742-6596/119/3/032033 (cit. on p. 46).

[74] R. Fruhwirth, W. Waltenberger, and P. Vanlaer. "Adaptive vertex fitting". *J. Phys. G* 34.CERN-CMS-NOTE-2007-008, CMS-NOTE-2007-008 (2007), N343. DOI: 10.1088/0954-3899/34/12/N01 (cit. on p. 46).

[75] ATLAS Collaboration. "Topological cell clustering in the ATLAS calorimeters and its performance in LHC Run 1". *Eur. Phys. J. C* 77.CERN-PH-EP-2015-304 (2017), p. 490. DOI: 10.1140/epjc/s10052-017-5004-5. arXiv: 1603.02934 [hep-ex] (cit. on pp. 46, 50).

[76] ATLAS collaboration. "Improved electron reconstruction in ATLAS using the Gaussian Sum Filter-based model for bremsstrahlung". ATLAS-CONF-2012-047 (May 2012) (cit. on p. 47).

[77] Georges Aad et al. “Electron and photon performance measurements with the ATLAS detector using the 2015–2017 LHC proton-proton collision data”. *JINST* 14.CERN-EP-2019-145 (2019), P12006. DOI: 10.1088/1748-0221/14/12/P12006. arXiv: 1908.00005 [hep-ex] (cit. on p. 47).

[78] Morad Aaboud et al. “Electron reconstruction and identification in the ATLAS experiment using the 2015 and 2016 LHC proton-proton collision data at $\sqrt{s}$ = 13 TeV”. *Eur. Phys. J. C* 79.CERN-EP-2018-273 (2019), p. 639. DOI: 10.1140/epjc/s10052-019-7140-6. arXiv: 1902.04655 [physics.ins-det] (cit. on pp. 48, 103, 143).

[79] Georges Aad et al. “Muon reconstruction performance of the ATLAS detector in proton–proton collision data at $\sqrt{s}$ =13 TeV”. *Eur. Phys. J. C* 76.CERN-EP-2016-033 (2016), p. 292. DOI: 10.1140/epjc/s10052-016-4120-y. arXiv: 1603.05598 [hep-ex] (cit. on pp. 49, 103, 144).

[80] Matteo Cacciari, Gavin P. Salam, and Gregory Soyez. “The anti-k_t jet clustering algorithm”. *JHEP* 04.LPTHE-07-03 (2008), p. 063. DOI: 10.1088/1126-6708/2008/04/063. arXiv: 0802.1189 [hep-ph] (cit. on p. 50).

[81] ATLAS collaboration. “Tagging and suppression of pileup jets”. ATLAS-CONF-2014-018 (May 2014) (cit. on pp. 51, 102).

[82] ATLAS collaboration. “Selection of jets produced in 13TeV proton-proton collisions with the ATLAS detector”. ATLAS-CONF-2015-029 (July 2015) (cit. on p. 51).

[83] David Krohn, Jesse Thaler, and Lian-Tao Wang. “Jet Trimming”. *JHEP* 02 (2010), p. 084. DOI: 10.1007/JHEP02(2010)084. arXiv: 0912.1342 [hep-ph] (cit. on p. 51).

[84] M. Aaboud et al. “Jet energy scale measurements and their systematic uncertainties in proton-proton collisions at $\sqrt{s} = 13$ TeV with the ATLAS detector”. *Phys. Rev. D* 96.CERN-EP-2017-038 (2017), p. 072002. DOI: 10.1103/PhysRevD.96.072002. arXiv: 1703.09665 [hep-ex] (cit. on pp. 52, 53, 101).

[85] Matteo Cacciari, Gavin P. Salam, and Gregory Soyez. “The Catchment Area of Jets”. *JHEP* 04.LPTHE-07-02 (2008), p. 005. DOI: 10.1088/1126-6708/2008/04/005. arXiv: 0802.1188 [hep-ph] (cit. on pp. 52, 59).

[86] Morad Aaboud et al. “In situ calibration of large-radius jet energy and mass in 13 TeV proton–proton collisions with the ATLAS detector”. *Eur. Phys. J. C* 79.CERN-EP-2018-191 (2019), p. 135. DOI: 10.1140/epjc/s10052-019-6632-8. arXiv: 1807.09477 [hep-ex] (cit. on pp. 52, 54).

[87] David Krohn, Jesse Thaler, and Lian-Tao Wang. "Jets with Variable R". *JHEP* 06 (2009), p. 059. DOI: 10.1088/1126-6708/2009/06/059. arXiv: 0903.0392 [hep-ph] (cit. on p. 54).

[88] Georges Aad et al. "ATLAS b-jet identification performance and efficiency measurement with $t\bar{t}$ events in pp collisions at $\sqrt{s} = 13$ TeV". *Eur. Phys. J. C* 79.CERN-EP-2019-132 (2019), p. 970. DOI: 10.1140/epjc/s10052-019-7450-8. arXiv: 1907.05120 [hep-ex] (cit. on p. 55).

[89] ATLAS collaboration. "Secondary vertex finding for jet flavour identification with the ATLAS detector". ATL-PHYS-PUB-2017-011 (June 2017) (cit. on p. 55).

[90] ATLAS collaboration. "Topological *b*-hadron decay reconstruction and identification of *b*-jets with the JetFitter package in the ATLAS experiment at the LHC". ATL-PHYS-PUB-2018-025 (2018) (cit. on pp. 55, 102).

[91] ATLAS collaboration. "$E_{\mathrm{T}}^{\mathrm{miss}}$ performance in the ATLAS detector using 2015-2016 LHC p-p collisions". ATLAS-CONF-2018-023 (June 2018) (cit. on pp. 57, 102, 103).

[92] ATLAS collaboration. "Object-based missing transverse momentum significance in the ATLAS detector". ATLAS-CONF-2018-038 (July 2018) (cit. on p. 58).

[93] Morad Aaboud et al. "Performance of top-quark and *W*-boson tagging with ATLAS in Run 2 of the LHC". *Eur. Phys. J. C* 79.CERN-EP-2018-192 (2019), p. 375. DOI: 10.1140/epjc/s10052-019-6847-8. arXiv: 1808.07858 [hep-ex] (cit. on pp. 60, 65).

[94] Amal Vaidya et al. *Optimisation procedure for two-variable top, W and Z substructure taggers for the ATLAS detector*. Tech. rep. ATL-COM-PHYS-2017-033. Geneva: CERN, 2017. URL: https://cds.cern.ch/record/2242865 (cit. on p. 59).

[95] ATLAS collaboration. "Jet mass reconstruction with the ATLAS Detector in early Run 2 data". ATLAS-CONF-2016-035 (July 2016) (cit. on p. 61).

[96] Jesse Thaler and Ken Van Tilburg. "Identifying Boosted Objects with N-subjettiness". *JHEP* 03.MIT-CTP-4191 (2011), p. 015. DOI: 10.1007/JHEP03(2011)015. arXiv: 1011.2268 [hep-ph] (cit. on p. 61).

[97] Jesse Thaler and Ken Van Tilburg. "Maximizing Boosted Top Identification by Minimizing N-subjettiness". *JHEP* 02.MIT-CTP-4287 (2012), p. 093. DOI: 10.1007/JHEP02(2012)093. arXiv: 1108.2701 [hep-ph] (cit. on p. 61).

[98] Andrew J. Larkoski, Gavin P. Salam, and Jesse Thaler. "Energy Correlation Functions for Jet Substructure". *JHEP* 06.MIT-CTP-4446, CERN-PH-TH-2013-066, LPN13-026 (2013), p. 108. DOI: 10.1007/JHEP06(2013)108. arXiv: 1305.0007 [hep-ph] (cit. on p. 61).

[99] Andrew J. Larkoski, Ian Moult, and Duff Neill. "Analytic Boosted Boson Discrimination". *JHEP* 05.MIT-CTP-4681 (2016), p. 117. DOI: 10.1007/JHEP05(2016)117. arXiv: 1507.03018 [hep-ph] (cit. on p. 61).

[100] Ian Moult, Lina Necib, and Jesse Thaler. "New Angles on Energy Correlation Functions". *JHEP* 12.MIT-CTP-4825 (2016), p. 153. DOI: 10.1007/JHEP12(2016)153. arXiv: 1609.07483 [hep-ph] (cit. on p. 61).

[101] S. Bethke et al. "New jet cluster algorithms: Next-to-leading order QCD and hadronization corrections". *Nucl. Phys. B* 370.CERN-TH-6222-91 (1992). [Erratum: Nucl.Phys.B 523, 681–681 (1998)], pp. 310–334. DOI: 10.1016/0550-3213(92)90289-N (cit. on p. 61).

[102] Stephen D. Ellis and Davison E. Soper. "Successive combination jet algorithm for hadron collisions". *Phys. Rev. D* 48.CERN-TH-6860-93 (1993), pp. 3160–3166. DOI: 10.1103/PhysRevD.48.3160. arXiv: hep-ph/9305266 (cit. on p. 61).

[103] Jesse Thaler and Lian-Tao Wang. "Strategies to Identify Boosted Tops". *JHEP* 07 (2008), p. 092. DOI: 10.1088/1126-6708/2008/07/092. arXiv: 0806.0023 [hep-ph] (cit. on p. 61).

[104] Carola F. Berger, Tibor Kucs, and George F. Sterman. "Event shape / energy flow correlations". *Phys. Rev. D* 68.YITP-SB-03-06 (2003), p. 014012. DOI: 10.1103/PhysRevD.68.014012. arXiv: hep-ph/0303051 (cit. on p. 61).

[105] Andrew J. Larkoski, Ian Moult, and Duff Neill. "Power Counting to Better Jet Observables". *JHEP* 12.MIT–CTP-4588 (2014), p. 009. DOI: 10.1007/JHEP12(2014)009. arXiv: 1409.6298 [hep-ph] (cit. on p. 62).

[106] François Chollet et al. *Keras*. https://keras.io. 2015 (cit. on pp. 64, 65).

[107] The Theano Development Team et al. *Theano: A Python framework for fast computation of mathematical expressions*. 2016. arXiv: 1605.02688 [cs.SC] (cit. on pp. 64, 65).

[108] Diederik P. Kingma and Jimmy Ba. *Adam: A Method for Stochastic Optimization*. 2014. arXiv: 1412.6980 [cs.LG] (cit. on pp. 64, 65).

[109] ATLAS collaboration. "Boosted hadronic vector boson and top quark tagging with ATLAS using Run 2 data". ATL-PHYS-PUB-2020-017 (Aug. 2020) (cit. on p. 64).

[110] Daniel Hay Guest et al. *lwtnn/lwtnn*. Version Release for athena v21. 2017 (cit. on p. 65).

[111] Georges Aad et al. "Performance of jet substructure techniques for large-R jets in proton-proton collisions at $\sqrt{s}$ = 7 TeV using the ATLAS detector". *JHEP* 09.CERN-PH-EP-2013-069 (2013), p. 076. DOI: 10.1007/JHEP09(2013)076. arXiv: 1306.4945 [hep-ex] (cit. on p. 71).

[112] G. Ridolfi and S. Forte. "Renormalization and factorization scale dependence of observables in QCD". *J. Phys. G* 25 (1999). Ed. by R. Devenish and W.James Stirling, pp. 1555–1556. DOI: 10.1088/0954-3899/25/7/351 (cit. on p. 71).

[113] ATLAS Collaboration. "Search for a scalar partner of the top quark in the jets plus missing transverse momentum final state at $\sqrt{s}$=13 TeV with the ATLAS detector". *JHEP* 12.CERN-EP-2017-162 (2017), p. 085. DOI: 10.1007/JHEP12(2017)085. arXiv: 1709.04183 [hep-ex] (cit. on p. 77).

[114] C. G. Lester and D. J. Summers. "Measuring masses of semi-invisibly decaying particle pairs produced at hadron colliders". *Phys. Lett. B* 463 (1999), pp. 99–103. DOI: 10.1016/S0370-2693(99)00945-4. arXiv: hep-ph/9906349 (cit. on p. 77).

[115] Christopher G. Lester and Benjamin Nachman. "Bisection-based asymmetric MT2 computation: a higher precision calculator than existing symmetric methods". *Journal of High Energy Physics* 2015.3 (2015), p. 100. ISSN: 1029-8479. DOI: 10.1007/JHEP03(2015)100 (cit. on p. 77).

[116] Cowan G. "Discovery sensitivity for a counting experiment with background uncertainty" (2012). URL: http://www.pp.rhul.ac.uk/~cowan/stat/medsig/medsigNote.pdf (cit. on p. 79).

[117] Georges Aad et al. "Jet energy scale and resolution measured in proton-proton collisions at $\sqrt{s} = 13$ TeV with the ATLAS detector". CERN-EP-2020-083 (July 2020). arXiv: 2007.02645 [hep-ex] (cit. on pp. 101, 102).

[118] Georges Aad et al. "Jet energy measurement and its systematic uncertainty in proton-proton collisions at $\sqrt{s} = 7$ TeV with the ATLAS detector". *Eur. Phys. J. C* 75 (2015), p. 17. DOI: 10.1140/epjc/s10052-014-3190-y. arXiv: 1406.0076 [hep-ex] (cit. on p. 101).

[119] William Buttinger. *Using Event Weights to account for differences in Instantaneous Luminosity and Trigger Prescale in Monte Carlo and Data*. Tech. rep. ATL-COM-SOFT-2015-119. Geneva: CERN, 2015. URL: https://cds.cern.ch/record/2014726 (cit. on p. 103).

[120] John Kenneth Anders and Monica D'Onofrio. *V+Jets theoretical uncertainties estimation via a parameterisation method*. Tech. rep. ATL-COM-PHYS-2016-044. Geneva: CERN, 2016. URL: https://cds.cern.ch/record/2125718 (cit. on p. 103).

[121] Chris D. White et al. "Isolating Wt production at the LHC". *JHEP* 11.NIKHEF-2009-013, CERN-TH-2009-136, ITF-UU-09-31, CP3-09-33 (2009), p. 074. DOI: 10.1088/1126-6708/2009/11/074. arXiv: 0908.0631 [hep-ph] (cit. on p. 104).

[122] Kyle Cranmer et al. *HistFactory: A tool for creating statistical models for use with RooFit and RooStats*. Tech. rep. CERN-OPEN-2012-016. New York: New York U., 2012. URL: https://cds.cern.ch/record/1456844 (cit. on p. 105).

[123] Lorenzo Moneta et al. "The RooStats Project". *PoS* ACAT2010 (2010). Ed. by T. Speer et al., p. 057. DOI: 10.22323/1.093.0057. arXiv: 1009.1003 (cit. on p. 105).

[124] Wouter Verkerke and David P. Kirkby. "The RooFit toolkit for data modeling". *eConf* C0303241.CHEP-2003-MOLT007 (2003). Ed. by L. Lyons and Muge Karagoz, MOLT007. arXiv: physics/0306116 (cit. on p. 105).

[125] M. Baak et al. "HistFitter software framework for statistical data analysis". *The European Physical Journal C* 75.4 (2015), p. 153. ISSN: 1434-6052. DOI: 10.1140/epjc/s10052-015-3327-7 (cit. on p. 105).

[126] Walter W. Hauck and Allan Donner. "Wald's Test as Applied to Hypotheses in Logit Analysis". *Journal of the American Statistical Association* 72.360 (1977), pp. 851–853. ISSN: 01621459. URL: http://www.jstor.org/stable/2286473 (cit. on p. 108).

[127] Glen Cowan et al. "Asymptotic formulae for likelihood-based tests of new physics". *Eur. Phys. J. C* 71 (2011). [Erratum: Eur.Phys.J.C 73, 2501 (2013)], p. 1554. DOI: 10.1140/epjc/s10052-011-1554-0. arXiv: 1007.1727 (cit. on p. 108).

[128] Alexander L. Read. "Modified frequentist analysis of search results (The CL(s) method)". *Workshop on Confidence Limits*. CERN-OPEN-2000-205. Aug. 2000, pp. 81–101 (cit. on p. 110).

[129] Georges Aad et al. "Search for a scalar partner of the top quark in the all-hadronic $t\bar{t}$ plus missing transverse momentum final state at $\sqrt{s}$=13 TeV with the ATLAS detector". *Eur. Phys. J. C* 80.CERN-EP-2020-044 (2020), p. 737. DOI: 10.1140/epjc/s10052-020-8102-8. arXiv: 2004.14060 [hep-ex] (cit. on pp. 120, 123).

[130] Albert M Sirunyan et al. "Searches for physics beyond the standard model with the M_{T2} variable in hadronic final states with and without disappearing tracks in proton-proton collisions at $\sqrt{s} = 13$ TeV". *Eur. Phys. J. C* 80.CMS-SUS-19-005, CERN-EP-2019-180 (2020), p. 3. DOI: 10.1140/epjc/s10052-019-7493-x. arXiv: 1909.03460 [hep-ex] (cit. on p. 127).

[131] ATLAS Collaboration. *SUSY July 2020 Summary Plot Update*. Tech. rep. ATL-PHYS-PUB-2020-020. Geneva: CERN, 2020. URL: http://cds.cern.ch/record/2725258 (cit. on p. 128).

[132] ATLAS Collaboration. *Search for new phenomena in events with two opposite-charge leptons, jets and missing transverse momentum in pp collisions at* $\sqrt{s} =$ 13 *TeV with the ATLAS detector*. Tech. rep. ATLAS-CONF-2020-046. Geneva: CERN, 2020. URL: http://cds.cern.ch/record/2728056 (cit. on p. 128).

[133] ATLAS Collaboration. *Search for new phenomena with top quark pairs in final states with one lepton, jets, and missing transverse momentum in pp collisions at* $\sqrt{s} = 13$ *TeV with the ATLAS detector*. Tech. rep. ATLAS-CONF-2020-003. Geneva: CERN, 2020. URL: https://cds.cern.ch/record/2711489 (cit. on p. 128).

[134] Michael L. Graesser and Jessie Shelton. "Hunting Mixed Top Squark Decays". *Phys. Rev. Lett.* 111.12 (2013), p. 121802. DOI: 10.1103/PhysRevLett.111.121802. arXiv: 1212.4495 [hep-ph] (cit. on p. 128).

Appendices

A Discussion on the physical objects used in the event reconstruction

The reconstruction of the physical objects is limited by the performance and coverage of the sub-detectors. The coverage of the inner detector is in the range of $|\eta|$ <2.5, which affects all the reconstruction requiring the track information.

In the reconstruction of the electrons, all the electron candidates need tracks matched with topo-clusters, which results in the requirement of $|\eta|$ <2.47 for the precision measurements. The lowest p_{T} (4.5 GeV) of the electron candidates is limited by the calibration of the efficiency and energy by using $J/\Psi \to ee$ and $Z \to ee$ samples. If the p_{T} is smaller than 4.5 GeV, the Monte Carlo simulation cannot be trusted. Figure 73 (a) shows the efficiencies of three working points, *Loose*, *Medium*, and *Tight*. *LooseAndBLayer* is required for the *baseline* electrons. *Loose* shows the highest efficiencies. The additional requirement of the hit in the innermost layer for the *LooseAndBLayer* criteria reduces the background from photon conversions. The *signal* electrons require *Tight* criteria for the identification and *Fix (Loose)* for the isolation. *Tight* criteria have 5 times higher background rejection against the multijet production. *Fix (Loose)* shows the flat efficiencies above 20 GeV as shown in Figure 73 (b).

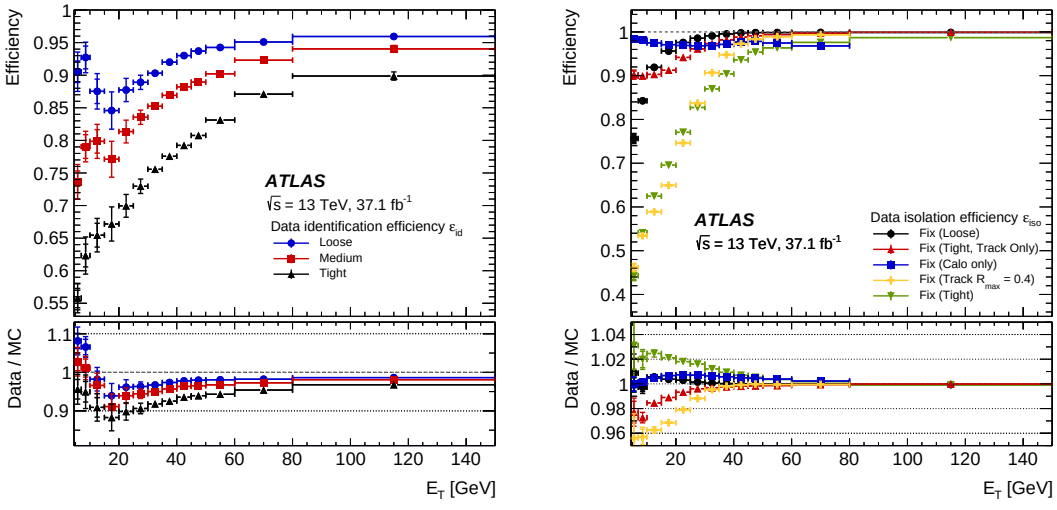

(a) (b)

Figure 73: Data (a) identification and (b) isolation efficiency as a function of p_{T} [78].

Table 32: Efficiency for the prompt muons from W decays and non-prompt muon from the hadronic decays with four working points by using $t\bar{t}$ MC samples [79].

	$4 < p_{\mathrm{T}} < 20$ GeV		$20 < p_{\mathrm{T}} < 100$ GeV	
Selection	$\epsilon_{\mu}^{\mathrm{MC}}$ [%]	$\epsilon_{\mathrm{Hadrons}}^{\mathrm{MC}}$ [%]	$\epsilon_{\mu}^{\mathrm{MC}}$ [%]	$\epsilon_{\mathrm{Hadrons}}^{\mathrm{MC}}$ [%]
Loose	96.7	0.53	98.1	0.76
Medium	95.5	0.38	96.1	0.17
Tight	89.9	0.19	91.8	0.11
High-p_{T}	78.1	0.26	80.4	0.13

In the reconstruction of the muons, the coverage of pseudorapidity in the muon spectrometers is up to 2.7. Therefore, the reconstruction of muon can be in the range of $|\eta|$ <2.7. The lowest p_{T} (4 GeV) of the muon candidates is due the calibration of the efficiency and energy by using $J/\Psi \to \mu\mu$ and $Z \to \mu\mu$ samples. Table 32 shows the efficiencies of the identification of prompt muons and the misidentification of non-prompt muon from hadronic decays. *Medium* criteria show high efficiencies in low and high p_{T} region and good background rejection in high p_{T} region, which is the best choice for the boosted topology with zero lepton. *FixedCutLoose* keeps high efficiency of prompt muons and high rejection of non-prompt muon in the high p_{T} region. Figure 74 shows the efficiencies and scale factors of *FixedCutLoose* isolation with *Medium* criteria.

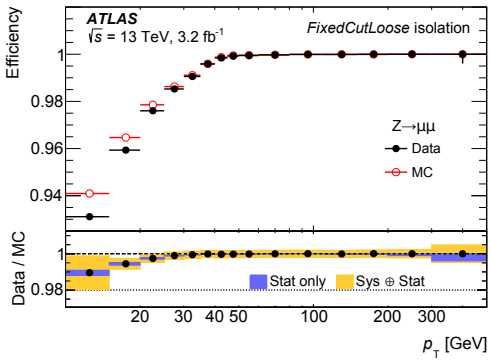

Figure 74: Data and MC efficiencies of the *FixedCutLoose* isolation with the *Medium* criteria in $Z \to \mu\mu$ events [79].

For the reconstruction of small-*R* jets, the jet response in the central region ($|\eta| <$ 3.2) is well understood as shown in Figure 27 (a). By taking the radius of small-*R* jets into account, the pseudorapidity is required to be smaller than 2.8. The available p_{T} is also limited from the calibration of jet energy scale by Z+jets samples. For this thesis, we are aiming for the boosted topology. The requirement of 20 GeV is not critical in the stop analysis.

B Impact on the extrapolation of signal scale factors of DNN top taggers

The uncertainties of the signal scale factors evaluated in Chapter 5 are evaluated in the large-R jet p_{T} range up to 1 TeV. The extrapolation from 1 TeV is directly from the information of the last bin. In this section, the impact on the stop analysis from the extrapolation is estimated. The signal region A and benchmark signal point ($m_{\tilde{t}}$,$m_{\tilde{\chi}_1^0}$) = (1300,1) GeV are used for the high stop mass region. The post-fit results of the yields and uncertainties are shown in Tables 26 and 24. In Table 24, the "Large-R jet + DNN" represents the uncertainties of the scale factors and JES for the large-R jets. To test the signal scale factors in high p_{T} range, the "Large-R jet + DNN" uncertainties of events with leading large-R jet p_{T} higher than 1 TeV are replaced into 100%. The modified uncertainties of signal scale factors are only applied to $\mathrm{t\bar{t}}$, $\mathrm{t\bar{t}}Z$, and single top samples. The effect on the uncertainties of the signal scale factors is estimated by using expected discovery significance as shown in Eq. 45.

Table 33 shows the results with the original and modified uncertainties. The correlation of nuisance parameters is not considered in this study. The total uncertainties are calculated in the root of the quadratic sum. SRATT-1b shows the 12% difference of total uncertainties, but $Z_{0,A}$ shows the only 5% difference, which affects the upper limit of the cross section for the stop production. By using the quadratic sum of significance in each region, the values of the total significance are 2.55 for the original uncertainties and 2.51 for the modified uncertainties. Less than 2% decrease is found. If the modified uncertainties are included in the fit, the impact can be neglected.

Table 33: Comparisons of the results between original and modified "Large-R jet + DNN" uncertainties. "Signal yields" column shows the yields of ($m_{\tilde{t}}$,$m_{\tilde{\chi}_1^0}$) = (1300,1) GeV. "SM yields" shows the total SM background predictions. "Events ($>$ 1 TeV)" shows the yields with the leading large-R jet p_{T} over 1 TeV. "Systematics" column shows uncertainties in yields with original and modified "Large-R jet + DNN" uncertainties. "$Z_{0,A}$" column shows expected discovery significance with original and modified "Large-R jet + DNN" uncertainties. The numbers in the parenthesis indicate the percentage based on the total SM yields.

Signal regions	Signal yields	SM yields	Events ($>$ 1 TeV)	Systematics		$Z_{0,A}$	
				Original	Modified	Orignal	Modified
SRATT-2b	2.01	0.69	0.05 (7%)	0.34 (49%)	0.37 (54%)	1.61	1.58
SRATW-2b	1.79	1.94	0.01 (1%)	0.42 (22%)	0.42 (22%)	1.08	1.08
SRAT0-2b	1.96	2.44	0.11 (5%)	0.54 (22%)	0.58 (24%)	1.05	1.04
SRATT-1b	1.14	0.74	0.14 (19%)	0.29 (39%)	0.38 (51%)	1.03	0.98
SRATW-1b	1.16	2.80	0.27 (10%)	0.61 (22%)	0.71 (25%)	0.61	0.60
SRAT0-1b	1.51	5.83	0.16 (3%)	1.78 (31%)	1.84 (32%)	0.47	0.47